

**LORENZO NOTARI**

# **DYNAMIC RADIATION EFFECTS INDUCED BY SHORT-PULSED U-ION BEAMS IN METALLIC TARGETS**

*Editorial Series on ACCELERATOR SCIENCE*





**SAPIENZA**  
UNIVERSITÀ DI ROMA

FACOLTÀ DI INGEGNERIA  
CORSO DI LAUREA MAGISTRALE IN INGEGNERIA ENERGETICA  
INDIRIZZO NUCLEARE

# **Dynamic radiation effects induced by short-pulsed U-ion beams in metallic targets**

CANDIDATO:

Lorenzo Notari

RELATORE:

Prof. Michele Pasquali

CO-RELATORE:

dott. Federico Carra

Anno Accademico 2021-2022



*To those who search.*

# Preface and acknowledgements

The thesis originates from the collaboration between the Department of Mechanical and Aerospace Engineering (DIMA) and the Department of Astronautical Electrical and Energy Engineering (DIAEE) of "La Sapienza" University in Rome.

The research presented here is part of the I.FAST (Innovation Fostering in Accelerator Science and Technology) project that has received funding from the European Union's Horizon 2020 Research and Innovation Programme under Grant Agreement No 101004730.

From December 2021 to June 2022, I worked as a trainee at CERN in Geneva. I conducted my research on the radiation-induced effects on components for particle accelerators, and in particular on the "beam windows", as a member of the Mechanical and Materials Engineering - Engineering Design and Simulations Group (EN-MME-EDS).

The research presented here results from the U-ions beams irradiation experiment, held at the M3-Branch of the UNILAC accelerator beamline of the GSI Helmholtzzentrum für Schwerionenforschung in Darmstadt in March 2022.

I'm extremely grateful to Marcello Losasso (IFAST WP4.3 Task Leader) for the opportunity to take part in this exciting research project. I am deeply indebted to Marilena Tomut (Professor at the University of Münster) for her contribution of ideas to the research and for her direction and assistance during the experiments at GSI. I am also thankful to Philipp Bolz (PhD student at GSI) for his assistance with the experiment of microindentation and for the suggestions on how to perform the numerical simulations.

I would like to extend my sincere thanks to Said Atieh (Group Leader MME) and Alessandro Bertarelli (Deputy Group Leader MME-EDS).

A special thanks goes to my colleagues Carlotta Accettura, Jorge Guardia-Valenzuela, Marco Masci and Leonardo Sito of the MME research group at CERN with whom I had the pleasure to collaborate closely and who have always provided me with their constant support and advice.

I cannot forget the help of Marco Garlaschè (CERN workshop) and Michael Kitzmantel (RHP-Technology) for the production of the experimental samples and I thank Anitè Perez for the operation of the SEM microscope.

I want to express my deep gratitude to my CERN supervisor, Federico Carra, who

guided me during the months of my stay in Geneva and throughout this project and who introduced me to this fantastic world of scientific research on particle accelerators. My gratitude also extends to the period following my stay at CERN, when he continued to accompany me as co-advisor in drafting my thesis.

Finally, a real special thanks to Michele Pasquali, my advisor, for giving me the trust that he has granted me and having given me the opportunity to access this area of study that permitted me to embark on such an important experience for both my professional and personal development. Professor Pasquali has followed and encouraged the construction of this thesis at every stage, providing helpful advice and discussing various aspects with me. He has never failed to support me, not only from the scientific point of view.

Obviously, I alone am responsible for what is written.

# Contents

<b>Acronyms</b>	<b>18</b>
<b>1 Introduction</b>	<b>1</b>
1.1 Selection criteria for beam windows materials . . . . .	2
1.1.1 Transparency to beam particles . . . . .	2
1.1.2 Thermal requirements . . . . .	2
1.1.3 Resistance to pressure loads . . . . .	4
1.1.4 Leak tightness . . . . .	5
1.1.5 Machinability and fabrication . . . . .	6
1.1.6 Lifetime and failures . . . . .	7
1.2 Overview of metallic materials adopted for beam windows in relevant ex- perimental facilities . . . . .	10
1.2.1 Beryllium . . . . .	10
1.2.2 Titanium alloys . . . . .	12
1.2.3 Inconel 718 . . . . .	15
1.2.4 Stainless steels . . . . .	18
1.2.5 Aluminium alloys . . . . .	23
1.3 Need for present study . . . . .	31
1.4 Description of the thesis structure . . . . .	32
<b>2 Selection of materials</b>	<b>34</b>
2.1 Description of eligible materials . . . . .	34
2.2 Material selection: figures of merit and other indicators . . . . .	35
2.3 Preliminary analytical findings . . . . .	42
2.3.1 Preliminary thermal analysis . . . . .	42
2.3.2 Preliminary dynamic analysis . . . . .	48
2.4 Materials selection . . . . .	56
2.4.1 Geometry of the samples . . . . .	56
2.4.2 Production of the samples . . . . .	57

<b>3</b>	<b>Experimental investigations</b>	<b>60</b>
3.1	Introduction to GSI facilities . . . . .	60
3.2	Description of the experimental facilities — UNILAC, M-Branch and M3 beamline . . . . .	62
3.3	Description of the experimental setup . . . . .	66
3.3.1	Sample preparation . . . . .	66
3.3.2	<i>In situ</i> measurement instruments . . . . .	68
3.3.3	Report of the experiment . . . . .	69
3.4	Preliminary results of the online monitoring . . . . .	72
3.4.1	Temperature development recorded by the Thermal Camera . . . . .	72
3.4.2	Measurement of beam-induced stress waves by Laser Doppler Vi- brometry . . . . .	77
3.5	Description and results of post irradiation examinations (PIEs) . . . . .	86
3.5.1	Microindentation . . . . .	87
3.5.2	Scanning Electron Microscopy . . . . .	94
<b>4</b>	<b>Numerical and analytical investigations</b>	<b>109</b>
4.1	Radiation effects on materials . . . . .	109
4.1.1	Interaction of charged particles with matter . . . . .	109
4.1.2	Basic concepts of radiation damage . . . . .	111
4.1.3	Evolution of radiation damage and mechanical properties . . . . .	114
4.1.4	The SRIM-2013 code . . . . .	115
4.2	Thermomechanical simulations . . . . .	125
4.2.1	Model description . . . . .	125
4.2.2	Transient thermal simulations . . . . .	129
4.2.3	Modal and Transient structural simulations . . . . .	137
<b>5</b>	<b>Conclusions</b>	<b>146</b>



# List of Figures

1.1	NuMI Beryllium beam window . . . . .	11
1.2	Technical designs and pictures of two Titanium Grade 5 beam windows at CERN: a beam dump (TDE) window (a) at TI8 beamline to transfer protons and ions to the LHC and a beam stopper (TBSE) window (b) at the beginning of the TT41 beamline for protons directed to the CNGS neutrino target [15]. . . . .	13
1.3	Technical designs and pictures of Titanium Grade 5 beam windows at FNAL: an example of vacuum windows in SY120 beamline (a), an example of window failure (b) and a sketch of a typical assembly of a titanium vacuum window (c) [11]. . . . .	14
1.4	Pictures of Titanium Grade 5 beam windows at JPARC neutrino facility: primary beam window (a) and target containment window (b) [28]. . . . .	14
1.5	(a) CAD drawing of the INC718 IPF testing apparatus used to measure beam window deformation under different loading conditions. (b) IPF beam window and weld flange and (c) full beam window assembly [34]. . . . .	16
1.6	First generation curved dual-wall Inconel 718 PBW at the Spallation Neutron Source: (a) Alloy 718 window and frame, (b) complete Alloy 718 window, and (c) cross-sectional view of complete PBW assembly [19]. . . . .	16
1.7	CAD drawings and pictures of the entrance window, showing (a) the 200 $\mu\text{m}$ -thick stainless steel foil and (b) the 15 mm-thick CC plate [39]. . . . .	19
1.8	Sketch (a) and picture (b) of the LHC dump block and surrounding shielding, showing the location of entrance window [17][40]. . . . .	20
1.9	CAD drawings of the new conception of the entrance window for the beam dump of LHC Run 3 and, in the future, of HL-LHC at CERN [40]. . . . .	20
1.10	Schematic view of the MEGAPIE target assembly with the T91 window and the other main components indicated [43]. . . . .	23
1.11	Schematic view of the design of the LBE cooled ADS and its beam window proposed by the JAEA [44]. . . . .	23
1.12	A schematic sketch of the lower part of SINQ Target-3 AlMg <sub>3</sub> Safety-hull [46]. . . . .	25

1.13	A schematic sketch (a) and a picture (b) of the TS2 Proton Beam Window of the ISIS facility at the Rutherford Appleton Laboratory [47]. . . . .	26
1.14	Schematic drawing of the proton beam window of the spallation neutron source (JSNS) at J-PARC [48]. . . . .	26
1.15	The cross-section of three PBW structures designed for CSNS: (a) Single layer structure. (b) Sandwiched structure. (c) Single-double layer structure [50]. . . . .	27
1.16	Second generation Al-6061-T651 PBW at the Spallation Neutron Source: (a) sectional view of flat-plate aluminium window and (b) cross-sectional view of complete SNS proton beam window assembly [19]. . . . .	30
1.17	Overview of the PBW assembly of the 5 MW ESS Target Station (a). Detail of the PBW welded to the frame (b) and without side supports (c) [54]. . .	31
2.1	Operating temperatures [ $^{\circ}\text{C}$ ] (left) and thermally induced deflection [m] (right) of an LHC secondary collimator jaw in steady-state conditions [57].	39
2.2	Schematic drawing in side and front views of a quarter of the target disc, where $z$ is the direction of thickness and $x$ and $y$ are the directions of the plane of the disc. All units are in mm. . . . .	42
2.3	Electronic, nuclear and total energy loss as a function of the specific energy for uranium ions in six targets (Be, C, Al, Ti, Fe, Ni). All the graphs were realised by processing the data extracted from the SRIM-2013 libraries. . .	44
2.4	Roots of the general vibration equation for circular plates in three boundary conditions (clamped edge, free edge and simply supported edge) [62]. . . .	52
2.5	T91 steel samples produced by RHP-Technology. . . . .	57
2.6	Al-6082-T6, Titanium Grade 23 and Inconel 718 samples produced by CERN Workshop. . . . .	58
3.1	Picture of the entrance of GSI and sketch of main accelerator facilities . . .	61
3.2	Schematic overview of the GSI UNILAC [72] . . . . .	62
3.3	(a) Floor-plan of the M-Branch cave of UNILAC. (b) Schematic sketch of the M3 beamline of the GSI UNILAC accelerator. The beam is marked by a green dotted arrow, while the blue squares indicate the potential positions for irradiated samples. Courtesy of Philipp Bolz [60]. . . . .	64
3.4	M3-beamline software screens during (a) calibration of the slits and (b) Faraday Cup in operation to verify the stability of the U-ion flux. . . . .	65

3.5	(a) Perforated aluminium plate with holes of different sizes to resize the square-shaped beam after the slits to obtain a smaller circular-shaped beam. (b) Interior view of the Spectroscopy chamber. (c) The software screen of the spectroscopy chamber camera focused on a material sample before the irradiation experiment. . . . .	66
3.6	Pictures of the process of sample preparation: (a) high accuracy length gauge to measure the effective thickness of the samples, (b) mounting of the T91 steel sample in the upper housing of the sample holder, (c) back side of the first sample holder, where the application of the graphite spray and of the tiny piece of adhesive reflective tape can be noticed, (d) front side of the first sample holder, set to be installed inside the Spectroscopy Chamber. . . . .	67
3.7	Arrangement of (a) Laser Doppler Vibrometer (green frame) and (b) thermal camera (orange frame) in front of the spectroscopy chamber of the M3-beamline for the SW-U-2022 experiment. (c) A sketch of the top view configuration of online measurement instruments. . . . .	70
3.8	(a) Picture of the oscilloscope connected to the LDV during the experiment. (b) Screen capture of Altair software used to analyse the data from the Thermal Camera. . . . .	72
3.9	Temperature development in five seconds of Titanium Grade 23 at fluence $2 \cdot 10^{11}$ U-ions $\text{cm}^{-2}$ . The peaks associated with the expected pulses at a frequency of 1 Hz are indicated in green. In red the peak that occurred only 0.5 seconds after the fourth, known as <i>parasitic pulse</i> . . . . .	73
3.10	Detail of a 50 ms thermal profile of the fully irradiated Titanium Grade 23 sample. Four thermal images recorded by the TC are reported. . . . .	74
3.11	Steel T91 sample — Thermal profile recorded by TC at three fluence levels.	76
3.12	Inconel 718 sample — Thermal profile recorded by TC at three fluence levels.	76
3.13	Aluminium 6082 T6 sample — Thermal profile recorded by TC at three fluence levels. . . . .	76
3.14	Titanium Grade 23 sample — Thermal profile recorded by TC at five fluence levels. . . . .	76
3.15	Velocity signal in the time domain (on the left) and corresponding power spectral density in the frequency domain (on the right) measured by LDV at the rear side of the pristine Inconel 718 disc sample at the first pulse of the U-ion beam. . . . .	79

3.16	Steel T91 sample — (a) Time-dependent velocity signal measured by LDV and (b) corresponding FFT spectra at the rear side ( $x=0.213$ mm, $y=z=0$ ) of a disc-shaped sample for the irradiation with 1.14 GeV Uranium ions at different levels of fluence. . . . .	81
3.17	Steel T91 sample — On the right, the time-dependent velocity signal measured by the LDV, with two zoom-ins related to the first 2 ms (0-2 ms) and last 2 ms (16-18 ms) and, on the right, the FFT spectra corresponding to the two parts of the signal of which the magnification was carried out. . . .	82
3.18	Inconel 718 sample — (a) Time-dependent velocity signal measured by LDV and (b) corresponding FFT spectra at the rear side ( $x=0.219$ mm, $y=z=0$ ) of a disc-shaped sample for the irradiation with 1.14 GeV Uranium ions at different levels of fluence. . . . .	83
3.19	Aluminium 6082 T6 — (a) Time-dependent velocity signal measured by LDV and (b) corresponding FFT spectra at the rear side ( $x=0.405$ mm, $y=z=0$ ) of a disc-shaped sample for the irradiation with 1.14 GeV Uranium ions at different levels of fluence. . . . .	84
3.20	Titanium Grade 23 sample — (a) Time-dependent velocity signal measured by LDV and (b) corresponding FFT spectra at the rear side ( $x=0.220$ mm, $y=z=0$ ) of a disc-shaped sample for the irradiation with 1.14 GeV Uranium ions at different levels of fluence. . . . .	85
3.21	Measured bending frequency of the four disc-shaped samples with diameter 2 cm as a function of accumulated 4.8 MeV/u Uranium ion fluence. . . . .	86
3.22	Pictures of the four material samples in two sample holders before and after irradiation inside the Spectroscopy chamber of GSI Darmstadt M3-beamline.	87
3.23	(a) NanoTest Vantage produced by Micro Materials. (b) Picture of the internal part, where the pendulum, the permanent magnet and other parts of the equipment are visible. On the bottom right (orange square), a zoom-in of the sample stub, the indenter tip and the integrated optical microscope.	88
3.24	Aluminium supports for microindentation test with (a) pristine and (b) fully-irradiated samples of the four materials investigated. . . . .	89
3.25	Captures from the NanoTest software for microindentation. (a) Camera view of the indenter and of the sample, extremely useful to align the indenter to the beam spot of the U-ions irradiated samples. (b) Page of results for the indentation of irradiated Al6082 T6 sample, where the most important data are summarised (contact depth, mean hardness and mean reduced elastic modulus, number of indentation cycles, etc.). . . . .	90

3.26	(a) Schematic illustration of indentation load-displacement data. (b) Schematic illustration of the unloading process [80]. . . . .	90
3.27	Selected Load-Displacement curves from microindentation analysis of pristine and irradiated (at the maximum applied fluence of $2 \cdot 10^{13}$ ions $\text{cm}^{-2}$ ) T91 Steel samples. . . . .	93
3.28	Selected Load-Displacement curves from microindentation analysis of pristine and irradiated (at the maximum applied fluence of $2 \cdot 10^{13}$ ions $\text{cm}^{-2}$ ) Inconel 718 samples. . . . .	93
3.29	Selected Load-Displacement curves from microindentation analysis of pristine and irradiated (at the maximum applied fluence of $2 \cdot 10^{13}$ ions $\text{cm}^{-2}$ ) Aluminium 6082 T6 samples. . . . .	93
3.30	Selected Load-Displacement curves from microindentation analysis of pristine and irradiated (at the maximum applied fluence of $2 \cdot 10^{13}$ ions $\text{cm}^{-2}$ ) Titanium Grade 23 samples. . . . .	94
3.31	Scanning Electron Microscope (SEM) employed in the MM section at CERN (a). Sample holder with the irradiated specimens inserted in the Sigma-500 SEM system (b). . . . .	96
3.32	High quality picture of the sample holder with the irradiated specimens. . . . .	96
3.33	SEM images of Steel T91 sample of the reference material region (top) and the central irradiated beam spot (bottom) with a resolution scale of $100 \mu\text{m}$ . . . . .	97
3.34	SEM images of Steel T91 sample of the reference material region (top) and the central irradiated beam spot (bottom) with a resolution scale of $10 \mu\text{m}$ . . . . .	98
3.35	SEM images of Steel T91 sample of the reference material region (top) and the central irradiated beam spot (bottom) with a resolution scale of $3 \mu\text{m}$ . . . . .	99
3.36	SEM images of Inconel 718 sample of the reference material region (top) and the central irradiated beam spot (bottom) with a resolution scale of $100 \mu\text{m}$ . . . . .	100
3.37	SEM images of Inconel 718 sample of the reference material region (top) and the central irradiated beam spot (bottom) with a resolution scale of $10 \mu\text{m}$ . . . . .	101
3.38	SEM images of Inconel 718 sample of the reference material region (top) and the central irradiated beam spot (bottom) with a resolution scale of $3 \mu\text{m}$ . . . . .	102
3.39	SEM images of Al-6082-T6 sample of the reference material region (top) and the central irradiated beam spot (bottom) with a resolution scale of $100 \mu\text{m}$ . . . . .	103



3.40	SEM images of Al-6082-T6 sample of the reference material region (top) and the central irradiated beam spot (bottom) with a resolution scale of 10 $\mu\text{m}$ . . . . .	104
3.41	SEM images of Al-6082-T6 sample of the reference material region (top) and the central irradiated beam spot (bottom) with a resolution scale of 3 $\mu\text{m}$ . . . . .	105
3.42	SEM images of Titanium Grade 23 sample of the reference material region (top) and the central irradiated beam spot (bottom) with a resolution scale of 100 $\mu\text{m}$ . . . . .	106
3.43	SEM images of Titanium Grade 23 sample of the reference material region (top) and the central irradiated beam spot (bottom) with a resolution scale of 10 $\mu\text{m}$ . . . . .	107
3.44	SEM images of Titanium Grade 23 sample of the reference material region (top) and the central irradiated beam spot (bottom) with a resolution scale of 3 $\mu\text{m}$ . . . . .	108
4.1	Results of the particle transport simulations, that show the tracking of 4.8 MeV/u Uranium ions passing through Stainless Steel T91, as a function of the target depth. All the calculations were performed using both the Q-C (left) and F-C (right) options of the TRIM-2013 code. . . . .	116
4.2	Results of the particle transport simulations, that show the tracking of 4.8 MeV/u Uranium ions passing through Inconel 718, as a function of the target depth. All the calculations were performed using both the Q-C (left) and F-C (right) options of the TRIM-2013 code. . . . .	116
4.3	Results of the particle transport simulations, that show the tracking of 4.8 MeV/u Uranium ions passing through Al-6082-T6, as a function of the target depth. All the calculations were performed using both the Q-C (left) and F-C (right) options of the TRIM-2013 code. . . . .	117
4.4	Results of the particle transport simulations, that show the tracking of 4.8 MeV/u Uranium ions passing through Titanium Grade 23, as a function of the target depth. All the calculations were performed using both the Q-C (left) and F-C (right) options of the TRIM-2013 code. . . . .	117
4.5	Nuclear and electronic energy loss as a function of penetration depth for 1.14 GeV U-ions for the four material samples irradiated during the experiment. All the calculations were performed using the "Ion Distribution and Quick calculation of damage" (Q-C) option of the TRIM-2013 code. . . . .	118

4.6	Mass stopping power as a function of penetration depth for 1.14 GeV U-ions for the four material samples irradiated during the experiment. All the calculations were performed using the "Ion Distribution and Quick calculation of damage" (Q-C) option of the TRIM-2013 code. . . . .	119
4.7	Displacements per atom as a function of penetration depth for 1.14 GeV U-ions for the four material samples irradiated during the experiment. The dpa calculations were performed by both "vacancy.txt" and "damage energy" methods of the "Quick Calculation" option of the TRIM-2013 code. .	120
4.8	Target displacements per ion as a function of penetration depth for 1.14 GeV U-ions for the four material samples irradiated during the experiment, as calculated and displayed using the "Full Cascade" option of the TRIM-2013 code. . . . .	121
4.9	Comparison of the results obtained in terms of displacements per atom, as a function of penetration depth for 1.14 GeV U-ions for the four material samples irradiated, using the "vacancy.txt" method for both "Quick Calculation" and "Full Cascade" options in the TRIM-2013 code. . . . .	122
4.10	Displacements per ion, as a function of penetration depth for 1.14 GeV U-ions for the four materials, as calculated by the "Quick Calculation" (top) and "Full Cascade" (bottom) options in the TRIM-2013 code. The graphs have been produced to allow an easier comparison of the penetration depth and the vacancy peak for all the materials. . . . .	123
4.11	Bar graph of the total displacements per atom calculated using "Quick Calculation" and "Full cascade" options of the TRIM-2013 code. . . . .	124
4.12	(a) Inconel 718 sample analysed by ImageJ software to identify the size of the beam spot. (b) ANSYS SpaceClaim model of Inconel sample. . . . .	126
4.13	Convergence criterion: the four graphs were plotted with the aim of correlating the results in the calculation of a certain quantity (temperature, vibration frequency, etc.) to the computational time to solve the simulation and to the number of elements in the mesh. . . . .	127
4.14	Mesh on the front side of the Inconel 718 sample. The highlighted parts on the right show the difference in mesh density as the radius increases, with the element width that changes from 2 mm up to 10 mm. . . . .	128
4.15	Mesh on the lateral side of the Inconel 718 sample. The highlighted part on the right shows the number of elements along the thickness. . . . .	129
4.16	Temperature distribution at the centre of the Steel T91 sample on the front side (top) and on the back side (bottom) at the first pulse and comparison with both the Thermal Camera data and the analytical findings. . . . .	132

4.17	Temperature distribution at the centre of the Steel T91 sample on the front side (top) and on the back side (bottom) at the last pulse and comparison with both the Thermal Camera data and the analytical findings. . . . .	132
4.18	Temperature distribution at the centre of the Inconel 718 sample on the front side (top) and on the back side (bottom) at the first pulse and comparison with both the Thermal Camera data and the analytical findings. .	133
4.19	Temperature distribution at the centre of the Inconel 718 sample on the front side (top) and on the back side (bottom) at the last pulse and comparison with both the Thermal Camera data and the analytical findings. .	133
4.20	Temperature distribution at the centre of the Al-6082-T6 sample on the front side (top) and on the back side (bottom) at the first pulse and comparison with both the Thermal Camera data and the analytical findings. .	134
4.21	Temperature distribution at the centre of the Al-6082-T6 sample on the front side (top) and on the back side (bottom) at the last pulse and comparison with both the Thermal Camera data and the analytical findings. .	134
4.22	Temperature distribution at the centre of the Titanium Grade 23 sample on the front side (top) and on the back side (bottom) at the first pulse and comparison with both the Thermal Camera data and the analytical findings.	135
4.23	Temperature distribution at the centre of the Titanium Grade 23 sample on the front side (top) and on the back side (bottom) at the last pulse and comparison with both the Thermal Camera data and the analytical findings.	135
4.24	Temperature distribution at the centre of the Titanium Grade 23 sample on the front side as a function of time. The temperature distribution is divided into four plots, representing significant stages in the heat diffusion process. An ANSYS screenshot corresponding to the end time of each plot is reported. . . . .	137
4.25	Focus on the temperature distribution at the centre of the Titanium Grade 23 sample on the front side at the first pulse as a function of relevant moments of the heat diffusion process. . . . .	138
4.26	Comparison of the FFT results in terms of frequency of the ANSYS velocity signal and LDV velocity signal for pristine materials. . . . .	139
4.27	Screenshot from ANSYS Transient Structural of a disc sample, with results of the Velocity Probe. . . . .	140
4.28	Comparison of the FFT results in terms of frequency of the ANSYS velocity signal for pristine and irradiated materials. . . . .	141

4.29	Time-dependent velocity signal measured by LDV and velocity results obtained by ANSYS Structural Transient simulations for Steel T91 at last pulse. . . . .	142
4.30	Time-dependent velocity signal measured by LDV and velocity results obtained by ANSYS Structural Transient simulations for Inconel 718 at last pulse. . . . .	143
4.31	Time-dependent velocity signal measured by LDV and velocity results obtained by ANSYS Structural Transient simulations for Al-6082-T6 at last pulse. . . . .	143
4.32	Time-dependent velocity signal measured by LDV and velocity results obtained by ANSYS Structural Transient simulations for Titanium Grade 23 at last pulse. . . . .	144
4.33	Effect of Young's modulus change and change of the boundary conditions due to the variation of temperature on the irradiated samples. . . . .	144

# List of Tables

1.1	Features of double-layer vacuum beam windows designs at CERN [2][8][17][18].	6
2.1	Overview of the materials adopted worldwide for beam windows. . . . .	36
2.2	Properties and figures of merit of materials relevant for beam windows. The values reported in these tables have been calculated at room temperature ( $T_{\text{room}}=20^\circ$ ), except for the coefficient of thermal expansion (CTE), which was averaged between $20^\circ$ and $100^\circ$ in most cases. For transversely anisotropic materials, such as the Carbon fibre-reinforced carbon (C-C) composite materials, the values were estimated through the formula: value = $[2 \cdot (\text{best direction}) + (\text{weak direction})]/3$ . . . . .	41
2.3	Values of stopping power and peak temperature for materials of interest for beam windows, in the particular case of 4.8 MeV/u U-ions beams irradiation.	45
2.4	Thermal diffusion times on three length scales for materials of interest for beam windows. . . . .	47
2.5	Analytical results of natural bending frequencies and frequencies of propagating waves for cylindrical plates with diameter 20 mm and thickness 0.2 mm. In red, frequency values are higher than the sampling frequency (25 MHz) of the experimental measuring instrument (Laser Doppler Vibrometer). In green, frequency values are below this threshold. . . . .	55
2.6	Chemical composition of the material selected for the U-ions irradiation experiment. . . . .	58
2.7	Physical and mechanical properties of the material specimens produced for the U-ions beams irradiation experiment. . . . .	59
3.1	Materials investigated during the beam time. . . . .	66
3.2	Radial and axial thermal diffusion times for the four cylindrical samples irradiated during the GSI experiment. . . . .	69
3.3	U-ion beam parameters . . . . .	71



3.4	Analytical results of natural bending frequencies and frequencies of propagating waves for the four material samples irradiated during the GSI experiment. . . . .	78
3.5	Bending frequency of the four material samples at certain levels of fluence. . . . .	86
3.6	Results of the microindentation analysis for pristine and irradiated samples in terms of Young's modulus. . . . .	94
4.1	Penetration depth, stopping power, displacements for atom and other nuclear parameters calculated with the SRIM-2013 code for the four tested materials. . . . .	119
4.2	Thermal data for ANSYS transient thermal simulations and analytical findings. . . . .	131
4.3	Summary table of the first-order bending frequencies obtained by experimental measurements, analytical calculations and numerical simulations. . . . .	145

# Acronyms

**ADS** Accelerator-Driven Systems. 1, 21, 22, 56

**BIDs** Beam-Intercepting Devices. 7

**BLIP** Brookhaven Linac Isotope Producer. 14

**BNL** Brookhaven National Laboratory. 13, 14

**CEA** *Commissariat à l'énergie atomique et aux énergies alternatives*. 22

**CERN** *Organisation européenne pour la recherche nucléaire*. 6, 11, 12, 24, 56, 67

**CFL** Courant–Friedrichs–Lewy. 126, 128

**CLIC** Compact Linear Collider. 6

**CNGS** CERN Neutrinos to Gran Sasso. 6, 11, 12

**CSNS** China Spallation Neutron Source. 27, 28

**dpa** Displacement per atom. 8, 109

**DUNE** Deep Underground Neutrino Experiment. 15

**EBR-II** Experimental Breeder Reactor-II. 19

**EDM** Electrical discharge machining. 58, 67

**EDS** Engineering Design and Simulation. 32

**ESS** European Spallation Source. 3, 30, 56

**F-C** Detailed calculation with Full Damage cascades. 12, 116, 117

**FAIR** Facility for Antiproton and Ion Research. 62

**FC** Faraday Cup. 65, 71

**FNAL** Fermi National Accelerator Laboratory. 10, 13, 14, 56

**FoM** Figures of Merit. 37, 39

**FZJ** *ForschungsZentrum Jülich*. 21

**GSI** *Gesellschaft für Schwerionenforschung*. 8, 32, 34, 42, 56, 57, 60–64, 69, 80, 88

**HFIR** High Flux Isotope Reactor. 19, 28

**HiRadMat** High-Radiation to Materials. 6, 11, 14

**HL-LHC** High-Luminosity Large Hadron Collider. 20, 56

**I.FAST** Innovation Fostering in Accelerator Science and Technology. 32

**ILC** International Linear Collider. 15

**IPF** Isotope Production Facility. 15, 17, 18

**ISOLDE** Isotope mass Separator On-Line facility. 19

**ITER** International Thermonuclear Experimental Reactor. 15

**J-PARC** Japan Proton Accelerator Research Complex. 3, 13, 14, 26, 28

**JAEA** Japan Atomic Energy Agency. 22

**JSNS** Japan Spallation Neutron Source. 27

**LANL** Los Alamos National Laboratory. 21

**LANSCÉ** Los Alamos Neutron Science Center. 15, 17, 21

**LBE** Lead-Bismuth Eutectic. 10

**LBNF** Long Baseline Neutrino Facility. 11, 15

**LDV** Laser Doppler Vibrometer. 9, 48, 54, 57, 68, 71, 72, 77, 79, 83

**LHC** Large Hadron Collider. 6, 12, 19, 39

**LINAC** LINear ACcelerator. 3

**MEGAPIE** MEGAwatt Pilot Experiment. 22

**MME** Mechanical and Materials Engineering Group at CERN. 32

**NuMI** Neutrinos at the Main Injector. 11

**OC** Oven Chamber. 65

**ORNL** Oak Ridge National Laboratory. 15, 19, 21

**PBW** Proton Beam Window. 15, 27, 30

**PKA** Primary Knock-out Atom. 112

**PS** Proton Synchrotron. 19

**PSI** Paul Scherrer Institut. 3, 21, 22, 27

**Q-C** Ion Distribution and Quick calculation of damage. 12, 13, 116–119

**RaDIATE** Radiation Damage In Accelerator Target Environments. 13

**RAL** Rutherford Appleton Laboratory. 15, 25

**RHP** RHP-Technology GmbH. 67

**SC** Spectroscopy Chamber. 65, 69–71, 130

**SEM** Scanning Electron Microscope. 60, 95

**SINQ** Swiss Spallation Neutron Source. 3, 18, 22, 25, 28

**SNS** Spallation Neutron Sources. 1, 3, 4, 15, 17, 24

**SPS** Super Proton Synchrotron. 12, 19, 24

**SRIM** The Stopping and Range of Ions in Matter. 109, 115

**TC** Thermal Camera. 9, 68, 69, 72, 73, 129

**TEM** Transmission Electron Microscopy. 95

**TRI** Thermomechanical Robustness Index. 37

**TSI** Thermal Stability Index. 38

**UNILAC** Universal Linear Accelerator. 8, 34, 42, 56, 61, 62, 64, 65, 69, 74

# Chapter 1

## Introduction

A **beam vacuum window** is a thin interface of separation between a volume under vacuum and a volume at higher pressure traversed by particle beams. Their application is not limited to particle accelerators, where they are typically installed inside the beamline to separate vacuum sectors, but also extends to other fields of nuclear research and to high-power hadron beam applications, such as the Spallation Neutron Sources (SNS) and the Accelerator-driven systems (ADS) [1].

The history of beam windows is extensive but not well defined: international standard designs have never been proposed and each research centre has independently developed very different designs based on the unique characteristics of the beam. In the past, when accelerator facilities operated at energies significantly lower than those of today, it was not infrequent to find windows constructed from common materials like steel or aluminium.

The thickness of a beam window is an important element of its use: in the case of the high thickness of the interface, the interaction with the beam increases and the probability of intercepting particles which release heat inside the component. The thickness of the window is therefore supposed to be as thin as possible to allow the passage of the particles through matter with minimal interaction but, at the same time, enough resistant to maintain the required differential pressure between the two environments: the satisfaction of these competing demands is the main issue concerning the beam-window technology.

The research and development of innovative materials and designs capable of withstanding higher pressure loads and more severe beam-induced thermal stresses has become extremely relevant as the energy and pulse intensities of new accelerator facilities have increased. Another critical requirement is the safe operation of future facilities, as well as the prevention of failures resulting from radiation damage and the combined effect of pressure waves and thermal stresses.



## 1.1 Selection criteria for beam windows materials

This section is intended to give a general overview of the characteristics of the materials that best suit for the construction of beam windows.

### 1.1.1 Transparency to beam particles

The first element to consider is the effect of the particles traversing the beam window. In passing through matter, charged particles ionise or excite the atoms or molecules they encounter. Thus, the particles gradually lose energy in many small steps, and a part of the beam energy  $E$  is transferred to the matter [2].

An indication of a material's ability to slow down energetic particles travelling through its interior is called stopping power ( $S = -dE/dx$ ). Given a specific type of particle with a certain kinetic energy and a target material, the *stopping power* is the amount of kinetic energy lost in relation to the thickness of material travelled [3]. For a particle accelerator facility designed and engineered to operate at a given energy level, the atomic number  $Z$  and mass number  $A$  are the two main variables that can be taken into account to minimise the interaction between particles and matter.

Since the stopping power scales with  $Z$ , the high transparency to high-energy particles can be achieved only by resorting to **low- $Z$  materials**. A useful parameter to determine the transparency of a beam window is given by the ratio between the thickness and the radiation length of the material [4]:

$$N = \frac{d}{X_0} \quad (1.1)$$

where  $d$  is the thickness of the beam window and  $X_0$  is the radiation length of a material, i.e. the mean length to reduce the energy of an electron by the factor  $1/e$ :

$$E = E_0 e^{-x/X_0} \quad (1.2)$$

Since  $X_0$  is inversely proportional to the atomic number  $Z$ , it follows that the bigger the radiation length of a material, the more “transparent” to radiation it is. When designing a beam window, it must be ensured that its thickness  $d$  remains significantly smaller than one radiation length. A few examples of low- $Z$  materials selected for beam windows are Aluminium, Beryllium and graphitic materials.

### 1.1.2 Thermal requirements

The thermal properties of materials are another important factor to consider, as they are directly related to particle penetration into matter. The particles, while passing through

matter, lose energy by different interaction mechanisms (ionisation is by far the primary mechanism of energy loss). All the energy content deposited into the matter is ultimately converted into heat.

This heat generation focused on a small portion of matter may result in a significant increase in temperature: the persistent and prolonged application of thermo-mechanical stresses induced by the beam to the structure can weaken the material and even lead to unexpected failure. It is precisely for this reason that the candidate materials for beam windows must have **extremely high thermal conductivity** ( $k$ ), **high specific heat capacity** ( $c_p$ ) and **very low thermal expansion coefficients** ( $CTE$ ). If the  $k$  is too low, the heat produced by the beam passage can take too much time to propagate towards the window's edge, thereby accumulating at the centre of the window that, in the worst-case scenario, may even melt. In light of this, when designing the beam window, it's essential to analytically calculate the thermal profile and verify that the highest temperature obtained is lower than the melting temperature of the material by a specific safety margin.

The thermal design of vacuum windows must clearly consider specific beam characteristics and, especially, the power of the type of incident beams. In the case of Spallation Neutron Sources (SNS), at least three types of time structures may be distinguished: **continuous sources**, **short pulse sources** and **long pulse sources**. Most of the large-scale currently operational SNS employ a short-pulsed proton beam (of the order of a few  $\mu s$ ) to produce neutrons [5]. Examples of short-pulsed high-power proton accelerators currently in operation for the major existing SNS facilities may be found at the British Rutherford Appleton Laboratory, at the American Los Alamos National Laboratory and at the Japan Proton Accelerator Research Complex (J-PARC). A long-pulsed source consists in a Spallation Neutron Source fed directly from a pulsed LINAC: a long proton pulse of 2.86 ms at 2 GeV is expected to be produced by the European Spallation Source (ESS) under construction at Lund, Sweden. A high value of specific heat is particularly sought after in beam windows exposed to pulsed beams, as it is directly connected to the increase in temperature of the material for a given power absorbed. The continuous Spallation Neutron Sources are much less widespread than pulsed ones and the only significant example of this type is provided by the Swiss Spallation Neutron Source (SINQ), where the continuous proton beam is sent by the PSI Ring Cyclotron. In the case of continuous beams, materials with extremely high thermal conductivity values, capable of spreading the heat continuously deposited, are even more appreciated for beam-window applications [6][7].

In the case of pulsed beams, the instantaneous temperature rise at the centre of the beam distribution is undoubtedly the most critical factor in the thermal design of beam windows. A simple conservative estimation of the largest temperature increase is proposed

here. Consider a window whose thickness is much less than the radiation length  $d \ll X_0$  (it is, therefore, reasonable to suppose that all energy is deposited inside the target) and assume a typical round Gaussian beam with a rms width  $\sigma_{beam}$  for the incident particles. By neglecting the temperature dependence of the heat capacity  $C$ , the instantaneous temperature increase at the centre of the beam distribution is given by the following formula [8]:

$$\Delta T_{inst} = \left( \frac{dE}{\rho dx} \right) \frac{N_p}{2\pi\sigma_{beam}^2 C} \quad (1.3)$$

where  $dE/\rho dx$  is the mass stopping power and  $N_p$  the number of particles passing through the window.

Another aspect related to thermal loads concerns the **cooling method**. The strict requirement of a thin interface makes it usually impossible to install heat exchangers to remove heat from the window's centre. The predominant heat removal mechanism is the thermal diffusion from the beam spot at the centre to the edge. The thermal radiation (which varies like  $T^4$  according to the Stefan–Boltzmann law) has a significant influence only for very high-energy incident particles and for thick windows in which heat deposition is considerable. In contrast, thermal convection is prevented on the under-vacuum side of the window. On the side kept at atmospheric pressure, the windows installed into the beam dump lines (usually with reduced beam power) are passively air-cooled in most circumstances. However, in the case of windows installed in pulsed Spallation Neutron Sources, the main cooling method is water cooling, and different water cooling structures have been designed to adapt to the specific beam power [9][10].

### 1.1.3 Resistance to pressure loads

The other fundamental issue related to beam windows concerns the maintenance of the required differential pressure between the beam line vacuum and the experimental area, which is kept under atmospheric pressure. The materials adopted for vacuum window assemblies must have **high mechanical strength** to withstand the repeated loads due to the beam-induced thermal stress; at the same time, these separation interfaces must provide reliable mechanical performance to handle both a static differential pressure between the vacuum and the atmosphere and occasional pressure cycling during maintenance work in which the beamline is vented [11].

A vacuum window is typically designed to be able to withstand a pressure difference  $\Delta P$  of about 1 atm between its two faces. The static stress corresponding to this differential pressure depends significantly on the thickness and size of the window: in particular, stress reduces with decreasing the size and with increasing the thickness of the interface.

Since the choice of the thickness of windows greatly affects their ability to withstand pressure loads, it is essential to ensure that their design meets strict mechanical safety requirements. By way of example, a design criterion for circular thin windows from the TM-1380 Fermilab guidelines is described below [12].

For circular rigid thin ( $d > 0.003$  inch) windows fixed on the edge, as is the case with most of stainless steel and titanium windows, the allowable stress when a uniform pressure  $q$  is distributed over entire plate must meet the following inequality:

$$\sigma_{amm} > E \left( \frac{d}{a} \right) \left[ K_3 \left( \frac{y}{d} \right) + K_4 \left( \frac{y}{d} \right)^2 \right] \quad (1.4)$$

where  $d$  is the thickness of the window (in inch),  $a$  the unclamped radius (in inch),  $q$  the uniform pressure on the window (in psid),  $\sigma_{amm}$  the allowable stress (in psi),  $E$  the Young's modulus of the window material (in psi),  $\nu$  the Poisson's ratio,  $y$  the window deflection (in inch), that can be calculated from:

$$\frac{qa^4}{Ed^2} = K_1 \left( \frac{y}{d} \right) + K_2 \left( \frac{y}{d} \right)^3 \quad (1.5)$$

and  $K_1, K_2, K_3, K_4$  the coefficients for maximum stress at centre of window [13]:

$$K_1 = \frac{5.33}{1 - \nu^2} \quad K_2 = \frac{2.6}{1 - \nu^2} \quad K_3 = \frac{2}{1 - \nu} \quad K_4 = 0.976 \quad (1.6)$$

The most stringent of the two following equations shall be used to determine the allowable stress  $\sigma_{all}$  for thin windows:

$$\sigma_{all} = 0.5 \sigma_u \quad \sigma_{all} = 0.9 \sigma_y \quad (1.7)$$

where  $\sigma_u$  is the ultimate tensile strength (in psi) and  $\sigma_y$  the yield stress (in psi).

For a selected material with known mechanical properties ( $E, \nu, \sigma_y, \sigma_u$ ), if the size (depending on  $a$ ) is a quantity fixed by the beamline design, the minimum thickness required to withstand the static pressure load can be calculated by the previous formulae by means of an iterative procedure.

### 1.1.4 Leak tightness

In the design phase, low-Z materials with low thermal expansion coefficient and high thermal conductivity are usually chosen to fulfil the requirements of withstanding differential pressure loads and being transparent to particles crossing the vacuum window. An excellent choice to meet these demands is the use of carbon-composites (CC) and, more in general, graphitic materials, whose best properties are the low density ( $1.5\text{-}1.7 \text{ g cm}^{-3}$ ), the large radiation length ( $X_0 \cong 29 \text{ cm}$ ) and the low thermal expansion coefficient. On

the other hand, the quite high porosity and permeability<sup>1</sup> of carbon-composites do not allow to meet the vacuum requirements since this involves an unacceptably high leak rate through the interface [15].

This suggests that materials with **high impermeability** to gasses (including He, that can be generated inside the matter from nuclear reactions during irradiation [16]) are needed to realise the leak-tightness condition of vacuum windows, especially when ultra-high vacuum (UHV) is required (pressure lower than  $10^{-9}$  mbar).

A recurring design solution adopted at CERN over the last twenty years to meet the vacuum requirements, without ceasing to exploit the advantages offered by the carbon-carbon composites, consists of applying an additional thin impermeable leak-tight metallic layer. This impermeable foil is recommended to be installed on the high-pressure side, such that it remains forced on the supporting CC plate due to the pressure differential. A few examples of beam windows with this distinctive design are summarised in the table 1.1.

**Table 1.1:** Features of double-layer vacuum beam windows designs at CERN [2][8][17][18].

Proposed designs for double-layer vacuum windows		Accelerator facilities at CERN			
		LHC	CLIC	HiRadMat	CNGS
		beam dump beamline	beam dump beamline	LHC to HiRadMat connection beamline	Proton beam exit window
Shape		Circular	Racetrack square	Circular	Circular
Upstream layer	Material	SIGRABOND 1501G	SIGRABOND 1501G	SIGRABOND 1001G	C-C
	Thickness	15 mm	15 mm	5 mm	2.5 mm
	Diameter	600 mm	260 mm x 500 mm	70 mm	68.5 mm
Downstream layer	Material	AISI 316L	Aluminium	Beryllium PF-60	Beryllium
	Thickness	0.2 mm	0.2 mm	0.254 mm	0.254 mm
	Diameter	600 mm	260 mm x 500 mm	70 mm	60 mm

### 1.1.5 Machinability and fabrication

The **machinability**, namely the ease at which a material can be cut or shaped with a satisfactory finish, is an important factor when choosing materials to be adopted in beam-window applications. Besides the reduction in terms of time and costs, the ease of machining allows the production of high-precision machining components, for instance, the window-integrated cooling circuits and the multi-material multi-layer beam-window designs.

<sup>1</sup>The carbon-carbon composites utilised at CERN for beam windows are of the type SIGRABOND 1001G and SIGRABOND 1501G, with a coefficient of permeability of  $7 \cdot 10^{-2}$  and  $5 \cdot 10^{-2}$  cm<sup>2</sup> s<sup>-1</sup>, respectively [14].

As an example, beryllium, a metal that, as will be seen, exhibits excellent characteristics for beam-window applications, presents several problems in terms of manufacturing, since it is hard and brittle and produces powder instead of chips when machined, reason why special machining techniques are required to avoid cracking. Moreover, its extreme toxicity and the allergic reactions provoked in the case of inhalation exacerbate the manufacturing and handling issues.

The shape and dimensions of beam windows vary considerably depending on the specific purpose for which they are designed. Passively air-cooled windows have essential geometries and particularly thin thicknesses, whereas helium or water-cooling systems are characterised by more articulate and complex beam-window designs. In the first case, circular or rectangular flat-plate beam windows are commonly adopted: this type of design is considerably easier to fabricate and requires minimal machining operations and little need for welding for manufacturing. Moreover, the addition of pre-curvature to windows is under investigation in certain accelerator facilities with the purpose of reducing the stress induced by the pressure differential [11].

Another aspect to be taken into account during the design and manufacturing process of the beam windows concerns the integration of this component inside the accelerator beamline. In most cases, the beam window is securely mounted on a coupling flange, that guarantees a reliable adhesion between the component and the beamline capable of satisfying the needs of leak tightness and maintaining the vacuum inside the line throughout the entire accelerator running time. In addition to the sealing via coupling vacuum flanges, usually made of steel 304 or pure titanium, other joining/sealing methods are currently considered, including TIG welding, brazing and explosive bonding. The choice of the most optimal solution to seal the window and contain any leakage clearly depends on the pressure conditions and on the chosen design, but also on the material selected for the window: it is precisely for that reason that the properties of **weldability** and brazability cannot be ignored in the selection process of materials for beam windows [11][19]. Finally, after the installation, the entire assembly is leak checked by a series of leak-detection tests before being put into service.

### 1.1.6 Lifetime and failures

Another factor to consider during the design process is the estimated lifetime of a beam window, which is mainly dependent on the effects of radiation damage and on mechanical fatigue.

The influence of **radiation damage** on the longevity and the reliability of beam windows' constituent materials and, more generally, of the beam-intercepting devices (BIDs) of the major accelerator facilities, is considered as one of the most critical challenges for

future high-energy facilities. Regardless of how transparent the window's materials are to the crossing particles, they experience significant microstructure alterations as a result of their interaction. Both primary and secondary radiation may induce a high level of atomic displacements, resulting in the formation of defect structures such as dislocation and vacancy loops, voids, vacancy clusters, helium and hydrogen bubbles. The window's macroscopic material properties could be drastically altered as a result of these cumulative factors, making it less ductile and more prone to failure in use. To select the materials to be used for beam windows it is necessary to understand if and how much the mechanical properties are affected by the high radiation environment. To this end, the mechanical properties of materials taken from components after removal from service are frequently characterised and the radiation-induced change in the main properties is quantified. The displacement per atom (dpa) and gas production are two major indices of radiation damage in irradiated materials.

The **residual radiation** produced by particle interaction during beam operation is an important issue for the lifetime of vacuum windows. The **nuclear activation**, due to the charged particle radiation over a long period of beam exposure, involves the production of different mixes of radioactive isotopes, which undergo a series of radioactive decays until eventually a stable isotope is reached. Such radioactive nuclei, with half-lives ranging from small fractions of a second to many years, can have a dramatic effect on the residual radiation of the window. An example concerns the use of copper beam windows: activated copper produces modest quantities of cobalt-60 (usually through the reaction  $^{63}_{29}\text{Cu}(n, \alpha)^{60}_{27}\text{Co}$ ), which has a long half-life and high-energy radiated daughter particles, and releases a high dose over a prolonged period [20]. If water cooling structures are present, the possible activation of the water exposed to high energy particles must be considered and monitored carefully: the main contributors to its activity are radioactive isotopes of oxygen and nitrogen produced by activation of oxygen isotopes in the cooling water, including  $^{16}\text{N}$ ,  $^{17}\text{N}$  and  $^{19}\text{O}$  [21].

The use of a certain material for beam windows applications requires that this material has been tested under irradiation before the installation since it is essential to know in advance how and how much the mechanical properties are affected if exposed to high-energy irradiation environments. The amount of radiation-induced change in the mechanical properties of materials is frequently determined by characterising the mechanical properties of material taken from components after removal from service in a radiation environment.

The other common cause of window failure is the **fatigue**, a mechanical phenomenon due to the cyclic loading-induced initiation and propagation of cracks in the window's material. The fatigue can be brought about by two distinct conditions, to which correspond

the kinds of mechanical and thermomechanical fatigue. The first condition is due to the cyclic variation of static pressure inside the beamline: the continuous oscillation between states of maximum stress (when the vacuum is established inside the beamline) and near-zero stresses (when the beamline is evacuated and the atmospheric pressure is restored) can weaken the vacuum sealing system and eventually determine the failure of the component. Furthermore, the cyclic deposition of energy on the window and the consequent heating and cooling cycles, concurrently with the radiation-induced material damages, may have detrimental effects on the material and speed up the onset of fatigue failures. For this reason, materials capable of maintaining sufficient mechanical properties, including adequate **ductility** and **fracture toughness** throughout the beam window lifetime, are required to minimise the risk of failure during operation.

When the heat deposited on the beam window is considerable, and the temperature is constantly high, the phenomenon of creep deformation may have detrimental effects on the mechanical properties of the material. **Creep** is the tendency of a material to deform when exposed to temperature, structural load, and time. The temperature range at which creep deformation can occur varies depending on the material. As a general rule, the effects of creep deformation become noticeable at about 35% of the melting point. Beam windows made of aluminium alloys, with melting points of around 600 °C, are currently adopted at working temperatures slightly above this threshold and therefore continuously monitored to prevent creep failures and ensure safe operation conditions [22].

Finally, the effects of **corrosion** and **oxidation** on the beam-window material exposed to the pressure side have an important role in the lifetime of this accelerator component. For vacuum windows installed in accelerator beamlines, the material is in contact with air at atmospheric pressure and, in dry conditions, corrosive phenomena are generally unlikely to be established. Excellent performance in terms of corrosion resistance is, in fact, exhibited by many materials, such as Copper, Titanium and Nickel alloys, selected for this component in many particle accelerator facilities. Exposure to air can have detrimental effects in those cases in which harmful and corrosive gases, such as ozone ( $O_3$ ) and nitrogen oxides ( $NO_x$ ), have been produced by means of the activation of air that interacts with high-energy particle beams. High concentrations of these gases are particularly corrosive for Beryllium, a material widely used for beam windows: a greenish copper oxide was observed for Be windows in humid and nitric acid environments, and it is considered accountable for small vacuum leaks and the initiation of Beryllium contamination [11]. The oxidation of Beryllium windows can be prevented by applying anti-corrosion coatings of various kinds on the atmospheric side of the component: metallic (Ti, Al, Ni, Nb) and polymeric (Parylenes and Epoxies, mainly used for X-ray window applications) coatings are capable of protecting Be windows and extending their operating lifetime [2][23]. In



the case of beam windows inside Spallation Neutron Sources, the pressure side is even more exposed to the radiation of high-energy particles and neutrons, originating from the spallation target. Air is often replaced by other gases or liquids which suppress the production of radioactive corrosive gases and are inactive and non-corrosive, such as helium. The corrosion resistance is vitally important for accelerator-driven subcritical reactors: the main candidate for the spallation target material to produce neutrons for the transmutation of long-lived nuclear wastes is the liquid Lead-Bismuth Eutectic (LBE), an alloy with the advantage of having a melting point of about 200°C lower than that of pure lead, but at the same time highly corrosive for all the components of the reactor [24].

## 1.2 Overview of metallic materials adopted for beam windows in relevant experimental facilities

This section intends to provide an overview, as complete as possible, of materials and designs adopted for beam windows in the most important experimental facilities in the whole world.

### 1.2.1 Beryllium

Beryllium (Be) is typically used in vacuum beam windows because of its thermal qualities and very low-Z properties: it is one of the lightest metals, with low nuclear interaction cross-section, and possesses extremely high specific heat, thermal conductivity and high melting point [25]. It has excellent mechanical properties, including high rigidity, high strength and structural stability at high temperatures. Beryllium stands out among metals in terms of specific rigidity, i.e. the ratio of elastic modulus and density: with an elastic modulus about 50% greater than that of steel and a density 30% lower than that of aluminium, Be exhibits optimum characteristics for beam windows. It is very ductile, easily machined, and can be rolled, drawn, or extruded. It is a well-known material in the nuclear field, and it is usually utilised as the main component for neutron moderators and reflectors of nuclear plants as well as for windows of X-ray tubes, by virtue of the very low absorption of X-rays.

The main issue in using Beryllium is that it is toxic: if a Be window fails, it contaminates the beamline and, potentially, the entire beam enclosure, with severe consequences on clean-up costs. The effects of Beryllium contamination include inhalation of Be dust which can cause Chronic Beryllium Disease (CBD), a chronic and sometimes fatal lung condition.

Five of the approximately 80 windows at FNAL use beryllium [20]. At CERN, both

HiRadMat TT66 vacuum window and CNGS proton beam exit window make use of Be as thin metallic foil applied onto the C-C layer [17][18].

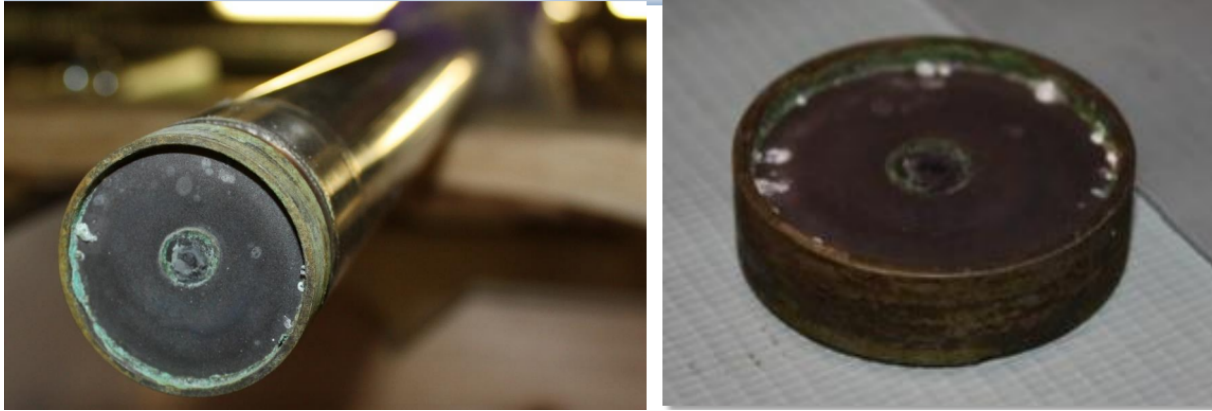


**Figure 1.1:** NuMI Beryllium beam window

An example of a beryllium beam window is shown in figure 1.1: the picture represents the NuMI (Neutrinos at the Main Injector) Be vacuum window, located at the most downstream end of the NuMI beamline at Fermilab. This window failed after seven years and  $7 \cdot 10^7$  pulses. On the other hand, signs of corrosion from a humid and nitric acid environment and oxidation are clearly visible in the outer braze area and in the central beam spot. For the HiRadMat vacuum window at CERN, a thin  $0.5 \mu\text{m}$ -thick coating of Titanium and Niobium was applied on the atmospheric side of the foil to minimise the Be oxidation at high temperatures.

Beryllium is currently being intensively investigated for the next generation of multi-megawatt high-intensity proton accelerator facilities notwithstanding the toxicity issue and the clean-up difficulties in the eventuality of a failure. In a new generation of proton accelerator-driven particle sources, such as, for instance, the Long Baseline Neutrino Facility (LBNF), a higher power version of NuMI, Be has been identified as one of the very few options for beam windows. Recently, the RaDIATE (Radiation Damage In Accelerator Target Environments), an international research partnership whose purpose is to investigate radiation damage issues in several candidate materials, have performed some test on the industrial beryllium grades used in accelerator components, such as the PF-60 beryllium, a highly textured and non-homogeneous alloy. The first results reveal that the use of beryllium as beam window material in next-generation particle accelerator facilities may be limited by higher dose and higher temperatures of operation: the grain matrix hardening occurs at relatively modest dpa, the impurities strongly create grain boundary precipitation and segregations and, finally, high swelling and He bubble formation at grain boundaries were detected for proton beam windows irradiated at high temperatures [26].

### 1.2.2 Titanium alloys

Titanium is a transition metal well known for its properties of lightness, high strength and good heat-transfer properties. The most valuable characteristics of this metal are the high resistance to fatigue stress and corrosion and the highest specific strength (strength-to-density ratio) of any metallic element. Moreover, its coefficient of thermal expansion has the advantage of being slightly lower than that of steel and less than half that of aluminium. In comparison with other common industrial metals, commercially pure grades of titanium have an ultimate tensile strength that is comparable to that of low-grade steel alloys but are less dense (4.5 versus 7.85 g/cm<sup>3</sup>), while they are more than twice as strong as the most used 6061-T6 aluminium alloy, but 60% denser.

Titanium can be alloyed with iron, aluminium, vanadium, and many other elements, to produce strong, lightweight, high corrosion-resistant alloys for aerospace (jet engines, missiles, and spacecraft), nuclear (nuclear waste storage) and several other applications. The most commonly used alloy is Titanium Grade 5 (also known as Ti-6Al-4V), which exhibits an outstanding balance between strength, corrosion resistance, weldability, and fabricability. Unlike the commercially pure (CP) titanium (grades 1-4), this alloy is considerably stronger, have the same stiffness and thermal properties (except for thermal conductivity, which is roughly 60% lower) and, most importantly, is heat treatable.

So, in summary, this material was chosen for beam windows because of its high specific strength, good (albeit lower compared to graphitic materials and Beryllium) thermal shock resistance to pulsed beams (ascribable to the relatively low Young's modulus and modest coefficient of thermal expansion), and its strong fatigue endurance limits. It is also a ductile metal and resistant to corrosion/erosion as well as a reduced activation material, an essential requirement for adoption in the nuclear field. The main drawback is the reduced thermal conductivity, which can cause problems in the diffusion of heat deposited by the intercepted particles.

Two grades of Titanium are widely employed as beam windows material: **Titanium Grade 2** and **Titanium Grade 5**. The first one, an unalloyed commercially pure titanium, was used for three 100  $\mu\text{m}$ -thick mobile windows of the Super Proton Synchrotron (SPS) at CERN and in a few other accelerator facilities. The Ti-6Al-4V, a high-strength dual-phase titanium alloy, on the contrary, was adopted as a beam window material in many accelerators and high-power hadron beam applications around the world, notably among them:

- at CERN, as a single layer for two 100  $\mu\text{m}$ -thick windows of TI8 transfer-line between the SPS and LHC (figure 1.2(a)) and as a thin foil applied to a C-C plate for the two windows inside the transfer-line between SPS and CNGS (figure 1.2(b)) [27].

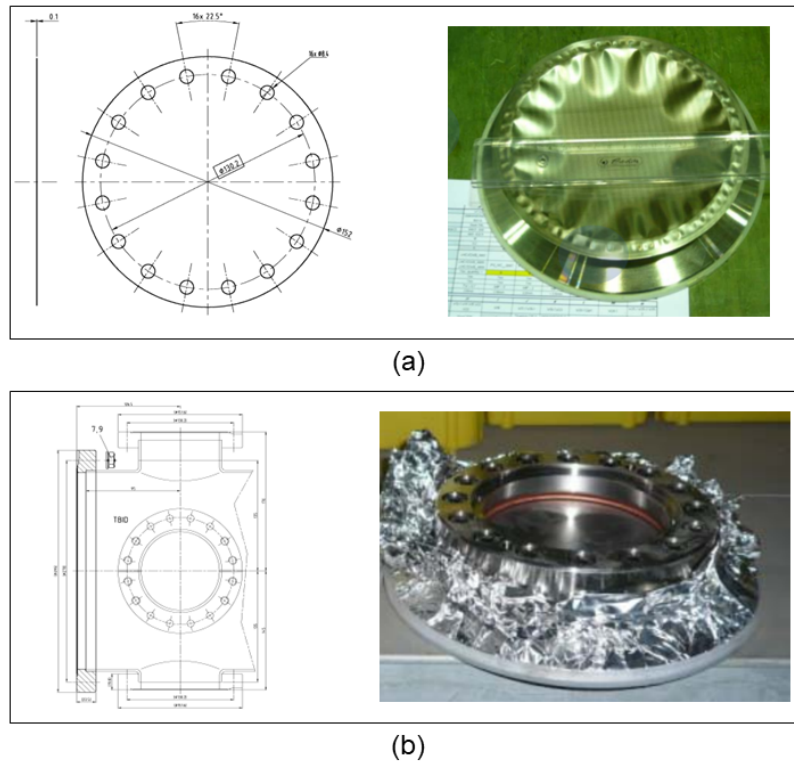


**Figure 1.2:** Technical designs and pictures of two Titanium Grade 5 beam windows at CERN: a beam dump (TDE) window (a) at TI8 beamline to transfer protons and ions to the LHC and a beam stopper (TBSE) window (b) at the beginning of the TT41 beamline for protons directed to the CNGS neutrino target [15].

- at Fermi National Accelerator Laboratory, where most of the 83 beam windows are in titanium alloy (figure 1.3 [11][20]). The figure 1.3(c) shows how a beam window is typically assembled: the window is firstly fabricated by an electron-beam process, then the foil is sandwiched between two titanium rings and, finally, the sub-assembly is hand-welded into a custom Titanium Conflat-flange.
- at J-PARC, where titanium alloy is adopted for the primary beam window and the target containment window of the neutrino facility (figure 1.4(a) and (b)) as well as for the target chamber window of the hadron facility. The primary beam window (fig. 1.4(a)) comprises two 300  $\mu\text{m}$ -thick partial hemispheres of titanium alloy window cooled by helium gas flowing between them.

In recent years, a collaboration between Brookhaven National Laboratory (BNL) and J-PARC is underway with the aim to predict how mechanical and micro-structural properties of certain titanium alloys change when exposed to high energy proton irradiation (extremely different to that of low energy neutrons) [29][30]. This research programme, in the framework of the RaDIATE collaboration, consists of conducting high-intensity proton beam irradiation experiments on various titanium alloys specimens at different

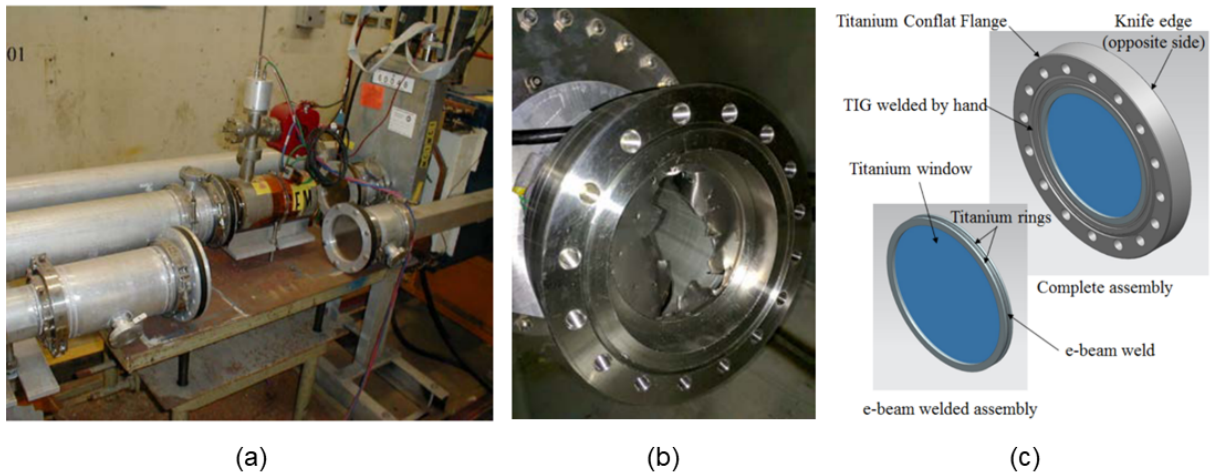


**Figure 1.3:** Technical designs and pictures of Titanium Grade 5 beam windows at FNAL: an example of vacuum windows in SY120 beamline (a), an example of window failure (b) and a sketch of a typical assembly of a titanium vacuum window (c) [11].

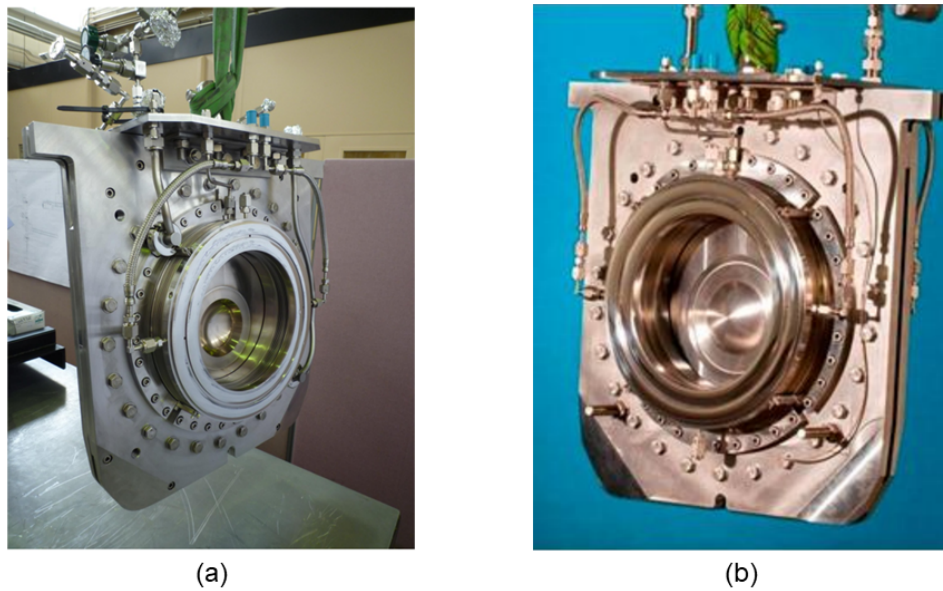


**Figure 1.4:** Pictures of Titanium Grade 5 beam windows at JPARC neutrino facility: primary beam window (a) and target containment window (b) [28].

facilities, such as HiRadMat at CERN and Brookhaven Linac Isotope Producer (BLIP) facility at BNL. Two principal goals were pursued: to test the mechanical properties of the Titanium Grade 5, currently the most widespread solution for beam windows at JPARC and FNAL, and to understand how elemental and phase variations of titanium alloy grades affect the irradiation performance. These tests underlined that the effects of radiation damage differ significantly between the grains of  $\alpha$  (Hexagonal Close Packed Structure) and  $\beta$  (Body Centered Cubic Structure) phases: high-density of defect clusters have been observed in each  $\alpha$ -phase grain, while no visible defects have been detected for

$\beta$ -phase grains at low radiation doses. The high susceptibility to irradiation damage of the dual  $\alpha+\beta$ -phase Ti-6Al-4V is macroscopically evidenced by tensile tests results, which show an increase of hardness and a large decrease in ductility for fluences even lower than 0.06 dpa.

These investigations about Titanium Grade 5 and other radiation-tolerant candidate grades are of vital importance for the projects of future accelerator facilities in whom titanium alloys were chosen as a beam window material, such as the Long Baseline Neutrino Facility (LBNF) at FNAL, the Fermilab PIP-II particle accelerator for the Deep Underground Neutrino Experiment (DUNE) [31], under construction in South Dakota, and the International Linear Collider (ILC).

### 1.2.3 Inconel 718

The Nickel-based superalloys, and in particular the Inconel 718 alloy, are a good candidate for beam windows applications where high strength and high corrosion resistance are primary demands for the correct and safe operation. The exceptional fatigue and creep strengths make the Inconel 718 a great choice for several structural applications in the aerospace and nuclear industries, such as jet engines, gas turbines and fusion reactors (for example, for the jackbolts of the ITER Central Solenoid) [32]. Moreover, this alloy has a large ultimate tensile strength of roughly 0.8-1.2 GPa, excellent corrosion resistance at ambient temperature and until 500 °C and a reasonable irradiation tolerance up to a dose of 20 dpa [33].

The beam window applications where Inconel 718 has been and still is utilised as a main component material are listed below:

- The proton beam window (PBW) of the Los Alamos Neutron Science Center (LANSCE), New Mexico, USA.
- The PBW of the Target Station 1 (TS1) of ISIS Neutron and Muon Source at the Rutherford Appleton Laboratory (RAL), United Kingdom.
- The beam window of the Isotope Production Facility (IPF) at LANSCE. The beam assembly and the IPF testing apparatus are shown in figure 1.5.
- The first generation of the PBW of the Spallation Neutron Source (SNS) at Oak Ridge National Laboratory (ORNL), Tennessee, USA. The design of this IN718 proton beam window (recently replaced with a second generation PBW in Aluminium alloy Al-6061-T651) is shown in figure 1.6: it consisted of two curved walls in Inconel 718 with a separation gap of 1.5 mm in which heat deposited during irradiation was removed by cooling water flow [19].



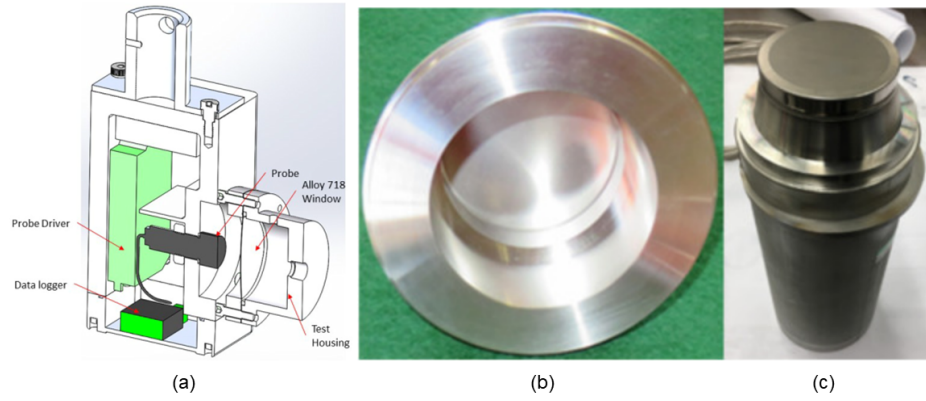


**Figure 1.5:** (a) CAD drawing of the INC718 IPF testing apparatus used to measure beam window deformation under different loading conditions. (b) IPF beam window and weld flange and (c) full beam window assembly [34].

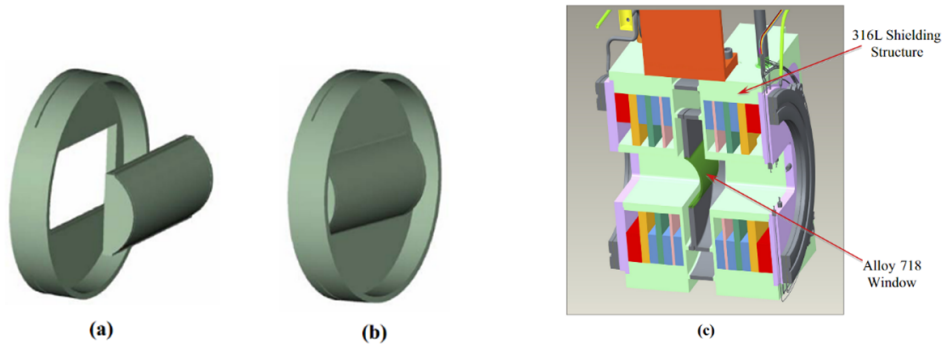


**Figure 1.6:** First generation curved dual-wall Inconel 718 PBW at the Spallation Neutron Source: (a) Alloy 718 window and frame, (b) complete Alloy 718 window, and (c) cross-sectional view of complete PBW assembly [19].

Much of the knowledge gained so far about the radiation-induced degradation in mechanical properties of this superalloy comes from the characterisation tests carried out on the just mentioned beam windows after removal from service. Moreover, the tensile properties of this precipitation hardenable alloy, whose microscopic structure is fairly complex, is strongly affected not only by the proton (or other particles) irradiation but also by the different temperatures and times of the heat treatments. It is therefore important to briefly report the characteristics and differences of the two production solutions most used for beam windows applications, such as the solution-annealed (SA) and precipitation-hardened (PH) conditions:

- **Precipitation-hardened condition:** This condition is achieved by introducing a fine dispersion of  $\gamma'$  ( $\text{Ni}_3(\text{Al,Ti})$ ) and  $\gamma''$  ( $\text{Ni}_3\text{Nb}$ ) phases in a composite structure of the austenitic matrix and by undergoing the alloy to multi-step heat treatments of aging with the purpose of increasing the strength. While the  $\gamma'$  phase, with a

face-centred cubic (fcc) structure, is quite stable, the semi-coherent body-centred-tetragonal  $\gamma''$  phase is metastable and tends to transform to ordered orthorhombic  $\delta$  ( $\text{Ni}_3\text{Nb}$ ) phase for temperatures higher than 850 °C.

- Solution annealing condition: In this case, a single-phase austenitic microstructure is not strengthened by precipitation of  $\gamma'$  and  $\gamma''$  phases and only  $\delta$  phase can be present if solution annealing is conducted at a temperature below the 1020 °C.

Alloy 718 in both PH and SA conditions was utilised for the construction of beam windows. Although the post-irradiation examinations that have been carried out over the last twenty years have led to a deeper understanding of the effects of the radiation-induced damage, even today the influence of irradiation on the mechanical properties and on the microstructure of this superalloy is not utterly unambiguous [35]. The differences in operational performance and in degradation of mechanical properties observed for the Inconel 718 beam windows (in the SA and PH conditions) are summarised below:

- The PH Inconel 718 PBW at LANSCE was removed from operation because it was leaking coolant. The tensile tests detected significant radiation-induced embrittlement during service and a decrease of the total elongation to 5% at 10 dpa and to 0% at 20 dpa.
- The SA Inconel 718 proton beam window of the ISIS TS1 was successfully in use for almost 25 years and was removed from operation after having received a dose of 30-40 dpa upon reaching the administrative maximum dose limit (not for reasons of structural embrittlement).
- In light of the results of embrittlement of the PH PBW at LANSCE, the Solution-annealed IN718 was chosen for the first generation of PBW of the Spallation Neutron Source. The service lifetime was determined in accordance with the administrative dose limit and the window was replaced after two years of high-energy proton irradiation, corresponding to a peak dose of 9.7 dpa, without having caused any problem to the operation of the SNS facility.

In conclusion, Inconel 718 in precipitation-hardened condition has been shown to be more susceptible to radiation-induced changes in structure, composition and cohesion with the matrix than the solution-annealed alloy under irradiation of neutrons, protons and ions [32][36][33]. The mechanical behaviour of PH IN718 is primarily influenced by the dissolution of the  $\gamma'$  and  $\gamma''$  phases, not stable under low-temperature irradiation. The  $\gamma''$  phase, the main responsible for the hardening of the alloy, disappears even at relatively low doses (0.7 dpa). A series of recent experiments conducted on the IPF beam window at LANSCE have proved that the  $\gamma'$  and  $\gamma''$  phases are no longer observable after irradiation to 11.3 dpa but still appreciable ductility and work-hardening capacity



has remained after irradiation [36]. The last tensile tests conducted at SINQ spallation source (Swiss Spallation Neutron Source) and at IPF on SA Inconel 718 samples concur that remarkable ductility is retained by the superalloy after irradiation, even at high doses, and that uniform elongation values increases from approximately 8% at 7.8 dpa to roughly 14% at 18.4 dpa [37]. However, the biggest impact on the mechanical behaviour is that of the exposure of the alloy to elevated temperatures during fabrication, irradiation or post-irradiation handling stages, since high temperatures are capable of inducing recombination and annihilation of radiation-induced defect structures via annealing. In fact, the thermal processes can have an even greater influence on the mechanical behaviour than the beam irradiation.

### 1.2.4 Stainless steels

#### Austenitic stainless steels

Austenitic steels are non-magnetic stainless steels with high chromium and nickel content and low levels of carbon. Austenitic steels, the most popular type of stainless steel, are renowned for their formability and corrosion resistance. Unlike the body-centred cubic (bcc) crystalline structure of the ferritic steels, austenitic steels have predominantly a face-centred cubic (fcc) grain structure that prevents them from being hardenable by heat treatment. This fcc grain structure is achieved by adding a sufficient quantity of austenite-stabilising elements, such as Ni, Mn and N, in a standard 18% chromium alloy.

The most popular grades of austenitic steels utilised for beam-windows components are **AISI 304L** and **AISI 316L**. Both are part of the 300 series, a subgroup of chromium-nickel alloys that achieve their austenitic microstructure almost exclusively by Nickel alloying. The reference nomenclature for stainless steel grades is the American Standard AISI (American Iron and Steel Institute). The 304 grade, the most common of the stainless steels, typically contains 18% chromium (minimum percentage of Cr needed to completely convert all the ferrite to austenite) and 8% nickel. The production of the 316 grade provides for the addition of about 2 per cent of molybdenum to increase corrosion resistance. The carbon content for austenitic stainless steels, which must not exceed 0.08 per cent for straight grades, can be reduced to produce steels less susceptible to intergranular corrosion. Since the mechanical effects due to carbide precipitations are a concern for irradiated components, low carbon grades (indicated by the letter "L"), with a maximum carbon content of 0.03%, are more suitable for beam windows applications.

These steel grades offer excellent performances in terms of corrosion resistance, ease of fabrication and welding and have good high-temperature properties. The main advantage of their use lies in the fact that their behaviour after long exposure to radiation

environment is well known and proven: austenitic steels are the typical choice for the cylindrical shell of the reactor pressure vessel in nuclear power plants, one of the most critical components for nuclear plants on which depends the lifetime of the reactor.

Numerous research centres and experimental reactors, such as the High Flux Isotope Reactor (HFIR) at ORNL and the Experimental Breeder Reactor-II (EBR-II) at Argonne National Laboratory, deal with the effects of radiation damage on these structural steels and several studies have been conducted about austenitic steels under irradiation of different types of particles at different energy levels [38]. The most life-limiting factors in the application of these stainless steels concern the precipitation of phases, the formation of cavities with the volumetric expansion of the material (the so-called Void Swelling) and the irradiation creep.

The **AISI 304L** (or X5CrNi18-10, according to the EN designation) was used as the main component for nearly the totality of the beam windows installed along the beamlines of the Super Proton Synchrotron (SPS) at CERN. On the other hand, the **AISI 316L** (or X5CrNiMo17-12-2) has been chosen for the windows of many other CERN facilities, among which the Proton Synchrotron (PS), the PS Booster and ISOLDE.

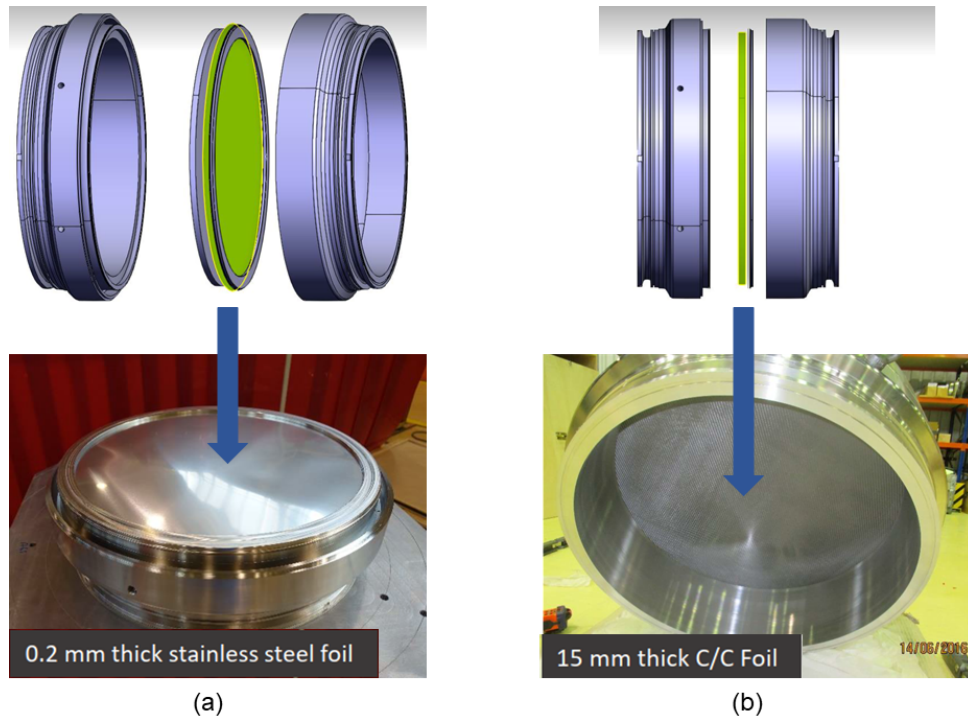


**Figure 1.7:** CAD drawings and pictures of the entrance window, showing (a) the 200  $\mu\text{m}$ -thick stainless steel foil and (b) the 15 mm-thick CC plate [39].

Moreover, it is important to point out that stainless steel has been selected for the entrance window of the LHC beam dump, the design of which provides for the application of a 200  $\mu\text{m}$ -thick 316L grade foil on a 1.5 cm-thick C-C plate in SIGRABOND 1501G.

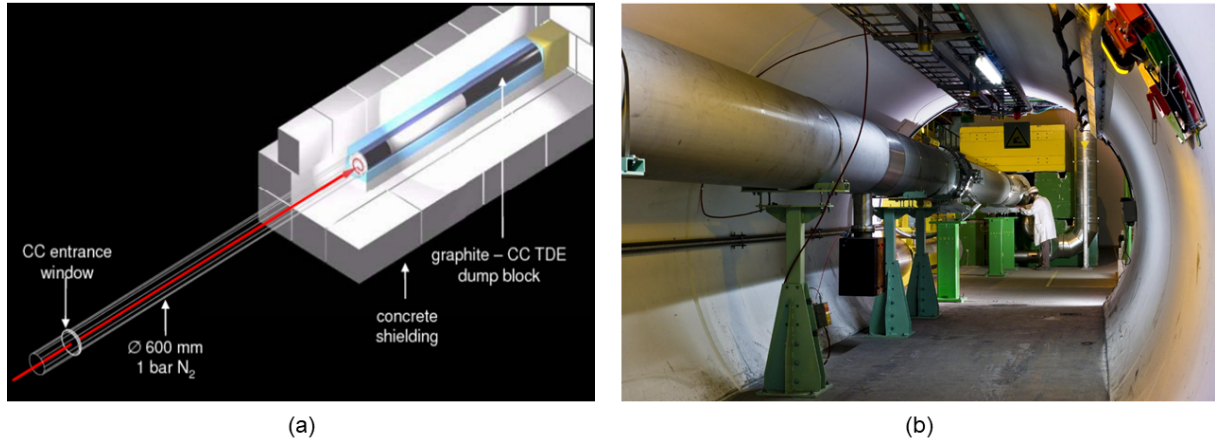


**Figure 1.8:** Sketch (a) and picture (b) of the LHC dump block and surrounding shielding, showing the location of entrance window [17][40].

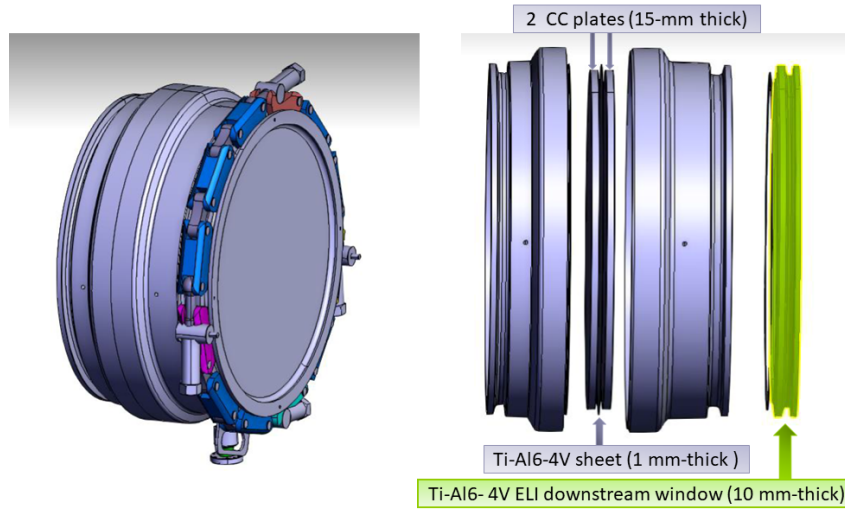


**Figure 1.9:** CAD drawings of the new conception of the entrance window for the beam dump of LHC Run 3 and, in the future, of HL-LHC at CERN [40].

This design solution proves that this metal was considered highly reliable for withstanding the repeated dynamic thermal loads which occur when the ultimate intensity LHC beam ( $4.77 \cdot 10^{14}$  protons at 7 TeV) is dumped [17]. The figures 1.7 and 1.8 show CAD drawings and pictures of the double-layer beam windows and of the LHC Dump cavern. At the end of 2021, this beam window was replaced by a beam window of new conception to cope with beams of even more increasing intensity, such as the ones of the LHC Run 3 and of the future High-Luminosity LHC (HL-LHC) project. This new design provides for a 1 mm-thick Titanium Grade 5 sheet sandwiched between two layers of 15 mm-thick C-C plates and a 10 mm-thick Titanium Grade 23 plate installed downstream (figure 1.9). This beam window conception increases the reliability and robustness of this critical system to the differential pressure and beam-induced thermal loads and is fully compatible with the future HL-LHC parameters [40].

## Martensitic stainless steels

Martensitic stainless steels represent one of the four main varieties of stainless steels (Ferritic, Austenitic, Duplex, and Martensitic). Such steels are characterised by high strength and hardness as well as by excellent resistance to wear and corrosion. They are ferromagnetic and, differently from austenitic and ferritic stainless steels, can be hardened and tempered through aging and heat treatments. They also possess a high value of Young's modulus, a low coefficient of thermal expansion and a high thermal conductivity coefficient, making them excellent for heat-transfer applications.

Martensitic stainless is distinguished by its particular crystal structure. Martensitic structures are obtained through a rapid cooling (called quenching) that has the aim of "freezing" a phase that is stable at high temperatures but unstable at room temperature. After quenching, the face-centred cubic (fcc) austenite transforms in the so-called martensite, a crystalline structure with body-centred tetragonal (bct) form. This microscopic change in the structure causes induces the formation of a large number of dislocations, which are responsible for the strengthening mechanism of the steel.

By virtue of the above-listed characteristics, the martensitic steels are good candidates for beam window applications in which the preservation of mechanical properties at high temperatures and decent resistance to radiation-induced embrittlement are required, such as spallation neutron source facilities and accelerator-driven subcritical reactors. Two martensitic stainless steels which provide excellent choices for beam window applications are **DIN 1.4926** and **T91**.

The martensitic steel **DIN 1.4926** (11% Cr) was used for a double-wall window in the LANSCE facility at the Los Alamos National Laboratory (LANL). The beam window, designed and realized by the Paul Scherrer Institut (PSI) at Villigen (Switzerland), was irradiated with 800 MeV protons at LANSCE and, finally, investigated at Forschungszentrum Jülich (FZJ), in Germany. The results obtained from this joint study between the three research centres showed that the tensile properties and the microstructure of DIN 1.4926 were considerably changed after irradiation, even at low levels of fluence (0.3 dpa). The radiation-induced hardening increases progressively with fluence up to 6.8 dpa (the maximum attained dose). The uniform elongation is strongly reduced from about 11% for pristine steel to less than 1.5% for irradiated steel. Lastly, small defect clusters were observed in all the samples of the irradiated martensitic steel [41].

The martensitic stainless steel **T91** (Mod. 9Cr-1Mo) is a suitable material for those beam window applications in which high mechanical strength (larger than those of austenitic steels) and excellent corrosion resistance are required, such as in the case of the beam window of the future ADS spallation targets. T91 steel was developed by the Oak Ridge National Laboratory in the 1970s. It has good thermal conductivity and a low coefficient

of thermal expansion, like the other martensitic steels, but stands out for its strong corrosion resistance and good creep rupture strength. It is, therefore, an ideal material for realising steam chambers and superheaters for boilers of power plants.

Two different projects involve the use of this steel for the proton beam window of an accelerator-driven system: the MEGAwatt Pilot Experiment (MEGAPIE) and the ADS proposed by the Japan Atomic Energy Agency (JAEA) [24][42]. An accelerator-driven subcritical reactor is a hybrid system of a high-energy proton accelerator and a substantially subcritical nuclear reactor core. These promising devices could be useful to develop Th-based energy production or to transmute high-level nuclear waste, such as minor actinides. The beam window forms the boundary component between the accelerator and the spallation target region. In this region, the liquid Lead-Bismuth eutectic (LBE) flows from the bottom up of the core while being heated by the proton beam.

The ADS beam window must be able to withstand many extreme conditions at the same time, including any of the following:

- The corrosion induced by the passage of the LBE coolant.
- The differential pressure between the core, in which LBE flows, and the accelerator region, kept under vacuum.
- The heat generation by the proton beam.
- The irradiation damage by neutrons and protons.

This martensitic steel was considered suitable for this purpose since it has a mechanical strength higher than those of austenitic stainless steels and it is less susceptible to corrosion damage than other materials.

MEGAPIE is an initiative launched by the French Atomic Energy Commission (CEA), the German Forschungszentrum Karlsruhe and the Paul Scherrer Institut, to demonstrate the feasibility of a liquid LBE target for ADS spallation facilities at a beam power level of 1 MW. The irradiation experiment of the MEGAPIE target took place at the SINQ facility of PSI from August to December 2006. The experiment was successful, and a series of planned measurements concerning thermal-hydraulics, structural mechanics and nuclear aspects were performed, in such a way that the use and application of certain materials for the beam window and other components were ascertained. The figure 1.10 shows the design of the MEGAPIE target assembly with the lower liquid container and the beam window made of steel T91 [24][43].

The ADS project proposed by the Japan Atomic Energy Agency consists of a high-intensity proton accelerator with 1.5 GeV beam energy, a liquid Lead-Bismuth eutectic spallation target and a subcritical core ( $k_{eff} = 0.97$ ) with 800 MW thermal power. The project of the T91 beam window is one of the critical issues for the realisation of the ADS, and different types of window design were suggested over the years, such as the

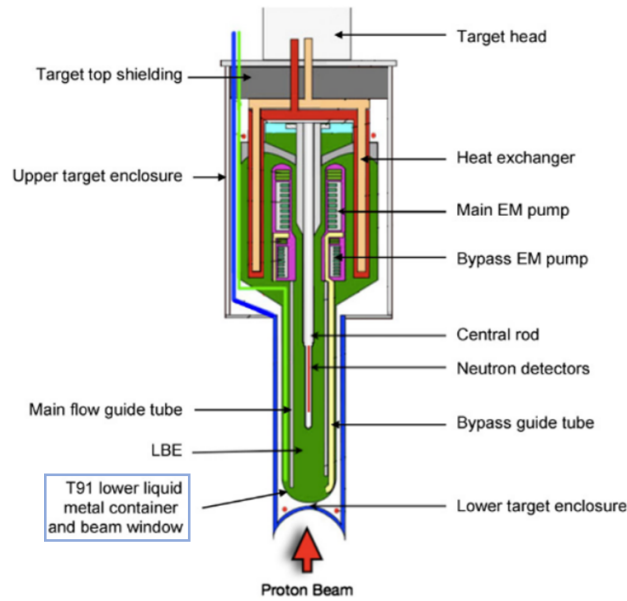


**Figure 1.10:** Schematic view of the MEGAPIE target assembly with the T91 window and the other main components indicated [43].

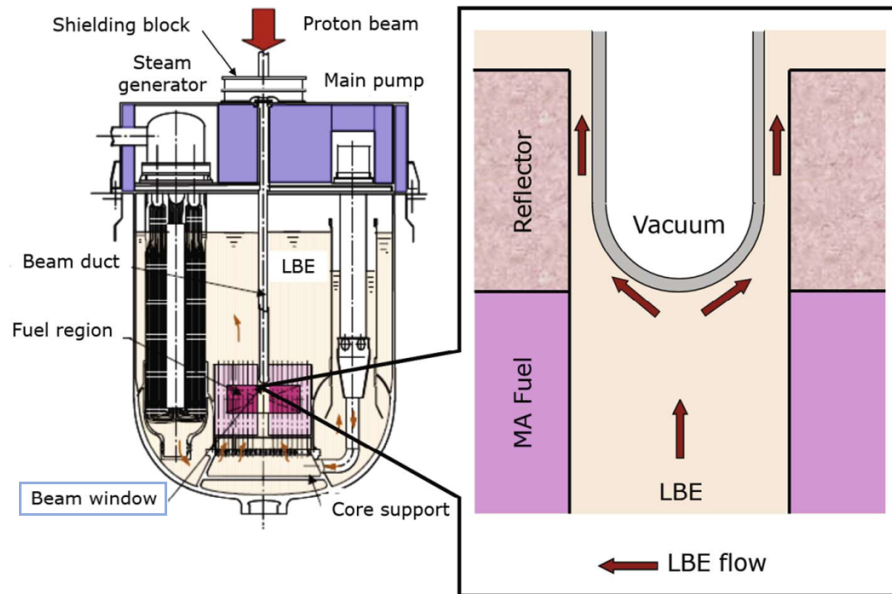


**Figure 1.11:** Schematic view of the design of the LBE cooled ADS and its beam window proposed by the JAEA [44].

ellipse-shape and the hemispherical-shape (in figure 1.11), to address the problems of creep deformation, corrosion and thermal stress caused by the proton beam [42][44].

### 1.2.5 Aluminium alloys

Aluminium is a very interesting material for ultrahigh vacuum systems for accelerators and, in particular, for beam window applications. It is a very light material ( $\rho \approx 2.7 \text{ g}$

$\text{cm}^{-3}$ ), with a density 2-3 times lower than that of steels or Nickel alloys.

The high transparency to radiation is an excellent quality of aluminium alloys: the particles, while crossing the material, have less interaction with the matter and deposit a lower amount of heat, resulting in a smaller peak of temperature. Since the relatively low melting point is among the main defects of this material, the maximum temperature reached during irradiation is a factor which always has to be taken into account.

Moreover, the property of high transparency ensures a reduction of the residual radioactivity after machine shutdown and increased efficiency in the particles transfer: for instance, the replacement of the Inconel 718 SNS PBW with an aluminium one has caused an approximate 3-5% increase in neutron production by the spallation target from the decreased scattering of protons having passed through the window [19].

Other characteristic properties are the high thermal conductivity, the resistance to embrittlement induced by radiations and the possibility to be easily shaped into complicated profiles by extrusion and drawing [45].

Aluminium alloys are classified into eight groups or series, according to their main alloy element. The aluminium alloys most frequently utilised for beam windows applications in radiation environments fall into two general alloy groups: the 5000-Series (Al-Mg alloys) and the 6000-Series (Al-Mg-Si alloys).

### Aluminium 5000-Series alloys

The Al-Mg alloys are solid-solution strengthened alloys with superb corrosion resistance in flowing water and good formability. They are used in a wide variety of industrial sectors and for marine and naval applications. Because of their high thermal conductivity and, most importantly, the excellent radiation-induced damage resistance, Al-Mg alloys are also very common in the nuclear field, for applications where an aluminium alloy with resistance qualities halfway between those of the softer 1000-Series alloys (pure aluminium) and those of stronger precipitation-hardened (PH) 6000-Series alloys are required.

Within this category of aluminium alloys, three grades were essentially chosen for being used in beam windows applications: **Al-5052**, **AlMg<sub>3</sub>** (close to Al-5454) and **Al-5083**.

The **Al-5052** is an aluminium alloy primarily alloyed with Magnesium (roughly 2.5% by weight) and Chromium (0.25%). This grade, in the temper state Al-5052-H19 (where H indicates that its strength was increased by strain hardening and 19 specifies the approximate amount of cold work) was utilised for three beam windows at CERN, inside the Transfer Tunnel 20 (TT20) that connects the CERN Super Proton Synchrotron (SPS) with Targets T2 (TT23 line) and T4 (TT24 line), located in the CERN North Area [27].

The aluminium-magnesium alloy **AlMg<sub>3</sub>**, with the composition of Mg (2.72% by weight), Si (0.3%), Fe(0.25%) and Mn(0.35%), was used as the material for the safety-

hull of the SINQ Target-3 and irradiated in 1998 and 1999. In figure 1.12 the design of the safety-hull is illustrated schematically. The safety-hull is a double-walled container of about 20 cm in diameter and 2 m long, where the lower part acts as an entrance window for the proton beam coming up from the vacuum region below. Heavy water ( $D_2O$ ) flows in the gap between the two walls to cool the hull and the target block during irradiation [46].

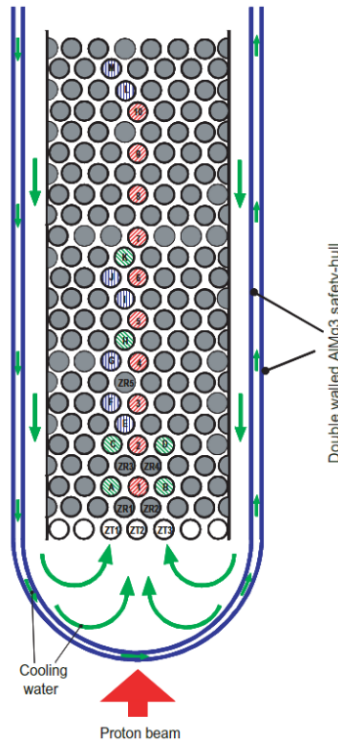


**Figure 1.12:** A schematic sketch of the lower part of SINQ Target-3 AlMg<sub>3</sub> Safety-hull [46].

The aluminium alloy most widely used for PBWs of spallation neutron sources is the **Al-5083**. This alloy, composed of magnesium (about 4.5% in wt.) with traces of manganese and chromium, features high corrosion resistance to water and an exceptional strength after welding, to the point of being unrivalled in terms of strength among the non-heat treatable aluminium alloys. It is always subjected to homogenising annealing (Al-5083-0) before use in beam windows to remove the effects of prior working and defects, like slag inclusions or air holes, and to be less susceptible to radiation damage.

At the ISIS Target Station 2 (TS2) of the Rutherford Appleton Laboratory (RAL) 5083 alloy is utilised for the proton beam window. Unlike the Target Station 1 PBW, where the design of a window with water flowing between two Inconel 718 plates had been adopted, a 0.5 mm-thick 5083-O aluminium alloy window with passive cooling by void vessel helium atmosphere was preferred for the more recent ISIS TS2. The design and a picture of the beamline in which the PBW was placed are presented in figure 1.13. The Al-5083 window was in operation between 2008 and 2017, when the occurrence of a failure



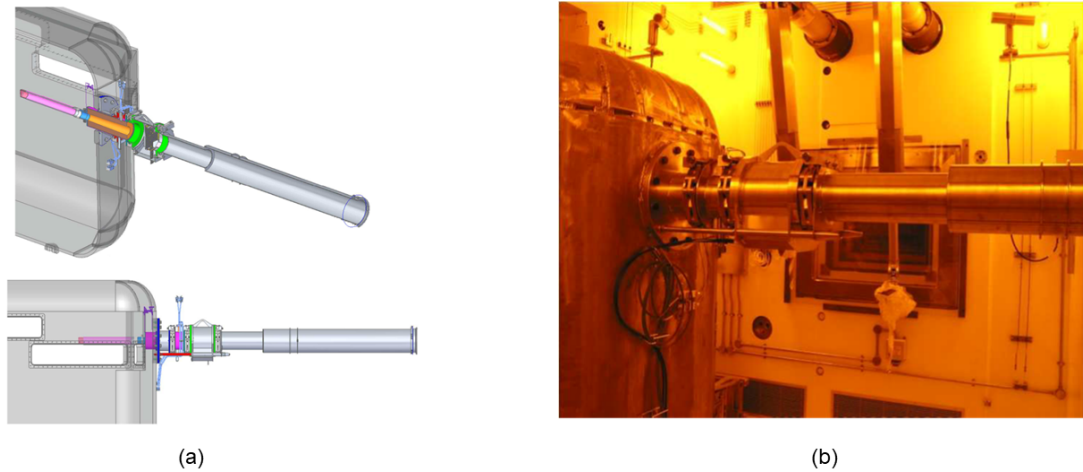


**Figure 1.13:** A schematic sketch (a) and a picture (b) of the TS2 Proton Beam Window of the ISIS facility at the Rutherford Appleton Laboratory [47].

forced the beamline to a two-months shutdown. A post-irradiation examination of the window is scheduled with the purpose of obtaining a better understanding of radiation damage and embrittlement mechanism in PBW [47].

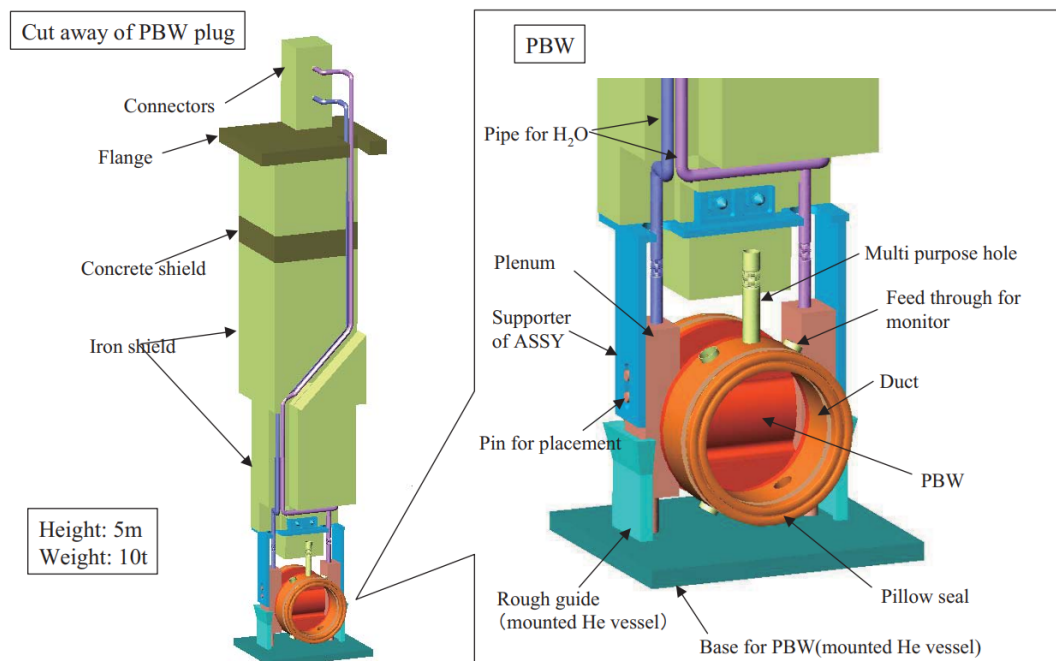


**Figure 1.14:** Schematic drawing of the proton beam window of the spallation neutron source (JSNS) at J-PARC [48].

A 5083 alloy PBW is installed inside the Spallation Neutron Source at the Japan Proton Accelerator Research Complex (J-PARC). The window, placed 1.8 m upstream of the mercury spallation target, is used to separate the ultra-high vacuum environment in the proton beam transport line from the target region filled with helium gas of 0.1

MPa [48]. As it can be seen in the figure 1.14, in which the whole assembly of the PBW is shown, the window consists of 2.5 mm-thick aluminium alloy plates (sandwiched structure) with coolant water flowing in a horizontal direction [49]. Originally, it was planned to use the Inconel alloy as window material by virtue of its structural strength. However, the optics calculation indicated that the beam scattering inside an IN718 window would have been too high and that a material with a lower atomic number was preferable. The aforementioned promising results obtained on the AlMg<sub>3</sub> alloy at PSI have directed the search in aluminium alloys materials and, finally, Al-5083 was chosen and used for the manufacturing of the JSNS PBW. It is interesting to note that, since the PBW is being highly activated during the beam operation and requires to be replaced every two years, a remote handling procedure was implemented for the replacement in order to minimise the shutdown period of the JSNS facility.

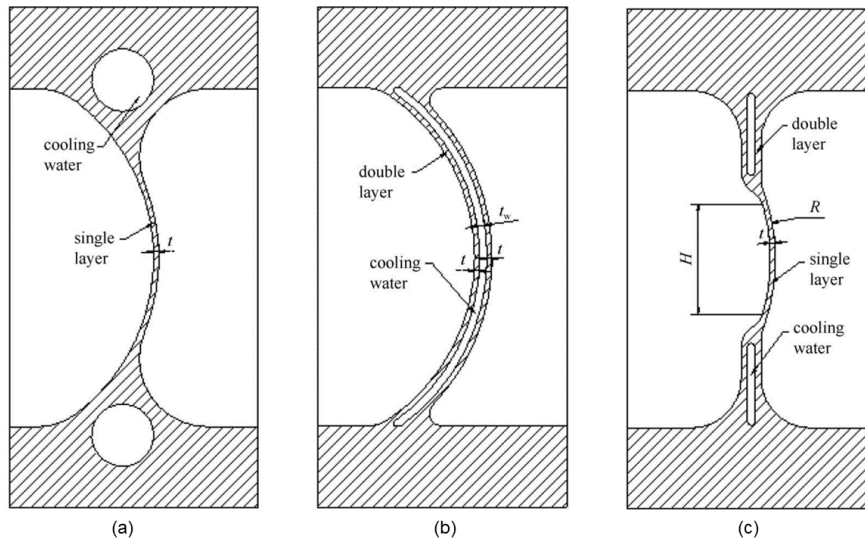


**Figure 1.15:** The cross-section of three PBW structures designed for CSNS: (a) Single layer structure. (b) Sandwiched structure. (c) Single-double layer structure [50].

Lastly, the 5083-O alloy was chosen as the PBW material of the China Spallation Neutron Source (CSNS). The CSNS is an accelerator-based neutron source built in Dongguan (Guangdong Province, China). The construction of the facility was completed in 2018 and the design aim of 100 kW (Phase I) was achieved in 2020. A power upgrade is planned for the next years, from 100 kW of Phase I to 500 kW of Phase II, with an intermediate stage at 200 kW. The present China SNS PBW is used as a boundary to separate the high vacuum environment, where the 1.6 GeV proton beam comes from, and the helium-filled environment of the solid tungsten station, where neutron scattering experiments occur. The choice of Al-5083-0 for the Proton Beam Window has followed a similar path to that of the JSNS PBW: both Inconel 718 and 5083 alloy have been compared and the latter has been considered more suitable for the purpose in light of a better scattering effect and

a lower proton energy deposition (the heat deposition on Al-5083, calculated by SRIM, has resulted to be one-third of that on IN718) [50].

An extensively investigated aspect of the CSNS PBW design involves the analysis of the cooling structures. The design of the CSNS PBW introduces the advantages of the two more common PBW cooling structures:

- The sandwiched structure (figure 1.15 (b)), utilised for the Spallation Neutron Sources at the Oak Ridge National Laboratory and at J-PARC, which owns good strength, processability and thermal dissipation ability for high beam power, but results in a serious activation of the cooling water as well as in a high energy deposition and scattering effect.
- The single layer structure (figure 1.15(a)), the most suitable cooling structure for low beam power windows, which has low energy deposition, a small scattering effect and a little water activation, but a low capacity of thermal dissipation.

The single-double layer structure (figure 1.15(c)), a compromise between the previous cooling structures, was proposed for the CSNS PBW in 2013 and installed in 2018. Now the window has been failure-free operated for several years and is planned to be replaced after seven years of operation. Recent studies about the possibility of using this window design with a beam power of 200 kW show that the PBW must be changed despite the advantages of the single-double layer structure due to the excessive temperatures which would be reached [22].

The two mechanisms of radiation damage that most affect the mechanical properties and microstructure of the Al-Mg alloys are the formation of Helium bubbles and the radiation-induced Mg-Si precipitation. The irradiation hardening (an increase of yield stress) and embrittlement (decrease of elongation) on these alloys are strongly dependent on the nature and the intensity of the radiation.

The Al-5052 alloy, exposed to neutron irradiation at the High Flux Isotope Reactor (HFIR), showed signs of hardening due to the formation of dislocation loops and of small Mg<sub>2</sub>Si precipitates [51]. Under the exposure of thermal neutron flux, aluminium can transmute into silicon through the following two-stage reaction:



The Al-5052 alloy is thus continuously modified and converted to a ternary Al-Mg-Si alloy due to thermal neutron absorption and, because the solubility of silicon in aluminium is low, the transmutation-produced Si interacts with the Mg in the matrix to produce Mg<sub>2</sub>Si precipitates.

On the other hand, under high-energy proton irradiation, as in the case of the AlMg<sub>3</sub> safety-hull irradiated at SINQ, the Mg<sub>2</sub>Si precipitates could not be observed but high-

density small bubbles were detected [46]. The primary cause of high-density small bubble production may be ascribed to the high contents of helium and hydrogen produced by high-energy protons. These small and dense bubbles are strong enough to obstacle the dislocation motion: their presence can enhance the effects of embrittlement and irradiation hardening on the window material.

In conclusion, since the embrittlement caused by a large amount of He bubbles is expected to have the most detrimental effect on the mechanical properties of aluminium alloys, the gas production is considered to be more appropriate than the dpa calculation for the lifetime estimation of an aluminium beam window [22].

### **Aluminium 6000-Series alloys**

The Al-Mg-Si alloys are precipitation-hardened alloys with the characteristic of being easy to machine, weldable and equipped with good mechanical properties greatly dependent on the heat treatments. They find application in several fields and are used for the construction of aircraft structures and automotive parts as well as for different components in nuclear reactors, including reflector vessels.

Within the group of the 6000-Series alloys, **Al-6061** was selected to be adopted in beam windows applications. The 6000-Series aluminium alloys have magnesium (0.8-1.2 wt. %) and silicon as their major alloying elements (0.4-0.8 wt.% Si). Small quantities of Fe, Cu, Cr, Ti, and Zn are added to improve aqueous corrosion resistance and mechanical strength and to control the grain size. The 6061 alloys may be heat treated to produce a finely distributed  $Mg_2Si$  phase precipitate in order to enhance both strength and ductility. Different temper states can be found on the market, including the annealed state (Al-6061-O) and the tempered grades T6 and T651. The designation "Al-6061-T6" denotes the application of a heat treatment that results in the dispersion of small needle-shaped precipitates, while the designation "Al-6061-T651" denotes the straightening treatment, which was applied to the alloy after quenching but before the heat treatment.

This precipitate-strengthened alloy was subjected to neutron and proton irradiation in order to assess the effects of radiation on the mechanical properties. Under neutron irradiation, 6061 alloys exhibited very high tensile strengths (about 350-400 MPa) and conserved sufficient ductility at high doses (70 dpa) [52]. No new grain bubbles were observed in the samples of Al-6061-T6 irradiated with 800 MeV protons at the Los Alamos Meson Physics Facility and the He bubbles detected along the  $Mg_2Si$  phase precipitates are likely to have been produced during the treatment of thermal aging [53].

Due to the encouraging findings regarding the bubbles formation and the preservation of ductility of this alloy after high-dose irradiation, thermally treated 6061 alloys were taken into account for beam windows applications.

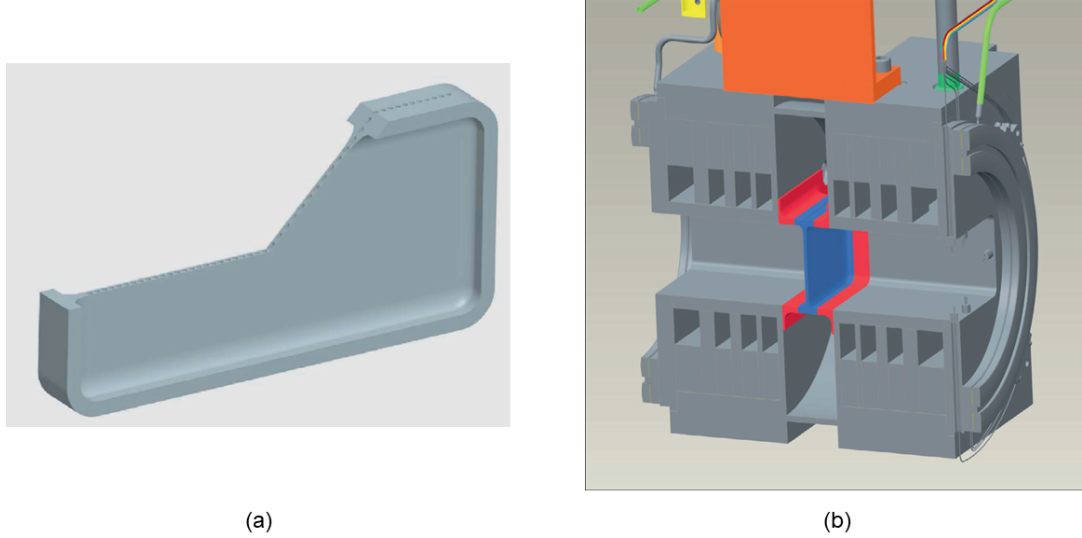


**Figure 1.16:** Second generation Al-6061-T651 PBW at the Spallation Neutron Source: (a) sectional view of flat-plate aluminium window and (b) cross-sectional view of complete SNS proton beam window assembly [19].

Al-6061-T651 was selected for the second generation PBW at the Spallation Neutron Source at Oak Ridge National Laboratory to replace the first generation PBW made of Inconel 718. As can be seen in the figure, the window consists of a 0.2-inch-thick flat aluminium plate with a series of small circular ducts (0.125 inches in diameter), which guarantee the dissipation of the thermal energy deposited by the proton beam through the passage of cooling water inside (the so-called multipipe cooling structure) [19].

The 6061-T6 alloy was eventually chosen as a structural material for the PBW of the European Spallation Source (ESS) Target station, currently under construction in Lund, Sweden. The proton beam window will be installed inside the accelerator tube that will lead 2 GeV protons to a tungsten target, depositing a record value of around 5 MW of energy in a rotating He cooled wheel, as can be observed in figure 1.17(a). Initially, a multipipe design with a helium-based cooling system was proposed for the PBW [55]. This design concept was recently replaced with a water-cooled sandwiched structure, capable of providing larger cooling rates to evacuate all the power deposited (a considerable amount of energy of 6 kW, equal to around 0.1% of the total power, is expected) [54]. This new design of PBW, shown in figures 1.17(b) and 1.17(c), consists of two thin cylindrical plates (1.25 mm and 1 mm, respectively) separated by cooling channels. Since the passage of water can lead to undesired beam distortion (definitely higher than that of the helium-based cooling system proposed previously), a very thin 2 mm cooling channel, in which a 0.3 kg/s water flow rate circulates, is specially designed for this beam window.

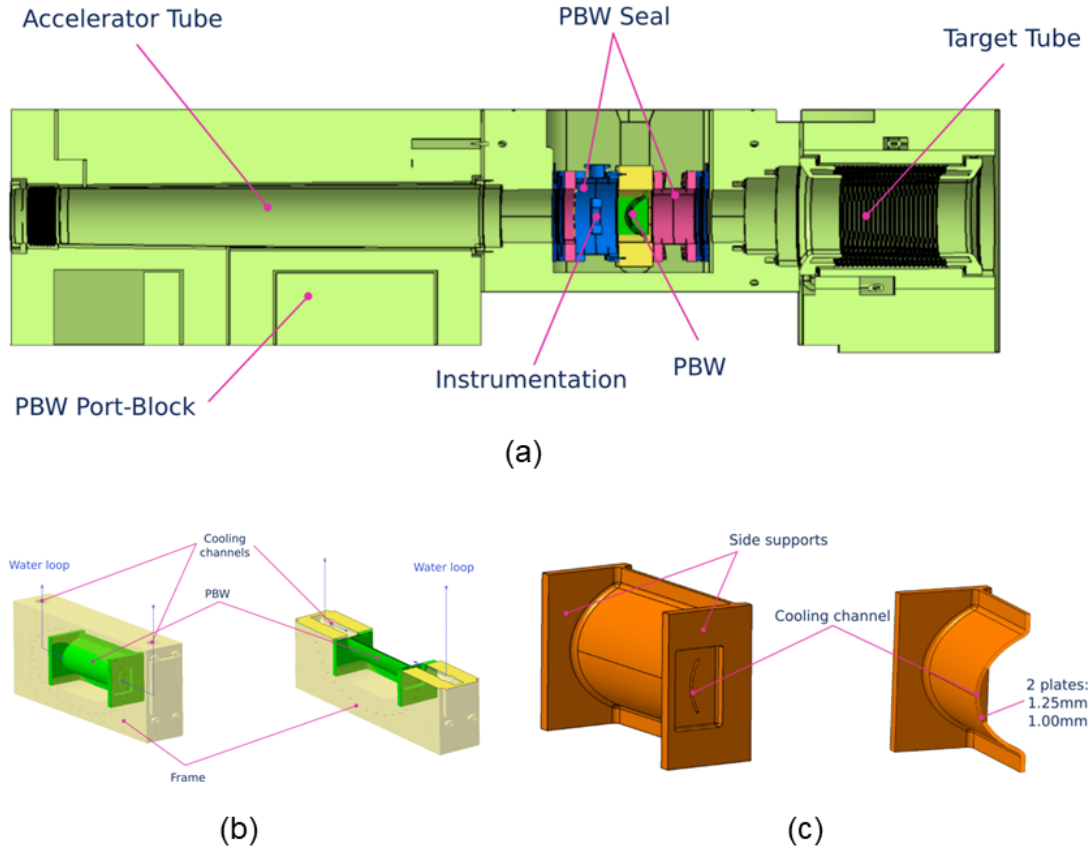


**Figure 1.17:** Overview of the PBW assembly of the 5 MW ESS Target Station (a). Detail of the PBW welded to the frame (b) and without side supports (c) [54].

### 1.3 Need for present study

To enhance the performance of next-generation accelerator facilities, studies are underway on accelerator equipment and components. The materials used in the new high-power and high-energy accelerators are intended to be exposed to particularly high radiation levels, which may deteriorate the thermophysical and mechanical properties of the components and reduce their performance and lifetime. To ensure the safe and optimal operation of these future accelerators, it is essential to examine the resilience of both currently used and promising materials exposed to high strain rate loads and extreme pulsed beam conditions.

Within the wide field of components for accelerator systems, the beam windows are undoubtedly one of the most critical components as well as one of the elements that experience more frequently failures throughout the course of a facility's lifetime. The next-generation accelerators' increased power necessitates the development of novel beam window designs.

The thesis's objective is to experimentally investigate potential beam window materials which could be adopted for both advanced accelerator facilities and other sectors

of nuclear research, such as the ADS and the spallation targets. This research is part of the "European Union's Horizon 2020 Research and Innovation programme" and it was promoted by the I.FAST Innovation Pilot project for the Particle Accelerator community. The research was made possible thanks to this project, and more specifically to the work packages 4.3 and 4.4, coordinated by Marcello Losasso (CERN), Marilena Tomut (University of Münster - GSI) and Federico Carra (CERN)<sup>2</sup>. The research project presented in this thesis was developed and conducted at the EN-MME-EDS group of CERN, under the supervision of Federico Carra. An experimental irradiation campaign was carried out at the GSI in Darmstadt: the behaviour of specific material samples under irradiation of U-ion beams has been investigated in order to determine which of these are most suitable for future beam window applications.

## 1.4 Description of the thesis structure

The thesis is structured as described below.

**Chapter 1** illustrates the definition of *beam windows* and describes why they are being used in a wide variety of particle accelerator applications. The general characteristics of materials adopted as components of beam windows, and the most sought-after properties for their application, are here highlighted. An overview of materials and designs adopted for beam windows in accelerator facilities and in other research centres from around the world is finally presented.

**Chapter 2** is dedicated to the process of selection of the materials to be utilised for the experiment of U-ions beam irradiation at the M3-beamline of the Darmstadt GSI research centre. The thermophysical properties of the materials mentioned in the previous chapter are here described with a quantitative and comparative perspective. The selection process is carried out on the basis of preliminary calculations aimed at identifying the characteristics considered most suitable for conducting the planned experiment.

**Chapter 3** focuses on the experimental survey conducted at GSI. The investigation is finalised to evaluate the thermomechanical dynamic response of the selected materials exposed to short pulses of uranium ions. The aim of the investigation is to contribute to a better understanding of radiation-induced effects on the mechanical and thermal properties of the materials chosen. The effects and possible radiation damage on the materials are detected by online monitoring techniques and post-irradiation examinations. The outcomes are discussed in detail within the chapter.

**Chapter 4** aims to develop computational models to examine and simulate the behaviour of the material samples exposed to irradiation and compare it with the findings

---

<sup>2</sup>Work Package 4.3: Innovative beam windows for high-power accelerator applications

gathered experimentally in the tests conducted at GSI. The particle transport simulations with the SRIM-2013 code enable to predict the effects produced by the interaction between the ions beam and the target samples. The ANSYS thermal and mechanical simulations allow us to benchmark the results with the experimental measurements.

**Chapter 5** summarises the main conclusions of this work, describes the thesis' key findings and makes suggestions for potential future directions of the work performed.



# Chapter 2

## Selection of materials

With this chapter, dedicated to the selection of materials, the dissertation takes a further step forward. The previous section has concentrated on illustrating the materials utilised in world nuclear research institutes for the realisation of beam windows. It is now important to select from among the identified materials which — in terms of hardness, lightness, fatigue resistance, and other previously discussed properties — are theoretically the most appropriate for the experiment that is intended to be conducted.

To that purpose, a series of preliminary analytical calculations on these materials have been performed in order to assist the decision in perspective of the experiment with Uranium ions to be conducted at the M-Branch of the UNILAC accelerator at GSI.

### 2.1 Description of eligible materials

This section is intended to briefly summarise the bibliographical research of the previous chapter about the materials worldwide adopted for beam windows before moving on to the findings from the preliminary analyses conducted on them.

A metal that exhibits excellent characteristics for beam windows applications is **Beryllium**. The high melting point, high specific heat, and low nuclear interaction cross-section are just a few causes that have led to the adoption of this metal in numerous beam-window designs. It is the best material for applications where it is essential to minimise to the maximum extent the absorption of the particles with the matter, and for this reason, it is frequently used for windows inside X-rays tubes and inside accelerator beamlines.

**Titanium alloys** are characterised by the highest specific strength compared to any other metallic element, by the high resistance to corrosion and fatigue stresses, and by the reduced activation in harsh radiation environments. These characteristics make these alloys incredibly interesting for use in the nuclear sector and explain why this material was adopted for beam windows in many internationally renowned accelerators and high-power

hadron beam applications around the world, including CERN, Fermilab and J-PARC.

The exceptional corrosion resistance and ultimate tensile strength of the Ni-based superalloy **Inconel 718** make it a great candidate for beam windows, in particular in those facilities in which the proper and safe operation must be ensured under critical exposure conditions to high-energy proton and neutron irradiation.

**Austenitic stainless steels** are frequently utilised in the construction of beam windows not only on the basis of their high corrosion resistance and ease of fabrication but especially by virtue of the well-established knowledge of their behaviour under radiation-exposed environments as a result of decades of experience in the nuclear power field. **Martensitic stainless steels** combine properties of good thermal conductivity and low coefficient of thermal expansion, desirable for beam windows applications, with steel-typical high mechanical strength and, above all, with excellent corrosion resistance. These characteristics make these metals particularly suited to implementations where very high-energy particle irradiation and strong corrosiveness conditions are established, as in the case of the future accelerator-driven subcritical reactors.

The excellent thermal conductivity and the radiation damage resistance of **Aluminium alloys** have led to the use of many types of this metal in different kinds of beam windows applications, including accelerator beamlines and Spallation Neutron Sources. Despite the relatively low melting point, the high lightness and transparency to particle interaction make it possible to minimise the scattering of the crossing beam and to reduce strongly the amount of deposited heat, with the effect of mitigating the thermal loads and delaying the occurrence of creep deformation.

Finally, the low thermal expansion coefficient, the high radiation length and the very low density make **carbon-carbon composites** excellent beam windows materials, although the high porosity makes their installation possible only upstream of the accelerator beamlines. Despite the research being addressed primarily to metals, the C-C materials are included in the following preliminary analyses to give the aforementioned metallic materials a term of reference to compare to.

The table 2.1 aims to summarise which facilities around the world use the materials for beam windows described above.

## 2.2 Material selection: figures of merit and other indicators

The choice of a particular material for beam windows is driven by the performance of the material under various operational conditions and is based on a number of criteria, which were discussed in Chapter 1.1.

Material	Specific Grade	Accelerator facilities, Accelerator-Driven Systems and Spallation Neutron Sources in which the material is adopted for beam windows
Beryllium	PF-60	CERN HiRadMat beamline, CERN CNGS exit line, Fermilab beamlines
Titanium	Ti Gr. 2	CERN SPS beamlines
	Ti Gr. 5	CERN SPS-LHC and SPS-CNGS transfer-lines, CERN HL-LHC dump beamline, Fermilab beamlines, J-PARC beamlines, Future Fermilab LBNF, Future Fermilab PIP-II to DUNE, Future ILC
Nickel alloy	Inconel 718	LANSCE PBW, ISIS Target Station 1 PBW, SNS 1 <sup>st</sup> gen. PBW
Stainless steel	AISI 304	CERN SPS beamlines
	AISI 316	CERN PS, PS Booster, ISOLDE beamlines
	DIN 1.4926	LANSCE PBW
	T91	PSI MEGAPIE PBW, JAEA ADS PBW
Aluminium	Al-5052	CERN SPS beamlines
	AlMg <sub>3</sub>	PSI SINQ Target-3 Safety-hull
	Al-5083	ISIS Target Station 2 PBW, Japan-SNS PBW, China-SNS PBW
	Al-6061	SNS 2 <sup>nd</sup> gen. PBW, Future ESS Target Station
Graphite	SIGRABOND 1001G	LHC to HiRadMat connection beamline
	SIGRABOND 1501G	LHC beam dump beamline, CLIC beam dump beamline

**Table 2.1:** Overview of the materials adopted worldwide for beam windows.

Besides general aspects of material availability, manufacturing feasibility, costs, delivery times, production timeline, etc., there are other crucial factors which contribute to the final design choice and that must necessarily be taken into account to address the specific needs of beam windows applications. Among these requirements, it is important to include high transparency to high-energy particles, excellent thermal conductivity to efficiently dissipate the heat deposited by the beam, high mechanical robustness to withstand pressure difference and beam-induced thermal repeated loads, impermeability to gasses to guarantee absolute leak tightness and resistance to radiation.

In the early stages of design, a set of indices can be particularly useful to orient material choice and to get a clearer picture of the strengths and weaknesses of each ma-

terial. A common method for classifying and ranking potential materials according to this large number of requirements consists in introducing *Figures of Merit* (FoM) which allow condensing into a single indicator the multitude of material properties concerning a specific design demand. These indicators, derived from simplified, linearised and temperature-independent material properties, can give reliable qualitative information about the advantages of using a certain material for a particular project purpose since they are constructed in such a way that a higher value is equivalent to a better performance of the material in respect to the specific requirement.

Two figures of merit deemed important for the design of components subjected to high-energy beam impacts, as the beam windows, are the **Thermomechanical robustness index** and the **Thermal stability index**, developed within the Mechanical and Materials Engineering Group at CERN for the design of beam intercepting devices [56][57].

### Thermomechanical robustness index

The Thermomechanical Robustness Index (TRI) is associated with the mechanical robustness of the material and serves to give qualitative information on the material's ability to withstand the impact of a short particle pulse.

Considering that thermal shock problems are largely dictated by the thermal deformation caused by a fast temperature increase, it seems appropriate to build this index on the ratio between material admissible strain (or strain to failure)  $\varepsilon_{\text{adm}}$  and actual strain  $\varepsilon_{\text{act}}$ :

$$\text{TRI} = \frac{\varepsilon_{\text{adm}}}{\varepsilon_{\text{ref}}} \cdot \left( \frac{T_{\text{melt}}}{\Delta T_{\text{q}}} - 1 \right)^m \quad (2.1)$$

where  $T_{\text{melt}}$  [K] is the melting (or degradation) temperature,  $\Delta T_{\text{q}}$  [K] is the temperature increase generated by a reference energy deposition (equation 2.4) and  $m$  a coefficient related to the material loss of strength when the temperature increases.

The actual reference strain is defined by:

$$\varepsilon_{\text{ref}} = \bar{\alpha} \cdot \Delta T_{\text{q}} \quad (2.2)$$

where  $\bar{\alpha}$  [ $10^{-6}$  K] is the (averaged) coefficient of thermal expansion and  $\Delta T_{\text{q}}$  the temperature increase generated by a reference quasi-instantaneous energy deposition  $q_{\text{d}}$ , that can be expressed as a function of the material density  $\rho$  [ $\text{g cm}^{-3}$ ], the specific heat  $c_{\text{p}}$  [ $\text{J g}^{-1} \text{K}^{-1}$ ], the scaling factor  $C_{\text{R}}$ , the coefficient  $n$ , that indicates how density affects the energy distribution generated by the impact, and the geometrical radiation length  $X_{\text{g}}$  [cm]:

$$q_{\text{d}} = \frac{C_{\text{R}} \rho^n}{X_{\text{g}}} \quad (2.3)$$

$$\Delta T_q = \frac{q_d}{c_p} = \frac{C_R \rho^n}{c_p X_g} \quad (2.4)$$

The radiation length in the previous formula provides an important indication of the "transparency" of a certain material to radiations: it is defined as the mean length [cm] required to reduce the energy of an electron by a factor  $1/e$  [4]. The radiation length  $X_0$ , expressed in  $\text{g cm}^{-2}$ , can be approximated by the analytical formula below<sup>1</sup>:

$$X_0 = \frac{716.4 A}{Z(Z+1) \cdot \ln \left( \frac{287}{\sqrt{Z}} \right)} \quad (2.5)$$

The radiation length in cm is obtained by dividing by the density:

$$X_g = \frac{X_0}{\rho} \quad (2.6)$$

The value of the strain to failure ( $\varepsilon_{\text{adm}}$ ), i.e. the measure of how much the material is elongated to failure, is rarely available for many materials, so it is convenient to express this quantity as a function of values generally easier to find in the literature, such as the (averaged) Young's modulus  $\bar{E}$  [GPa], the Poisson's ration  $\nu$  and the failure strength  $R_M$  [MPa]. For simplicity, the ultimate tensile strength was utilised to describe the failure strength, despite the latter value being usually related to fracture for brittle materials and to yield strength for ductile ones. The admissible strain is therefore computed by the following relation:

$$\varepsilon_{\text{adm}} = \frac{R_M}{\bar{E} \cdot (1 - \nu)} \quad (2.7)$$

Combining the previous equations, the Thermomechanical Robustness Index can be finally written as:

$$\text{TRI} = \frac{R_M c_p X_g}{\bar{E}(1 - \nu) \bar{\alpha} C_R \rho^n} \cdot \left( \frac{T_{\text{melt}} c_p X_g}{C_R \rho^n} - 1 \right)^m \quad (2.8)$$

It is worth noting that, as the melting point is reached, TRI tends to zero.

### Thermal stability index

The Thermal Stability Index (TSI) indicates a material's capacity of preserving geometrical stability and minimising deformation when subjected to steady-state beam losses.

---

<sup>1</sup>For more precise calculations, it is possible to use radiation length values measured experimentally and available, for example, on the Particle Data Group website. Anyway, the values calculated using the equation deviate no more than 2% from the data measured experimentally [58].

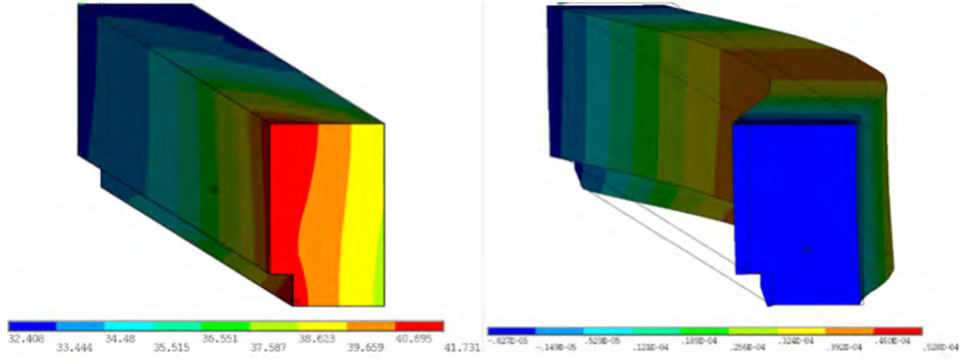


**Figure 2.1:** Operating temperatures [°C] (left) and thermally induced deflection [m] (right) of an LHC secondary collimator jaw in steady-state conditions [57].

When heat is deposited locally inside a small portion of matter in a larger body, as is the case of the components which intercept high-energy charged particle beams, a deflection of the structure is thermally induced, as shown in the figure 2.1 for a LHC secondary collimator jaw. Assuming that this heat deposition is steady-state and that the heat is flowing from the surface exposed to the beam through the thickness of the component, then the index TSI is developed to be proportional to the radius of curvature  $\rho_c$  of an elongated structure induced by a non-uniform temperature distribution:

$$\rho_c = \frac{\bar{\lambda}}{\dot{q} \bar{\alpha}} \quad (2.9)$$

where  $\bar{\lambda}$  [W m<sup>-1</sup> K<sup>-1</sup>] is the (averaged) thermal conductivity and  $\dot{q}$  [W m<sup>-2</sup>] the steady-state heat flux deposited on the structure:

$$\dot{q} = \frac{C_S \rho^n}{X_g} \quad (2.10)$$

where  $C_S$  represents a scaling factor.

Combining eq.2.9 and eq.2.10, the Thermal stability index can be finally written as:

$$\text{TSI} = \frac{\bar{\lambda} X_g}{\bar{\alpha} C_S \rho^n} \quad (2.11)$$

The findings related to the two figures of merit, originally conceived for beam-intercepting devices, are presented in the table 2.2. All the physical and mechanical properties utilised for their evaluation are contained in the table. The carbon-carbon composites have very high values for both the FoM, which explains why this kind of material has been selected for being used as an absorber for new collimators and why the design of CERN windows of the last decade provided for their use in combination with metallic foils. The only metal with comparable TSI and TRI values to the carbon-carbon composites is Beryllium. Among the other metals, only aluminium alloys have a TSI value that exceeds the unit as well as relatively high values of TRI, very similar to those found for Ti-6Al-4V.

---

The AISI 316 and AISI 304 austenitic steels share very low values of TSI with Inconel 718, but exhibit TRI values around a third lower than with respect to the Nickel superalloy and values halved of both the figures of merit with respect to the martensitic steels.

Parameter	Unit	Material												
		Beryllium	Titanium		Nickel			Stainless Steel				Aluminium		
		PF-60	Ti Grade 2	Ti Grade 5	Inconel 718	AISI 304	AISI 316	DIN 1.4926	T91	Al-5052	AlMg <sub>3</sub>	Al-5083	Al-6061	C/C
Physical properties	Density	1,84	4,51	4,43	8,19	8,00	8,00	7,85	7,77	2,68	2,70	2,66	2,70	1,36
	Radiation length	35,20	3,69	3,89	1,66	1,79	1,78	1,83	1,84	9,03	8,95	9,09	8,94	31,86
	Thermal conductivity	216,00	16,40	6,70	11,40	15,15	14,95	24,00	27,00	138,00	130,00	119,70	167,00	116,67
	Specific heat capacity	1,93	0,52	0,53	0,44	0,50	0,50	0,44	0,46	0,88	0,90	0,90	0,90	0,71
	Volumetric CTE	14,50	8,60	8,60	13,00	17,30	17,20	10,50	11,30	23,80	24,00	24,20	23,60	3,03
	Melting temperature	1278,00	1665,00	1632,00	1298,00	1425,00	1388,00	1425,00	1450,00	628,10	617,00	570,00	616,85	3650,00
Mechanical properties	Young's modulus	303,00	103,00	113,80	205,00	197,00	193,00	217,00	207,00	70,00	68,00	70,30	68,90	45,75
	Poisson's ratio	0,15	0,37	0,34	0,29	0,15	0,15	0,28	0,30	0,33	0,33	0,32	0,33	0,15
	Yield strength	240,00	145,00	880,00	1100,00	210,00	290,00	417,00	415,00	325,00	280,00	164,30	276,00	93,30
	Tensile strength	370,00	344,00	950,00	1375,00	564,00	560,00	767,00	585,00	330,00	330,00	285,80	310,00	93,30
Figures of merit	Thermomechanical Robustness Index	1057,01	87,58	226,57	27,69	9,74	9,79	20,62	16,88	219,62	226,70	188,42	212,52	2955,62
	Thermal Stability Index	21,621	0,240	0,104	0,044	0,048	0,047	0,127	0,134	1,996	1,844	1,717	2,408	53,916
														6,844

**Table 2.2:** Properties and figures of merit of materials relevant for beam windows. The values reported in these tables have been calculated at room temperature ( $T_{\text{room}}=20^\circ$ ), except for the coefficient of thermal expansion (CTE), which was averaged between  $20^\circ$  and  $100^\circ$  in most cases. For transversely anisotropic materials, such as the Carbon fibre-reinforced carbon (C-C) composite materials, the values were estimated through the formula:  $\text{value} = [2 \cdot (\text{best direction}) + (\text{weak direction})]/3$ .



## 2.3 Preliminary analytical findings

Preliminary analytical calculations were performed in this section with the aim of helping in the choice of which are the most appropriate materials to be investigated for beam window applications, also in view of the specific conditions of the future experiment of U-ion beam irradiation.

The beam parameters taken into account for the following analytical computations are those related to the last U-ion beam irradiation experiments held at the M3-beamline of the UNILAC at Darmstadt GSI [59][60]. Cylindrical samples with a diameter of 20 mm and thickness lower than 0.5 mm were exposed to 100  $\mu$ s-long U-ion pulses with a kinetic energy per nucleon of 4.8 MeV/u (1.14 GeV, in total), an intensity of around  $5 \cdot 10^9$  ions/cm<sup>2</sup>·pulse and a beam repetition rate of 0.5 Hz. As can be seen in the figure 2.2, the Uranium ions hit the target samples in the centre, resulting in a homogeneous beam spot with a circular shape and with a radius of approximately 10 mm.

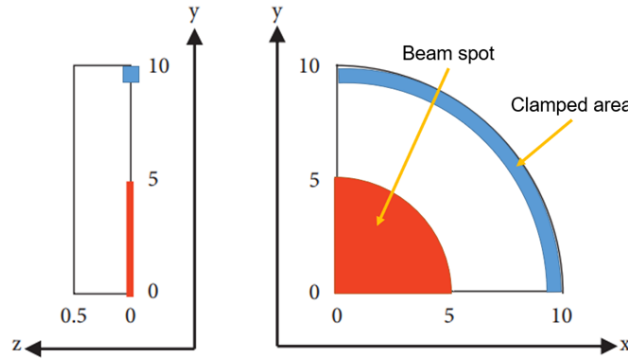


**Figure 2.2:** Schematic drawing in side and front views of a quarter of the target disc, where  $z$  is the direction of thickness and  $x$  and  $y$  are the directions of the plane of the disc. All units are in mm.

### 2.3.1 Preliminary thermal analysis

#### Estimation of the maximum temperature

A simple calculation about the increase of temperature in the target sample provoked by single-pulse irradiation is here described. As indicated in the preceding chapter, the instantaneous temperature rise at the centre of the beam distribution is undoubtedly the most critical factor in the thermal design of beam windows. For our specific case, the equation 1.3 can be modified in the following shape:

$$\Delta T_{inst} = \left( \frac{dE}{\rho dx} \right) \frac{\varphi}{c_p} \quad (2.12)$$

where  $dE/\rho dx$  is the mass stopping power,  $\varphi$  is the intensity of the U-ions beam, namely the flux of ions passing through the beam spot of the sample per pulse, equal to approximately  $5 \cdot 10^9$  ions/cm<sup>2</sup>·pulse, and  $c_p$  the specific heat capacity. The equation above is valid under the conservative assumptions that all the energy of the incident beam particles is converted into heat because of the ionising energy losses and that the heat cannot spread outside the beam spot while the energy is deposited, which is reasonable for a very short deposition time of 100  $\mu$ s. Since the flux is a constant parameter and the heat capacity is known for all the materials of interest for beam windows, the solution to the equation lies in the research of the values of mass stopping power.

The mass stopping power depends on the amount, the type and the energy of ions impacting the target sample as well as on the density and the physical properties of the material itself. Its calculation can be carried out by sophisticated computational algorithms based on Monte Carlo methods, as will be described in chapter 4 about the materials selected for the irradiation experiment, but reliable data for a preliminary analysis as the one described here may be extracted by nuclear libraries.

The data relating to stopping power for uranium ions impacting on six targets were extracted from the SRIM-2013 library and plotted as a function of the kinetic energy per nucleon in the graphs of the figure 2.3. The graphs refer to the main component elements of the materials for beam windows and are sorted from the lightest element, Beryllium ( $Z = 5$ ,  $A = 9$ ), for which the Bragg peak is just pronounced, to the heaviest element, Nickel ( $Z = 28$ ,  $A = 58.7$ ), for which the peak is far higher. The total stopping power  $dE/dx$  (black curve) is obtained by summing the values of the nuclear stopping power (dashed orange curve), which refers to the elastic collisions between the projectile ion and atoms in the sample, and the electronic stopping power (dashed blue curve), which refers to the inelastic collisions between bound electrons in the medium and the ion moving through it.

It is worth noting that the stopping power for 4.8 MeV/u U-ions is almost entirely affected by the phenomenon of electronic loss and that its value is very close to the top of the Bragg peak: this fact is not just a coincidence, but a typical and deliberate choice in many experimental beamlines, whose aim is to maximise the interaction between the ion beam and the target matter and thus increase the radiation-induced effects and damages (within the same amount of beamtime).

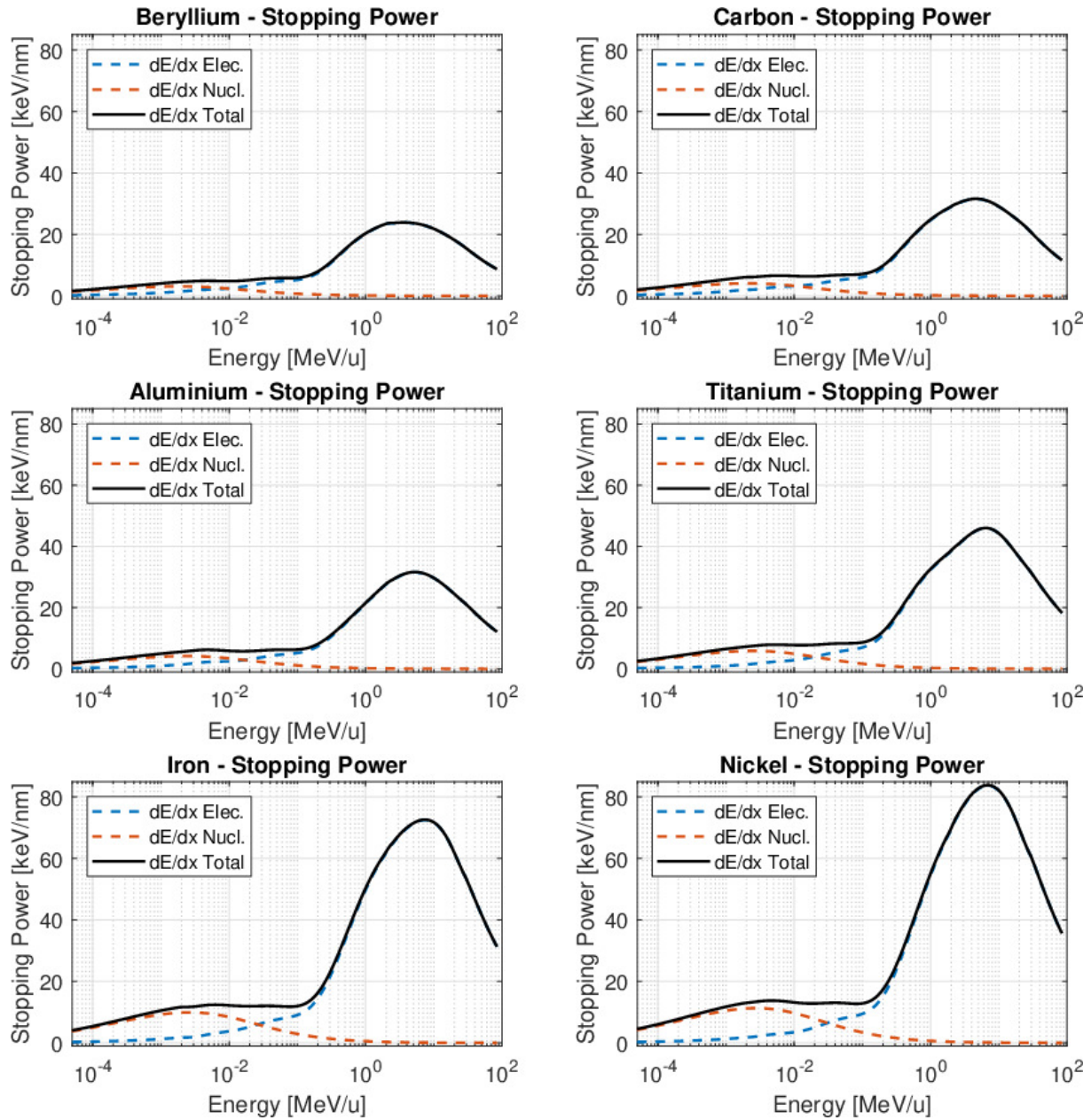


**Figure 2.3:** Electronic, nuclear and total energy loss as a function of the specific energy for uranium ions in six targets (Be, C, Al, Ti, Fe, Ni). All the graphs were realised by processing the data extracted from the SRIM-2013 libraries.

Material	Physical properties			Total Stopping Power		Peak Temperature	
	Density	Thermal conductivity	Specific heat capacity	Melting temperature	Linear stopping power	Mass stopping power	Maximum temperature
	$\rho$ [g cm <sup>-3</sup> ]	$\bar{\lambda}$ [W m <sup>-1</sup> K <sup>-1</sup> ]	$c_p$ [J g <sup>-1</sup> K <sup>-1</sup> ]	$T_{\text{melt}}$ [°C]	$dE/dx$ [keV nm <sup>-1</sup> ]	$dE/\rho dx$ [MeV cm <sup>2</sup> mg <sup>-1</sup> ]	$T_{\text{max}}$ [°C]
							$T_{\text{max}}/T_{\text{melt}}$ [K/K]
Beryllium	1,84	216,00	1,93	1278,00	23,67	128,36	78,42
Titanium	4,51	16,40	0,52	1665,00	45,54	100,98	180,57
	4,43	6,70	0,53	1632,00	45,54	102,81	181,48
Nickel	8,19	11,40	0,44	1298,00	82,83	101,14	211,25
Stainless Steel	8,00	15,15	0,50	1425,00	71,50	89,38	168,20
	8,00	14,95	0,50	1388,00	71,50	89,38	168,20
	7,85	24,00	0,44	1425,00	71,50	91,09	191,22
	7,77	27,00	0,46	1450,00	71,50	92,03	185,27
Aluminium	2,68	138,00	0,88	628,10	31,61	117,96	132,39
	2,70	130,00	0,90	617,00	31,61	117,09	129,22
	2,66	119,70	0,90	570,00	31,61	118,85	130,67
	2,70	167,00	0,90	616,85	31,61	117,09	129,69
C/C	1,36	116,67	0,71	3650,00	31,55	231,96	286,72
	1,47	19,60	0,71	3650,00	31,55	214,60	267,14

**Table 2.3:** Values of stopping power and peak temperature for materials of interest for beam windows, in the particular case of 4.8 MeV/u U-ions beams irradiation.

The values of total mass stopping power for all the materials are presented in the table 2.3. Since most of these materials are not composed of a single chemical element, the values of  $dE/\rho dx$  were adjusted to take into account the density of each specific material. Just as an example, in the case of Titanium Grade 5, composed of roughly 90% Titanium, total mass stopping power was computed in the following way:

$$\left(\frac{dE}{\rho dx}\right)_{\text{Ti-6Al-4V}} = \left(\frac{\rho_{\text{Ti-6Al-4V}}}{\rho_{\text{Ti}}}\right) \cdot \left(\frac{dE}{\rho dx}\right)_{\text{Ti}} = \frac{4.43}{4.52} \cdot 102.81 = 100.98 \frac{\text{MeV} \cdot \text{cm}^2}{\text{mg}} \quad (2.13)$$

The values of maximum temperatures calculated by the equation 2.12 and of the ratio between the peak temperature and the melting temperature are presented in table 2.3. A room temperature of 25°C was considered for all the materials. The highest temperatures are observed for carbon composite materials, due to large values of mass stopping power and low specific heat capacity, followed in descending order by Inconel 718, titanium alloys, stainless steels, aluminium alloys and finally beryllium, by virtue of its high value of specific heat capacity. As regards the maximum vs. melting temperature ratio, beryllium and titanium alloys behave better than the other metallic materials ( $T_{\text{max}}/T_{\text{melt}} < 0.25$ ), while the ratio increases almost up to 0.5 for aluminium alloys, which have lower melting temperatures than the other materials considered.

### Heat diffusion process

An other aspect to be considered in the thermal design of a beam window concerns the process of diffusion of heat from the irradiated beam spot at the centre to the edge of the window. It is fundamental that most of the heat produced from the beam impact is transported away from the centre before the next impact occurs: in the event that the heat deposited inside the beam spot took too much time to propagate towards the edge, the heat could accumulate at the centre of the window and, after many pulses, even reach the melting point and cause the breakage of the window.

The parameter that most of all describes the heat transfer rate of a material and is, therefore, a key element in studying transient problems like this is the *thermal diffusivity*  $a$ , given by the equation:

$$a = \frac{\lambda}{\rho c_p} \quad (2.14)$$

It is defined as the ratio between the thermal conductivity  $\lambda$  and the volumetric heat capacity ( $\rho c_p$ ). Since the thermal diffusivity is a term that describes the propagation rate of the temperature through a material, a characteristic time  $\tau$ , called *thermal diffusion time*, can be identified:

$$\tau = \frac{L^2}{a} \quad (2.15)$$

Material		Physical properties				Thermal diffusion time [ms]		
		Density	Thermal conductivity	Specific heat capacity	Thermal diffusivity	R=5 mm	R=7.5 mm	R=10 mm
		$\rho$ [g cm <sup>-3</sup> ]	$\lambda$ [W m <sup>-1</sup> K <sup>-1</sup> ]	$c_p$ [J g <sup>-1</sup> K <sup>-1</sup> ]	$a$ [mm <sup>2</sup> s <sup>-1</sup> ]			
Beryllium	PF-60	1,84	216,00	1,93	60,85	411	924	1643
Titanium	Titanium Grade 2	4,51	16,40	0,52	6,99	3575	8044	14300
	Titanium Grade 5	4,43	6,70	0,53	2,87	8700	19574	34799
Nickel	Inconel 718	8,19	11,40	0,44	3,20	7813	17579	31251
Stainless Steel	AISI 304	8,00	15,15	0,50	3,79	6601	14851	26403
	AISI 316	8,00	14,95	0,50	3,74	6689	15050	26756
Steel	DIN 1.4926	7,85	24,00	0,44	6,96	3590	8077	14359
	T91	7,77	27,00	0,46	7,55	3309	7446	13238
Aluminium	Al-5052	2,68	138,00	0,88	58,51	427	961	1709
	AlMg <sub>3</sub>	2,70	130,00	0,90	53,50	467	1051	1869
	Al-5083	2,66	119,70	0,90	49,94	501	1126	2002
	Al-6061	2,70	167,00	0,90	69,03	362	815	1449
C/C	Sigrabond 1001 G	1,36	116,67	0,71	120,83	207	466	828
	Sigrabond 1501G	1,47	19,60	0,71	18,78	1331	2995	5325

**Table 2.4:** Thermal diffusion times on three length scales for materials of interest for beam windows.

where  $L$  is the typical dimension of a physical system, or *characteristic dimension*. For very thin discs with a radius of 1 cm, as in the case of the samples that will be produced for the irradiation experiment, the radius  $R$  can be taken as a typical dimension, from which:

$$\tau = \frac{R^2}{a} \quad (2.16)$$

The time  $\tau$  is the time required for the thermalization of the system: this parameter is therefore related to the time needed to reach, through heat diffusion processes, a uniform temperature distribution in the region [61]. This relationship is valid under the assumption of quasi-instantaneous heat deposition, namely when the thermal diffusion time is much longer than the duration of beam impact: in the case of the irradiation experiment, in which the length of U-ion beam impact and the beam repetition rate is expected to be 100  $\mu$ s and 1 Hz, respectively, this condition is definitely met.

The values of thermal diffusion time computed for three characteristic lengths are shown in the table 2.4 for materials of interest for beam windows. The values of  $\tau$  for  $R = 10$ mm (at the edge of the samples for the experiment) are marked with different colours in order to allow us to see at a glance which materials are more performing in the process of heat spreading. A strong difference can be observed between aluminium alloys, for which only 1.5-2 seconds are required for the thermalization of the system, and Titanium Grade 5, for which around 35 seconds are necessary to establish a uniform temperature distribution in the sample surface. All this suggests that the peak temperature after several impacts might be higher than was expected from the previous calculations for titanium, Inconel 718 and steel samples, whereas slight differences in the peak temperature are expected for beryllium and aluminium alloys samples, even after many beam impacts.

### 2.3.2 Preliminary dynamic analysis

The pulsed deposition of heavy ions with energy close to the Bragg peak on metallic samples induces high thermal stresses to the irradiated targets, from which vibrations, stress waves and other dynamic effects are generated. The optimal solution for studying the dynamic effects of pulsed beams is to directly observe the impact of beam pulses on the target by means of online measuring instruments during the irradiation experiment. To that end, a Laser Doppler Vibrometer (LDV) will be adopted during the experimental stage and will enable the measurement of the velocity on the target surface during the whole beam time. The purpose of this paragraph is to describe which dynamic effects are expected to appear during the irradiation experiment and which phenomena will be possible to catch with the equipment supplied.

#### Vibration of circular plates

When heavy ions impinge on target samples, their energy is almost entirely converted into heat and rapid growth in temperature occurs quasi-instantaneously inside the beam spot. This rise in temperature causes the thermal expansion of the irradiated material. Since the heating initially affects only one surface of the disc-shaped samples, only the superficial part tends to expand and, as a result, bending modes are generated.

The natural bending frequencies of samples under irradiation can be predicted analytically by treating the samples as circular plates and then by using the fundamental equations of classical plate theory for the precise determination of this characteristic frequency. A plate can be defined as a two-dimensional sheet of elastic material that possesses bending rigidity as a result of its thickness and of the elasticity of the constituent material. As expected for samples exposed to ion beam irradiation, plates deform mainly by flexing perpendicular to their own plane. General assumptions used in the analysis of plates concern the shape (perfect flatness and constant thickness of the specimens) and the nature of the material involved (homogeneous, isotropic, linear elastic, etc.) Moreover, the plates must be thin and have a thickness at least ten times smaller than their own diameter [62].

In general, the transverse displacement  $w$  of a thin plate can be calculated by the classical differential equation of motion, derived by the Kirchhoff–Love theory of plates [63]:

$$D\nabla^4 w + \gamma \frac{\partial^2 w}{\partial t^2} = 0 \quad (2.17)$$

where  $D$  is the flexural density, defined by the relation:

$$D = \frac{Eh^3}{12(1 - \nu^2)} \quad (2.18)$$

$h$  is the plate thickness,  $E$  is the Young's modulus,  $\nu$  is the Poisson's ratio,  $\gamma$  is the mass density per unit area of the plate ( $\gamma = \rho h$ ),  $t$  is the time and  $\nabla^4 = \nabla^2 \nabla^2$ , where  $\nabla^2$  is the Laplacian operator. Under the assumption of free vibrations, the motion is described as:

$$w = W \cos(\omega t) \quad (2.19)$$

where  $W$  is a function of the position coordinates and  $\omega$  is the circular frequency. If the equation 2.19 is substituted into equation 2.17 using the parameter  $k^4 = \gamma \omega^2 / D$ , the following equation is obtained:

$$(\nabla^4 - k^4)W = 0 \quad (2.20)$$

from which, using the factorisation:

$$(\nabla^2 + k^2)(\nabla^2 - k^2)W = 0 \quad (2.21)$$

The complete solution to the previous equation can be derived by superimposing the solutions to the equations:

$$\begin{cases} \nabla^2 W_1 + k^2 W_1 = 0 \\ \nabla^2 W_2 - k^2 W_2 = 0 \end{cases} \quad (2.22)$$

The equations 2.22 must be written in polar coordinates (where  $r$  is the radial coordinate and  $\vartheta$  is the angular coordinate) for the case of cylindrical plates. The Laplacian operator can be expressed as:

$$\nabla^2 = \frac{\partial^2}{\partial r^2} + \frac{1}{r} \frac{\partial}{\partial r} + \frac{1}{r^2} \frac{\partial^2}{\partial \vartheta^2} \quad (2.23)$$

from which:

$$\begin{cases} \frac{\partial^2 W_1(r, \vartheta)}{\partial r^2} + \frac{1}{r} \frac{\partial W_1(r, \vartheta)}{\partial r} + \frac{1}{r^2} \frac{\partial^2 W_1(r, \vartheta)}{\partial \vartheta^2} + k^2 W_1(r, \vartheta) = 0 \\ \frac{\partial^2 W_2(r, \vartheta)}{\partial r^2} + \frac{1}{r} \frac{\partial W_2(r, \vartheta)}{\partial r} + \frac{1}{r^2} \frac{\partial^2 W_2(r, \vartheta)}{\partial \vartheta^2} - k^2 W_2(r, \vartheta) = 0 \end{cases} \quad (2.24)$$

It is convenient to explicit the function  $W$  as a Fourier series to replace the partial derivatives with ordinary ones:

$$W(r, \vartheta) = \sum_{n=0}^{\infty} W_n(r) \cos(n\vartheta) + \sum_{n=1}^{\infty} W_n^*(r) \sin(n\vartheta) \quad (2.25)$$

from which two pairs of equations are obtained:

$$\begin{cases} \frac{d^2 W_{n1}}{dr^2} + \frac{1}{r} \frac{dW_{n1}}{dr} - \left( \frac{n^2}{r^2} - k^2 \right) W_{n1} = 0 \\ \frac{d^2 W_{n2}}{dr^2} + \frac{1}{r} \frac{dW_{n2}}{dr} - \left( \frac{n^2}{r^2} + k^2 \right) W_{n2} = 0 \end{cases} \quad (2.26)$$



$$\begin{cases} \frac{d^2 W_{n1}^*}{dr^2} + \frac{1}{r} \frac{dW_{n1}^*}{dr} - \left( \frac{n^2}{r^2} - k^2 \right) W_{n1}^* = 0 \\ \frac{d^2 W_{n2}^*}{dr^2} + \frac{1}{r} \frac{dW_{n2}^*}{dr} - \left( \frac{n^2}{r^2} + k^2 \right) W_{n2}^* = 0 \end{cases} \quad (2.27)$$

The previous equations have solutions that can be written in terms of Bessel's equations:

$$\begin{cases} W_{n1} = A_n J_n(kr) + B_n Y_n(kr) \\ W_{n2} = C_n I_n(kr) + D_n K_n(kr) \end{cases} \quad (2.28)$$

$$\begin{cases} W_{n1} = A_n^* J_n(kr) + B_n^* Y_n(kr) \\ W_{n2} = C_n^* I_n(kr) + D_n^* K_n(kr) \end{cases} \quad (2.29)$$

where  $J_n$  and  $Y_n$  are Bessel functions of the first and second kind, respectively,  $I_n$  and  $K_n$  modified Bessel functions of the first and second kind, respectively, and  $A_n, \dots, D_n^*$  coefficients associated with the mode shapes that can be determined using the boundary conditions. Thus, the general solution of the equation in polar coordinates is obtained by substituting the equations 2.28 and 2.29 into the equation 2.25:

$$\begin{aligned} W(r, \vartheta) = & \sum_{n=0}^{\infty} [A_n J_n(kr) + B_n Y_n(kr) + C_n I_n(kr) + D_n K_n(kr)] \cos(n\vartheta) \\ & + \sum_{n=1}^{\infty} [A_n^* J_n(kr) + B_n^* Y_n(kr) + C_n^* I_n(kr) + D_n^* K_n(kr)] \sin(n\vartheta) \end{aligned} \quad (2.30)$$

For circular plates, for which the origin of the polar coordinate system coincides with the centre of the plate, the terms  $I_n$  and  $K_n$  must be discarded from the equations : those terms tend to infinity when the radial coordinate goes to zero, and this event is impossible because it would imply infinite deflections and stresses at the centre of the plate. Since the boundary conditions possess symmetry with respect to the diameters of the circle, even the terms which include  $\sin(n\vartheta)$  are not needed anymore and the equation, for a typical mode, may be reduced to:

$$W(r, \vartheta) = [A_n J_n(kr) + C_n I_n(kr)] \cos(n\vartheta) \quad (2.31)$$

where  $n$  corresponds to the number of nodal diameters.

The nature of the boundary condition that the target samples will experience under irradiation during the experimental phase is obviously not known a priori. As a result, the analytical solution to the aforementioned equation 2.31 is offered in various forms, so as to take into consideration the several boundary conditions that could emerge during the experiment.

In the case of **circular plates clamped all around**, the boundary conditions can be written as [63]:

$$\begin{cases} W(a) = 0 \\ \frac{\partial W(a)}{\partial r} = 0 \end{cases} \quad (2.32)$$

where  $a$  is the "unclamped" radius. After having substituted the equation 2.32 into the general equation 2.31 and after short mathematical steps, the solution in the case of the clamped edge is:

$$J_n(\lambda)I_{n+1}(\lambda) + I_n(\lambda)J_{n+1}(\lambda) = 0 \quad (2.33)$$

where the eigenvalues  $\lambda = ka$  are the roots of the equation. Finally, the natural frequency of vibration can be obtained by the relation:

$$f_{ij} = \frac{\lambda_{ij}^2}{2\pi a^2} \sqrt{\frac{Eh^2}{12\rho(1-\nu^2)}} \quad (2.34)$$

where  $i$  refers to the number of nodal diameters and  $j$  to the number of nodal circles, with the boundary circle excluded.

The search for the roots of the equation for circular plates with different boundary conditions may be conducted in a similar way to that of the previous case. In the case of **completely free circular plates**, with an outside radius equal to  $a$ , the expression of the solution is quite complex and can be written in a matrix form [64]:

$$\det \begin{bmatrix} C_1 & C_2 \\ C_3 & C_4 \end{bmatrix} = 0 \quad (2.35)$$

where:

$$\begin{cases} C_1 = n[n(1-n)(1-\nu) - \lambda^2]J_n + \lambda[n^2(1-\nu) + \lambda^2]J_{n+1} \\ C_2 = n[n(1-n)(1-\nu) + \lambda^2]I_n - \lambda[n^2(1-\nu) - \lambda^2]I_{n+1} \\ C_3 = [n(n-1)(1-\nu) - \lambda^2]J_n + \lambda(1-\nu)J_{n+1} \\ C_4 = [n(n-1)(1-\nu) + \lambda^2]I_n - \lambda(1-\nu)I_{n+1} \end{cases} \quad (2.36)$$

In the absence of nodal diameters ( $i = 0$ ), the previous equation can be expressed in the simplified form:

$$2(1-\nu)J_1I_1 - \lambda_{0j}[J_1I_0 + J_0I_1] = 0 \quad (2.37)$$

In the case of **plates simply supported all around**, with outside radius equal to  $a$ , the frequency equation can be written as [63]:

$$\frac{J_{n+1}}{J_n} + \frac{I_{n+1}}{I_n} = \frac{2\lambda}{1-\nu} \quad (2.38)$$

and, in the interesting case of  $i = 0$ , as:

$$\frac{J_1}{J_0} + \frac{I_1}{I_0} = \frac{2\lambda}{1-\nu} \quad (2.39)$$

Since the solution of frequency equations is often problematic, the values of  $\lambda^2$  are tabulated for the first few numbers of nodal circles and diameters, while certain parameters (Poisson's ratio, for example) are kept fixed. The tables for the three most important cases (clamped edge, free edge and simply supported edge) are reported in the figure 2.4. It is notable from the tables that the eigenvalues  $\lambda$  (and therefore the natural frequencies) do not depend on the Poisson's ratio or other parameters only in the case of the clamped condition [63][65].

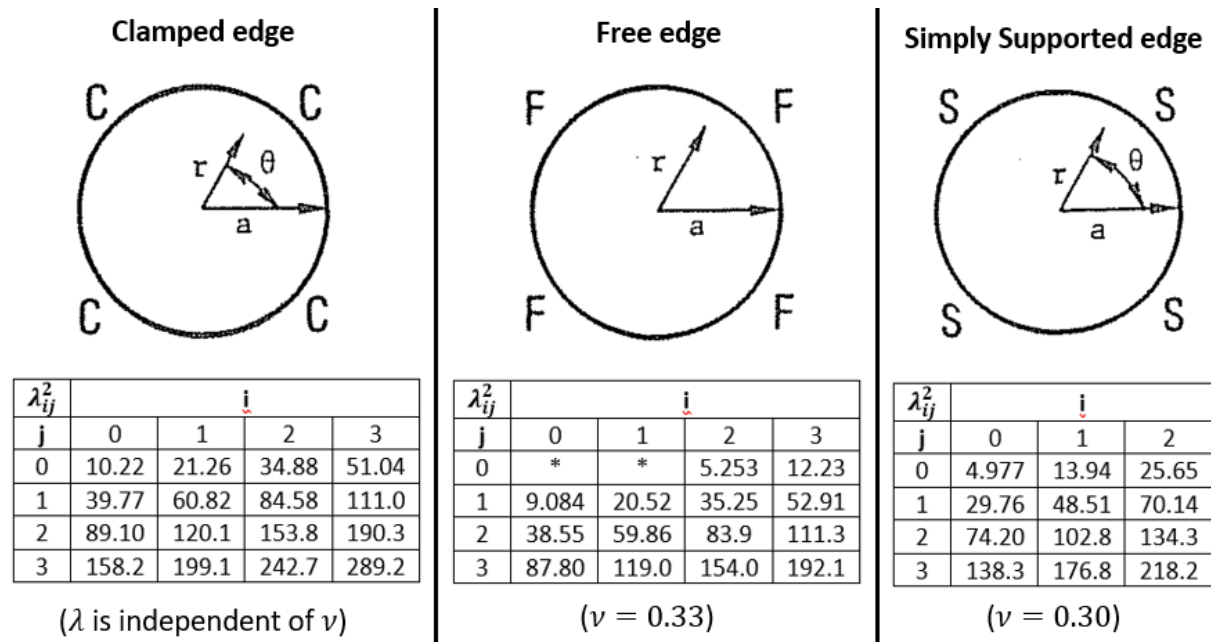


**Figure 2.4:** Roots of the general vibration equation for circular plates in three boundary conditions (clamped edge, free edge and simply supported edge) [62].

In addition to the three boundary conditions just mentioned, there are a number of alternative binding conditions for which the eigenvalues  $\lambda$  are included between the simply supported and the clamped condition. Among these, it is important to remember the **elastically supported circular plates**, in which the plate is supported elastically by springs uniformly distributed about its contour that prevent the translation and the edge rotation, and the **circular plates with initial tension or compression**, in which the effects of in-plane compressions or tensions that may develop in the plate due to thermal or mechanical phenomena are taken into account. For these and other boundary conditions, appropriate tables containing the roots of the general vibration equation can be easily found in literature [62][63][65].

## Wave propagation phenomena

The short duration of the ion pulse may result in a further dynamic effect. The thermal expansion, due to the quasi-instantaneous heat deposition into the beam spot, is initially prevented from spreading by the thermal inertia of the outer material. This results in thermal stresses which propagate in the sample in the form of elastic waves.

The wavefront thus produced propagates from the beam spot throughout the material sample and in all directions. Two types of body waves are generated simultaneously by the heated beam spot: the P waves (also called primary waves or pressure waves) and the S waves (secondary waves or shear waves). Among all the waves generated, only a few of these survive long enough to be potentially detectable at the rear side of the samples by measurement instruments of the surface velocity, namely the **pressure waves along the thickness** and the **vertical shear waves in the radial direction**.

The **P-waves** are high-velocity compression waves that move from the front to the back surface of the samples and go back, travelling for a distance equal to two times the thickness of the samples ( $2h$ ). Their velocity in an isotropic solid can be computed by the equation:

$$v_P = \sqrt{\frac{\lambda + 2\mu}{\rho}} \quad (2.40)$$

where  $\lambda$  and  $\mu$  are, respectively, the Lamé's first and secondary parameters. In a homogeneous isotropic linear elastic material,  $\mu$  coincides with the shear modulus  $G$  and both can be written as follows:

$$\lambda = \frac{E\nu}{(1+\nu)(1-2\nu)} \quad \mu = \frac{E}{2(1+\nu)} \quad (2.41)$$

The equation of the velocity of the pressure waves along the thickness takes the form:

$$v_P = \sqrt{\frac{E(1-\nu)}{\rho(1+\nu)(1-2\nu)}} \quad (2.42)$$

The frequency ( $f_P$ ) with which the primary waves move between the front and rear surface of the samples can be calculated as the ratio between the velocity of the P-wave ( $v_P$ ) and the distance travelled by the wave before returning to its starting point ( $2h$ ) [66]:

$$f_P = \frac{v_P}{2h} = \frac{1}{2h} \sqrt{\frac{E(1-\nu)}{\rho(1+\nu)(1-2\nu)}} \quad (2.43)$$

The **shear vertical (SV) waves** are a type of elastic wave, caused by the shear stresses inside the beam spot, perpendicular to the direction of wave propagation and with a polarisation perpendicular to the surface plane. Additional S-waves are generated by the incidence of the P-waves with the sample boundaries, through a partial conversion

of the energy of the primary to the secondary waves (based on the principle of Snell's law). These shear vertical waves propagate radially, moving towards the edges of the samples and then to the opposite side of the diameter, returning to the starting point after having travelled for two times the diameter of the cylindrical samples. In a homogeneous isotropic linear elastic material, their velocity of propagation  $v_S$  can be calculated likewise to the velocity of the primary waves by the equation:

$$v_S = \sqrt{\frac{\mu}{\rho}} = \sqrt{\frac{E}{2\rho(1+\nu)}} \quad (2.44)$$

The frequency ( $f_S$ ) with which this kind of secondary wave moves between the edges of the cylindrical samples can be calculated as the ratio between the velocity of the S-wave ( $v_S$ ) and the distance travelled by the wave before returning to its starting point ( $4R$ , where  $R$  is the radius):

$$f_S = \frac{v_S}{4R} = \frac{1}{4R} \sqrt{\frac{E}{2\rho(1+\nu)}} \quad (2.45)$$

## Results

The table 2.5 presents the natural bending frequencies and the frequencies of propagating waves, determined using the analytical equations just treated for circular plates. The calculations, carried out for all the materials adopted for beam-window applications, were based on the assumption of being able to manufacture cylindrical samples all of the same size, i.e. with a thickness of 0.2 mm and diameter of 2 cm. The natural frequencies were computed by the equation 2.34 for the first two modes of vibration (when  $i = 0$ ), since these are the modes of vibration for which the bending at the centre of each sample should be larger, making the frequency measurement by the Laser Doppler Vibrometer easier. The values of  $\lambda^2$  to be included in the equation 2.34 were calculated for the boundary conditions of clamped edge, free edge and simply supported edge by the equations 2.33, 2.37 and 2.38, respectively. The frequencies of the P-waves and of the SV-waves were calculated by the equations 2.43 and 2.45.

The LDV that will be used during the irradiation experiment has a maximum sampling frequency of 25 MHz. In the table, the frequency values below this threshold were highlighted in green, whilst the values with a higher frequency than 25 MHz were highlighted in red. It may be noticed at a glance that all the frequencies of the primary waves cannot be detected by the instrument in use and that the two types of frequencies cannot be confused with each other, because they differ by around three orders of magnitude (at most tens of kHz for natural bending frequencies, tens of MHz for the frequencies of the pressure waves). The frequency values of the shear vertical waves are lower than the sampling threshold and are potentially detectable by the LDV.

**Table 2.5:** Analytical results of natural bending frequencies and frequencies of propagating waves for cylindrical plates with diameter 20 mm and thickness 0.2 mm. In red, frequency values are higher than the sampling frequency (25 MHz) of the experimental measuring instrument (Laser Doppler Vibrometer). In green, frequency values are below this threshold.

Material	Properties				Natural bending frequency								Propagation of waves						
	Density $\rho$ [g cm <sup>-3</sup> ]	Young's modulus E [GPa]	Poisson's ratio $\nu$	Flexural rigidity D [Pa m <sup>3</sup> ]	Clamped plate				Free plate				Simply supported plate		P-waves $f_P$ [kHz]	SV-waves $f_S$ [kHz]			
					$\lambda_{00}$	1 <sup>st</sup> mode $f_{01}$ [kHz]	$\lambda_{01}$	2 <sup>nd</sup> mode $f_{02}$ [kHz]	$\lambda_{01}$	1 <sup>st</sup> mode $f_{01}$ [kHz]	$\lambda_{02}$	2 <sup>nd</sup> mode $f_{02}$ [kHz]	$\lambda_{00}$	1 <sup>st</sup> mode $f_{01}$ [kHz]			$\lambda_{01}$	2 <sup>nd</sup> mode $f_{02}$ [kHz]	
Beryllium	1.84	303,00	0,15	0,560	3,197	15,033	6,306	58,488	2,941	10,305	6,174	45,412	2,168	6,913	5,435	43,447	32930,050	211,308	
Titanium	4,51	103,00	0,37	0,088	3,197	5,964	6,306	23,205	3,026	4,328	6,212	18,240	2,244	2,938	5,459	17,390	15888,894	72,176	
	4,43	113,80	0,34	0,097	3,197	6,254	6,306	24,331	3,016	4,508	6,207	19,094	2,235	3,056	5,456	18,214	15783,468	77,342	
Nickel	8,19	205,00	0,29	0,091	3,197	6,061	6,306	23,583	2,997	4,315	6,199	18,459	2,218	2,917	5,451	17,621	14318,076	77,869	
Stainless Steel	AISI 304	8,00	197,00	0,15	0,084	3,197	5,820	6,306	22,642	2,941	3,989	6,174	17,580	2,168	2,676	5,435	16,819	12747,929	81,802
	AISI 316	8,00	193,00	0,15	0,082	3,197	5,760	6,306	22,411	2,941	3,948	6,174	17,401	2,168	2,649	5,435	16,647	12617,845	80,967
	DIN 1.4926	7,85	217,00	0,28	0,100	3,197	6,350	6,306	24,706	2,993	4,508	6,197	19,326	2,215	3,048	5,449	18,447	14861,751	82,151
	T91	7,77	207,00	0,30	0,098	3,197	6,274	6,306	24,408	3,001	4,478	6,200	19,112	2,222	3,031	5,452	18,245	14971,386	80,025
Aluminium	Al-5052	2,68	70,00	0,33	0,098	3,197	6,277	6,306	24,423	3,001	4,480	6,205	19,154	2,231	3,057	5,455	18,276	15552,269	78,340
	AlMg <sub>3</sub>	2,70	68,00	0,33	0,094	3,197	6,164	6,306	23,982	3,011	4,429	6,205	18,808	2,231	3,002	5,455	17,946	15271,606	76,926
	Al-5083	2,66	70,30	0,32	0,098	3,197	6,292	6,306	24,478	3,008	4,511	6,204	19,191	2,228	3,056	5,454	18,310	15374,220	79,100
	Al-6061	2,70	68,90	0,33	0,095	3,197	6,205	6,306	24,141	3,011	4,458	6,205	18,932	2,231	3,022	5,455	18,065	15372,336	77,433
Graphitic	Sigrabond 1001G	1,36	45,75	0,15	0,115	3,197	6,802	6,306	26,464	2,941	4,662	6,174	20,548	2,168	3,128	5,435	19,658	14899,704	95,610
	Sigrabond 1501G	1,47	56,25	0,15	0,130	3,197	7,254	6,306	28,225	2,941	4,973	6,174	21,915	2,168	3,336	5,435	20,966	15891,106	101,971

## 2.4 Materials selection

The bibliographical research of Chapter 1 and the preliminary calculations in this second chapter helped to first understand what materials were selected for beam windows and then which of these would be more interesting to examine in the upcoming experiment of irradiation.

In this section, the materials chosen for the experiment, the reasons that influenced their choice, and the process of production of the specimens are all described.

In addition to the considerations emerging from the preliminary analyses, the selection of materials took into account other aspects, such as availability, non-toxicity and manufacturability. For instance, beryllium was not regarded as an attractive material since, because of its intrinsic toxicity, it was preferred not to incur the risk of its rupture during the shipping phase from Geneva (CERN) to Darmstadt (GSI) or during the irradiation experiment inside the UNILAC M3-Branch beamline.

Out of the several investigated materials, the following downselection was proposed:

- Among the stainless steels, the **T91 Steel** (9Cr-1Mo), which exhibits strong corrosion resistance, good creep rupture strength and low coefficient of thermal expansion, and that has been selected for the realisation of the ADS beam windows.
- **Inconel 718**, a Ni-based superalloy, which has exceptional corrosion resistance and ultimate tensile strength, is particularly interesting in the solution annealing condition for its radiation resistance even under low-temperature irradiation.
- Among the aluminium alloys, **Al-6061-T6**, that has the typical advantages of aluminium alloys, including the excellent thermal conductivity and lightness, but also very high tensile strength, the reason why it was planned to be adopted as baseline material of the 5W-Proton Beam Window at European Spallation Source (ESS).
- Among the titanium alloys, **Titanium Grade 5** (Ti-6Al-4V), characterised by the excellent specific strength and by reduced activation for severe radiation exposure, which is one of the most widely used metals for future beam windows designs in accelerator facilities, such as the HL-LHC at CERN and Long Baseline Neutrino Facility at FNAL.

### 2.4.1 Geometry of the samples

The samples of the selected materials must be cylindrical and 2 cm in diameter in order to be securely clamped to the sample holder. The mounting of the specimens in the

ring-shaped sample holders will be made directly at the GSI control room and will be described in the next chapter.

As regards the thickness of the samples, this must be very reduced to improve the quality of the experimental results which will be obtained by the Laser Doppler Vibrometer (LDV): the smaller the thickness, the greater the amount of matter that will be irradiated in proportion to the total volume of the specimen. In other terms, small thicknesses of samples are particularly appreciated since thinner profiles make it easier to identify the possible radiation-induced damages, in terms of change of Young's modulus, by the peak frequency measurement carried out by the LDV. The lower limit of this thickness is dictated by the penetration depth of the U-ions inside the matter: if the penetration thickness for a lighter material, such as the isotropic graphite tested at the last U-ions beamtime, was approximately  $60\text{ }\mu\text{m}$ , then thicknesses larger than  $50\text{ }\mu\text{m}$  are sufficient for the complete deposition of the beam inside the specimen [59].

### 2.4.2 Production of the samples

The cutting of round bars into thin cylindrical slices was deemed to be the most appropriate technique to manufacture the specimens. The production process of the samples started from the research for round bars on catalogues of manufacturers and sellers of the metals selected.



**Figure 2.5:** T91 steel samples produced by RHP-Technology.

The production of the **T91 Stainless Steel** samples was completely entrusted to Austrian company RHP-Technology, a renowned material and solution provider of powder metallurgy. Five specimens were produced with a thickness of about  $220\text{ }\mu\text{m}$  (figure 2.5).

The **Inconel 718** samples were produced from 40 mm in diameter round element (called M20 jackbolt), part of the tensioning components of the ITER Central Solenoid, analysed for a metallurgical assessment by the EN-MME-MM section at CERN. All the Central Solenoid components were manufactured from precipitation-hardened Inconel 718,



which was melted, remelted, forged, solution annealed, quenched and double ageing heat treated [67].

The Titanium and Aluminium alloy round bars were retrieved by CERN Stores. The **Al-6082-T6** aluminium alloy was preferred to the previously selected Al-6061-T6 alloy on account of a higher value of tensile strength (other mechanical and physical properties being equal). As regards the Titanium alloy, it was finally decided to test the Titanium Grade 5 ELI (Extra Low Interstitials), also known as **Titanium Grade 23**, whose main difference compared to the more common Ti-6Al-4V is the maximum oxygen content lowered to 0.13%, with the benefit of improved fracture toughness.

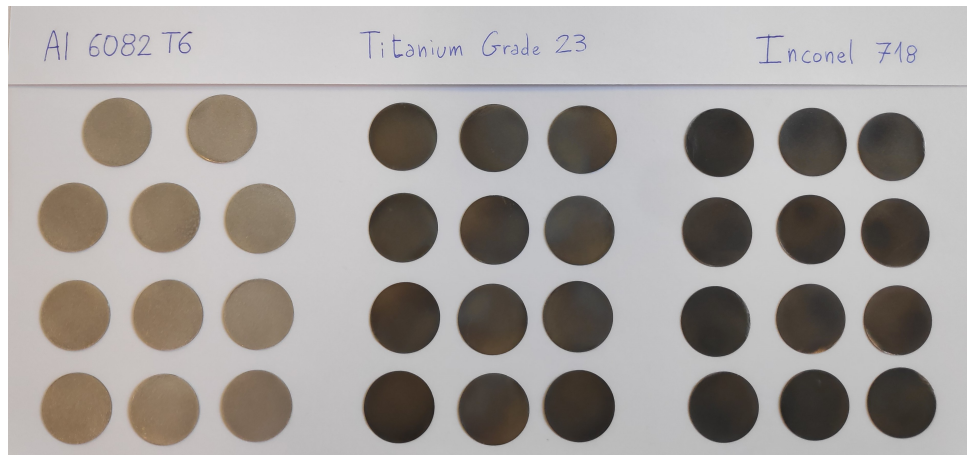


**Figure 2.6:** Al-6082-T6, Titanium Grade 23 and Inconel 718 samples produced by CERN Workshop.

Material	Chemical composition								
ASTM A213 T91 Steel (EN 1.4903 grade)	C	Si	Mn	P	S	Cr	Ni	Mo	V
	0.11	0.3	0.39	0.013	0.004	8.7	0.2	1	0.21
Inconel 718	Al	Ti	Nb	N2	Zn	Zr	Fe		
	0.011	0.002	0.083	0.046	0.001	0.002	Balance		
EN AW 6082 T6 (Aluminium alloy)	Cu max	Zn max	Si	Fe max	Mn	Ti max	Mg	Cr max	Al
	0.1	0.2	0.6-1.6	0.5	0.4-1	0.2	0.4-1.4	0.35	Balance
Titanium Grade 5 ELI (Grade 23)	Fe max	O max	N max	C max	H max	Al	V	Ti	
	0.25	0.13	0.05	0.08	0.015	5.5-6.5	3.5-4.5	Balance	

**Table 2.6:** Chemical composition of the material selected for the U-ions irradiation experiment.

The manufacturing of the other samples was executed at the CERN Workshop. The round bars were manufactured using electrical discharge machining (EDM). The use of a wire-cut EDM machine has allowed the production of a dozen very thin samples for each material, with a thickness of about 220  $\mu\text{m}$  for titanium alloy and Inconel 718 and of around 400  $\mu\text{m}$  for the aluminium alloy. After the cutting, the surfaces of the samples

		Materials			
		T91 Steel	Inconel 718	Al 6082 T6	Titanium Grade 23
<b>Physical properties</b>					
Density	$\rho$ [g cm <sup>-3</sup> ]	7,77	8,234	2,7	4,43
Thermal conductivity	$\bar{\lambda}$ [W m <sup>-1</sup> K <sup>-1</sup> ]	27	11,4	180	6,7
Specific heat capacity	$c_p$ [J g <sup>-1</sup> K <sup>-1</sup> ]	0,460	0,435	0,900	0,526
Volumetric CTE	$\bar{\alpha}$ [10 <sup>-6</sup> K <sup>-1</sup> ]	11,3	13	24	8,6
Melting temperature	$T_{\text{melt}}$ [°C]	1450	1298	650	1630
<b>Mechanical properties</b>					
Young's modulus	$E$ [GPa]	207	203	70	113,8
Poisson's ratio	$\nu$	0,3	0,29	0,33	0,342

**Table 2.7:** Physical and mechanical properties of the material specimens produced for the U-ions beams irradiation experiment.

have been polished in order to take away the oxides created during the cut. The pictures of these samples are reported in figure 2.6.

The tables 2.6 and 2.7 present the chemical compositions and the physical and mechanical properties of the materials selected for the irradiation experiment. The data reported in the tables were obtained from the technical data sheets of the various manufacturers or, if unavailable, from the online reference data sheets for the specific material [68][67][69][70].

# Chapter 3

## Experimental investigations

The experimental investigation on the selected materials conducted at GSI and the following microindentation and SEM microscopic analyses on the irradiated samples are covered in depth in this chapter.

### 3.1 Introduction to GSI facilities

The GSI Helmholtz Centre for Heavy Ion Research (*GSI Helmholtzzentrum für Schwerionenforschung*, in German) is a heavy ion research centre in the Wixhausen suburb of Darmstadt, in the Hesse region in Germany [71].

The centre, founded in 1969 as *Gesellschaft für Schwerionenforschung* (hence the acronym GSI), has developed during the decades from a national research institute to an international campus with worldwide collaborations. In addition to the 1520 employees working at GSI, approximately one thousand researchers from universities and research institutes visit the centre every year to use the accelerator facilities for experiments.

The fundamental study area of the GSI concerns the fields of nuclear and atomic physics. Parallel to these, nuclear medicine, plasma physics, biophysics and materials science are central to a multitude of research programs. In just over 50 years of activity, the centre achieved scientifically remarkable results, among which the discovery of six new chemical elements (for instance, Hassium  $_{108}\text{Hs}$  and Darmstadtium  $_{110}\text{Ds}$ , in honour of the region and the city) and a new type of tumour therapy using accelerated carbon ion beams.

The accelerator system at GSI consists of five main facilities, essential to provide heavy ions for the GSI investigations:

- The **ion sources**, devices where the ions are generated by stripping electrons off the shells of the atoms. Many different elements are produced at GSI (more than

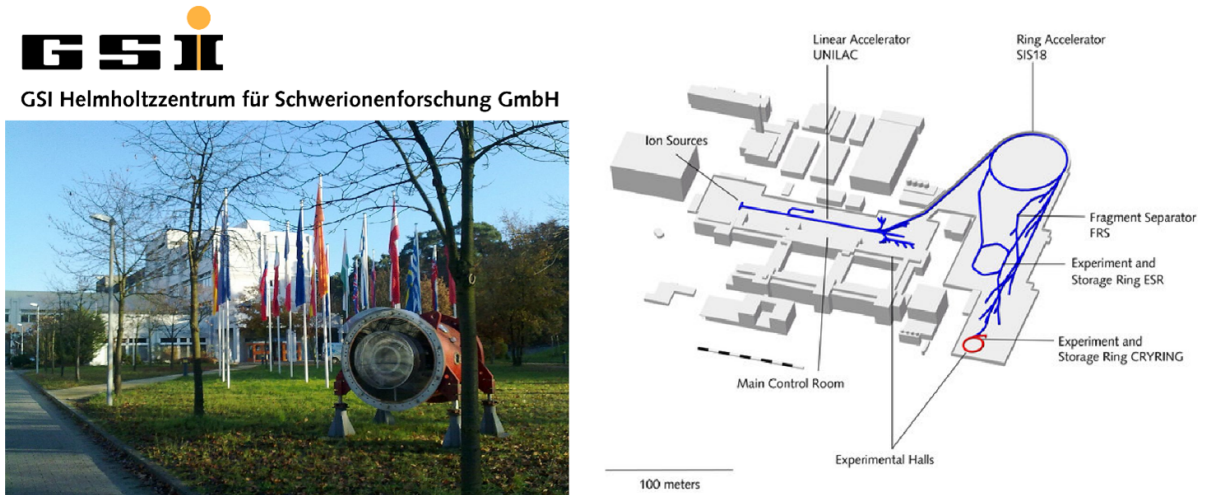


**Figure 3.1:** Picture of the entrance of GSI and sketch of main accelerator facilities

any other laboratory in the world) and distinct kinds of ion sources are employed depending on the different kinds of elements.

- The linear accelerator **UNILAC** (Universal Linear Accelerator), where the ion acceleration starts. The length of 120 metres allows the acceleration of all kinds of ions up to 20% of the speed of light. After the acceleration, ions can be employed in experiments of different natures (as is the case of the experiment addressed in this chapter) or else injected into the ring accelerator SIS18 for additional acceleration.
- The ions coming from the UNILAC can be accelerated to up to 90% of the speed of light by the 216-metre diameter ring accelerator **SIS18** (*Schwerionensynchrotron 18*). The ions are kept in a circular motion within the ultra-high vacuum chamber by magnets while being subjected to high voltage on every circulation. As soon as the ions reach the desired speed, they are either transferred to experiments to impact a material sample or into the experimental ring ESR for storage and additional analyses.
- The experimental storage ring **ESR** is used to store and accumulate ions coming from the previous accelerator facilities. The ESR is the only storage system in the whole world where it is possible to accumulate all the chemical natural elements - from He ( $Z=2$ ) to U ( $Z=92$ ) — and for ion speed ranging from below 10% to approximately 90% of the speed of light.
- The fragment separator **FRS** receives the accelerated ions from SIS18 and separates the interesting isotopes from the other reaction products. These rare isotopes can be produced, isolated, identified and then either directed to different experimental areas or kept in the storage ring.

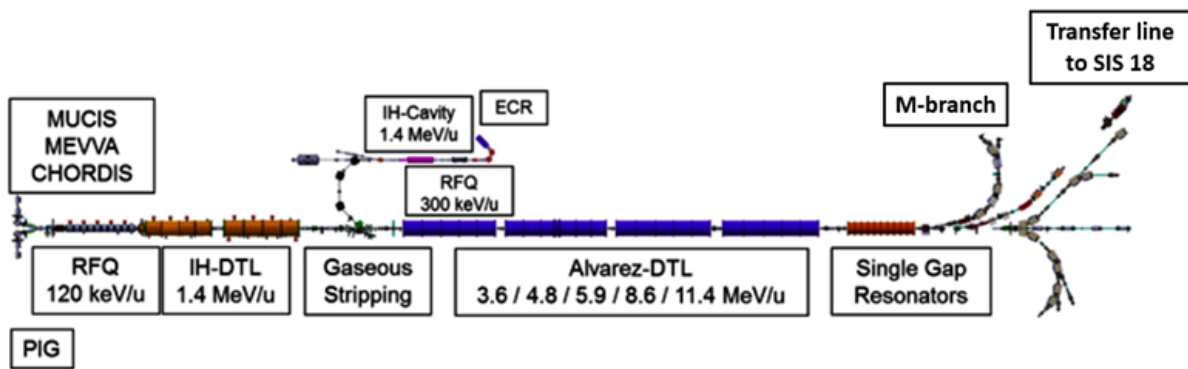


**Figure 3.2:** Schematic overview of the GSI UNILAC [72]

Currently, one of the largest and most complex worldwide construction projects in the framework of particle accelerators and nuclear physics research is the Facility for Antiproton and Ion Research (**FAIR**), under construction at GSI in Darmstadt. All the chemical elements (or their ions), as well as antiprotons, will be available as particle beams through FAIR accelerator facility, giving the opportunity to produce particle beams of unprecedented quality and intensity. The SIS100, an underground ring accelerator with a circumference of 1100 meters, will be able to accelerate the ions of all the natural elements to speeds up to 99.9% the speed of light. As the initial acceleration stage, the existing GSI accelerators will be used. The mission of the FAIR project consists of unveiling unsolved secrets regarding the nature and the composition of matter and the formation of the Universe. In order to do so, it is necessary to replicate in the lab the extreme conditions (such as very high temperatures, densities and pressures) that occur during planet collisions and stellar explosions by subjecting tiny samples of matter to ion bombardment, thus creating a tiny portion of cosmic matter on the impact zone for extremely short periods of time.

## 3.2 Description of the experimental facilities — UNILAC, M-Branch and M3 beamline

The irradiation experiment of the samples took place at the materials research branch (M-branch) of GSI, where uranium ions with the kinetic energy of 4.8 MeV/u coming from the UNILAC irradiation facility collided with samples of previously selected materials.

In the figure 3.2 a schematic overview of the GSI UNILAC is shown. The charged ions for the acceleration are provided by three different ion source terminals:

1. The Penning Ionization Gauge (PIG), used since the beginning of GSI operation in the early 1970ies, delivers low intensities of low to intermediate charged ions.

Metallic (Al, Bi, Cr, Au, Pb, ...) and gaseous ions (Ar, Ne, Kr, Xe, ...) are produced and post-accelerated to the injection energy of 2.2 keV/u of the RFQ (radio-frequency quadrupole).

2. The CAPRICE-type Electron Cyclotron Resonance (ECR) source, capable to provide high charge-state ion beams at low intensities for practically all elements by utilising the electron cyclotron resonance effect for efficient plasma generation [73].
3. The low-charged ions with high-intensity beams are provided by a third terminal with three different kinds of ion sources:
  - Metal Vapor Vacuum Arc (MEVVA) source
  - MUlti-Cusp Ion Source (MUCIS)
  - Cold or HOt Reflex Discharge Ion Source (CHORDIS)

In the MEVVA ion source, the terminal utilised to produce the Uranium ions for this experiment, the ions are extracted from the metal plasma generated by means of a metal vapour arc discharge between two metallic electrodes in the vacuum on superficial “cathode spots” — tiny regions of intense current concentration [74]. The use of this ion source principle, developed by I.G. Brown in Berkeley National Laboratory (LBNL, USA) and present at GSI from 1995, is therefore essential to provide high current metal ion beams for ion implantation applications. The GSI MEVVA ion source works with all types of ductile conductive metals, with a low-duty cycle in the frequency range of 0.5-2 Hz and a pulse length of 50-500  $\mu$ s.

After electrostatic extraction from the MEVVA ion source, the beams are bunched and accelerated to 5% of the speed of light along a radio frequency quadrupole (RFQ) and Inter Digital cavities. For low-charged ion beams — as is the case of the U-ions — a gaseous stripper can be utilised at this stage to enhance the efficiency of acceleration by removing the outer electrons of the ions.

Five Alvarez-type cavities complete the acceleration of the ion beams to energies ranging from 3.6 to 11.4 MeV/u, i.e from 9 to 16% of the speed of light<sup>1</sup>. The ion beams, after being passed through a section of single gap resonators (ERs) for the final setting of the energy between 3.4 and 11.6 MeV/u, may be passed through the Transfer Channel towards the synchrotron SIS18 to be furtherly accelerated or diverted by means of a kicker magnet to various experimental branches, as the M-Branch in this case.

---

<sup>1</sup>The correlation between the kinetic energy of the ion per unit of atomic mass (MeV/u) and the velocity ratio ( $\beta = v/c$ ) is straightforward:  $E_k = \frac{1}{2}mv^2 = \frac{1}{2}m(\beta c)^2$ , where  $m = 1u \cong 1.661 \cdot 10^{-27}kg$ ,  $c \cong 2.997 \cdot 10^8 m/s$  and  $1 eV \cong 1.6022 \cdot 10^{-19} J$ .

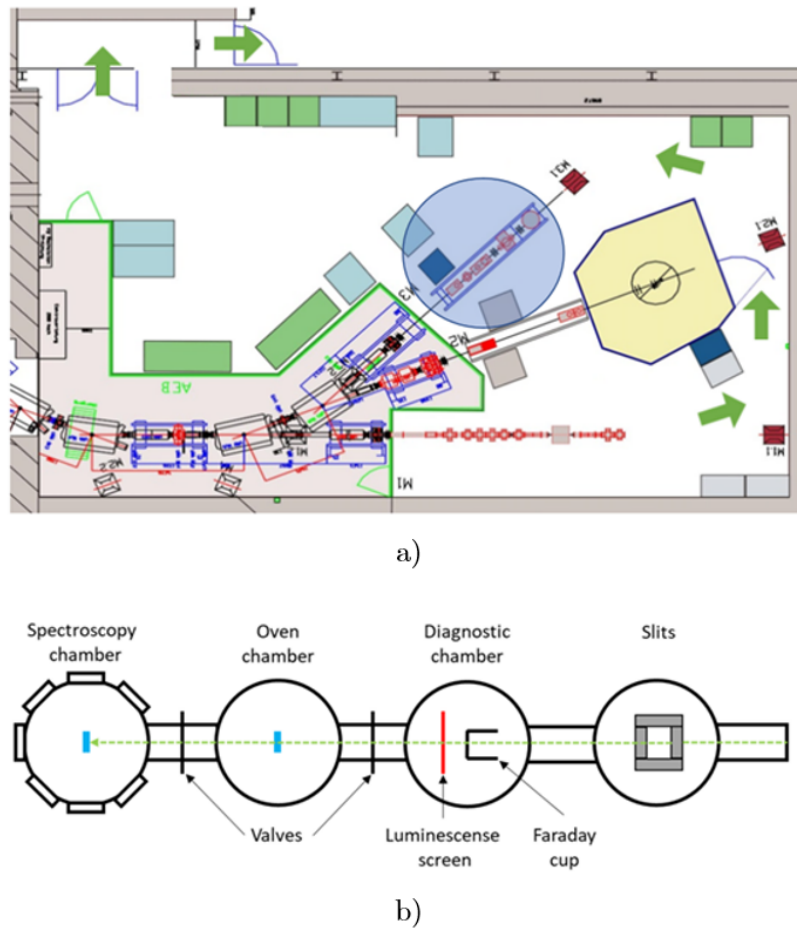


**Figure 3.3:** (a) Floor-plan of the M-Branch cave of UNILAC. (b) Schematic sketch of the M3 beamline of the GSI UNILAC accelerator. The beam is marked by a green dotted arrow, while the blue squares indicate the potential positions for irradiated samples. Courtesy of Philipp Bolz [60].

In the M-Branch cave, there are three experimental beamlines (M1, M2 and M3), largely utilised for irradiation experiments in collaboration between GSI Materials Research Group and the Universities of Darmstadt, München, Dresden, Jena, etc. The irradiation experiment took place at the M3-beamline of the M-Branch: this beamline consists of a multi-purpose chamber equipped with a closed-cycle He cryostat, a residual gas analyser, and a gas flow controller [75].

As can be seen from the figure 3.3 above, the M3-beamline contains different chambers:

- The **Slits chamber**, where the beam coming from UNILAC is properly shaped by horizontal and vertical slits into a square shape. In the figure 3.4(a) the slits calibration screen on the operation panel is shown: it can be noted that the ion beam is concentrated in a square shape of roughly 2 cm long sides.
- The **Diagnostic chamber**, where the homogeneity and size of the ions and the



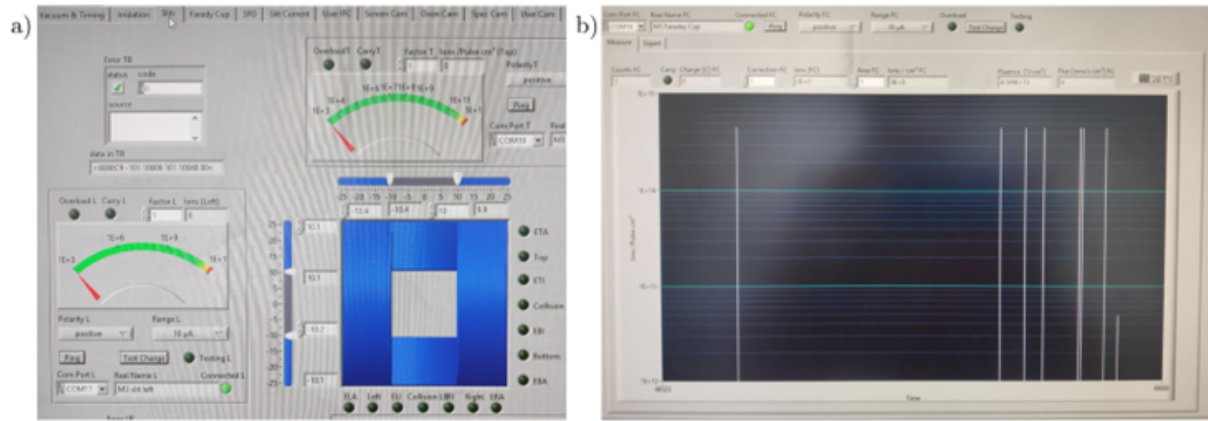


**Figure 3.4:** M3-beamline software screens during (a) calibration of the slits and (b) Faraday Cup in operation to verify the stability of the U-ion flux.

intensity of the ion beams are measured. Size and homogeneity of the U-ions are measured by a luminescence screen: the ion energy is deposited on the screen material and converted into atomic excitations, followed then by radiative relaxations. The ion beam profile is a direct result of the light intensity of these optical transitions. A Faraday Cup is instead adopted to check the intensity of the ion beams: when the Uranium ions, whose charge state is known, impact onto the metal of the cup, the ion charge is neutralised while the metal gains a small net charge that is distributed on the external surface of the cup and can be measured as an electrical current. In the 3.4(b) the Faraday Cup (FC) screen during the check of the operating condition of the ion flux from UNILAC is shown. Both the luminescence screen and the Faraday Cup are naturally removed from the beamline during the sample irradiation experiment.

- The **Oven Chamber** (OC) is typically the chamber designed to house samples for post-irradiation analysis. In this case, in order to focus the U-ion beams into a smaller circular beam spot (0.6 cm in diameter), a perforated aluminium plate with collimator holes of different sizes was mounted inside the Oven chamber, as can be seen in the Figure 3.5(a).
- The **Spectroscopy chamber** (SC), where the sample holders for *in situ* analysis were placed. The Figure 3.5(b) is a picture taken by the open View window of the SC during the phase of the replacement of two sample holders: inside the chamber, it is possible to distinguish the sample holder, clamped in the top to a support, and the infrared golden mirrors, installed for the temperature measurements by the thermal camera. The correct arrangement of the samples under the beam irradiation is checked by a dedicated camera, as shown in the Figure 3.5(c).



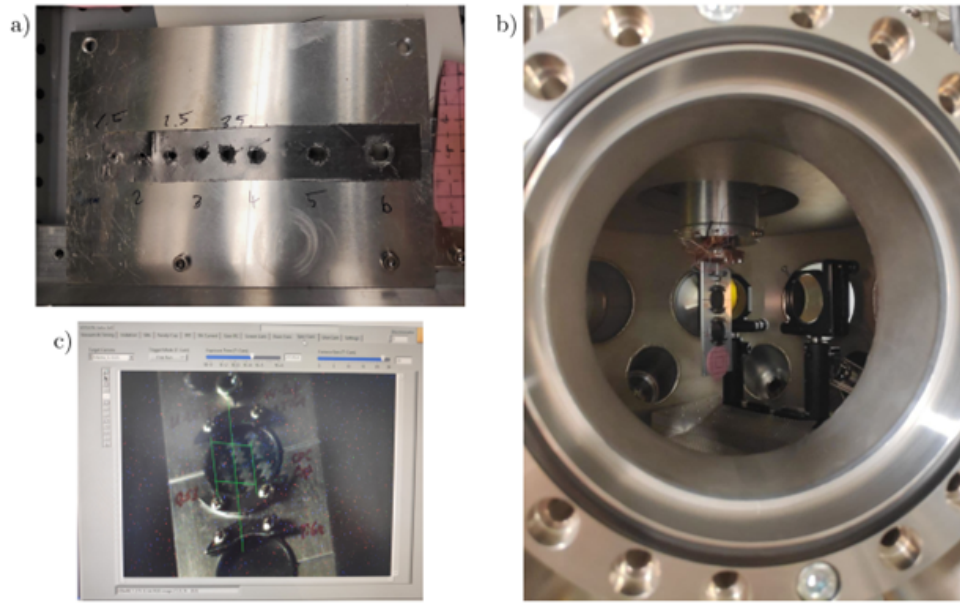


**Figure 3.5:** (a) Perforated aluminium plate with holes of different sizes to resize the square-shaped beam after the slits to obtain a smaller circular-shaped beam. (b) Interior view of the Spectroscopy chamber. (c) The software screen of the spectroscopy chamber camera focused on a material sample before the irradiation experiment.

### 3.3 Description of the experimental setup

The experiment consists of irradiating metal samples with U-ion beams in order to assess the dynamic radiation effects and the thermo-mechanical behaviour of the samples. The analysis of the response of these materials to beam impact allows us to better understand the radiation-induced damage phenomena and thereby detect and prevent potential failures while operating the beam windows.

#### 3.3.1 Sample preparation

The materials investigated during the beam time are reported in table 3.1. The criterion selection and the manufacturing procedure of these material samples were extensively presented in the previous chapter.

**Table 3.1:** Materials investigated during the beam time.

Material sample	Sample Holder	Average thickness	Diameter
ASTM A213 T91 Steel (EN 1.4903 grade)	#1, upper housing	$213.4 \pm 6.2 \mu\text{m}$	20 mm
Inconel 718	#1, lower housing	$219.3 \pm 4.9 \mu\text{m}$	20 mm
EN AW 6082 T6 (Aluminium alloy)	#2, upper housing	$405.4 \pm 4.9 \mu\text{m}$	20 mm
Titanium Grade 5 ELI (Grade 23)	#2, lower housing	$219.9 \pm 2.6 \mu\text{m}$	20 mm

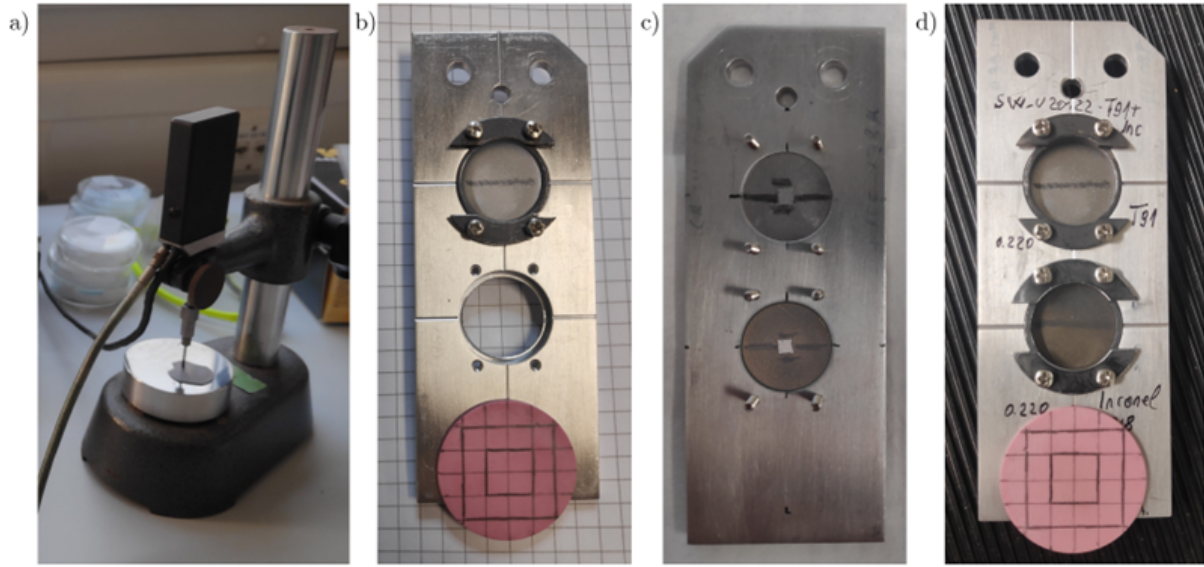


**Figure 3.6:** Pictures of the process of sample preparation: (a) high accuracy length gauge to measure the effective thickness of the samples, (b) mounting of the T91 steel sample in the upper housing of the sample holder, (c) back side of the first sample holder, where the application of the graphite spray and of the tiny piece of adhesive reflective tape can be noticed, (d) front side of the first sample holder, set to be installed inside the Spectroscopy Chamber.

For each material, only one sample was irradiated from those available (around 10 for each material) on the grounds of the limited availability of beam time. The effective thickness of the samples (subjected to the EDM wire cutting in the CERN and RHP workshop before transportation) was checked using a high accuracy length gauge by HeidenHain, as shown in figure 3.6(a). Different measures of the thickness in various positions of each sample were made and the average and its uncertainty were computed. As regards Steel T91, Inconel 718 and Titanium Grade 23, the samples with the closest average values (around  $220\text{ }\mu\text{m}$ ) were chosen, while the sample with the smallest average value was selected for the aluminium alloy sample. The preparation procedure of the sample holders can be summarised in the following few steps:

- The samples were mounted in a ring-shaped sample holder, resulting in a free-standing diameter of the disc of 18 mm (figure 3.6(b)).
- The four screws were tightened to ensure the best possible contact.
- A conductive graphite spray (GRAPHIT 33) was used to apply black paintings on the front and on the rear faces of the samples (horizontal black lines in figure 3.6) and on the ring surfaces in order to uniform and quantify the emissivity and allow the Thermal Camera to measure the temperature accurately.

- A tiny piece of adhesive reflective tape (1 mm<sup>2</sup> of area) was glued at the centre of the back of each sample to increase the reflectivity of the laser beam and to avoid the reflected laser beam to be lost during surface displacement (figure 3.6(c)).
- A piece of pink paper was glued in the lower part to refine the beam spot before irradiation during the calibration phase.
- The name of the experiment (SW-U-2022, i.e. Stress waves U-ions in 2022) and the names of the single materials were signed by a permanent pen on the front face of the sample holders (figure 3.6(d)).

### 3.3.2 *In situ* measurement instruments

The surface velocity related to the beam-induced bending and the increase in temperature due to the deposition of the kinetic energy of the beam on the material samples were measured online by means of two instruments, respectively a Laser Doppler Vibrometer (LDV) and a thermal camera (TC).

#### Laser Doppler Vibrometer (LDV)

The LDV High-Speed System is composed of the Polytec OFV-525 High-Speed Sensor Head (figure 3.7(a)) and the Polytec OFV-5000-S Vibrometer Controller. These instruments allow to measure vibration frequencies up to 2.5 MHz and vibration displacements from a few nanometres to many centimetres.

The basic principle of operation employs the frequency shift (Doppler Effect) of the laser pointed at the sample and reflected off its surface. It is thus possible to calculate the velocity of the sample surface and, consequently, the frequency and amplitude of the thermoelastic stress waves by comparing the frequency shift of the reflected light to the initial laser signal. The OFV-525 Sensor Head guarantees excellent performance for high-speed measurements by means of the high-sensitivity autofocus and a set of interchangeable lenses suitable for any technical surface.

To prevent any beam-induced damage to the LDV and the associated viewport at the beamline, the LDV was positioned at 45° angle on the rear side, as can be seen in the figure 3.7(a) and in the sketch 3.7(c). Signal acquisition was accomplished by connecting the LDV Vibrometer Controller to the oscilloscope inside the control room through the usual analogue BNC voltage output.

### Thermal camera (TC)

The high sensitivity and accuracy FLIR SC7000 Thermal Camera (figure 3.7(a)) was used to evaluate and monitor the temperature of the samples subjected to beam-induced heating. The excellent spatial resolution and speed of the SC7000 model enable it to capture up to 1475 frames per second in 320 x 240 pixels, each high-quality image being captured in snap-shot mode. This resolution, which gives the opportunity of capturing an image every approximately 0.678 ms, is undoubtedly appropriate for tracking the radial heat spreading after the impact of ions on the target samples (this range of resolution is many orders of magnitude lower than the radial thermal diffusion characteristic times, whose values are presented in the table 3.2). On the other hand, the TC resolution time does not seem to be completely adequate for tracking the diffusion phenomena along the sample thickness, in particular for diffusive materials such as the aluminium alloy and the steel T91, for which the thermal diffusion characteristic time is not even an order of magnitude larger than the resolution time of the Thermal Camera.

**Table 3.2:** Radial and axial thermal diffusion times for the four cylindrical samples irradiated during the GSI experiment.

Materials	Physical properties				Thermal diffusion time [ms]	
	Density $\rho$ [g cm <sup>-3</sup> ]	Thermal conductivity $\bar{\lambda}$ [W m <sup>-1</sup> K <sup>-1</sup> ]	Specific heat capacity $c_p$ [J g <sup>-1</sup> K <sup>-1</sup> ]	Thermal diffusivity $a$ [mm <sup>2</sup> s <sup>-1</sup> ]	Radial R = 10mm	Axial (thickness)
T91 Steel	7,77	27,00	0,460	7,55	13237,78	6,03
Inconel 718	8,23	11,40	0,435	3,18	31419,21	15,11
Al-6082-T6	2,70	180,00	0,900	74,07	1350,00	2,22
Ti Grade 23	4,43	6,70	0,526	2,87	34798,64	16,83

To allow the thermal camera to assess the temperature on both the front and back sides of the irradiated sample, the thermal camera was positioned orthogonally to the direction of the beam, and two infrared gold mirrors were mounted inside the Spectroscopy Chamber (figure 3.5(b)) to simultaneously reflect the two sides of the sample into the camera (sketch 3.7(c)). ALTAIR software was used to process the acquired image data.

### 3.3.3 Report of the experiment

The SW-U-2022 experiment took place in the M3 beamline of UNILAC GSI on the 27<sup>th</sup> and 28<sup>th</sup> of March under the supervision of the Marilena Tomut, professor at the University of Münster. The real-time monitoring of the experiment was carried out from the Control room outside the M-Branch cave, where from a few monitors it was possible to check the status of the beam parameters, the vacuum system, the M3-beamline chambers as

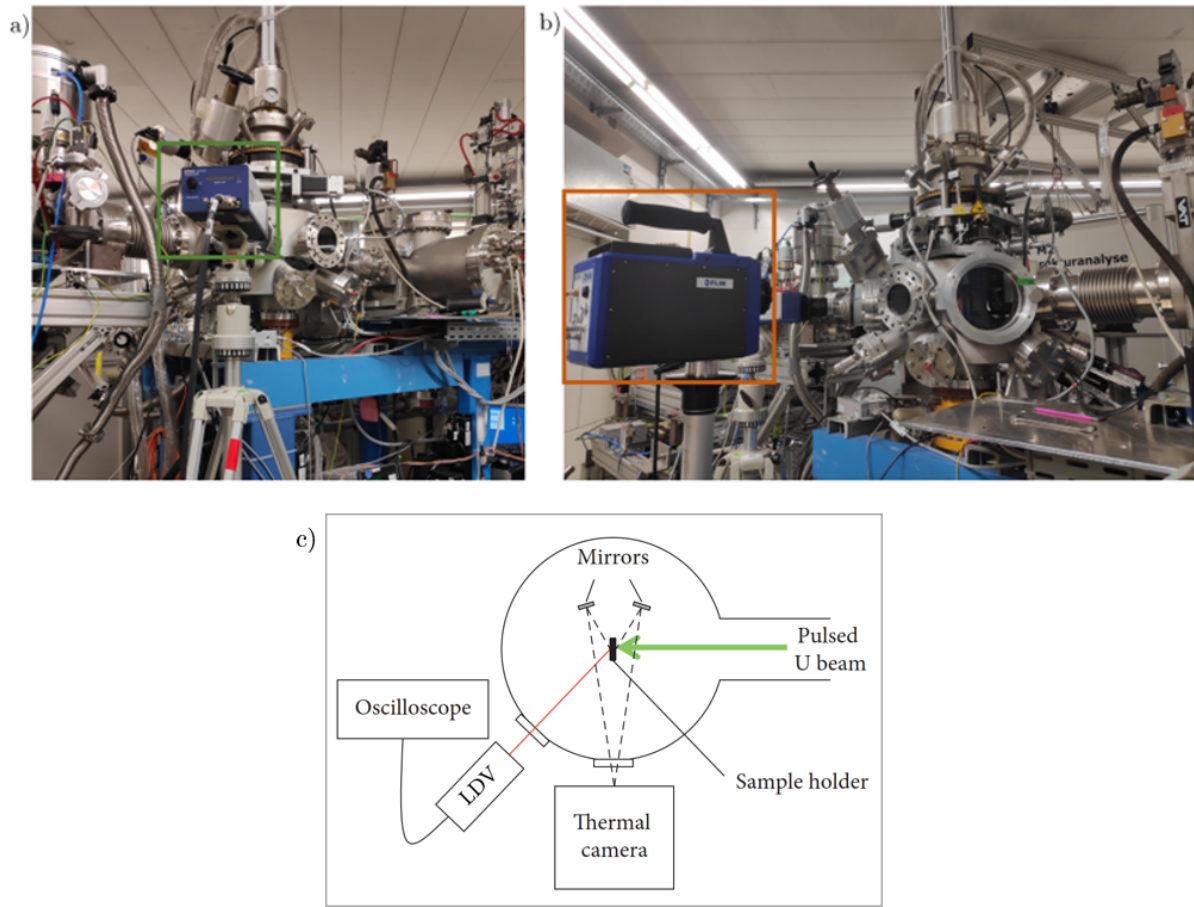


**Figure 3.7:** Arrangement of (a) Laser Doppler Vibrometer (green frame) and (b) thermal camera (orange frame) in front of the spectroscopy chamber of the M3-beamline for the SW-U-2022 experiment. (c) A sketch of the top view configuration of online measurement instruments.

well as the online measuring instruments (the Thermal Camera and the Laser Doppler Vibrometer).

The operational phases of the experimental set-up are reported below:

- The first sample holder and the aluminium plate with collimator holes were installed in the Spectroscopy and Oven chamber, respectively. The procedure of opening and closing the Spectroscopy Chamber requires the control of the vacuum system: before opening the chamber, maintained during the beam operation at a pressure lower than  $10^{-7}$  mbar (high vacuum condition), the vacuum valve is closed and the vent valve is opened so that the chamber pressure rises to the room pressure.
- Calibration phase: the shape of the U-ion beam was properly cut by the four slits to obtain a centred  $20 \times 20 \text{ mm}^2$  square beam spot in the Spectroscopy chamber. The positions of the eight collimator holes in the Oven chamber were checked and a beam spot of 6 mm in diameter was chosen for the irradiation test. The central

portions of the two samples in the Spectroscopy Chamber were calibrated and annotated in terms of spatial coordinates to allow the correct operation of the electronic manipulator in driving the sample holders during the experiment.

The fundamental parameters of the beam, monitored and checked remotely by the Faraday Cup and the luminescence screen, are presented in the table 3.3. It was ensured that all the samples were exposed to U-ion beams for the same amount of time so that the total fluence achieved was the same for the four samples irradiated.

**Table 3.3:** U-ion beam parameters

Ion	Energy per nucleon	Ion energy	Pulse repetition rate	Pulse length	Flux of ions	Achieved Fluence	Irradiation time	Average current
	[MeV/u]	[GeV]	[Hz]	[ $\mu$ s]	[ions cm <sup>-2</sup> s <sup>-1</sup> ]	[ions cm <sup>-2</sup> ]	[s]	[ $\mu$ A]
Uranium	4.8	1.14	1	100	5.0 x 10 <sup>9</sup>	2.0 x 10 <sup>13</sup>	4000	620

Using the two online measurement instruments, the thermo-mechanical behaviour of the investigated materials is thus examined during the experiment with increasing fluence levels, till reaching the maximum value fixed at 2.0 x 10<sup>13</sup> U-ions/cm<sup>2</sup>. In the beam control software, it is possible to track the number of incident ions on the sample during the irradiation time and set the fluence level at which the chopper is scheduled to stop the beam impact on the test piece.

Because of a problem in the update of the software for monitoring the beam, it was not possible to record the flux during the irradiation. To tackle the problem, it is decided to use the irradiation time as a reference parameter from which the fluence has been obtained by the following formula:

$$\Phi^i = \int_{t_0}^{t_1} \varphi(t) dt \cong \varphi_0(t_1 - t_0) \quad (3.1)$$

where  $\Delta t_i = t_1 - t_0$  is the i-th irradiation interval manually measured by a timer,  $\varphi_0$  the flow of uranium ions recorded by the software just before the incident ion beam is restored,  $\Phi_i$  the fluence accumulated in this last irradiation interval. This  $\Phi_i$  value added to the previous fluence values returns the entire accumulated fluence so far  $\Phi$ .

Two sets of data are then acquired at each restart of the beam (and of the timer) and written down on the experimental log:

- the velocity signal generated by the first pulse: this signal, transduced by the LDV and shown on the oscilloscope screen (figure 3.8 (a)), was saved by the oscilloscope software in terms of .TXT file.



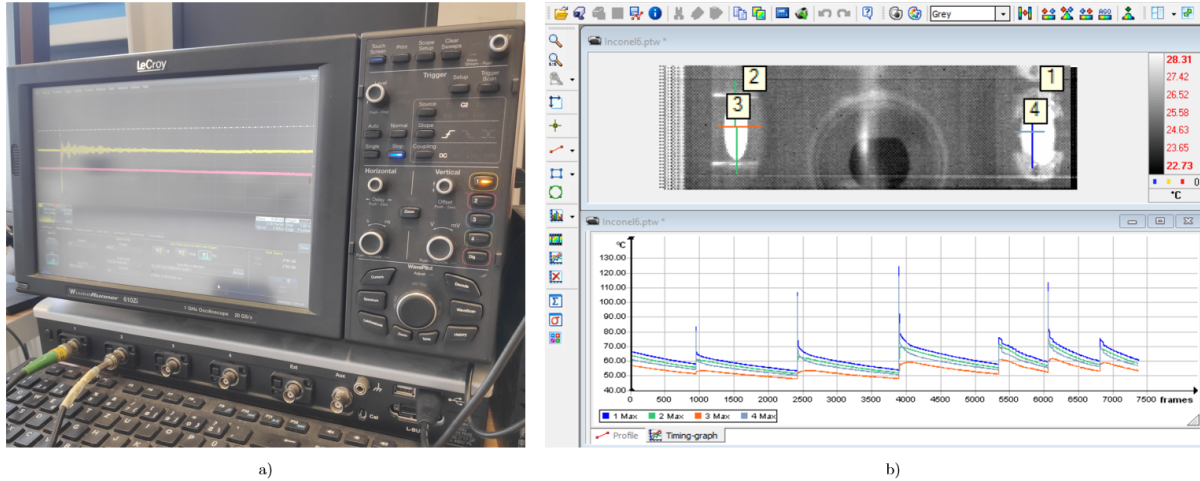


**Figure 3.8:** (a) Picture of the oscilloscope connected to the LDV during the experiment. (b) Screen capture of Altair software used to analyse the data from the Thermal Camera.

- the temperature profile on the front and rear sides of the sample: the data from the Thermal Camera are acquired by the software Altair and the first five seconds corresponding to 7375 frames (1 second = 1475 frames) are recorded in the form of captures and Altair files (figure 3.8 (b)).

### 3.4 Preliminary results of the online monitoring

This section presents the results of the online monitoring of the experiment, during which the temperature and the velocity at the rear side of the samples as a result of the impact of 4.8 MeV/u uranium ion pulses were recorded.

#### 3.4.1 Temperature development recorded by the Thermal Camera

The temperature development of the different samples under irradiation was analysed using the data provided by the Thermal Camera. This study has several purposes:

- check that the irradiated materials inside the Spectroscopy Chamber do not overheat and do not reach steady-state temperatures that will affect the operation of the other components (potentially hazardous situation above 200°C). Moreover, the temperature control prevents the annealing of the generated defects and secures that the properties of the target materials do not deviate too much from those at room temperature.
- examine to ensure the predetermined ion flow conditions are being used (in terms

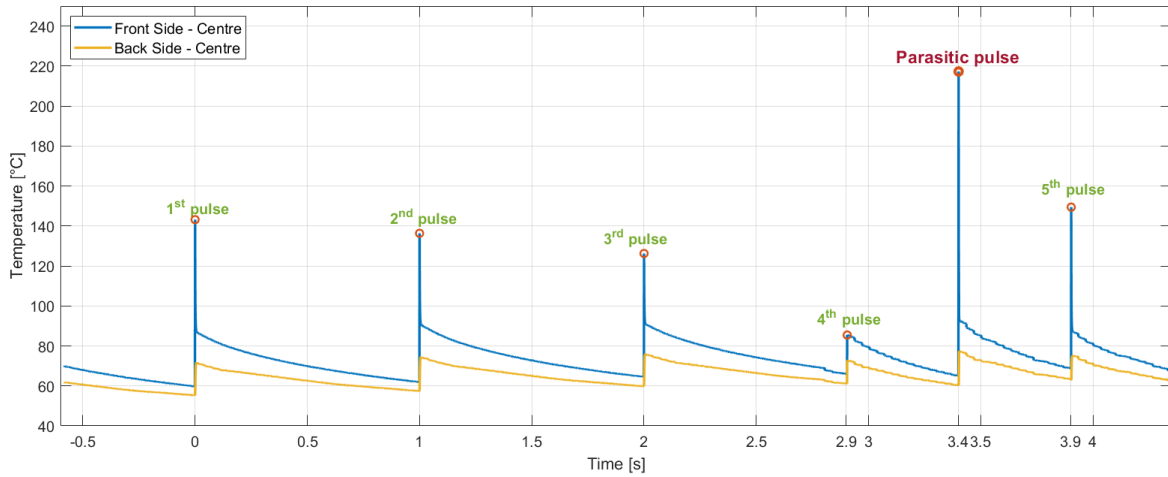


**Figure 3.9:** Temperature development in five seconds of Titanium Grade 23 at fluence  $2 \cdot 10^{11}$  U-ions  $\text{cm}^{-2}$ . The peaks associated with the expected pulses at a frequency of 1 Hz are indicated in green. In red the peak that occurred only 0.5 seconds after the fourth, known as *parasitic pulse*.

of frequency of pulses and flux stability, for example) the verification that the quantity of incident ions on the source is consistent with what was anticipated by the experiment (frequency and impulse).

- understand how and in what amount the thermal power transmitted by the pulse spreads inside the irradiated material and in the sample holder to which it adheres in order to be oriented on the selection of appropriate thermal boundary conditions for the following thermo-mechanical simulations.

Furthermore, the analysis of the temperature rise of the tested material as a result of the pulse impact is essential to understand if the progressive heating causes a change in the boundary conditions (loss of contact, etc.) and if the thermal properties remain constant as the fluence increases: a slowdown in the process of dissipation of the energy deposited in the central beam spot could denote a detrimental effect due to the U-ion radiation to the values of specific heat and thermal expansion coefficient.

As a typical case, the figure 3.9 represents the trend of the temperature on the front and back side of the Titanium Grade 23 sample recorded in five seconds by the thermal camera. With a fixed frequency of 1 Hz, a pulse (clearly identified by the corresponding temperature peak) is expected to be recorded every second, for a total of five peaks in five seconds of TC monitoring.

As can be seen from the figure, the first three pulses occur as expected, spaced by one-second intervals, while the fourth occurs 0.1 s earlier, after 0.9 seconds. It is worth noticing that an unexpected pulse appears halfway between the fourth and fifth pulse:



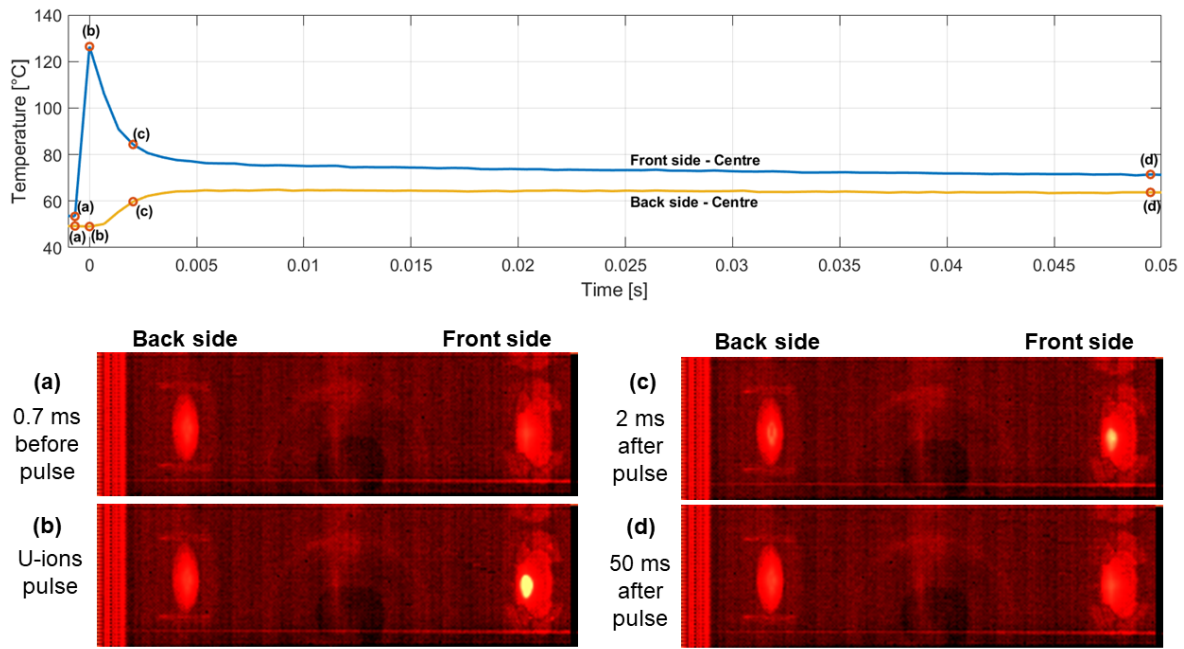


**Figure 3.10:** Detail of a 50 ms thermal profile of the fully irradiated Titanium Grade 23 sample. Four thermal images recorded by the TC are reported.

the latter pulse, known as *parasitic pulse*, can be attributed to UNILAC accidentally having transmitted to the M3-beamline a beam of uranium ions destined to a different experiment that was being run at the same time. By examining the other thermal profiles captured by the thermal camera, it was discovered that this pulse is detectable in the majority of cases, leading to the assumption that it occurs continuously throughout the experiment and has a frequency of 0.2 Hz. This detail undoubtedly has an impact on the estimation of the total fluence accumulated by the samples during the irradiation test, whose values could potentially be up to 20% higher than originally thought.

The figure 3.10 represents an extract of 50 ms of the thermal profile of the last data recorded by the TC for a completely irradiated Titanium Grade 23 sample. The exact peak value is not always observable, since the sampling frequency of the thermal camera (1475 Hz) enables for the acquisition of a thermal image every about 670  $\mu\text{s}$ , more than the duration of the pulse (100  $\mu\text{s}$ ).

The four captures displayed in the figure correspond to four remarkable instants of temperature development:

- (a) before the beam impact, when the temperature on the front and rear sides of the sample is almost uniform;
- (b) during the beam impact, which corresponds to the maximum temperature recorded on the front side.

- (c) 2 ms after the impact, during the stage of rapid cooling of the impacted beam spot, when the heat spreads in the rear side and then in the whole sample;
- (d) 50 ms after the impact, when the temperatures of the two sides are almost identical and the cooling is slow and constant.

The figures 3.11-3.14 show the temperature evolution of the four samples irradiated at different levels of fluence on both the front and rear sides. The comparison of these graphs allows the following considerations to be made:

- Materials having very high thermal diffusion coefficients, like aluminium (figure 3.13), cool down quickly and are able to dissipate practically all of the heat received by the pulse before the following impact, with nearly identical thermal profiles at all fluency levels. The low steady-state temperatures maintained throughout the irradiation time suggest that thermal radiation contributes only to a small part of heat removal from the beam spot and that the almost totality of heat dissipation is due to the thermal conduction, first toward the edges of the target sample, then along the sample holder and, finally, towards the containment structure of the Spectroscopy Chamber to which the sample holder is connected by a metallic support.
- The only significant variation between the thermal profiles of each material at different fluence levels is the initial temperature of the sample prior to the next uranium ions pulse, which is determined only by the amount of heat not dissipated by previous pulses. It follows that the U-ions irradiation does not appear to cause a slowdown in the cooling process ascribable to of the reduction of the specific heat and thermal expansion coefficients, but the latter remains constant and unaffected by the flux of uranium ions to which they have been subjected.
- The thermal profiles of titanium differ from those of other materials. The highest temperatures, as illustrated by the graphs in the figure 3.14, are not achieved for the highest levels of accumulated fluence, but rather for intermediate values. This was due to the replacement of the U cathode at fluence  $9 \cdot 10^{12}$  ions  $\text{cm}^{-2}$ , which interrupted the experiment for around 20 minutes and permitted the sample to almost totally cool down. When the experiment was finally restarted at flux  $4 \cdot 10^9$  U-ions  $\text{cm}^{-2} \text{ s}^{-1}$  (lower than  $5 \cdot 10^9$  U-ions  $\text{cm}^{-2} \text{ s}^{-1}$  maintained until that point), the sample started warming up again, but the temperatures reached before beam interruption was not restored.

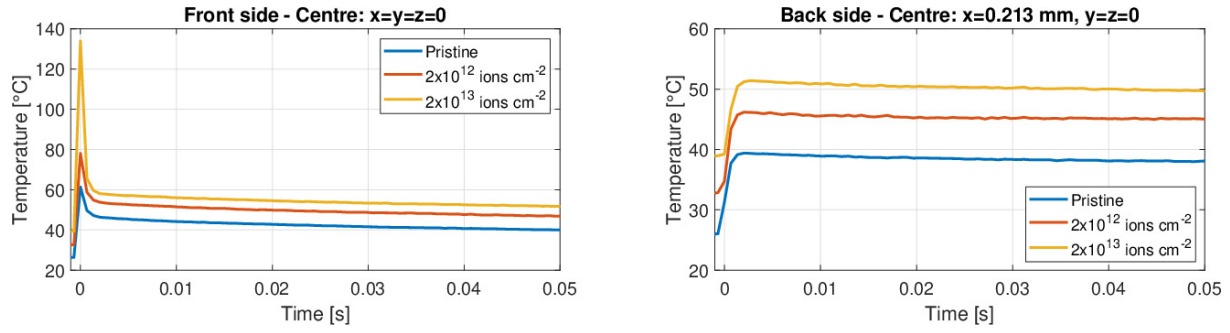


**Figure 3.11:** Steel T91 sample — Thermal profile recorded by TC at three fluence levels.

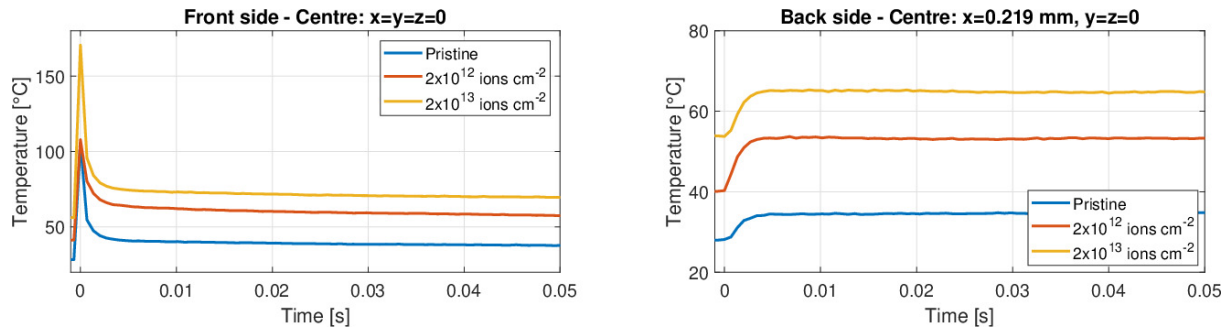


**Figure 3.12:** Inconel 718 sample — Thermal profile recorded by TC at three fluence levels.

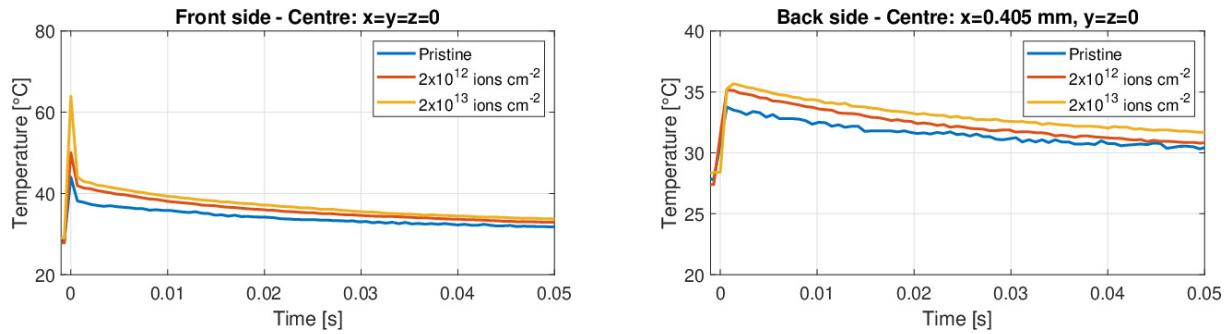


**Figure 3.13:** Aluminium 6082 T6 sample — Thermal profile recorded by TC at three fluence levels.

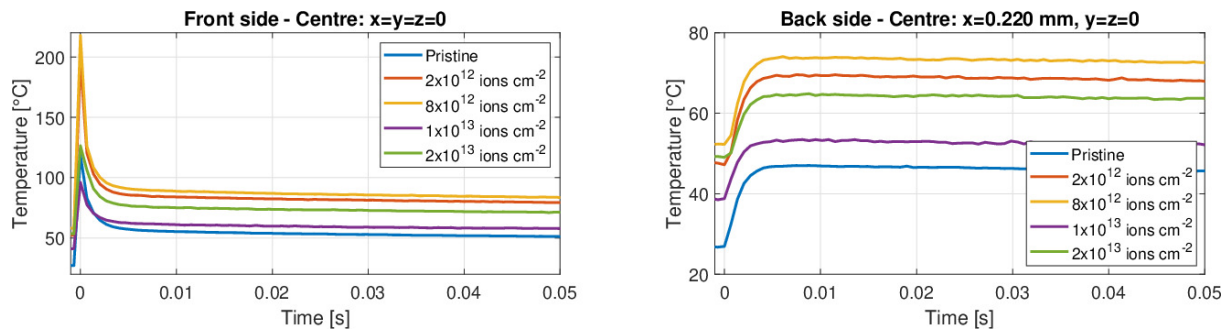


**Figure 3.14:** Titanium Grade 23 sample — Thermal profile recorded by TC at five fluence levels.

### 3.4.2 Measurement of beam-induced stress waves by Laser Doppler Vibrometry

The optimal solution for investigating the dynamic effects, like vibrations and stress waves, generated by the ions impacting on the matter, consists of the direct observation of these phenomena by means of appropriate online measurement tools, such as Laser Doppler Vibrometer, that enables to observe the velocity and displacement of a target surface at selected positions.

High thermal stresses are indispensable for ensuring the correct acquisition of dynamic effects by the measuring instrument. The beam conditions, including the nature of the ions, the pulse length and the beam intensity, were selected specifically to make the measurements of stress waves and beam-induced vibrations possible. The thermal stresses are particularly high when a large amount of energy is deposited inside a small portion of matter over a particularly short interval of time. The highest energy losses by ionising radiation inside the beam spot of the target samples occur when the mass of the ions is high (heavy ions) and when the energy of the incident ions is close to the Bragg peak. For this reason, 4.8 MeV/u U-ions with short pulse length (100  $\mu$ s) were adopted for the irradiation experiment.

The laser of Polytec LDV was directed towards the rear sides of the samples to measure the beam-induced vibrations, mainly parallel to the direction of the beam. By comparing the frequency shift of the reflected light to the initial laser signal, the velocity of the sample surface may be calculated. This online measurement, conducted with just one sample for which the fluence is step-wise increased, provides information on the frequency and amplitude of thermo-elastic stress waves.

The velocity signals recorded using the oscilloscope connected to the LDV were processed in order to extract information about the natural frequencies of vibration of the target materials as a function of beam-induced damage.

As it was described in the previous chapter with regard to the preliminary vibration analysis, the disc samples subjected to the pulsed beam exhibit two main frequencies of vibration:

- The natural frequencies of vibration, ( $f_b$ ), ascribable to the dynamic response of the whole body to the beam-induced thermal stresses. Since the thermal expansion of the samples, caused by the increase in temperature as a result of the beam-induced heat deposition, is prevented by the boundary clamping conditions, the whole body is forced to bend and several natural modes of vibration are therefore originated. These bending modes are typically in the order of magnitude of the kHz for samples of the selected shape and materials and the first and second-order

bending frequencies are expected to be captured by the LDV.

Parameter		Unit	Materials			
			T91 Steel	Inconel 718	Al-6082-T6	Ti Grade 23
Properties	Density	$\rho$ [g cm <sup>-3</sup> ]	7,77	8,23	2,70	4,43
	Young's modulus	E [GPa]	207,00	203,00	70,00	113,80
	Poisson's ratio	$\nu$	0,30	0,29	0,33	0,34
	Thickness	h [ $\mu$ m]	213,40	219,30	405,40	219,90
	Radius	R [cm]	1,00	1,00	1,00	1,00
	Flexural rigidity	D [Pa m <sup>3</sup> ]	0,18	0,19	0,44	0,11
Natural bending frequency	Clamped plate	1 <sup>st</sup> mode of vibration [kHz]	<b>6,69</b>	<b>6,60</b>	<b>12,68</b>	<b>6,88</b>
		2 <sup>nd</sup> mode of vibration [kHz]	26,04	25,66	49,32	26,75
	Free plate	1 <sup>st</sup> mode of vibration [kHz]	<b>4,78</b>	<b>4,70</b>	<b>9,11</b>	<b>4,96</b>
		2 <sup>nd</sup> mode of vibration [kHz]	20,39	20,09	38,68	20,99
	Simply-Supported plate	1 <sup>st</sup> mode of vibration [kHz]	<b>3,23</b>	<b>3,17</b>	<b>6,17</b>	<b>3,36</b>
		2 <sup>nd</sup> mode of vibration [kHz]	19,47	19,18	36,91	20,03
Frequency of propagating waves	P-wave velocity	$v_P$ [m/s]	5988,55	5683,98	6197,82	6313,39
	Frequency of P-wave	$f_P$ [kHz]	<b>14031,29</b>	<b>12959,36</b>	<b>7644,09</b>	<b>14355,13</b>
	S-wave velocity	$v_S$ [m/s]	3201,02	3091,24	3121,95	3093,70
	Frequency of S-wave	$f_S$ [kHz]	<b>80,03</b>	<b>77,28</b>	<b>78,05</b>	<b>77,34</b>

**Table 3.4:** Analytical results of natural bending frequencies and frequencies of propagating waves for the four material samples irradiated during the GSI experiment.

- The frequency related to the wave propagation phenomena:
  - The primary waves along the thickness ( $f_P$ ): these waves, reflected along the thickness of the samples between the rear and front sides, are originated from additional thermal stress due to the fact that the expansion of the heated beam spot is severely limited from the thermally inertial outer material. As foreseen by the analytical calculations in the previous chapter, it was not possible to experimentally capture the frequencies of these waves, generally in the order of magnitude of tens of MHz, since these frequencies exceed the maximum frequency detectable by the LDV employed (2.5 MHz).
  - The secondary waves in the radial direction ( $f_S$ ): these shear vertical waves, originated by the expansion of the heated beam spot or by the reflection of the primary waves with the surface of the sample, were not captured by the LDV because of the characteristic elusive nature of their propagation, despite the expected frequency (around 80 kHz) was within the sampling LDV threshold.

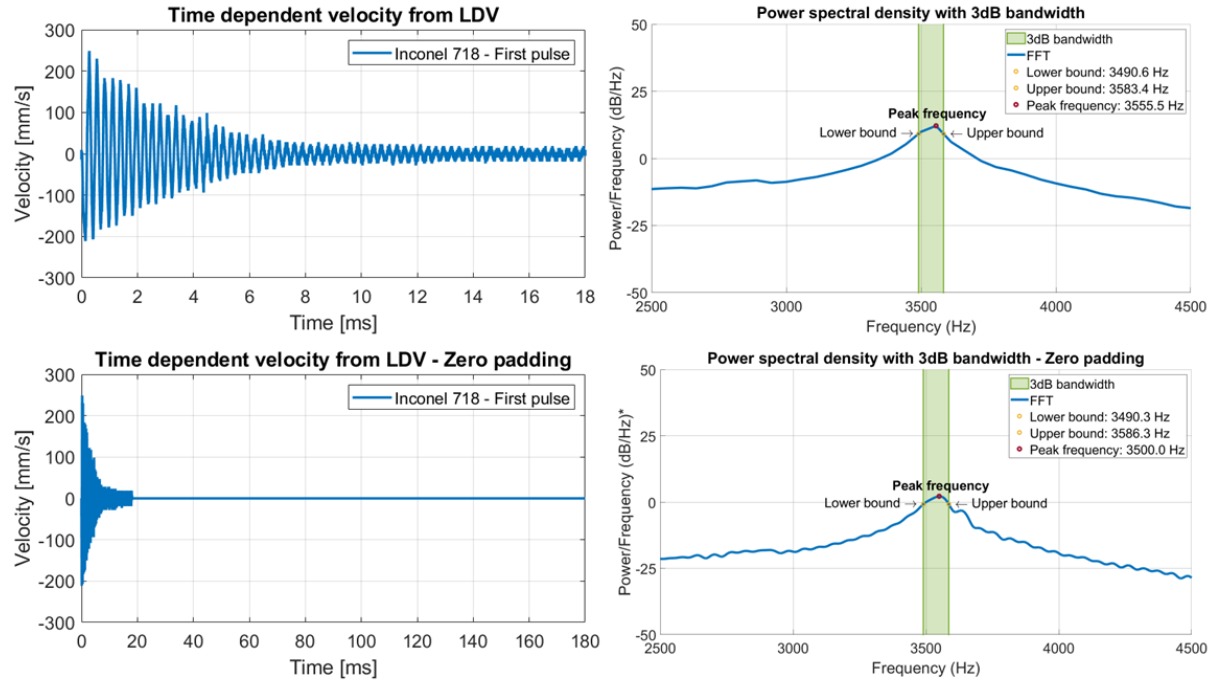


**Figure 3.15:** Velocity signal in the time domain (on the left) and corresponding power spectral density in the frequency domain (on the right) measured by LDV at the rear side of the pristine Inconel 718 disc sample at the first pulse of the U-ion beam.

The value of  $f_{b0}$  for each material sample at different levels of accumulated fluence can be identified using fast Fourier transformation (FFT) of the signal data recorded by the Laser Doppler Vibrometer and saved as .txt files. The table 3.4, in which the analytical results of the first and second modes of vibration of the natural bending frequencies are presented, facilitates the recognition of the experimental bending frequencies recorded by the LDV. The recorded voltage signal has first been converted to velocity signal ( $\text{mm s}^{-1}$ ) using appropriate multiplicative coefficients that account for the resolution of the oscilloscope and the LDV. Since the LDV Sensor Head is  $45^\circ$  oriented with respect to the direction of the vibration, parallel to the direction of the ion beams, the velocity signal was multiplied by the factor  $\sin(45^\circ) = 0.707$ .

Because of the huge damping of the velocity signal, the frequency resolution is so low that quantitative investigations about frequency changes as a function of the accumulated fluence are not feasible. In order to improve the frequency resolution of the fast Fourier transform, the procedure of zero-padding is commonly utilised in frequency analysis of sampled signals: it consists on appending artificial zeros to the signal in order to obtain a denser frequency grid when applying FFT to signal [76]. As shown in the left graphs of the figure 3.15 in the case of the Inconel 718 sample subjected to the first U-ions beam pulse, the time length has been increased by 10 times, from 18 ms to 180 ms, with the result of improving the frequency resolution of the corresponding FFT and allowing

a more precise determination of the first-order bending frequency (graphs of the power spectral density (PSD) on the right-hand panel of figure 3.15). To assess how accurately the peak frequency was computed using FFT, the 3 dB bandwidth technique, which is common in the signal processing field, was utilised [77]. The confidence interval of the peak frequency, represented by the green bands in figure 3.15, is equal to the difference between the upper frequency bound  $f_U$  and the lower frequency bound  $f_L$ : the latter identifies the points where the spectral density is half its maximum value or, in other words, where the PSD decreases by 3 dB<sup>2</sup>. Finally, the velocity signal in the time domain has also been examined to determine the magnitude of damping, an important parameter for carrying out the numerical simulations, which will be treated in the next chapter. The damping ratio  $\zeta$  can be found for any two adjacent peaks by the following formula:

$$\zeta = \frac{1}{\sqrt{1 + \left( \frac{2\pi}{\ln\left(\frac{x_0}{x_1}\right)} \right)^2}} \quad (3.2)$$

where  $x_0$  and  $x_1$  are amplitudes of any two successive peaks.

The figures 3.16-3.20 represent the time-dependent velocity signal (with a zoom-in of the first 2 ms of signal) recorded by LDV and the corresponding FFT spectra at the rear side of each disc-shaped sample tested during the GSI experiment under U-ion beams irradiation. The values of the amplitude of the plots related to FFT spectra of the signal were normalised: the position of the first-order bending frequency peaks and their eventual change in frequency with increasing the fluence accumulated are thus easier to be observed.

The figure 3.16 reports the dynamic effects of irradiation on the 213  $\mu\text{m}$ -thick disc-shaped sample of steel T91 (EN 1.4903 grade), with a diameter of 2 cm and a beam spot of 6 mm-diameter. The damping is relatively high ( $\zeta = 0.0229$ ), with the amplitude that decreases from the initial velocity of 200 mm s<sup>-1</sup> to 20 mm s<sup>-1</sup> in less than 20 milliseconds in the case of the first beam-induced impact on the target sample. In the quasi-pristine sample, a harmonic oscillation with frequency 4.441 kHz is generated: this frequency can be ascribed to first-order bending frequency and its value is intermediate between the values of frequency analytically found for simply supported (3.234 kHz) and free plate (4.778 kHz) boundary conditions (see table 3.4). Continuing with the irradiation, the peak frequency increases up to 4.517 kHz at the maximum applied fluence of  $2 \times 10^{13}$  U-ions cm<sup>-2</sup>. The 100 Hz increase in frequency could be caused by both the change in boundary conditions (due to the progressive rise in temperature of the sample) and by the hardening

---

<sup>2</sup>It is recalled that in physics the Decibel is defined as  $20 \log_{10}(P_1/P_2)$ , where  $P_1$  and  $P_2$  are two generic powers. If  $P_L = P_U = 0.5 P_{max}$ , then  $20 \log_{10}(0.5) = -3\text{dB}$

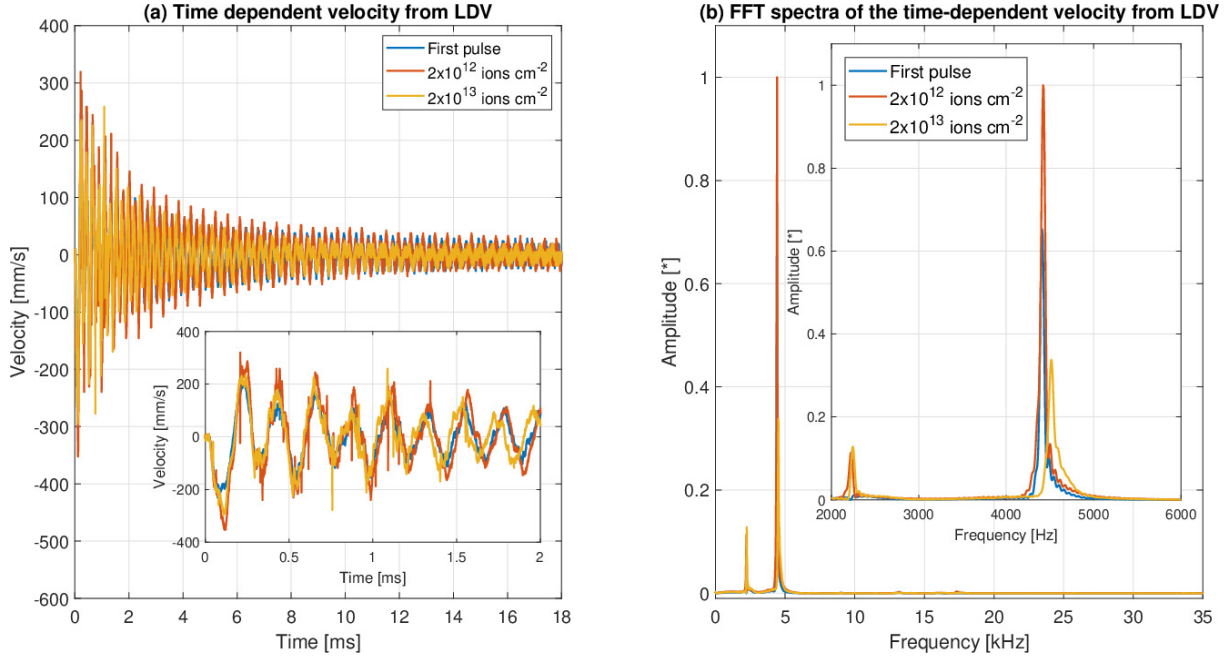


**Figure 3.16:** Steel T91 sample — (a) Time-dependent velocity signal measured by LDV and (b) corresponding FFT spectra at the rear side ( $x=0.213$  mm,  $y=z=0$ ) of a disc-shaped sample for the irradiation with 1.14 GeV Uranium ions at different levels of fluence.

of the material (and the corresponding increase of Young's modulus in the irradiated area). Post-mortem investigations (such as microindentation) and thermomechanical simulations will be performed to analyse and verify the cause of this variation frequency. The nearly imperceptible peak observed at  $\sim 18$  kHz is probably related to the second mode of vibration, despite having frequency values slightly higher than the values analytically calculated (19.467 kHz and 20.392 kHz for simply supported and free plate, respectively).

The peak observable at around 2000 Hz merits further examination. To this end, a focus on the first 2 ms (from 0 to 2 ms) and on the last 2 ms (from 16 ms to 18 ms) of the velocity signal recorded by the LDV was done for the signals related to the first and last pulse on the Steel T91 sample. The plots of the velocity signals in these limited time intervals are displayed in the zoom-ins of figure 3.17. The Fast Fourier Transforms of these specific parts of the signal were performed, and their plots are presented on the right side of the figure 3.17. In the first 2 ms, the frequency spectra are similar to the ones already discussed for the entire signal, with the maximum peak (relative to the natural vibration frequency in the intermediate condition between simply-supported and free disc) that slightly shifts forward, predominantly due the thermal effects on the boundary. On the contrary, a different behaviour can be observed for the last 2 ms: while the frequency spectra for the first-pulse signal is essentially identical to the one found for the first 2 ms, the frequency spectra associated with the last pulse (fully-accumulated fluence) show the maximum at a frequency that is about half that of natural vibration.



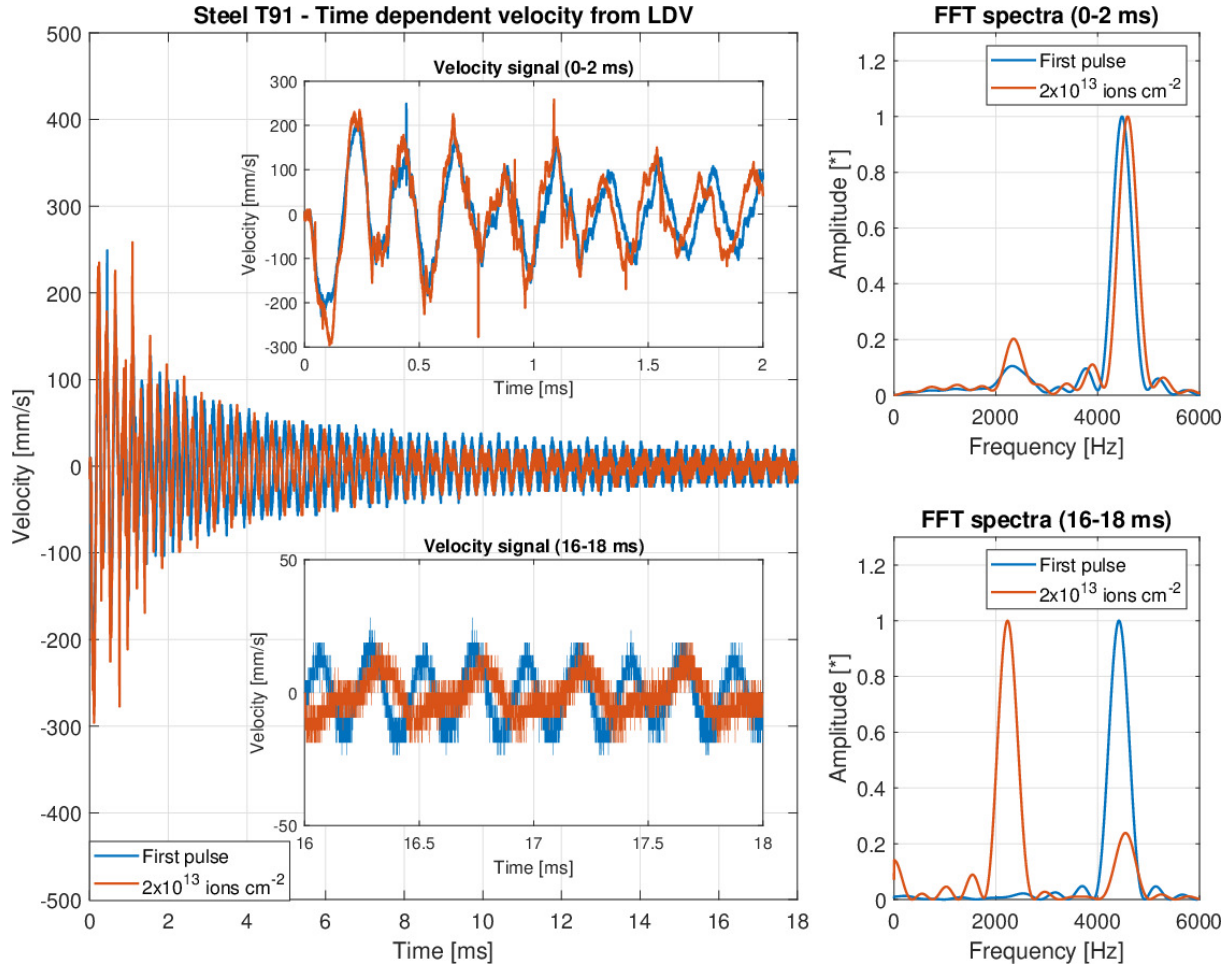


**Figure 3.17:** Steel T91 sample — On the right, the time-dependent velocity signal measured by the LDV, with two zoom-ins related to the first 2 ms (0-2 ms) and last 2 ms (16-18 ms) and, on the right, the FFT spectra corresponding to the two parts of the signal of which the magnification was carried out.

A peak at a frequency referable to the natural frequency of vibration is still visible, but it is significantly lower than the one at around 2200 Hz. Such a behaviour could be ascribed to the change of the boundary conditions that the sample experiences while the velocity signal is dampened: with the decrease of the amplitude of the velocity signal, the peak frequency of the T91 sample progressively shifts from the free edge towards the simply-supported edge condition as a result of an enhanced adherence to the sample holder. This peculiar aspect occurred only in the case of the fully-irradiated sample and it is due to the fact that beam-induced heating of the whole sample enhanced both axial and radial clamping effects between the outer radius of the sample and the ring-shaped sample holder.

The figure 3.18 shows velocity signals and corresponding FFTs spectra measured by LDV at the rear side of 219  $\mu\text{m}$  thick Inconel 718 disc-shaped sample. The amplitude of the velocity signal as well as the damping ( $\zeta = 0.0282$ ) is quite comparable to those

observed for the steel sample since their values of Young's modulus and coefficient of thermal expansion do not differ significantly. The only peak in the frequency domain (at 3.550 kHz) is undoubtedly related to the first-order bending frequency and the second-order bending frequency expected beyond 19 kHz is not observable. Also in this case, the first mode of vibration detected by the LDV lies between the analytical values for simply supported (3.175 kHz) and free (4.695 kHz) plate boundary conditions. Initially, with increasing U-ion fluence, the amplitude of the velocity signal increases and the frequency  $f_{b0}$  gradually decreases to  $\sim 3.3$  kHz at fluence  $2 \times 10^{12}$  U-ions  $\text{cm}^{-2}$ . Then, from this point on, the frequency starts to almost linearly increase until it settles at 3.656 kHz at the maximum accumulated fluence. The way in which the frequency changes as the accumulated fluence increases is not immediately explainable: the frequency reduction can probably be ascribed to the change of boundary conditions of the sample, while its rise is probably due to the hardening and the resulting increase of the Young's modulus in the irradiated volume as well as to the effect of the temperature increases on the edge clamping conditions.

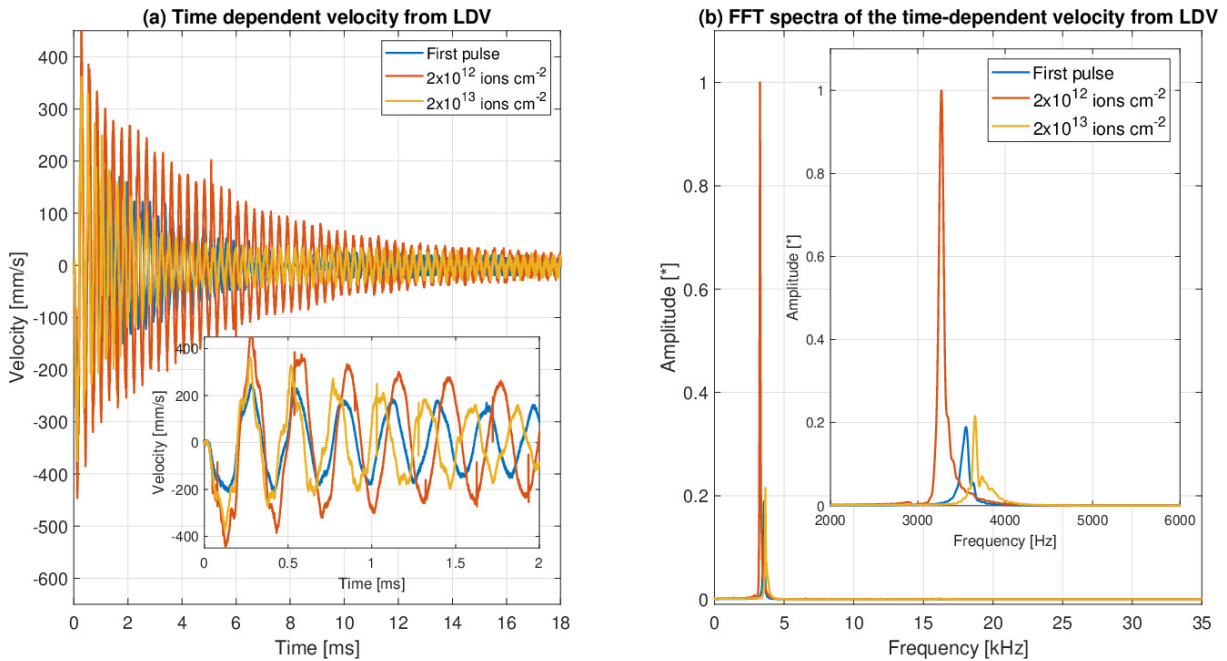


**Figure 3.18:** Inconel 718 sample — (a) Time-dependent velocity signal measured by LDV and (b) corresponding FFT spectra at the rear side ( $x=0.219$  mm,  $y=z=0$ ) of a disc-shaped sample for the irradiation with 1.14 GeV Uranium ions at different levels of fluence.

The velocity signals and associated FFT spectra obtained by LDV at the rear side of a  $405 \mu\text{m}$  thick 6082 T6 Aluminium alloy disc-shaped sample are illustrated in the figure 3.19. The signal attenuation is lower than that of the steel and Inconel samples, with a damping ratio of 0.0136, while the amplitude of the signal is significantly lower, with maximum values below the  $200 \text{ mm s}^{-1}$ . In the quasi-pristine sample, a harmonic

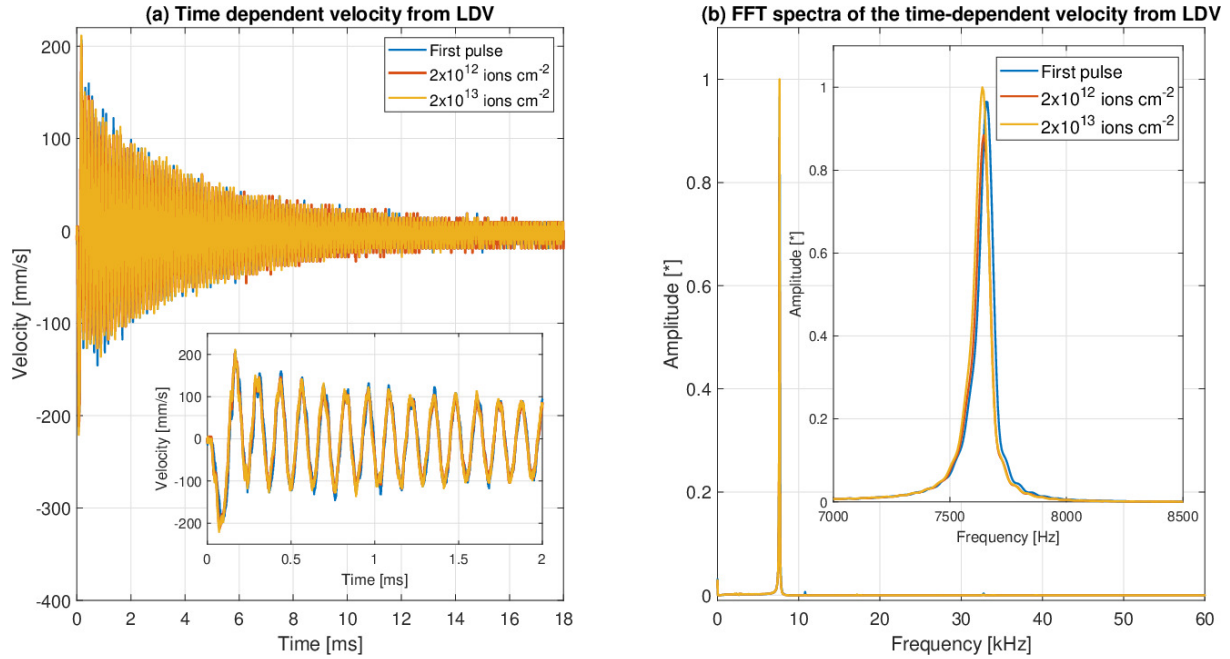


**Figure 3.19:** Aluminium 6082 T6 — (a) Time-dependent velocity signal measured by LDV and (b) corresponding FFT spectra at the rear side ( $x=0.405$  mm,  $y=z=0$ ) of a disc-shaped sample for the irradiation with 1.14 GeV Uranium ions at different levels of fluence.

oscillation with frequency 7.656 kHz, in the middle between the analytical values of 6.174 kHz for simply supported plate and 9.108 kHz for free plate condition, and therefore ascribable to the first-order bending frequency, was measured by means of FFTs. The peak corresponding to the second-order bending frequency was not observed. With increasing U-ion fluence, the frequency slightly fluctuates around the value of 7.6 kHz, but practically remains almost the same. This suggests that material properties, such as the Young's modulus, did not change within the beam region and that the target sample was not subjected to severe damage or fractures.

Results of the 4.8 MeV/u U-ion pulse irradiation of a 0.22 mm thick Titanium Grade 23 disc-shaped sample with a diameter of 2 cm and a circular beam spot with a diameter of 0.6 mm are shown in the figure 3.20. With increasing U-ion fluence, the amplitude of the velocity signal is reduced, primarily because the sample was subjected to a lower ion flux after the replacement of the Uranium cathode at fluence  $9 \cdot 10^{12}$  ions  $\text{cm}^{-2}$ . The signal attenuation is similar to that for the Inconel sample of comparable thickness, with a damping ratio of 0.0280 for the titanium alloy sample. Unlike what was previously seen for the signals of the other materials, the graph of the FFTs spectra presents several peaks at different frequencies. The first-order bending frequency rises considerably with increasing U-ion fluence, from 3.39 kHz for the quasi-pristine sample at the first impact to 4.217 kHz at the maximum applied fluence of  $2 \times 10^{13}$  ions  $\text{cm}^{-2}$ . The comparison with the values analytically found reveals that the boundary condition of free disc is

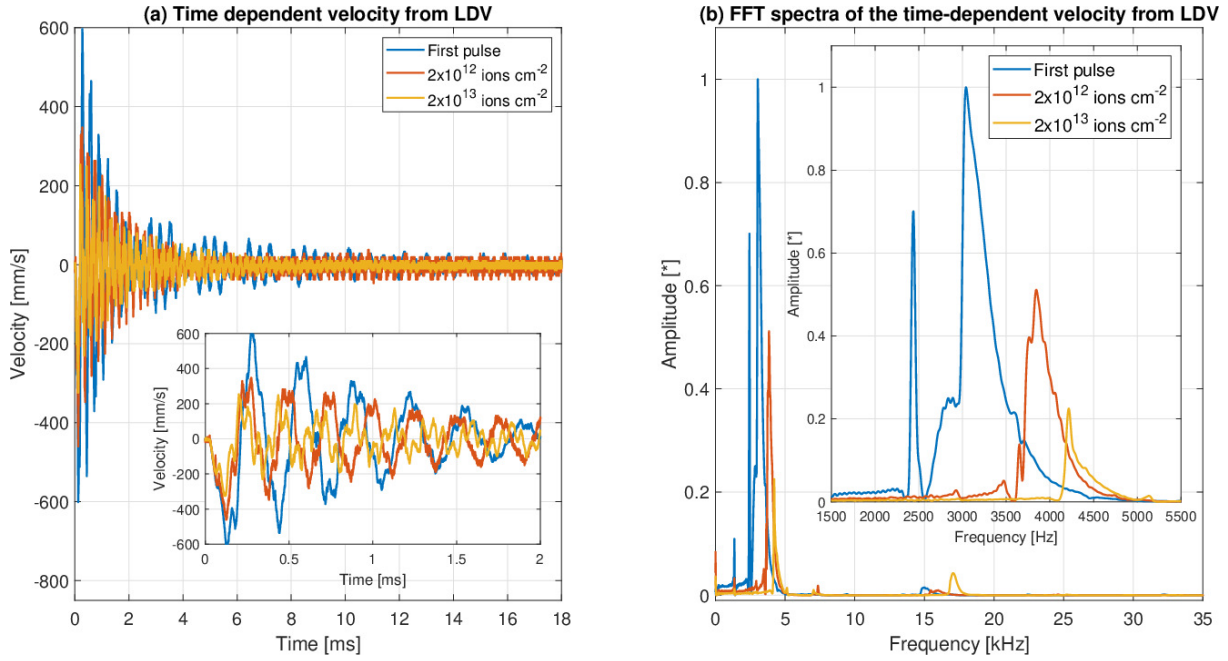


**Figure 3.20:** Titanium Grade 23 sample — (a) Time-dependent velocity signal measured by LDV and (b) corresponding FFT spectra at the rear side ( $x=0.220$  mm,  $y=z=0$ ) of a disc-shaped sample for the irradiation with 1.14 GeV Uranium ions at different levels of fluence.

absolutely appropriate for describing the natural vibration frequency of the titanium alloy sample (3.361 kHz from analytical calculations). The monotonous and growing trend of the frequency is arguably not only attributable to the microscopic defect accumulation induced by U-ions radiation, with consequent material hardening and increase of the Young's modulus within the beam spot, but also to the shift of frequency from the simply supported to the free plate condition as the temperature of the sample increases and the expansion of the material reinforces the tightening condition at the edges. A constant peak at 1.36 kHz was detected at all fluence levels, most likely due to the sample's imperfect axial symmetry with respect to the beam. Another peak, with an unknown bending mode and with growing frequency with increasing fluence, precedes the peak corresponding to first-order bending frequency by a few hundred Hz. The peaks between 15 and 18 kHz are not representative of the second mode of vibration, since the corresponding frequency is expected to emerge only beyond the 20 kHz.

The figure 3.21 graphically summarises how the first-order bending frequency, measured by LDV for the four samples subjected to irradiation during the experiment, changed as a function of accumulated U-ion fluence. The confidence intervals of the first-order bending frequencies measured using FFTs were represented by vertical error bars. The lower and upper values of these bars were calculated using the 3 dB bandwidth technique previously described. The table 3.5 contains some of these frequency values for four different levels of accumulated fluence.

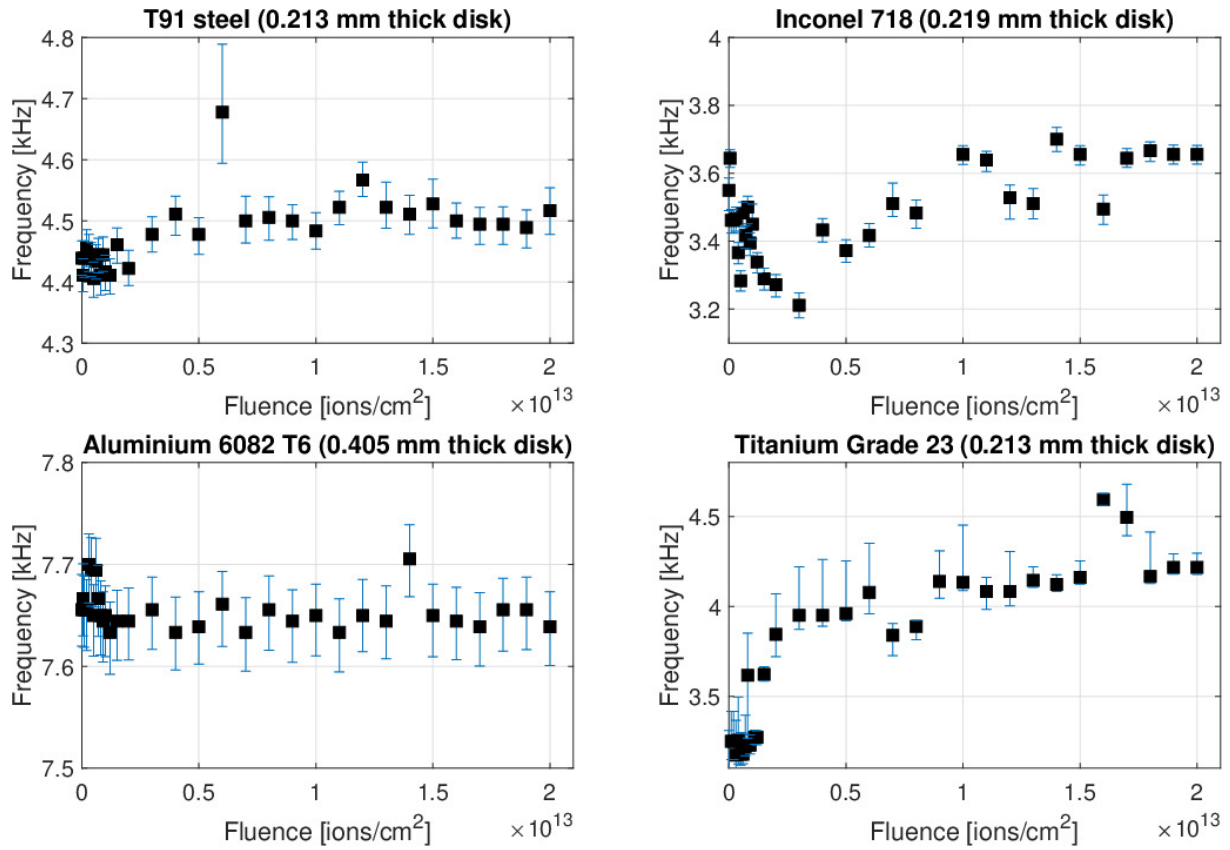


**Figure 3.21:** Measured bending frequency of the four disc-shaped samples with diameter 2 cm as a function of accumulated 4.8 MeV/u Uranium ion fluence.

**Table 3.5:** Bending frequency of the four material samples at certain levels of fluence.

Material sample	Measured bending frequency [kHz]			
	at fluence [U-ions cm <sup>-2</sup> ]			
	First pulse	2x10 <sup>11</sup>	2x10 <sup>12</sup>	2x10 <sup>13</sup>
ASTM A213 T91 Steel	4.411	4.456	4.478	4.517
Inconel 718	3.550	3.461	3.272	3.656
EN AW 6082 T6 (Aluminium alloy)	7.656	7.656	7.644	7.639
Titanium Grade 5 ELI (Grade 23)	3.039	3.250	3.844	4.217

### 3.5 Description and results of post irradiation examinations (PIEs)

The investigations carried out to determine material properties modified by U-ion irradiation once samples were removed from the M3-beamline are summarised in this section. The figure 3.22 illustrates the pictures of the two sample holders before and after the SW-U-2022 irradiation experiment.



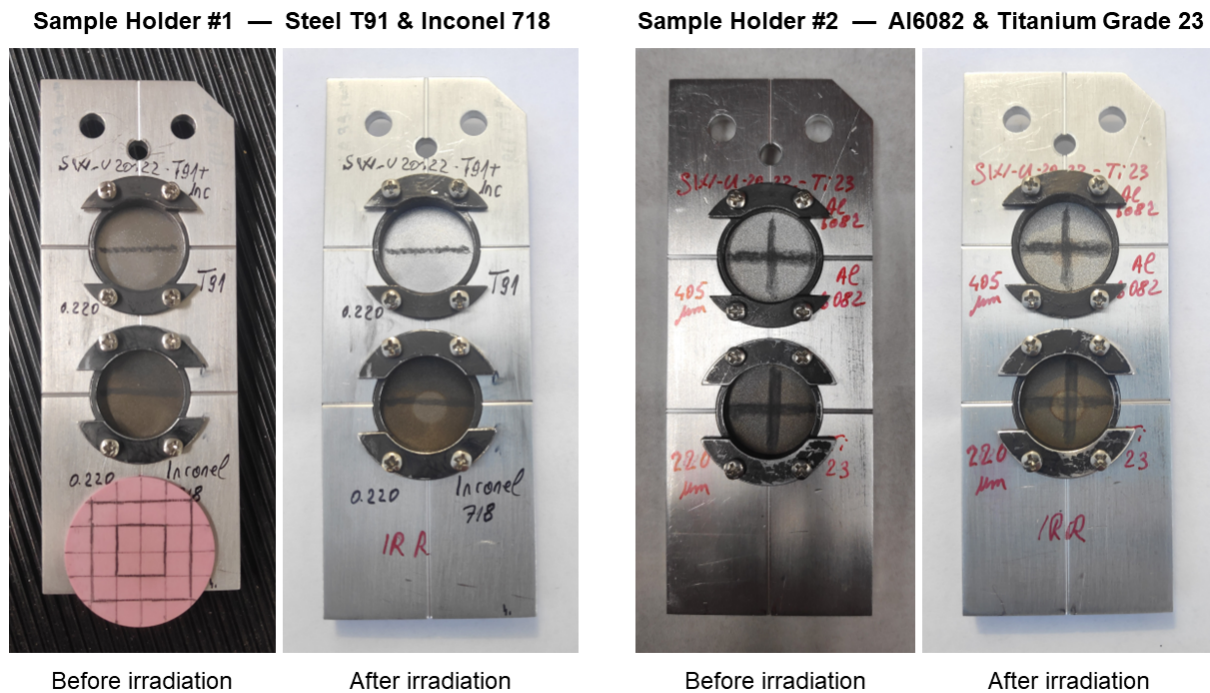


**Figure 3.22:** Pictures of the four material samples in two sample holders before and after irradiation inside the Spectroscopy chamber of GSI Darmstadt M3-beamline.

Two post-irradiation examination techniques are employed: the microindentation, which enables the estimation of the material's hardness and Young's modulus, and the Scanning Electron Microscopy (SEM), whose images contain information about the surface topography and the microscopical composition of the sample.

### 3.5.1 Microindentation

The microindentation is a non-destructive technique used in mechanical engineering to probe the mechanical properties of materials on the submicron scale. In a traditional indentation test, a hard tip (such as diamond and hardened steel) whose mechanical properties are known is pressed into a sample whose properties are unknown. As the indenter tip penetrates further into the specimen, the load imposed on it increases until it reaches a user-defined value. The load may now either be maintained constant for a while or eliminated. By comparing the ratio between the maximum load applied and the residual indentation area, which can be measured using light microscopy, the hardness of the sample can be assessed. For small sample volumes, this technique is limited: the indents resulting from the penetration of the material could not be visible and a detectable trace of the incision may require thicknesses larger than those of the specimen itself.

The instrumented indentation techniques (including microindentation and nanoindentation), developed in the last 30 years and nowadays widely adopted, allow to determine

mechanical properties directly from indentation load and displacements measurements without the necessity to produce a picture of the hardness impression. The high-resolution testing equipment provides the opportunity to collect and analyse with extreme accuracy the data obtained from complete cycles of loading and unloading and, finally, to measure material properties at the nanometre and micrometre scales, such as the hardness ( $H$ ) and the Young's modulus ( $E$ ).

### Experimental setup

The microindentation test took place in a laboratory of the Materials Research Department at GSI on the 25<sup>th</sup> and 26<sup>th</sup> of May under the supervision of the PhD student Philipp Bolz.

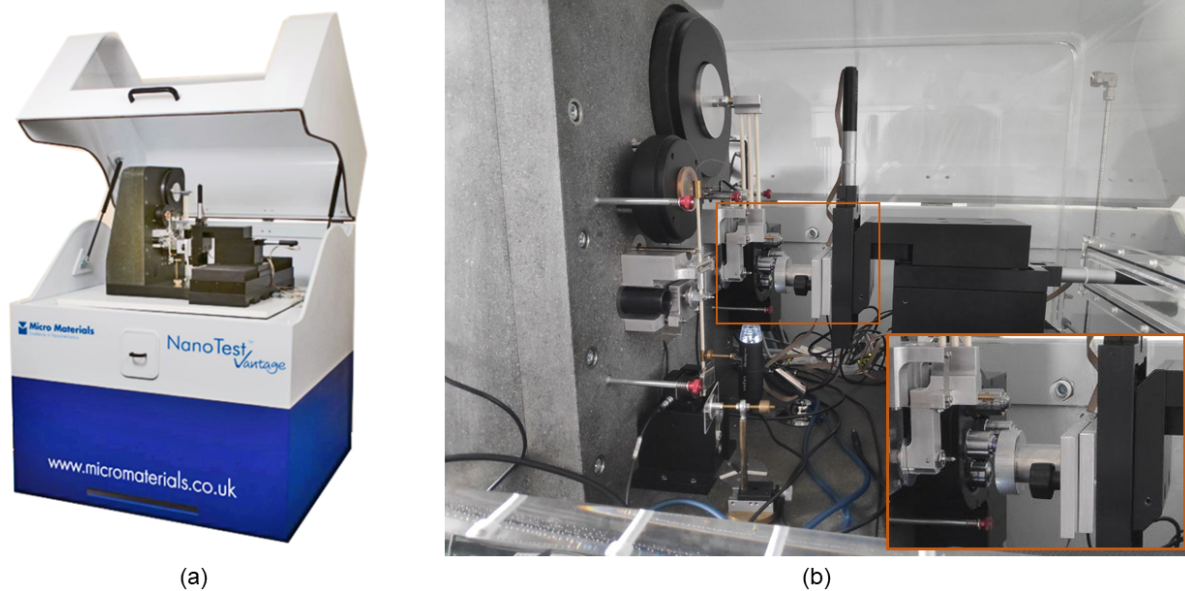


**Figure 3.23:** (a) NanoTest Vantage produced by Micro Materials. (b) Picture of the internal part, where the pendulum, the permanent magnet and other parts of the equipment are visible. On the bottom right (orange square), a zoom-in of the sample stub, the indenter tip and the integrated optical microscope.

For this test, a NanoTest Vantage produced by Micro Materials was employed, as shown in the figure 3.23. Behind the functioning of the NanoTest system, there is a pendulum, whose upper end is connected to a coil [78]. When a current flows through the coil, the coil is attracted toward a permanent magnet, which pushes the indenter tip (mounted at the centre of the pendulum) to move toward the sample. Parallel plate capacitors are attached behind the indenter tip and the indenter holder in order to measure accurately the displacement of the indenter according to the capacity change. Moreover, the aluminium support (where the investigated samples were glued) can be moved and

easily manipulated by using three DC motors driving micrometre stages in all directions. An integrated optical microscope placed close to the indenter permits inspecting the sample and determining precisely the desired location of the indentation. It was decided to mount a Berkovich tip, a diamond tip of three-sided pyramidal shape, with a very flat profile and a total included angle of  $142.3^\circ$ . Its area-to-depth ratio is identical to that of a Vickers indenter, but its three-sided geometry enables more accurate measurements at shallow depths.

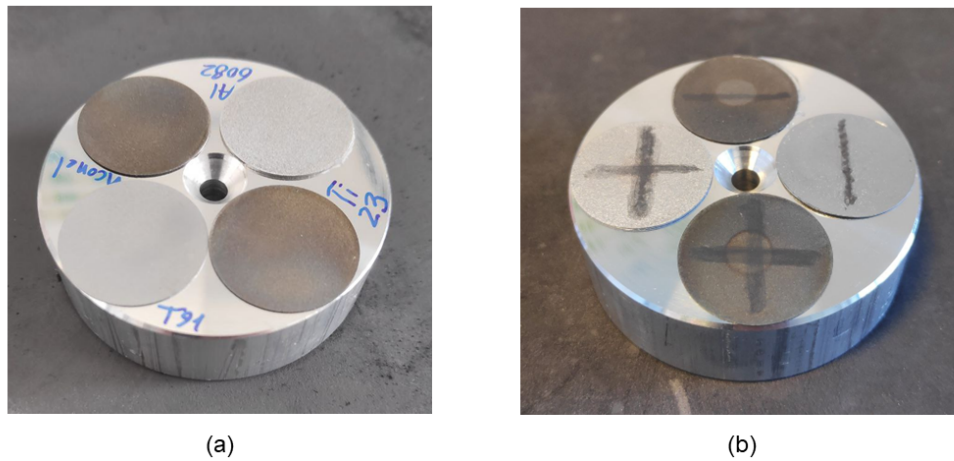


**Figure 3.24:** Aluminium supports for microindentation test with (a) pristine and (b) fully-irradiated samples of the four materials investigated.

The samples irradiated during the experiment were extracted from the holders (figure 3.22) and the tiny pieces of adhesive reflective tape were removed from the backside. The four irradiated samples were made to adhere to the aluminium support (with a diameter of 5 cm and thickness of 1.5 cm, in figure 3.24) using cyanoacrylate glue, making sure that the glue layer was as thin as possible to prevent compromising the microindentation test. A second aluminium support with pristine samples was prepared in the same way. These supports were then placed in the sample stub of the NanoTest Vantage and securely fixed by a screw at the centre of the support. For microindentation experiments, a maximum depth of 2000 nm was selected. This depth, equal to one-tenth of the penetration depth of the U-ions in the T91 steel sample, is small enough to minimise the influence of the non-irradiated substrate below the irradiated layer and at the same time to remain in the region of constant electronic energy loss. The main issue with the maximum depth selected is that the measurement is particularly sensitive to the location and orientation of the few penetrable metal grains in such a shallow depth. For each sample, both pristine and irradiated ones, 25 microindentation measurements were performed, in a square 5x5 pattern. The maximum load, the diamond area function, the holding and release times of the indenter on the samples and other factors were adjusted during the calibration stage.



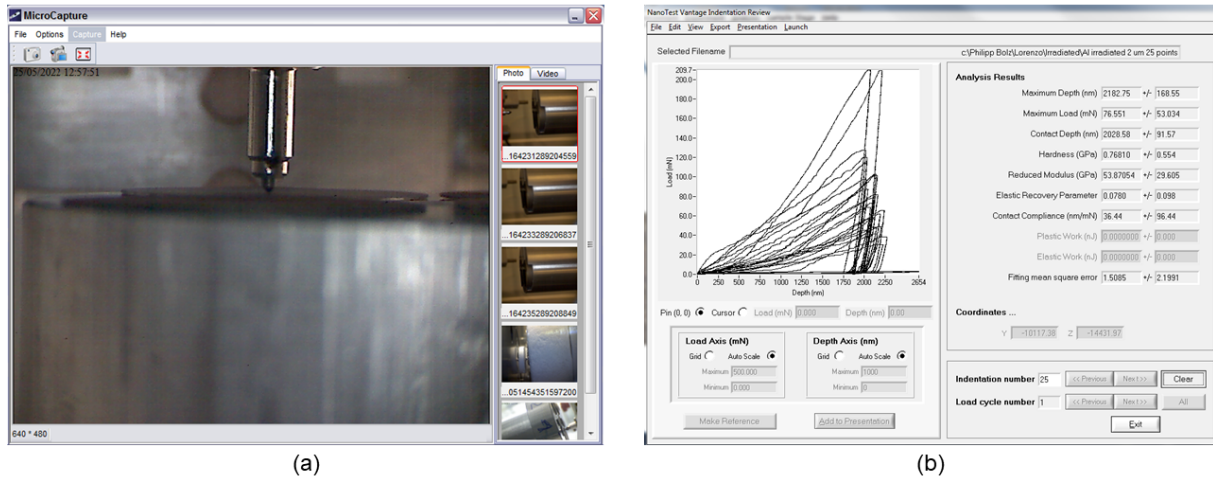


**Figure 3.25:** Captures from the NanoTest software for microindentation. (a) Camera view of the indenter and of the sample, extremely useful to align the indenter to the beam spot of the U-ions irradiated samples. (b) Page of results for the indentation of irradiated Al6082 T6 sample, where the most important data are summarised (contact depth, mean hardness and mean reduced elastic modulus, number of indentation cycles, etc.).

### Measuring method of the elastic modulus

The method developed by W.C. Oliver and G.M. Pharr to measure the hardness and the elastic modulus of a material using the microindentation data obtained from one complete cycle of loading and unloading is described below in its basic concepts [79][80].

In principle, the shape of the entire unloading curve and the total amount of recovered displacement can be precisely related to the Young's modulus and the size of the contact impression for indenters of different shapes.

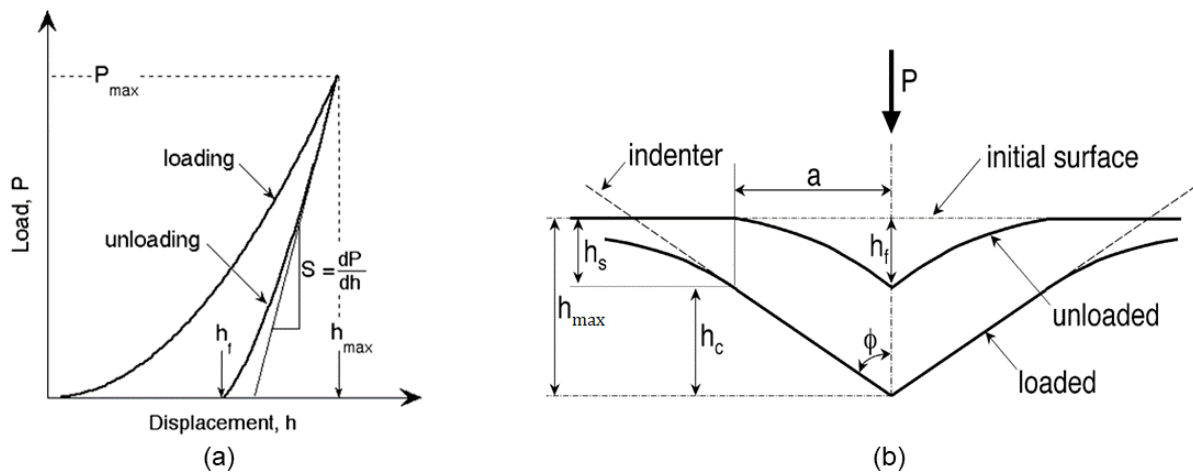


**Figure 3.26:** (a) Schematic illustration of indentation load-displacement data. (b) Schematic illustration of the unloading process [80].

The figure 3.26(a) illustrates a schematic representation of microindentation data,

where  $P$  designates the load and  $h$  the displacement relative to the initial undeformed surface. Four important quantities can be found in the graph:

- the maximum load,  $P_{max}$ ;
- the maximum displacement,  $h_{max}$ ;
- the elastic unloading stiffness, or contact stiffness,  $S = dP/dh$ , defined as the slope of the upper portion of the unloading curve, directly proportional to the reduced Young's modulus;
- the final depth,  $h_f$ , the permanent depth of penetration after the indenter is fully unloaded.

In addition to these quantities, the computation of hardness and elastic modulus requires comprehension of how the contact area varies during the indentation test. The most complex problem consists in modelling the indentation contact in a way that includes both plastic and elastic deformation phenomena. For the majority of the materials investigated, the deformation during loading is assumed to have both elastic and plastic nature, while only the elastic displacement is assumed to be recovered during unloading. If the contact area remained constant as the indenter is withdrawn, the resulting unloading curve would be linear, with a slope equal to the elastic unloading stiffness  $S$ . In contrast, as also shown in figure 3.26(a), the unloading curve is indubitably curved and can be approximated by the power law relation:

$$P = \alpha(h - h_f)^m \quad (3.3)$$

where  $\alpha$  and  $m$  are power law fitting constants, depending on the shape of the indenter and the type of tested material. Since the contact area changes as the indenter is withdrawn, the quantity  $A$ , called "area function" or indenter shape function, is introduced to describe the cross-sectional area of the indenter tip as a function of the depth:

$$A = F(h_c) \quad (3.4)$$

For a diamond tip of Berkovich geometry, the indenter area shape function approximated to the first order can be written as:

$$A \cong 24.56 h_c^2 \quad (3.5)$$

where  $h_c$  is the elastic contact between the indenter and the specimen.

The physical meaning of this quantity can be explained by the schematic illustration of the unloading process in figure 3.26(b). It is noted that:

$$h_c = h_{max} - h_s \quad (3.6)$$

where  $h_{max}$  is the maximum depth, experimentally measurable, and  $h_s$  is the deflection of the surface at the contact perimeter. This quantity depends on the shape of the indenter (angle  $\phi$ ) and on the way in which the contact periphery of the indenter sinks in the material. In the hypothesis that the indentation model is fundamentally elastic and that the accumulation of material in the contact periphery is negligible, the amount of sink-in  $h_{max}$  can be expressed by the following relation:

$$h_c = \epsilon \frac{P_{max}}{S} \quad (3.7)$$

where  $\epsilon$  is a constant that depends on the geometry of the indenter and is equal to 0.75 for a Berkovich indenter. As a first approximation, the indenter shape function can be written as:

$$A(h_c) \cong 24.56 \left( h_{max} - \epsilon \frac{P_{max}}{S} \right)^2 \quad (3.8)$$

Once the projected area is determined, the hardness  $H$  is calculated from:

$$H = \frac{P_{max}}{A(h_c)} \quad (3.9)$$

The reduced elastic modulus  $E_{red}$  can finally be estimated by correlating it with the area function  $A(h_c)$  and the elastic unloading stiffness  $S$  using the following relation:

$$E_{red} = \frac{S}{2\beta} \sqrt{\frac{\pi}{A(h_c)}} \quad (3.10)$$

where the factor  $\beta$  is a correcting factor for non-circular geometries, equal to 1.034 for the triangular pyramid shape of the Berkovich indenter. The evaluation of the Young's modulus of the tested material requires a final step: since the microindentation experiment causes the deformation of both the studied material and the indenter tip, the contribution of the tip must be thereby excluded. Considering that the indenter properties (Young's modulus and Poisson's ratio) are known ( $E_{ind} = 1197$  GPa and  $\nu_{ind} = 0.07$  for the diamond tip), the Young's modulus of the investigated material can be determined:

$$E = \frac{1 - \nu^2}{\frac{1}{E_{red}} - \frac{1 - \nu_{ind}^2}{E_{ind}}} \quad (3.11)$$

## Results

Results of microindentation experiments conducted on pristine and irradiated samples are provided in this section. At the end of each microindentation test, two series of data are released from the NanoTest software: a text file with data on load and displacement of each curve measured and a text file with the elastic modulus, the hardness and other parameters directly computed by the software. In several cases, the E values calculated by

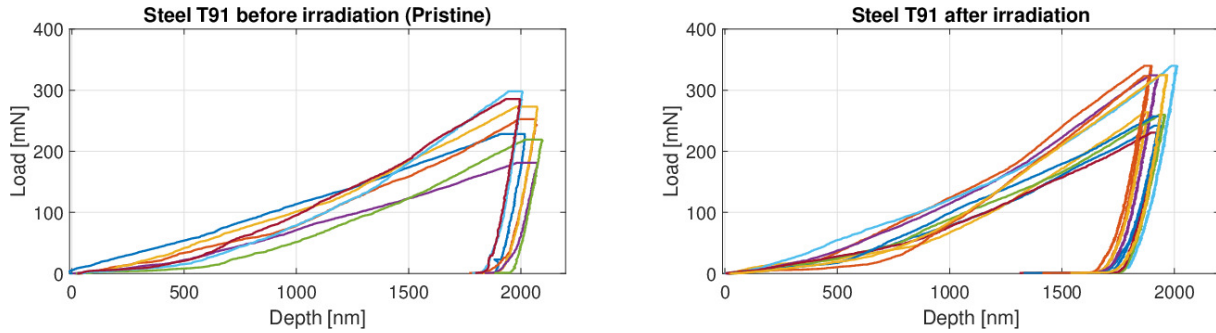


**Figure 3.27:** Selected Load-Displacement curves from microindentation analysis of pristine and irradiated (at the maximum applied fluence of  $2 \cdot 10^{13}$  ions  $\text{cm}^{-2}$ ) T91 Steel samples.

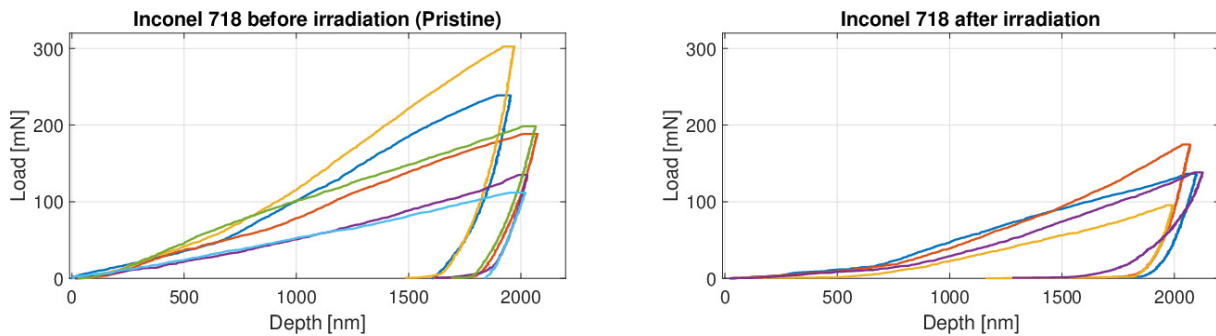


**Figure 3.28:** Selected Load-Displacement curves from microindentation analysis of pristine and irradiated (at the maximum applied fluence of  $2 \cdot 10^{13}$  ions  $\text{cm}^{-2}$ ) Inconel 718 samples.

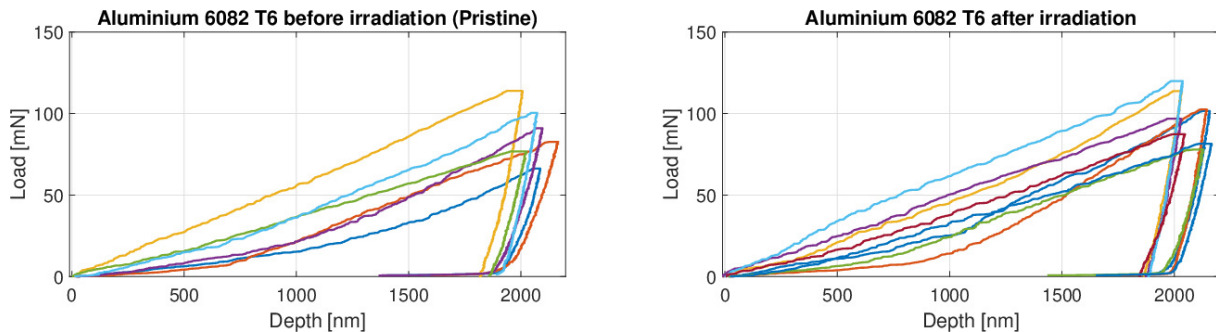


**Figure 3.29:** Selected Load-Displacement curves from microindentation analysis of pristine and irradiated (at the maximum applied fluence of  $2 \cdot 10^{13}$  ions  $\text{cm}^{-2}$ ) Aluminium 6082 T6 samples.

the software were very inaccurate and with a pretty wide margin of error. It was decided to manually calculate the Young's modulus using the Oliver and Pharr method exclusively on those microindentation curves that had to a certain extent physical significance; these selected curves are shown in the following figures 3.27-3.30. As can be observed from the graphs, the number of curves considered for each material is not equal: for instance, several curves have been taken into account for the irradiated T91 steel, whereas only four curves have been taken into consideration for the irradiated Inconel 718 sample material. This translates into a more reliable measurement of the Young's modulus (average Young's

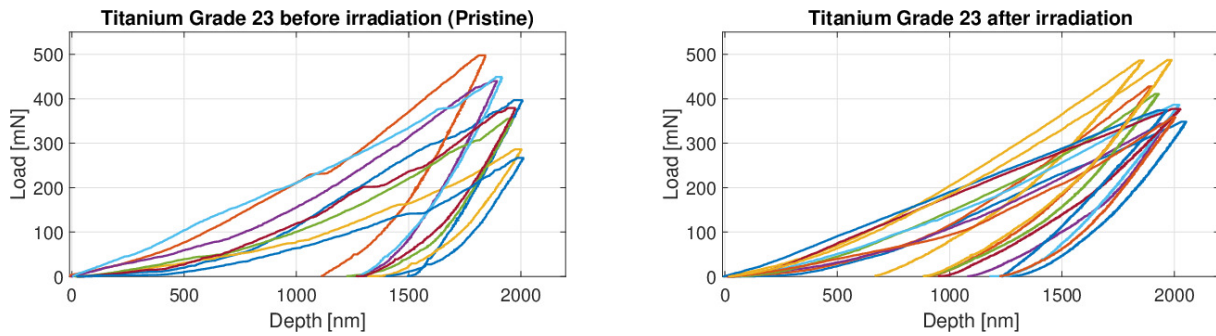


**Figure 3.30:** Selected Load-Displacement curves from microindentation analysis of pristine and irradiated (at the maximum applied fluence of  $2 \cdot 10^{13}$  ions  $\text{cm}^{-2}$ ) Titanium Grade 23 samples.

modulus value between the curves available) for the steel rather than for Inconel, for which it is hypothesised that the measurement was compromised by a thicker glue layer between the sample and the aluminium support.

Material sample	Young's modulus [GPa]		
	Data sheets	Microindentation	
	Pristine	Pristine	After irradiation
ASTM A213 T91 Steel	207.00	199.39	222.37
Inconel 718	203.00	193.79	206.74
EN AW 6082 T6 (Aluminium alloy)	70.00	77.47	67.73
Titanium Grade 5 ELI (Grade 23)	113.80	114.69	168.66

**Table 3.6:** Results of the microindentation analysis for pristine and irradiated samples in terms of Young's modulus.

In the table 3.6 the results of the microindentation tests in terms of Young's modulus for all the samples investigated are reported. It is noted that the values of  $E$  found for the pristine samples are quite similar to ones from data sheets. After the U-ions beam irradiation, the elastic modulus of aluminium 6082 T6 and steel T91 appear to remain approximately constant, while the highest growth is observed for the Titanium Grade 23, where the Young's modulus grows by more than 50 GPa.

### 3.5.2 Scanning Electron Microscopy

The microstructure of the material can be analysed using electron microscopy, which guarantees high resolution, high magnification and high-speed acquisition (30-60 s).

An electron microscope is composed of a column, which consists of the generator of electron beams and the specimen chamber. Inside the structure, a vacuum is obtained

by a pump and the so-called primary electrons, released by a V shape tungsten wire (thermionic gun) or by a field emission gun, travel through the column thanks to the potential difference between the thermionic cathode at the top, heated up by electric current and the below-installed anode, a metallic disc with a borehole.

An acceleration voltage is created to speed up the beam: its value differs between Transmission Electron Microscopy (50-100 kV) and Scanning Transmission Microscopy (5-30 kV). Additional components, such as electromagnetic lenses, electromagnetic deflectors and a raster scan generator remotely controlled, focus the beam on the sample.

On the micro and nano scales for a wide range of materials, SEMs are a powerful tool in determining the causes of failure by characterising the topography of the fracture surface and radiation-induced microscopic damages. Thanks to high resolution, great depth of field, and the ability to obtain chemical information via analysis of the X-rays generated by the electron, it is possible to identify in an SEM image defects and mechanical behaviours. Fractures can also be classified into microvoid coalescence, intergranular and transgranular fracture and fatigue striations [81].

SEM basic structure has big similarities with TEM and other electron microscopy techniques but differs radically in the final image obtained, due to a different system of detection and a different resolution power of 10 nm, compared to the TEM power of a maximum of 0.3-0.5 nm. SEM microscopy enables a magnification from 10x to  $3 \times 10^6$  x and delivers pictures of the surface morphology of the sample.

In SEM, the beam of primary electrons is used to scan the surface of the sample moving forward, behind and sideways on the specimen. At the point of incidence, primary electrons knock out electrons of the sample material. These knocked-out electrons are called secondary electrons. The ones attracted by a positively-biased grid placed in front of a SE detector (secondary electrons detector) are amplified and proportionally converted in photons by a scintillator to be immediately later displayed on the correspondent section of the computer monitor. Black dots represent scarce deflections on the surface, and bright dots a positive detection on the surface. Dots recreate a series of stacked rows until a complete two-dimensional pattern is formed. The SEM is also capable of determining the chemical compositions of specific points of the sample, crystalline structure, and crystal orientations using back-scattered electrons (BSE). Whereas secondary electrons are more valuable for showing morphology and topography on samples, back-scattered electrons are more suitable for illustrating contrasts in chemical composition in multiphase samples (the higher the atomic number, the brighter the signal) [82].

The SEM microscopic analysis was carried out at the laboratory of the CERN Materials, Metrology and Non-Destructive Testing Section. The Sigma-500 SEM system from ZEISS (figure 3.31) was utilised for the microscopic investigation of the irradiated sam-



ples (figure 3.32). The figures 3.33-3.44 below report the images obtained from the SEM microscopy analysis.

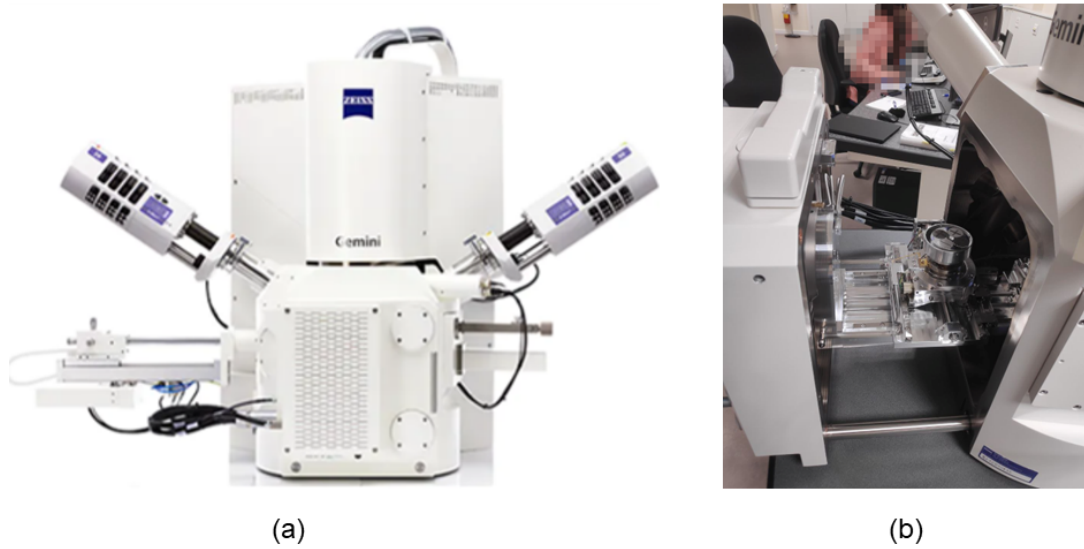


**Figure 3.31:** Scanning Electron Microscope (SEM) employed in the MM section at CERN (a). Sample holder with the irradiated specimens inserted in the Sigma-500 SEM system (b).

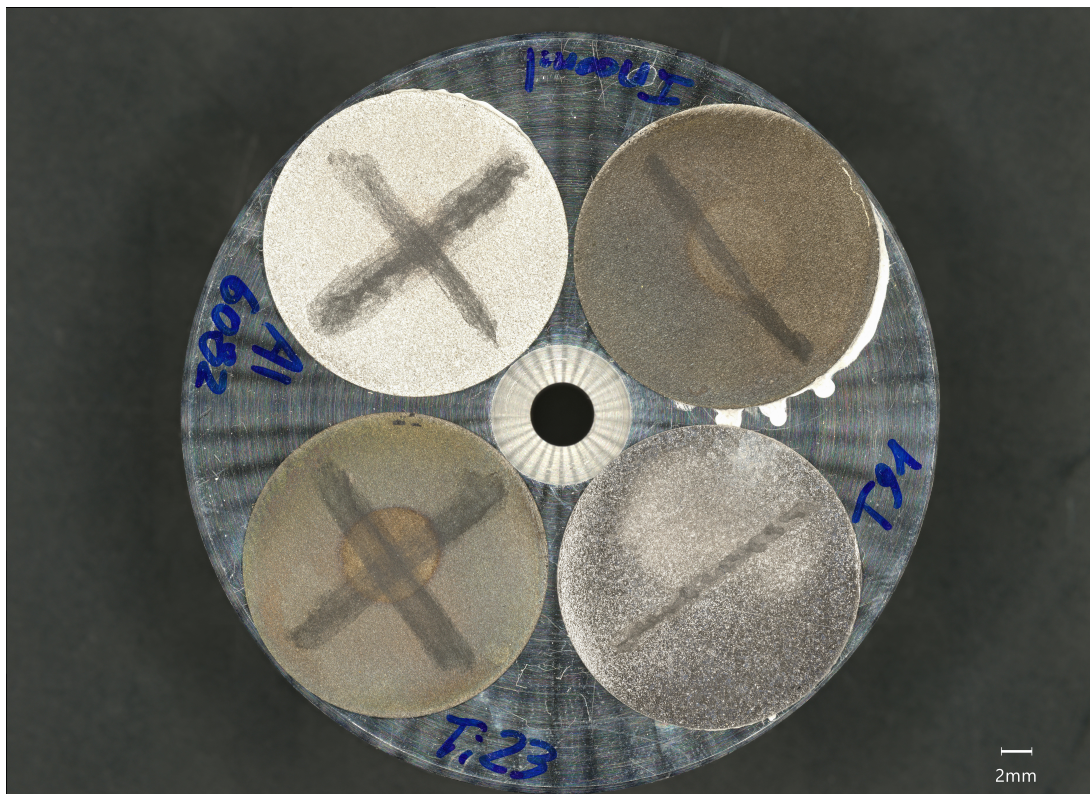


**Figure 3.32:** High quality picture of the sample holder with the irradiated specimens.



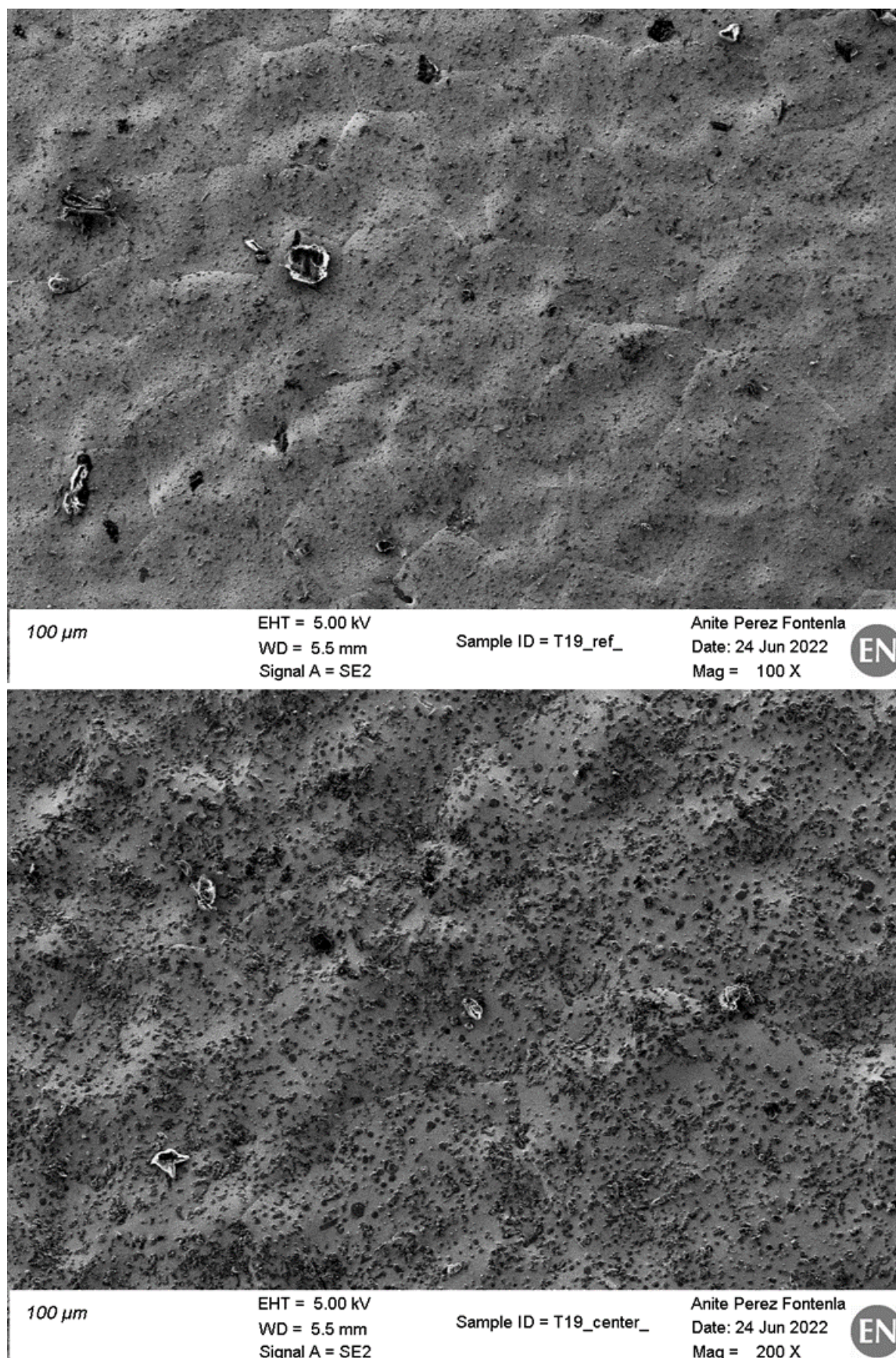


**Figure 3.33:** SEM images of Steel T91 sample of the reference material region (top) and the central irradiated beam spot (bottom) with a resolution scale of 100  $\mu\text{m}$ .



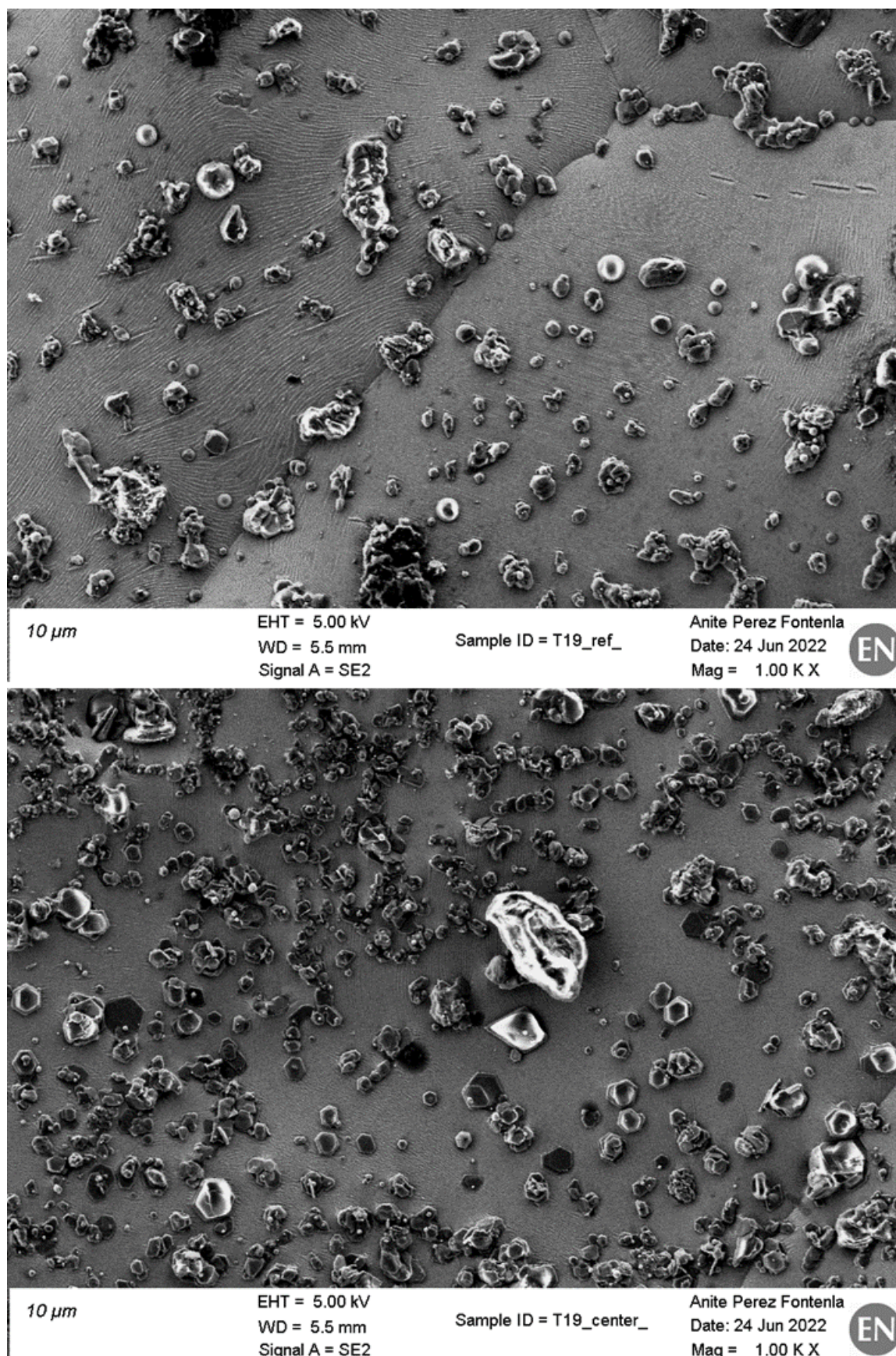


**Figure 3.34:** SEM images of Steel T91 sample of the reference material region (top) and the central irradiated beam spot (bottom) with a resolution scale of 10  $\mu$ m.

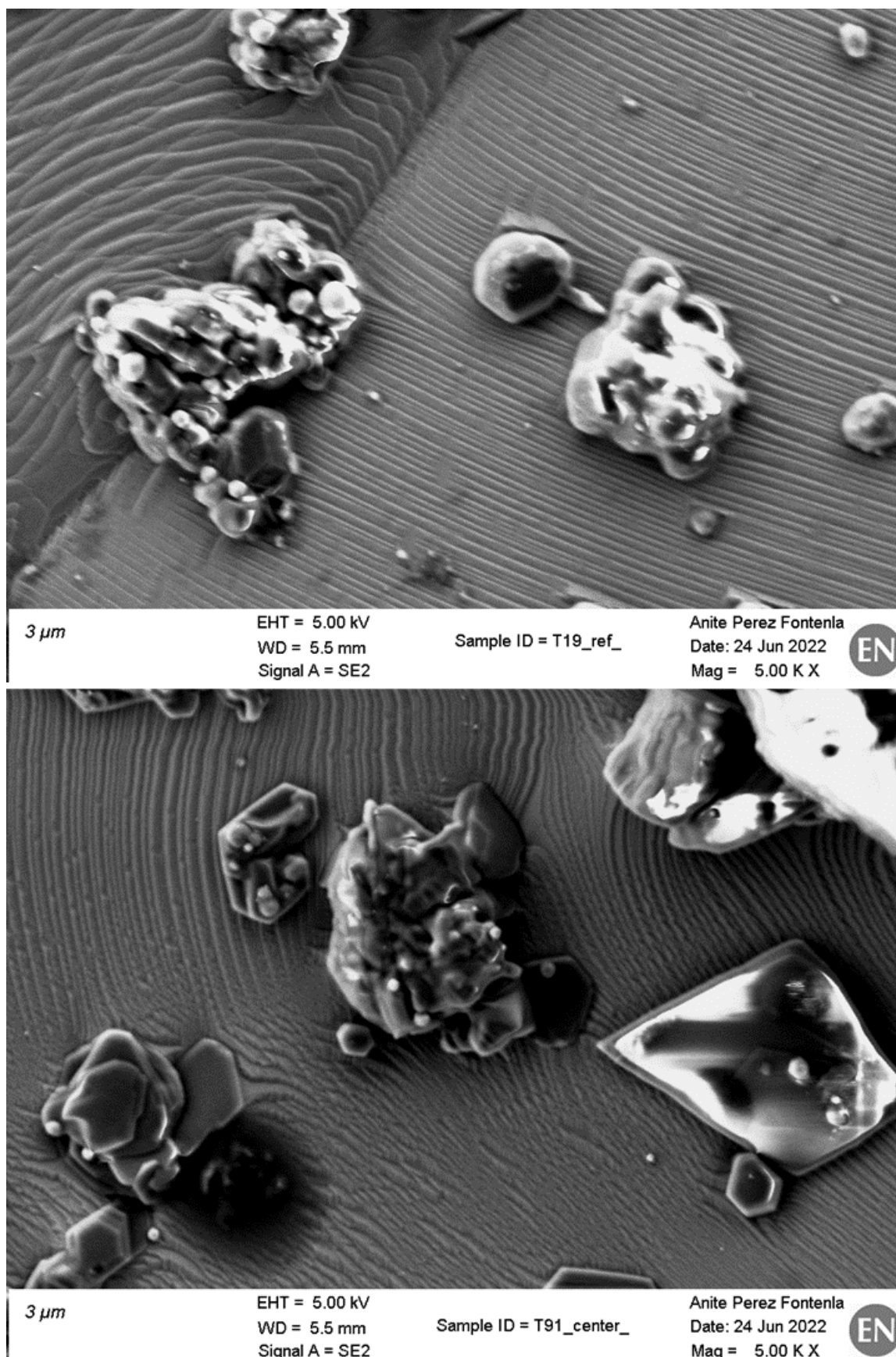


**Figure 3.35:** SEM images of Steel T91 sample of the reference material region (top) and the central irradiated beam spot (bottom) with a resolution scale of 3  $\mu\text{m}$ .



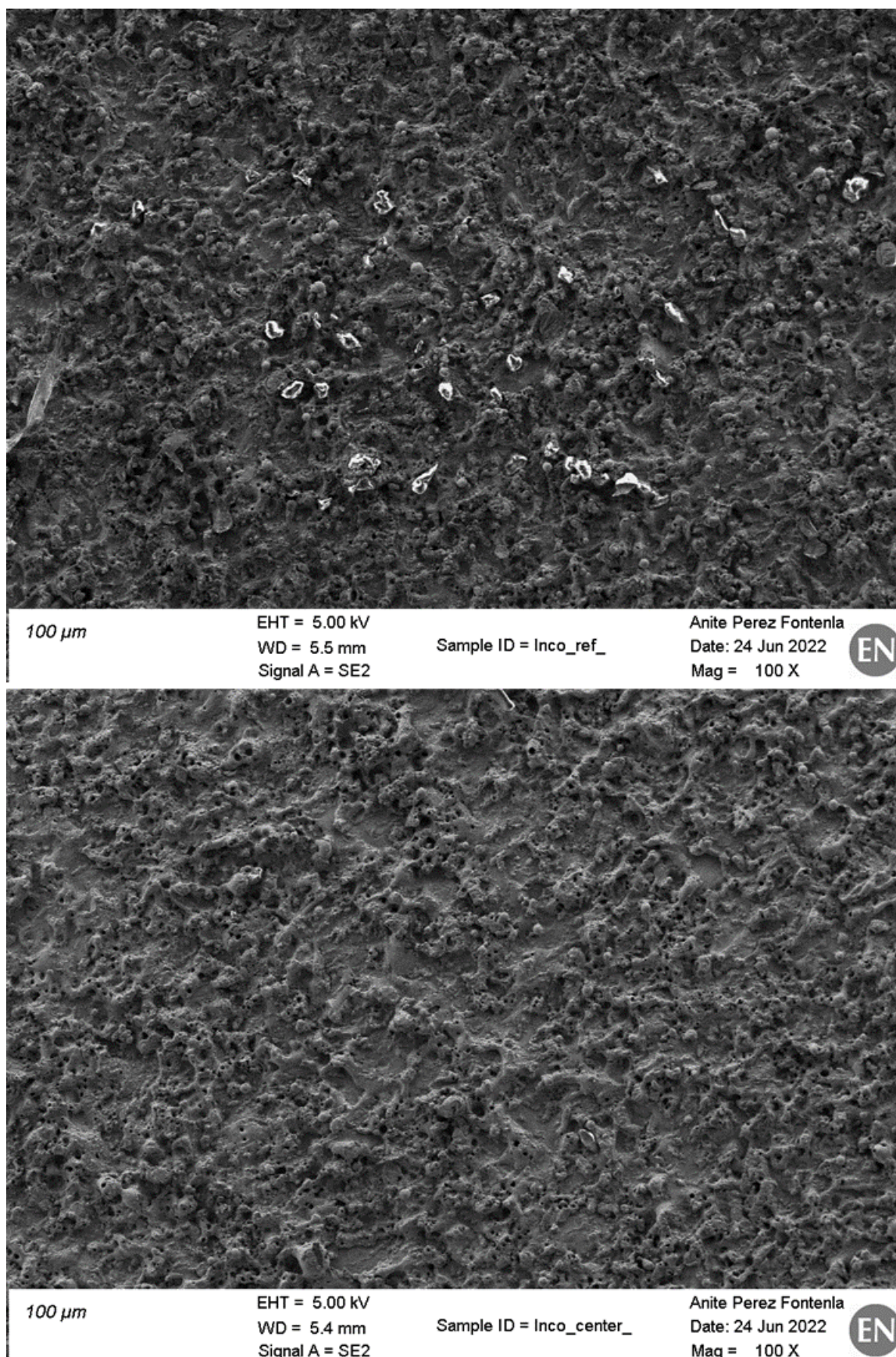


**Figure 3.36:** SEM images of Inconel 718 sample of the reference material region (top) and the central irradiated beam spot (bottom) with a resolution scale of 100 μm.



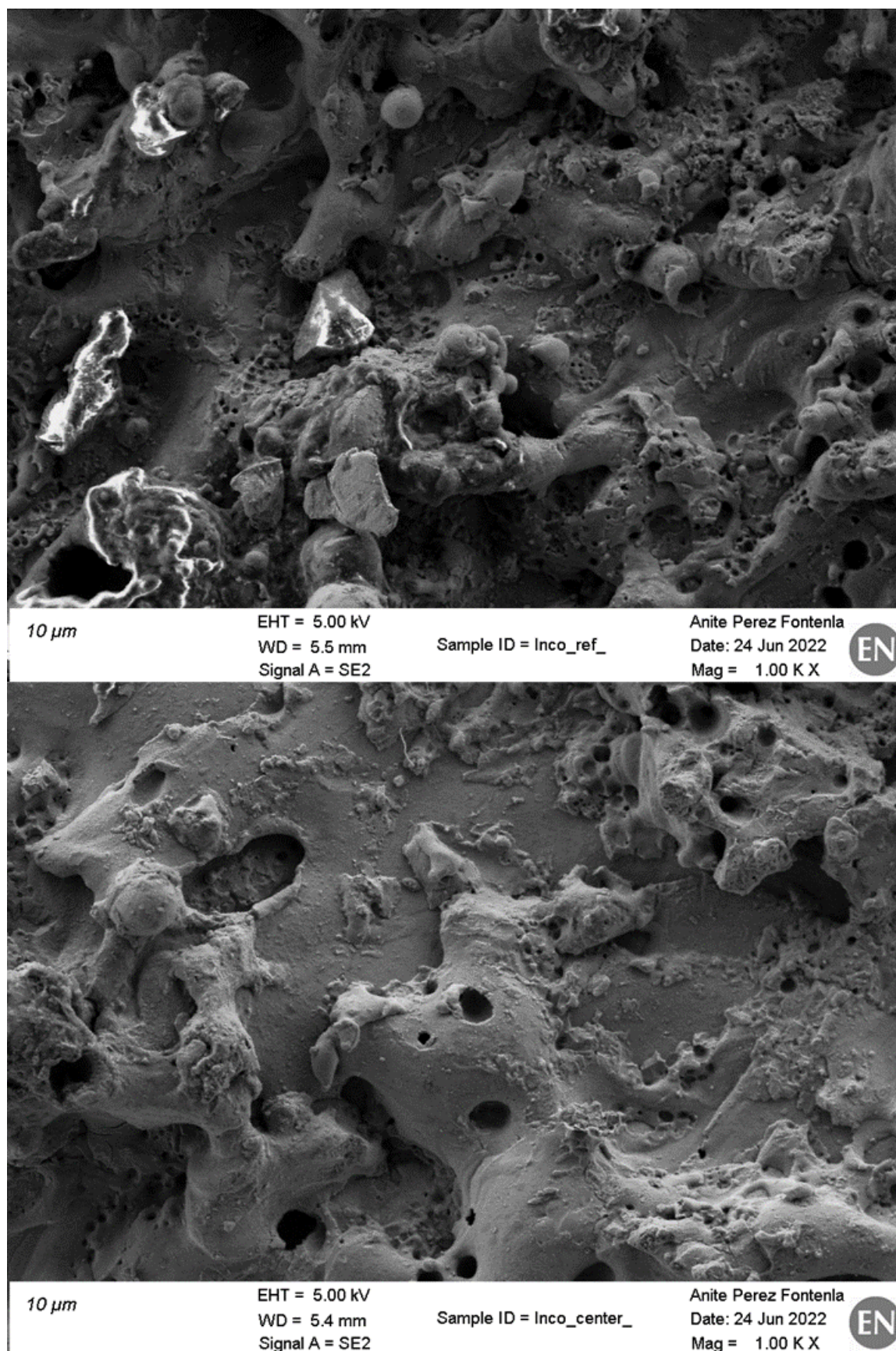


**Figure 3.37:** SEM images of Inconel 718 sample of the reference material region (top) and the central irradiated beam spot (bottom) with a resolution scale of 10 μm.



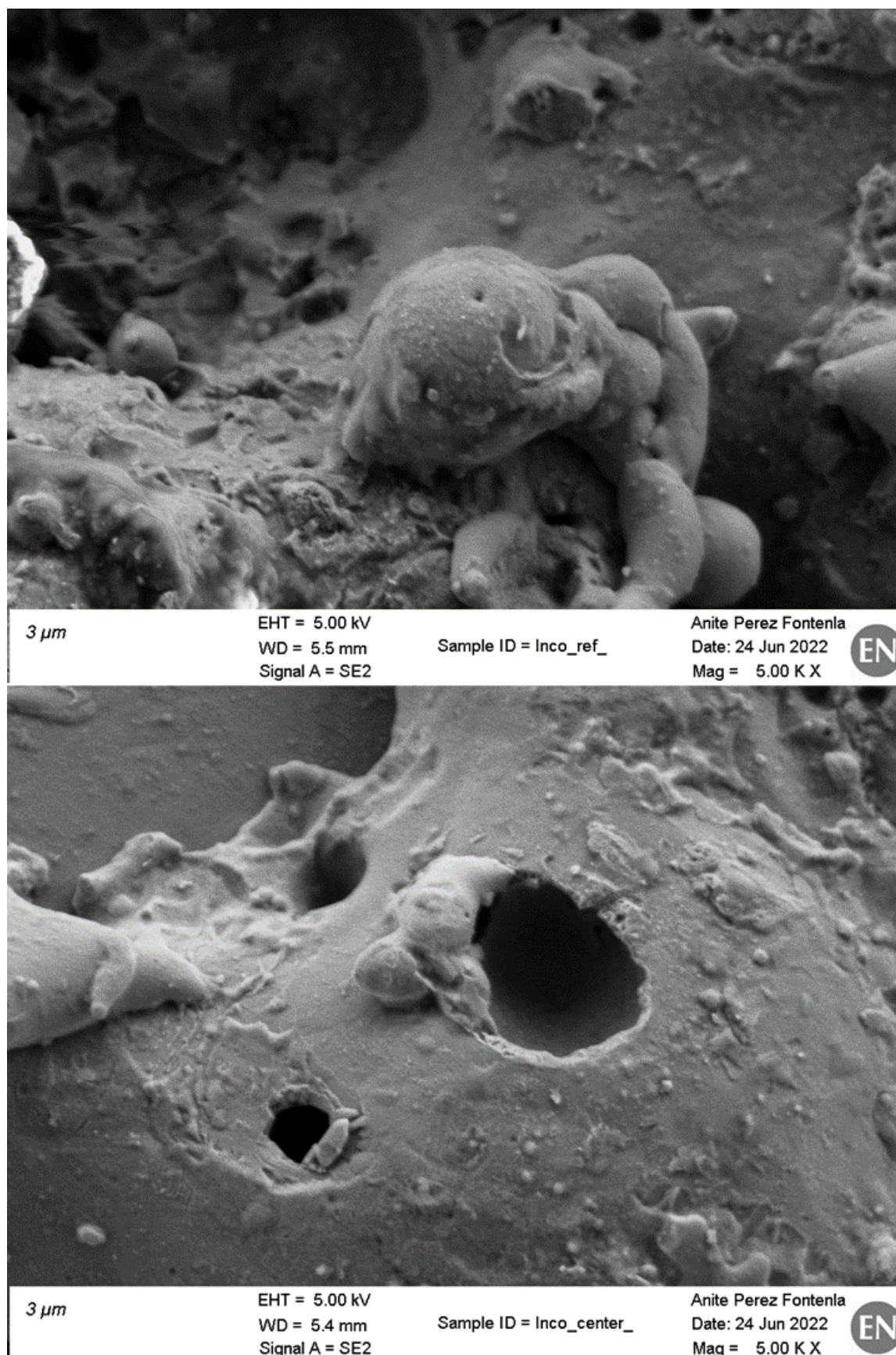


**Figure 3.38:** SEM images of Inconel 718 sample of the reference material region (top) and the central irradiated beam spot (bottom) with a resolution scale of 3  $\mu\text{m}$ .



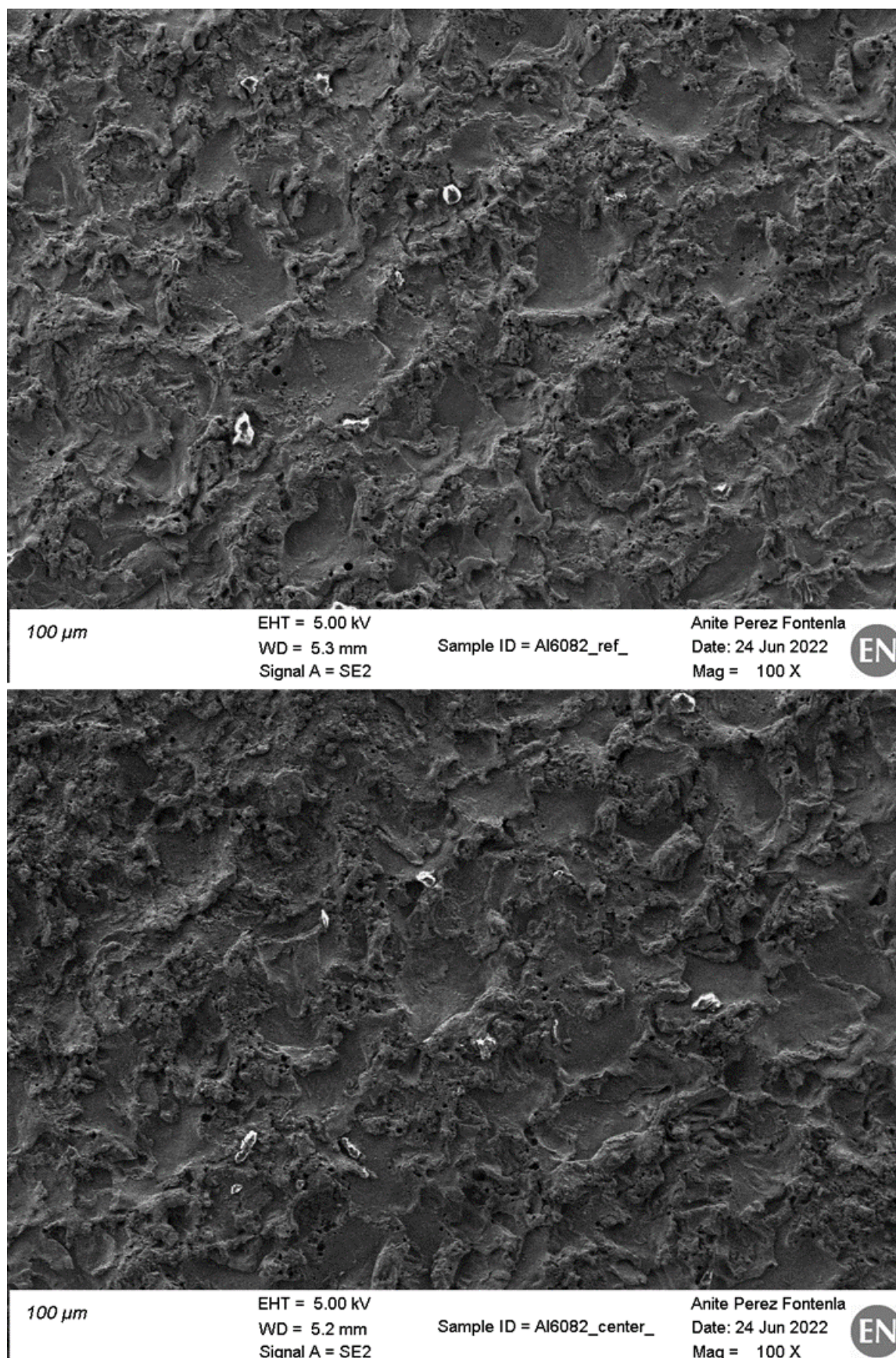


**Figure 3.39:** SEM images of Al-6082-T6 sample of the reference material region (top) and the central irradiated beam spot (bottom) with a resolution scale of 100  $\mu\text{m}$ .



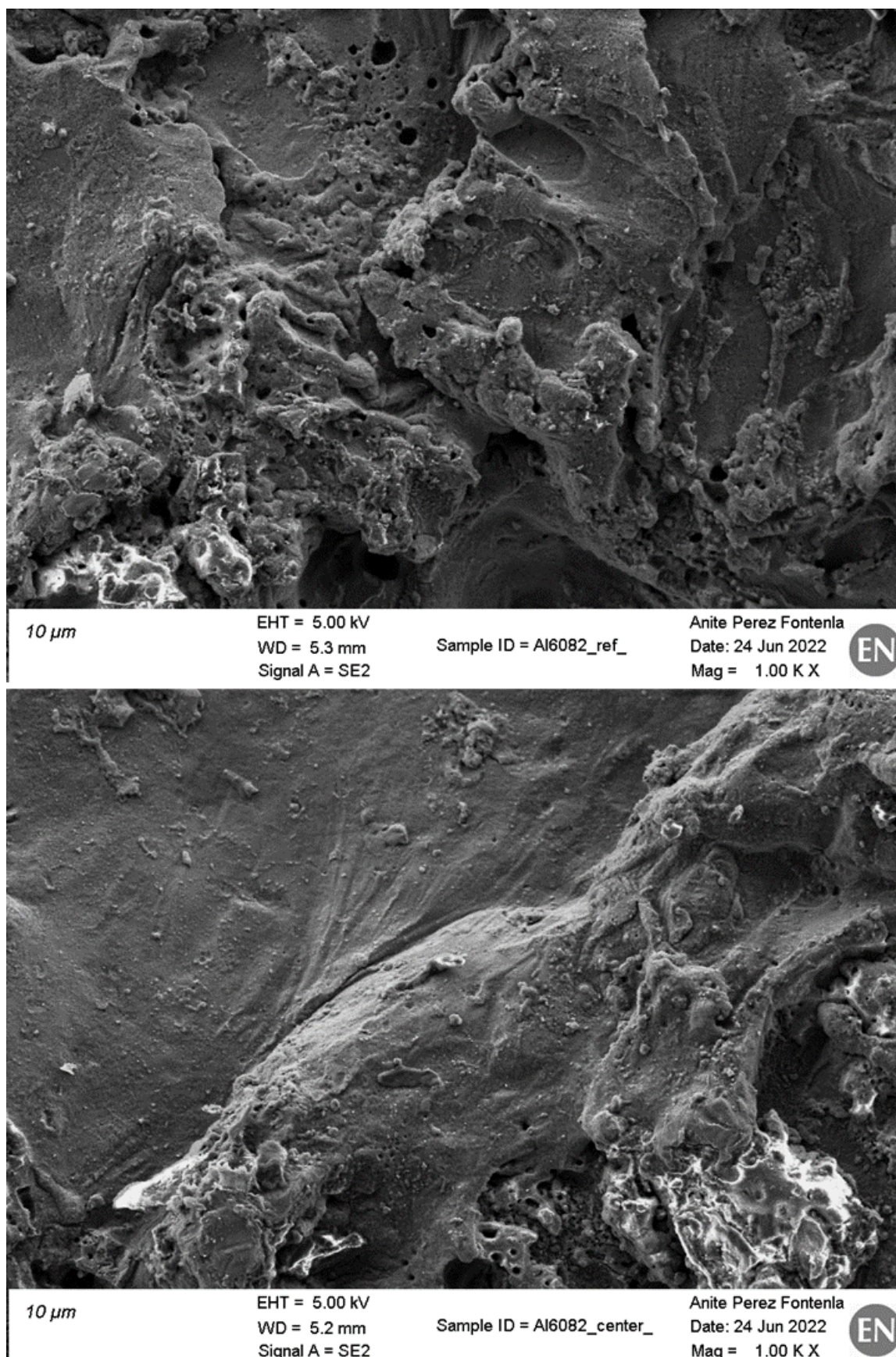


**Figure 3.40:** SEM images of Al-6082-T6 sample of the reference material region (top) and the central irradiated beam spot (bottom) with a resolution scale of 10 μm.



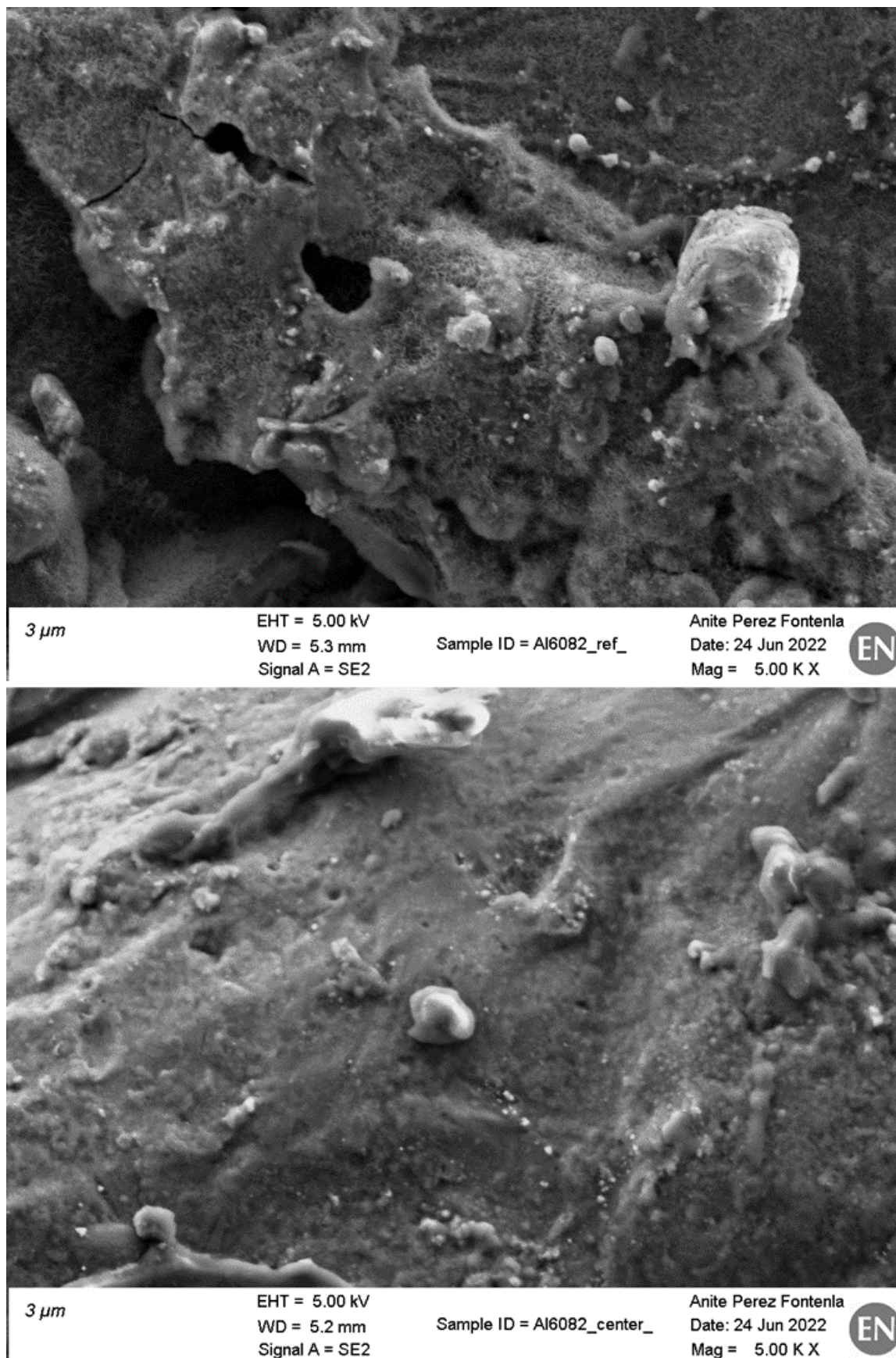


**Figure 3.41:** SEM images of Al-6082-T6 sample of the reference material region (top) and the central irradiated beam spot (bottom) with a resolution scale of 3  $\mu\text{m}$ .



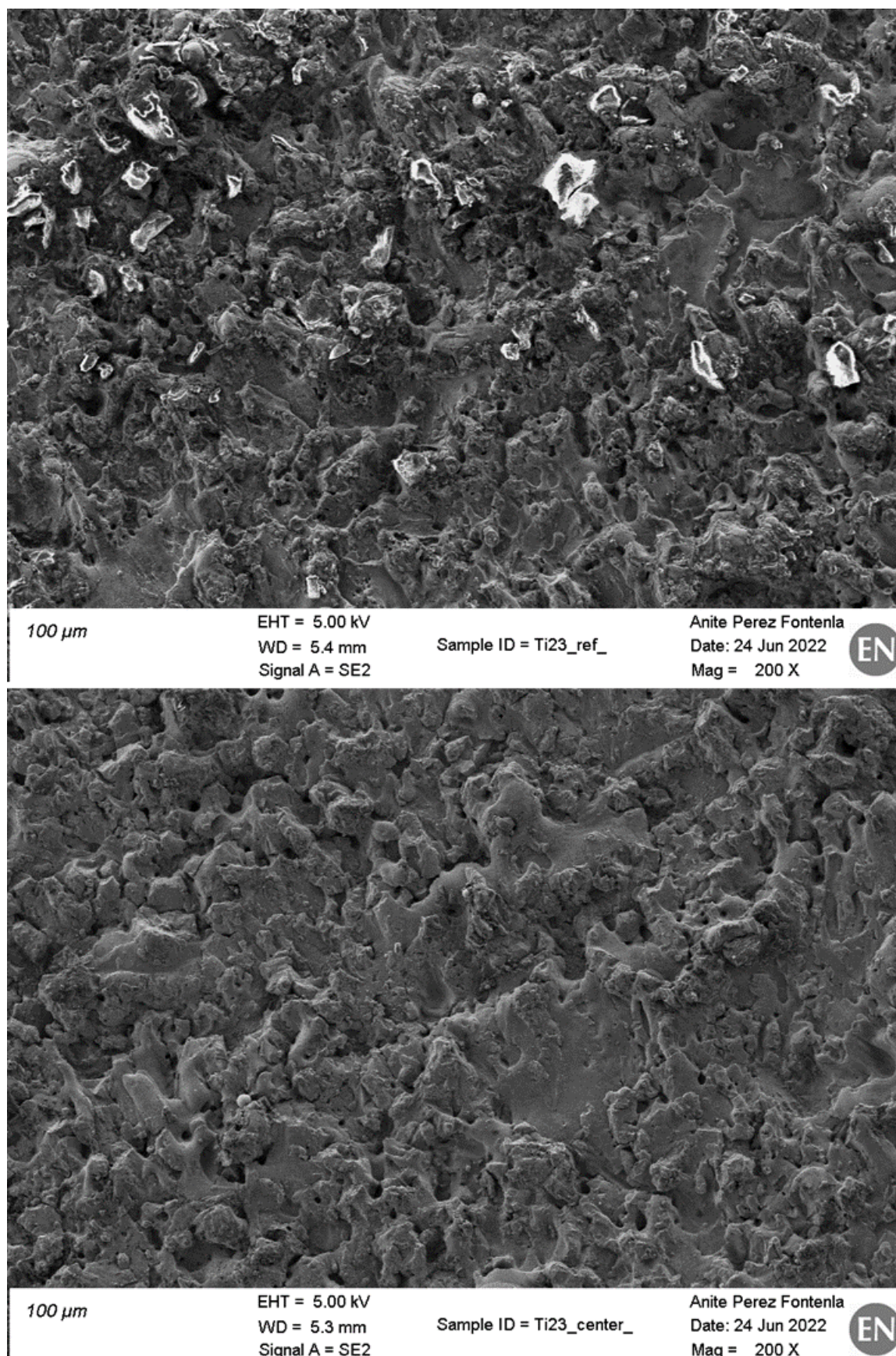


**Figure 3.42:** SEM images of Titanium Grade 23 sample of the reference material region (top) and the central irradiated beam spot (bottom) with a resolution scale of 100  $\mu\text{m}$ .



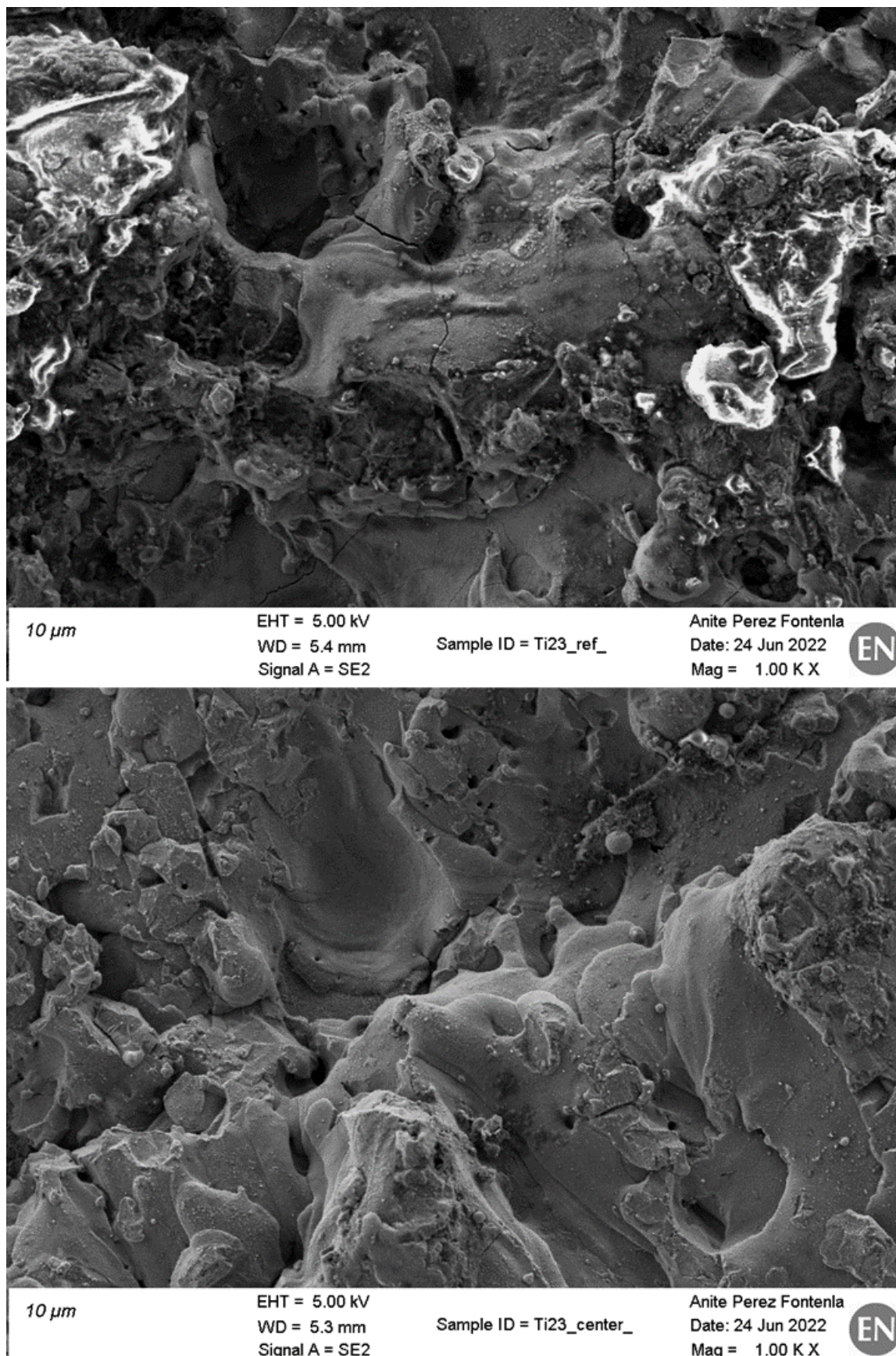


**Figure 3.43:** SEM images of Titanium Grade 23 sample of the reference material region (top) and the central irradiated beam spot (bottom) with a resolution scale of 10 μm.



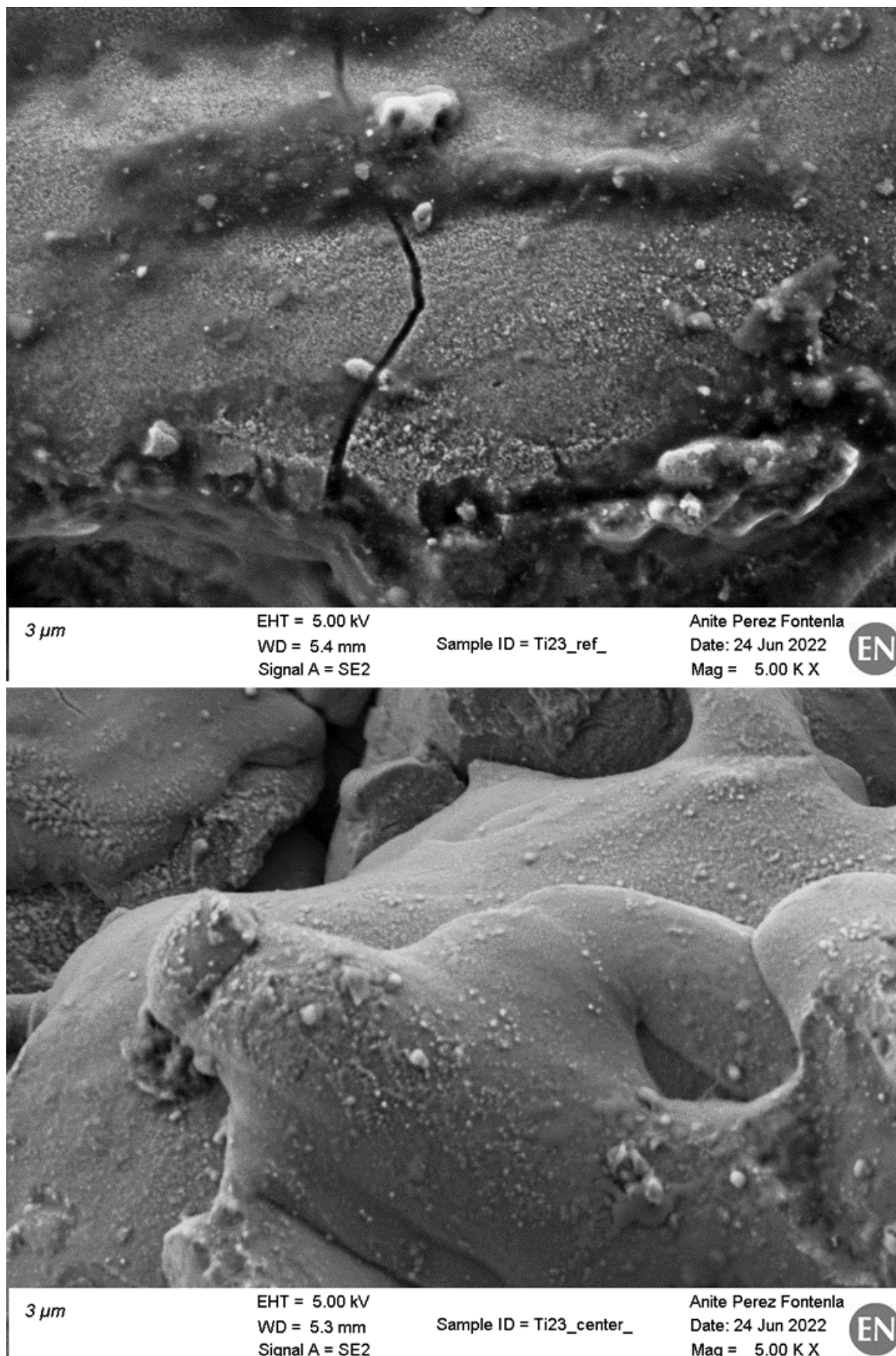


**Figure 3.44:** SEM images of Titanium Grade 23 sample of the reference material region (top) and the central irradiated beam spot (bottom) with a resolution scale of 3  $\mu\text{m}$ .

# Chapter 4

## Numerical and analytical investigations

### 4.1 Radiation effects on materials

The aim of this section is to provide a short overview of the phenomena of interaction between charged particles and matter. The concept of displacement per atom (dpa), the most common unit used to quantify the primary radiation damage, is here described. Finally, the operation of the software SRIM-2013, a commonly used software among the ion beam radiation material science community, is used to compute ion trajectories and dpa of the materials irradiated during the GSI experiment.

#### 4.1.1 Interaction of charged particles with matter

Ion irradiation offers many advantages for imitating the micro-structures and properties of materials exposed in radioactive environments and subjected to radiation damage. This technique has the added benefit of allowing researchers to systematically investigate certain features of irradiation conditions and achieve extremely high damage doses with little to no resultant radioactivity in samples.

When a charged particle, such as an ion, interacts with matter, it loses energy through various mechanisms, depending on its charge, mass, and energy. Coulomb interaction with atomic electrons induces charged particles such as electrons, protons, alpha or heavier ions to release a significant amount of energy. This type of radiation is known as directly ionising because it can cause atomic excitation or ionisation depending on the energy transferred to the electrons and the atom's electronic properties. The energy loss per unit length increases as a function of the particle charge, the density and the atomic number of the target material.

A very important parameter to determine the amount of energy loss as a result of the interaction of a charged particle with matter is the **Stopping Power**. It can be defined as the mean energy loss per unit path length, and it is indicated as  $-dE/dx$ . It depends on the charge and velocity of the projectile and, of course, on the target material [83]. The average energy loss ( $dE/dx$ ) per distance travelled by charged particles traversing matter can be analytically computed by specific derivations of the classical **Bethe-Bloch formula**, that can be expressed as follows:

$$-\frac{dE}{dx} = \left(\frac{e^2}{4\pi\epsilon_0}\right)^2 \frac{4\pi N_A Z_\rho}{mc^2 \beta^2 A} \left[ \ln\left(\frac{2mc^2 \beta^2}{I}\right) - \ln(1 - \beta^2) - \beta^2 \right] \quad (4.1)$$

where  $v$  is the particle velocity,  $c$  the speed of light,  $\beta = v/c$ ,  $m$  the particle mass,  $N_A$  the Avogadro's number,  $Z_\rho$  the absorber atomic number,  $A$  the absorber mass number,  $\epsilon_0$  the vacuum permittivity and  $I$  the mean excitation energy.

When an ion beam penetrates through the matter, it loses energy primarily due to collisions with electrons (electronic stopping) and target nuclei (nuclear stopping). The total stopping power is then just the sum of the stopping powers due to electronic and nuclear interactions. The slowing down of a projectile ion caused by inelastic collisions between bound electrons in the medium and the ion travelling through it is referred to as **Electronic stopping**. This collision is termed inelastic since part of the particle energy is lost throughout the process due to the effects of excitations of bound electrons in the medium and of the excitations of the electron cloud of the ion. The elastic collisions between the projectile ion and the atoms in the medium contribute to what is called **Nuclear stopping**. Nuclear stopping, contrary to what the name suggests, involves the interaction of ions with nuclei in the matter and has nothing to do with nuclear forces.

When a fast-charging particle moves inside matter, it ionises the atoms of the material and deposits a dose along its path. Since the energy lost is inversely proportional to the square of the velocity, the Stopping Power rises progressively until the end of the range and reaches a maximum, known as the **Bragg peak**, just before the energy goes to zero. Therefore, the Bragg peak represents the point in which the highest dose is deposited by the charged particles and in which the largest amount of radiation damage is accumulated. The identification of the Bragg peak plays a very important role in various areas of nuclear application, such as radiation protection and radiotherapy.

A useful quantity to express the rate of energy loss by a charged particle per  $\text{g cm}^{-2}$  of the medium traversed is the **mass stopping power** ( $-dE/\rho dx$ ). The latter can be obtained by dividing the stopping power by the target density  $\rho$ . The common unit for mass stopping power is  $\text{MeV cm}^2 \text{g}^{-1}$ .

Charged particles ionise and lose energy in many steps as they pass through matter until their energy is (almost) zero. The particle's range or **Penetration depth**, as

it is called in SRIM-code, is the distance between the surface of the material and the point where the particle comes to rest. The range is determined by the type of particle, its initial energy, and the material through which it passes. Since positive ions don't generally scatter at large angles, it is possible to define an accurate range for ion radiations by taking into account the energy, the charge, and the ionisation level of the stopping medium. Because of the statistical nature of these interactions, each radiation particle will require a slightly different number of collisions before coming to rest in the medium (i.e., some may travel further and undergo fewer collisions than others). As a result, there will be a small variation in the range, which is known as **straggling**.

### 4.1.2 Basic concepts of radiation damage

The interaction of high-energy particles with materials can have numerous consequences, such as the formation of lattice defects, the heating of the material, the production of secondary electrons and photons, etc. The multiple nuclear applications in the fields of physics, medicine and power generation make important and interesting the understanding of the fundamental effects of high-energy particles on the matter. Moreover, the radiation effect on the matter is strongly influenced not only by the nature of the incoming particle but also by the nature of the intercepting material. The damage is proportional to the total dose received by the material, i.e. the energy deposited by ionising radiation per unit mass.

The irradiation of materials by energetic particles causes microstructural defects, which impact the macro-structural characteristics of the materials and directly influence their performance [57]. The often-radical changes in the behaviour of the materials under irradiation are required to be deeply investigated and taken into account during the design phase of the components in high-energy radiation environments (as in the case of beam windows). A common issue in this field of research consists in distinguishing between the deterioration of material properties as a result of the particle-induced changes in the lattice structure, known as **radiation damage**, and the effects caused by heating of the material, which can lead to high deformation or thermal-shock phenomena. Furthermore, the activation of the materials due to the transmutation of stable nuclei into unstable (i.e., radioactive) and the consequent introduction of alien chemical species call for further studies to understand the proper handling and analysis of the components [16].

Most of the time, it is possible to divide the damage production mechanism into two categories according to time scale:

- The **primary damage**, that is produced immediately after the particle impact (the time scale for atomic collision processes is in the order of 0.1-1 ps) as long as

the material reaches the thermodynamic equilibrium (around 1-10 ps) after having experienced strong heating (called *thermal spike*) due to the reconfiguration of the distorted lattice.

- The long-timescale damage evolution, due to thermally activated diffusion processes, which may persist for longer periods (from nanoseconds to years).

In this section, the basic concepts of primary radiation damage will be discussed in order to give an overview of the methods of calculation used by the particle transport software SRIM-2013 to assess the effects of the primary radiation damage on the materials irradiated during the GSI experiment.

### Primary damage in materials

When a collision between an incoming particle and a nucleus occurs, there is the opportunity that the recoil can lead an atom to displace from its initial lattice site. In the case of charged particles, such as the uranium ions of the experiment, the interaction between the particles and the nucleus of the atom is governed by the Coulomb force and it, therefore, depends on the Nuclear Stopping Power. Part of the energy is transferred from the incident particle to the atom and, in the event of an amount of energy larger than the *threshold displacement energy*  $E_d$  of the atom, the latter will be ejected from its position inside the crystal lattice and will leave a vacancy in the initial position. The threshold displacement energy is one of the most fundamental quantities for describing radiation damage in materials and is defined as the «minimum recoil energy given to an atom in a material needed to create a stable defect» [84].

The atom ejected from its original position is known as **Primary Knock-out Atom** (PKA). If the energy transferred during the collision is greater than the displacement energy, then the atom has enough energy to displace other atoms inside the crystal lattice and thereby generate a collision cascade. When the energy of the projectile falls below  $E_d$ , the particle eventually comes to rest as an interstitial in the lattice. As a result of these collision and recoil processes, the lattice is characterised by a certain number of **Frenkel pairs**, which are a pair of point defects, a vacancy and an interstitial.

Different approaches to the problem of calculating the damage caused by a primary recoil atom of given initial energy were developed over the years. The simplest approach to assess the number of displaced atoms  $N_d$  generated by a PKA of kinetic energy  $T$  is

the *Kirchin-Pease model*, according to which:

$$N_d = \begin{cases} 0 & 0 < T < E_d \\ 1 & E_d < T < 2E_d \\ T/2E_d & 2E_d < T < E_1 \\ E_1/2E_d & E_1 < T < \infty \end{cases} \quad (4.2)$$

where  $E_1$  is the threshold energy below which the recoils slow down by hard-core elastic scattering and, above which, the recoils lose energy only by electron excitation [85].

Nowadays, the *Norgett, Robinson, and Torrens* (NRT) model, a modified version of the Kinchin-Pease formula, is commonly accepted in the literature as the right theoretical model for calculating the number of Frenkel pairs  $N_F$  generated by a PKA with initial kinetic energy  $T$ . It can be written as:

$$N_F = \frac{\kappa \hat{T}}{2E_d} \quad (4.3)$$

where  $\kappa$  is the displacement efficiency, commonly equal to 0.8, a parameter used to describe more realistically the scattering process and  $\hat{T}$  is energy available to generate atomic displacements by elastic collisions. It can be written as:

$$\hat{T} = \frac{T}{[1 + kg(\varepsilon)]} \quad (4.4)$$

where  $g(\varepsilon)$  is the Lindhard partition function that represents the fraction of energy available for a nuclear displacement, and  $k$  is a parameter that depends on the atomic and mass numbers. The term  $2E_d$  in the denominator represents the equal distribution of energy between two colliding atoms, according to the hard-sphere model [85].

The **displacement per atom** (dpa) is a helpful measure for characterising the displacement damage caused by different irradiation conditions. It represents the average number of times that an atom is displaced during irradiation and can be determined using the equation [16]:

$$dpa = \int \sigma_{disp}(E) \frac{d\phi(E)}{dE} dE \quad (4.5)$$

In this equation,  $E$  represents the incoming particle's energy, and  $\phi(E)$  is the energy-dependent particle fluence. The displacement cross-section  $\sigma_{disp}(E)$  is determined by the damage cross-section  $\sigma_{damage}(E, T)$ , which represents the probability of forming a PKA of energy  $T$ , and the number of atoms displaced by that PKA  $N_F$ , as indicated in the following equation:

$$\sigma_{disp}(E) = \int \sigma_{damage}(E, T) N_F(T) dT \quad (4.6)$$



Because it provides a direct comparison between different irradiation conditions, the dpa is an extensively used parameter in nuclear physics to assess radiation damage. The displacement cross section is, in practice, related to the atoms' recoil spectrum, which is affected by the incoming particle energy and type. Heavy particles have a larger displacement cross-section, higher nuclear stopping power, and a higher dpa in a shorter period.

### 4.1.3 Evolution of radiation damage and mechanical properties

The long timescale process of thermal diffusion, governed by Fick's law, can contribute to substantially changing the final microstructure of an irradiated crystal (whose configuration of the lattice is still unstable after the thermal spike) with respect to the primary damage. This paragraph intends to briefly summarise the macroscopic defects of radiation damage and to illustrate the effects on the mechanical properties of the material.

Basically, two are the precursor mechanisms that are responsible for a significant change in the crystal lattice of metals: the production of impurities and the displacement of an atom from its ideal position.

Nuclear processes in irradiated material can produce nuclei with variable atomic numbers. The transmuted nuclei that cannot fit entirely in the regular lattice and hence cause distortion in their surroundings are classified as **impurities**. On top of that, nuclear processes can produce **hydrogen and helium particles**. Because He is an insoluble gas, it tends to collect and precipitate into nanoscale He bubbles. Finally, during ion irradiation, the particles become trapped inside the medium and remain as contaminants. Nuclear processes generate transmuted nuclei, particularly gas species, which contribute to radiation damage and interact with lattice defects caused by atom displacement. From the macroscopic point of view, H and He transmutation gases can establish three-dimensional vacancy voids and migrate to grain boundaries, causing failure and embrittlement of the material. The interaction of these products with defects can alter defect recombination and diffusion. In light of the above, a large number of impurities produced during irradiation can have a detrimental effect on the properties of the material and their measurement is essential: a helpful parameter in this regard is the number of atomic parts per million (appm) of He and/or H.

Vacancies and interstitials, generated by the displacement of atoms into the crystal lattices, are mobile under thermal diffusion mechanisms: these radiation-induced defects can interact with one another and with the pre-existing lattice, and this characterises the evolution of radiation damage. Typical processes induced by thermal diffusion are the annihilation of a vacancy with an interstitial, the clustering of interstitials or vacancies and the capture of point defects at dislocations, grain boundaries, and voids. Therefore, at

the end of the recombining process, an irradiated crystal's final structure can differ significantly from the configuration immediately after the primary damage, which is composed of isolated Frenkel pairs or small defect clusters. At the end of the irradiation, various types of **defects** can arise, which is common to divide them according to their geometry: *surviving point defects*, such as Frenkel pairs and point defects clusters, *line defects* (dislocations), *planar defects*, such as the interphase boundaries, the grain boundaries, etc., and, finally, *volume defects*, such as voids, cracks and bubbles.

The macroscopic characteristics of the irradiated material are impacted by the radiation-induced defects and the corresponding evolution of the microstructure. For example, thermal and mechanical properties can be altered. Irradiation has a strong influence on the mechanical properties of crystals, particularly the creation of dislocation-like clusters. Dislocation motion is the mechanism that causes plastic deformation. Irradiation increases the concentration of dislocations, allowing for contact between two dislocations. This contact could result in the formation of a region of dislocations outside of the glide plane, impeding their mobility. As a result, the yield stress rises and the material's plastic deformability decreases: this phenomenon is known as **radiation hardening**. In addition, this phenomenon alters other mechanical properties of the material, such as the Young's modulus and the strain to rupture. Consequently, the quantification of the radiation damage of a material (that results in its embrittlement) is carried out by measuring the change of the just mentioned mechanical properties between the pristine and the irradiated conditions, just as was done for the elastic modulus of the samples irradiated during the GSI experiment by means of the online LDV measurements and the subsequent microindentation tests.

#### 4.1.4 The SRIM-2013 code

The SRIM (Stopping and Range of Ions in Matter) Monte Carlo simulation-based software evolved from an original simulation code for the transport of ions in targets published in 1980, which was revamped into the "Transport of Ions in Matter" (TRIM) code in 1984, with major SRIM updates in 1988, 1995, 1998, 2003, 2008, and 2013 (along with several minor intermediate updates).

SRIM is the most often used software in the ion beam radiation material science field to compute ion trajectories and dpa thanks to its user-friendly interface and vast high-quality stopping power database. The Binary Collision Approximation is used by the SRIM programme to calculate the interaction of ions with the matter for every ion implanted into either monoatomic or multiatomic targets at any energy [86].

Two SRIM options, namely the "Ion Distribution and Quick calculation of damage" (Q-C) and the "Detailed calculation with Full Damage cascades" (F-C), are commonly

used to calculate parameters related to ion-induced displacements. The difference between the two calculation options will be briefly discussed below.

In this study, both the options of the latest version SRIM-2013 were used to calculate ion penetration depth, stopping power and displacements per atom of the four materials irradiated.

### Results of the penetration depths and stopping power calculations

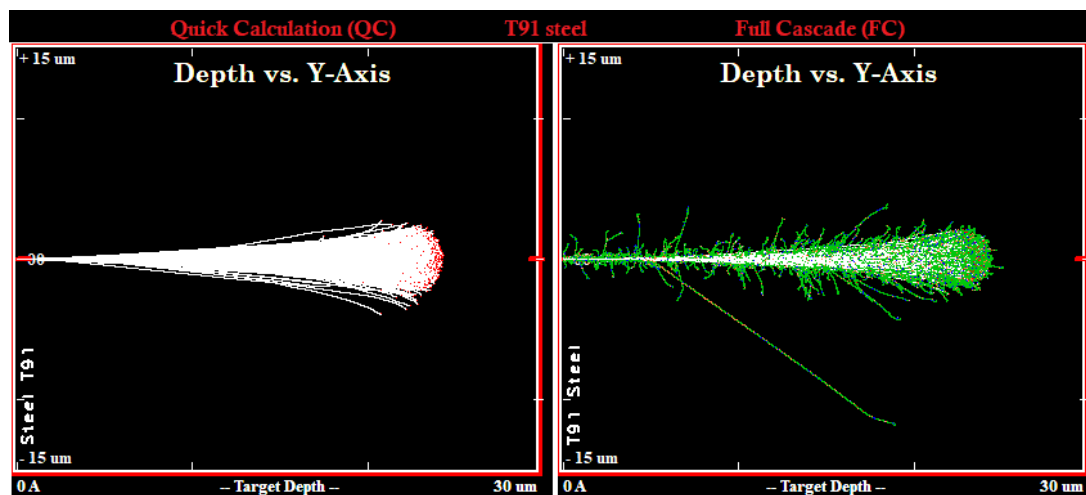


**Figure 4.1:** Results of the particle transport simulations, that show the tracking of 4.8 MeV/u Uranium ions passing through Stainless Steel T91, as a function of the target depth. All the calculations were performed using both the Q-C (left) and F-C (right) options of the TRIM-2013 code.

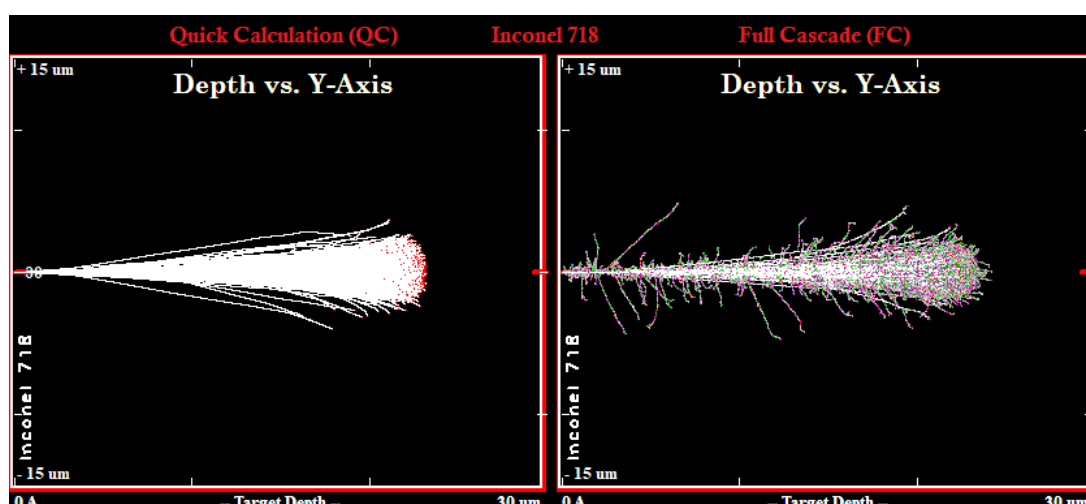


**Figure 4.2:** Results of the particle transport simulations, that show the tracking of 4.8 MeV/u Uranium ions passing through Inconel 718, as a function of the target depth. All the calculations were performed using both the Q-C (left) and F-C (right) options of the TRIM-2013 code.

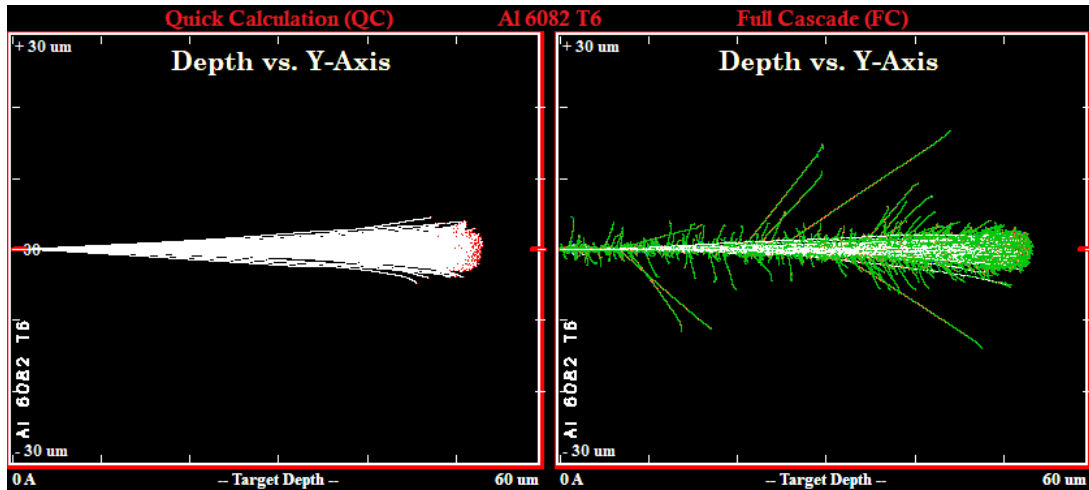


**Figure 4.3:** Results of the particle transport simulations, that show the tracking of 4.8 MeV/u Uranium ions passing through Al-6082-T6, as a function of the target depth. All the calculations were performed using both the Q-C (left) and F-C (right) options of the TRIM-2013 code.

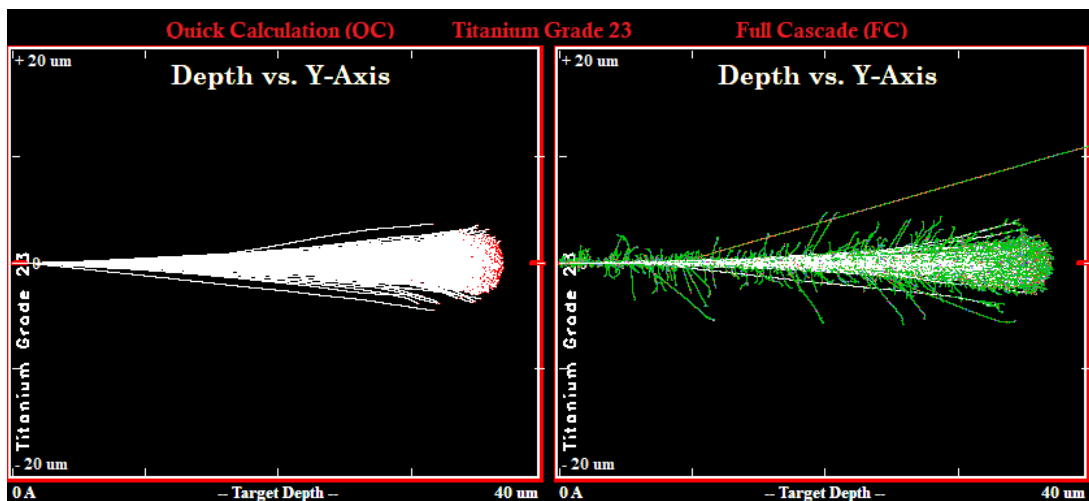


**Figure 4.4:** Results of the particle transport simulations, that show the tracking of 4.8 MeV/u Uranium ions passing through Titanium Grade 23, as a function of the target depth. All the calculations were performed using both the Q-C (left) and F-C (right) options of the TRIM-2013 code.

The first results obtained by the particle transport simulations carried out by SRIM software concern the distance travelled by the U-ions inside the matter and the amount of energy loss per unit distance. The figures 4.1-4.4 illustrate the results of the Monte Carlo simulations in terms of path travelled by the 4.8 MeV/u U-ions inside the four target materials. As a first observation, the graphs show that penetration depth calculated by both "Quick calculation" and "Full Cascade" options have the same results in terms of penetration depth and straggling.

The values of the stopping power are expressed in linear and mass terms for the four

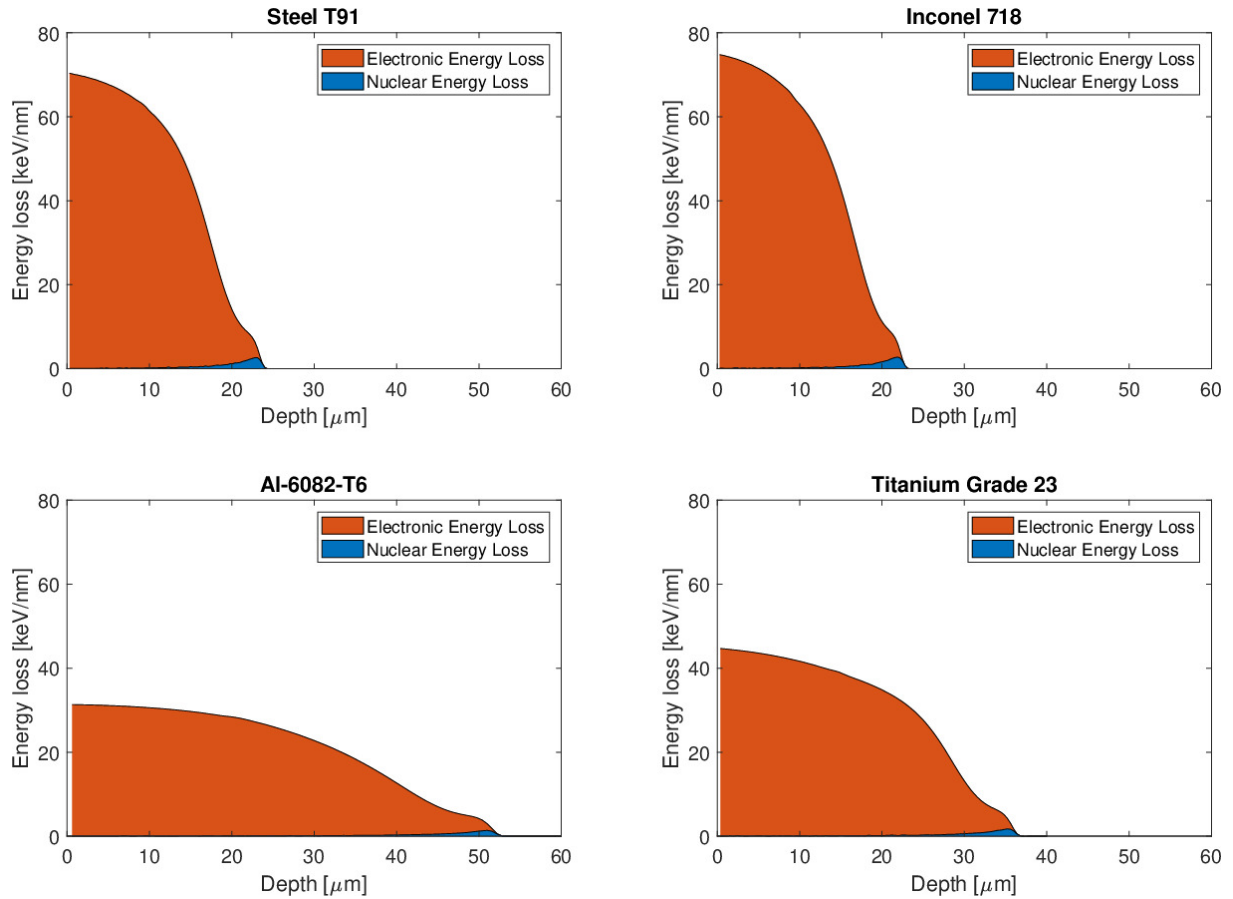


**Figure 4.5:** Nuclear and electronic energy loss as a function of penetration depth for 1.14 GeV U-ions for the four material samples irradiated during the experiment. All the calculations were performed using the "Ion Distribution and Quick calculation of damage" (Q-C) option of the TRIM-2013 code.

materials in the figures 4.5 and 4.6. The area under the Stopping Power curve of the figure 4.5 is, naturally, the same for all the materials and it is equal to the total kinetic energy of a 4.8 MeV/u U-ion, namely around 1.14 GeV. The energy distribution inside the matter is instead different for each material: in the case of the Inconel 718 sample, a large amount of energy is lost in the first few micrometres of the material (Surface energy loss of about 74.89 MeV cm<sup>2</sup> mg<sup>-1</sup>) and the  $-dE/dx$  steeply goes to zero after around 22.21 μm from the surface; on the other hand, in the case of the Aluminium alloy, the Surface energy loss is much lower (about 31.39 MeV cm<sup>2</sup> mg<sup>-1</sup>) and the Stopping Power decreases slightly until the end of the range (51.46 μm, more than double the In718 penetration depth). The values of penetration depth and stopping power for the four materials are summarised in the table 4.1 at the end of the paragraph.

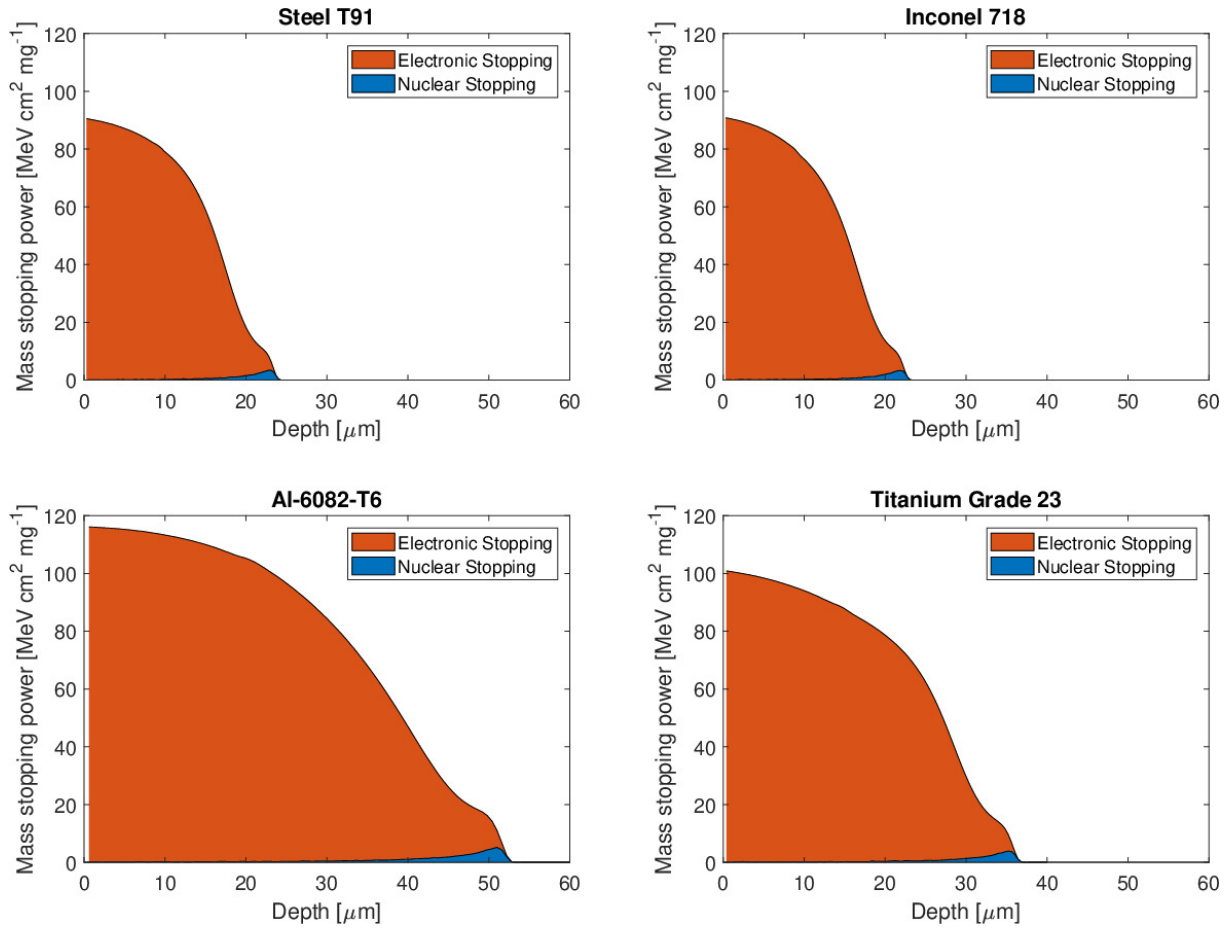


**Figure 4.6:** Mass stopping power as a function of penetration depth for 1.14 GeV U-ions for the four material samples irradiated during the experiment. All the calculations were performed using the "Ion Distribution and Quick calculation of damage" (Q-C) option of the TRIM-2013 code.

Nuclear parameters		Materials			
		Steel T91	Inconel 718	Al-6082-T6	Ti grade 23
Penetration depth	[μm]	23,25	22,21	51,46	35,71
Straggling	[Angstrom]	5382	5335	7392	6507
Energy loss at the surface	[keV nm <sup>-1</sup> ]	70,39	74,89	31,39	44,73
Surface mass stopping power	[MeV cm <sup>2</sup> mg <sup>-1</sup> ]	90,53	90,82	116,14	100,90
Displacements per atom - Quick calculation (QC)					
Dpa at surface	[dpa]	0,0021	0,0025	0,0010	0,0016
Dpa at the Bragg peak	[dpa]	0,1007	0,1052	0,0556	0,0904
Total dpa	[dpa]	0,0167	0,0180	0,0075	0,0127
Displacements per atom - Full Cascade (FC)					
Dpa at surface	[dpa]	0,0045	0,0048	0,0014	0,0026
Dpa at the Bragg peak	[dpa]	0,2214	0,2618	0,0811	0,1442
Total dpa	[dpa]	0,0355	0,0430	0,0105	0,0197

**Table 4.1:** Penetration depth, stopping power, displacements for atom and other nuclear parameters calculated with the SRIM-2013 code for the four tested materials.

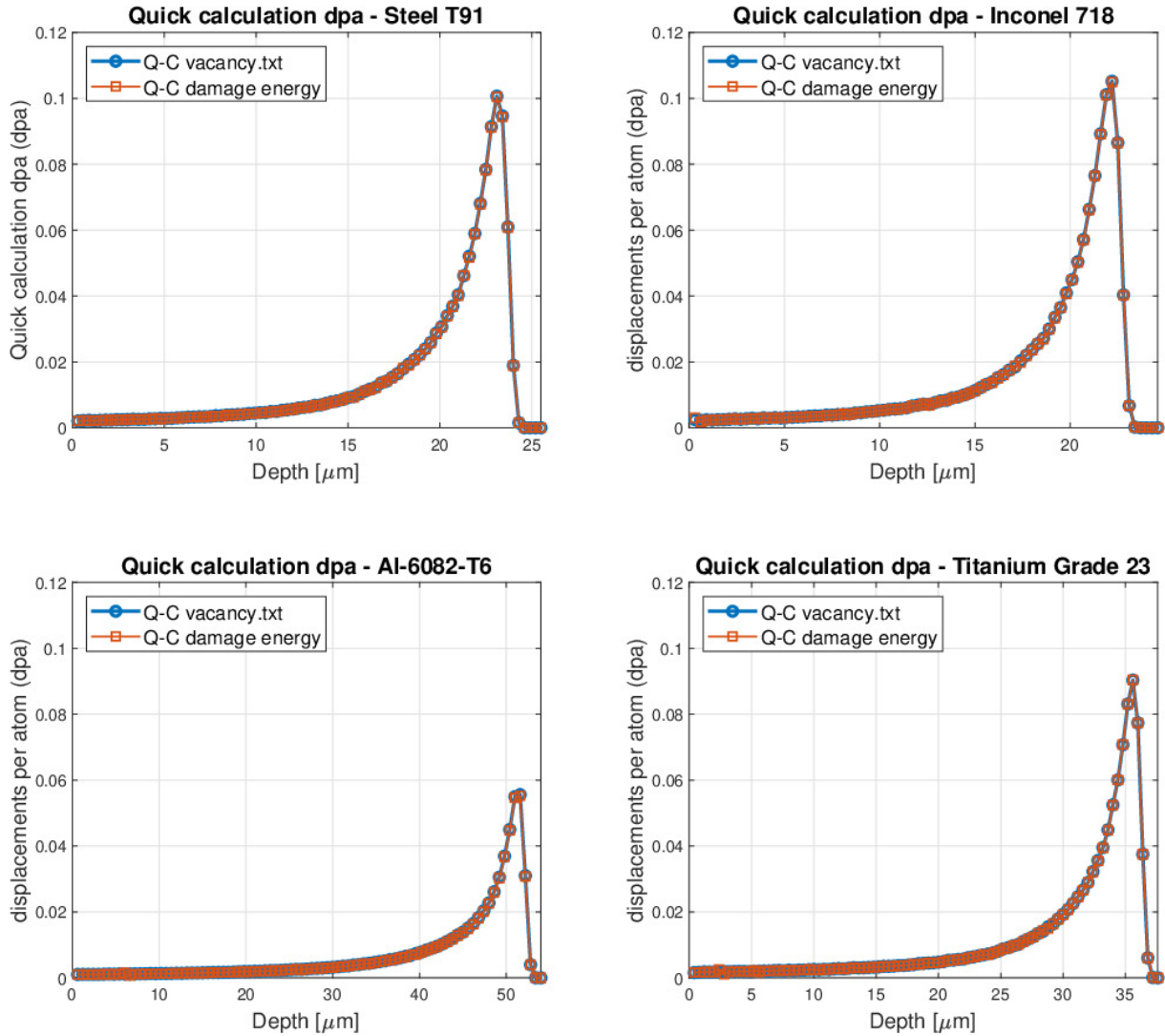


**Figure 4.7:** Displacements per atom as a function of penetration depth for 1.14 GeV U-ions for the four material samples irradiated during the experiment. The dpa calculations were performed by both "vacancy.txt" and "damage energy" methods of the "Quick Calculation" option of the TRIM-2013 code.

### Results of the dpa calculation with SRIM-2013

The two options in SRIM, namely “Ion Distribution and Quick calculation of damage” (Q-C) and “Detailed calculation with Full Damage cascades” (F-C), are commonly used to calculate parameters related to ion-induced displacements. In both options of SRIM, the easiest approach to calculate dpa is to make use of the depth-dependent vacancies produced by incident ion and recoils in the convenient SRIM output file called "vacancy.txt". However, as noted by several authors, there are large discrepancies obtained in the dpa value using the SRIM "vacancy.txt" file for F-C versus Q-C option for the same incident ion, target, and ion energy [87].

In order to achieve consistent statistics within low uncertainty, at least 10000 incident

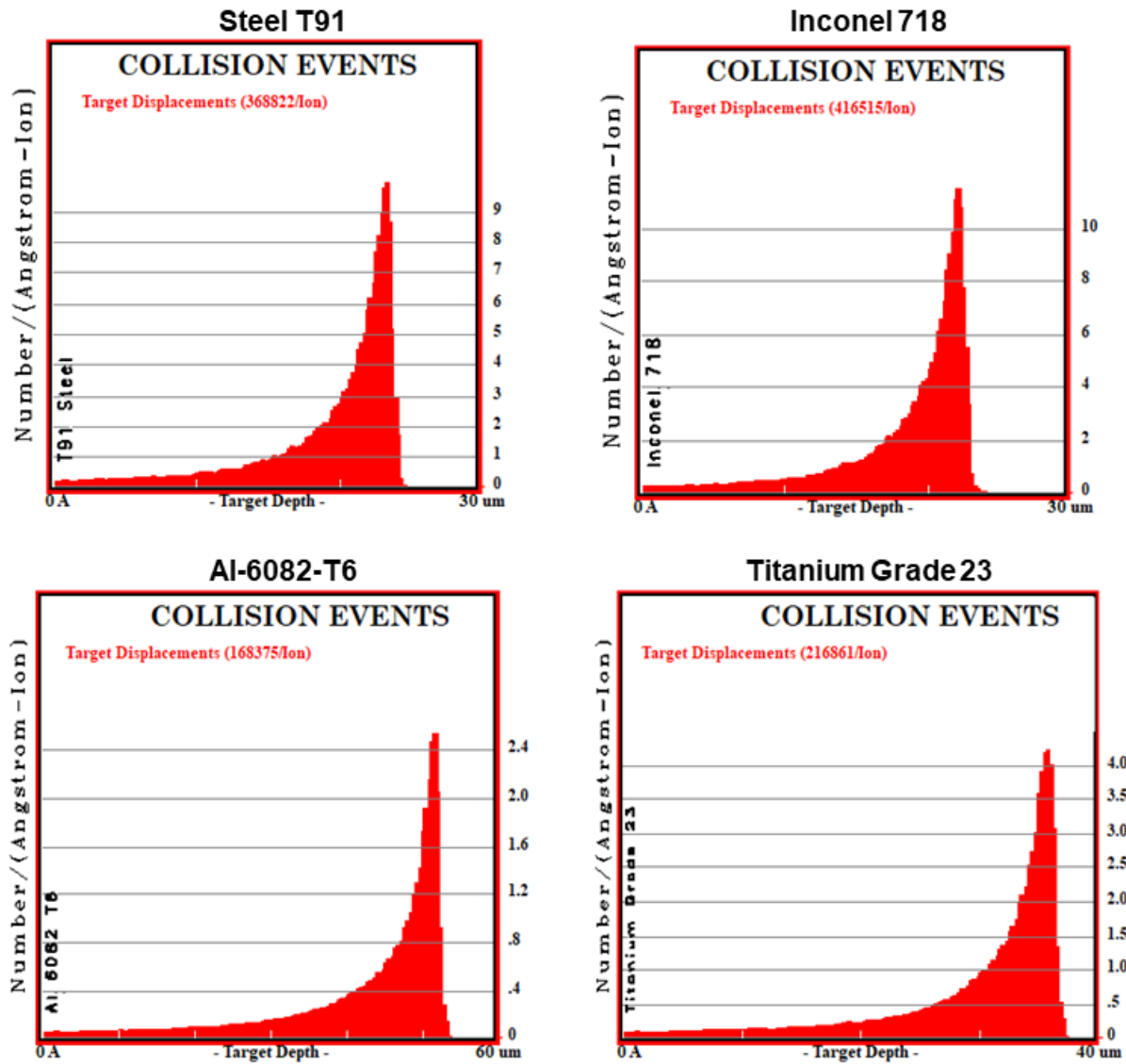


**Figure 4.8:** Target displacements per ion as a function of penetration depth for 1.14 GeV U-ions for the four material samples irradiated during the experiment, as calculated and displayed using the "Full Cascade" option of the TRIM-2013 code.

ions were used for all the calculations in Q-C option. Previous evaluations in SRIM calculations have found that 10000 to 20000 ions are a sufficient compromise between accuracy and computational time in obtaining results over a wide range of ion-target conditions [87]. For F-C option, only 1000 incident ions were simulated because of the very high computational time for longer simulations (1000 ions F-C option is equal to around 24 hours of numerical simulations).

It was therefore decided to calculate the dpa through both Q-C and F-C options and by using two methods:

- The "vacancy" method
- The damage energy method



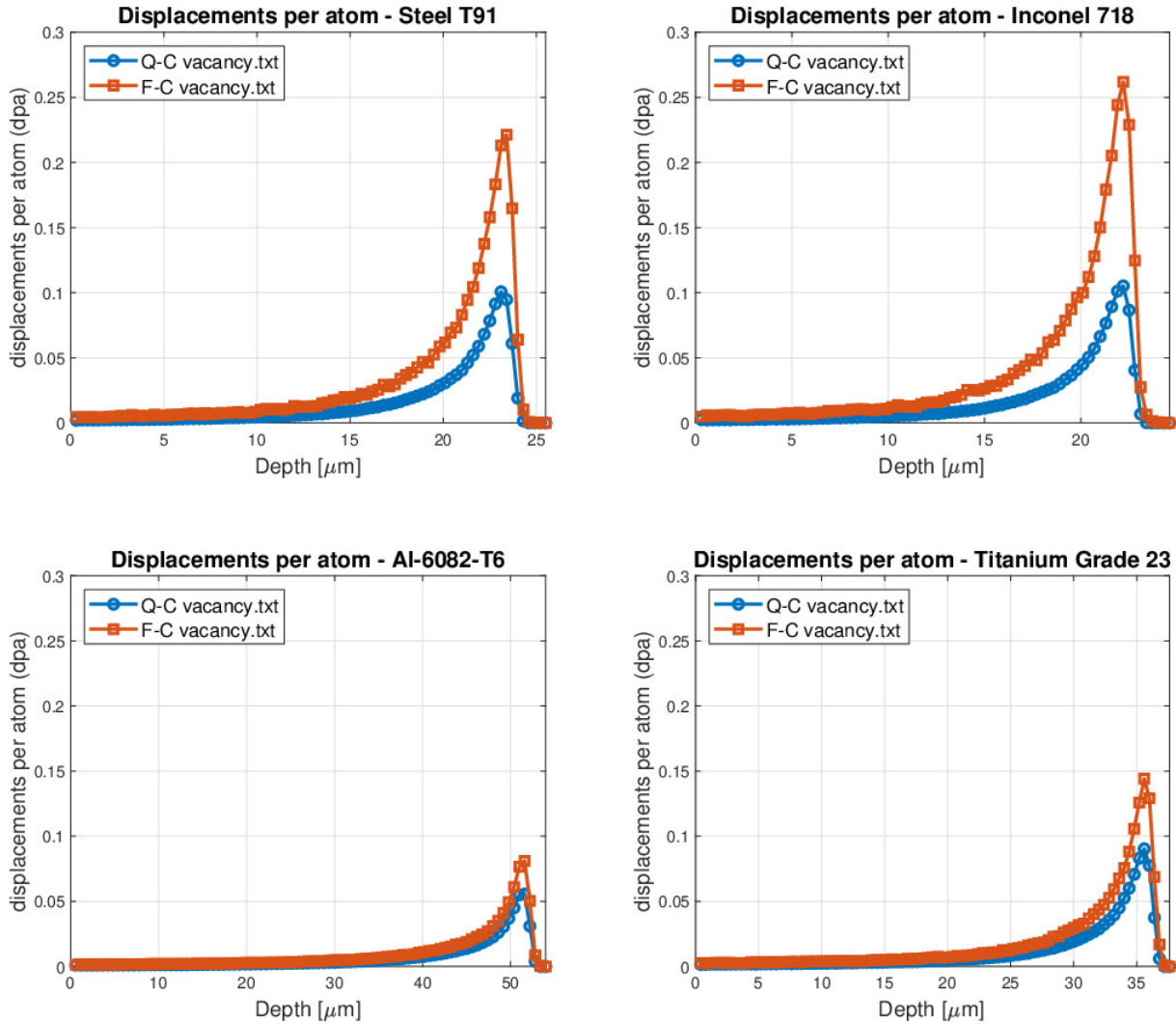


**Figure 4.9:** Comparison of the results obtained in terms of displacements per atom, as a function of penetration depth for 1.14 GeV U-ions for the four material samples irradiated, using the "vacancy.txt" method for both "Quick Calculation" and "Full Cascade" options in the TRIM-2013 code.

The first approach is the simplest to use. For each simulation, a text file is generated in the SRIM Outputs folder. Inside this text file, Vacancies by Ions and by Recoils are reported as a function of the range. From the sum of the two columns, the values of the total vacancies as a function of the range are obtained.

The second method of dpa calculation is based on the damage energy of recoil ionisation. It is briefly described how this method works in the following few lines. The incident ion transfers the kinetic energy via atomic collisions to the stationary target atoms. The resulting recoiling target atom (primary knock-on atom (PKA)) has initial kinetic energy  $E_{PKA}$ . A portion of  $E_{PKA}$  is lost through electronic excitation processes and, accordingly, the kinetic energy available for producing atomic displacements via collision processes with other atoms in the lattice is reduced. The remaining portion of the

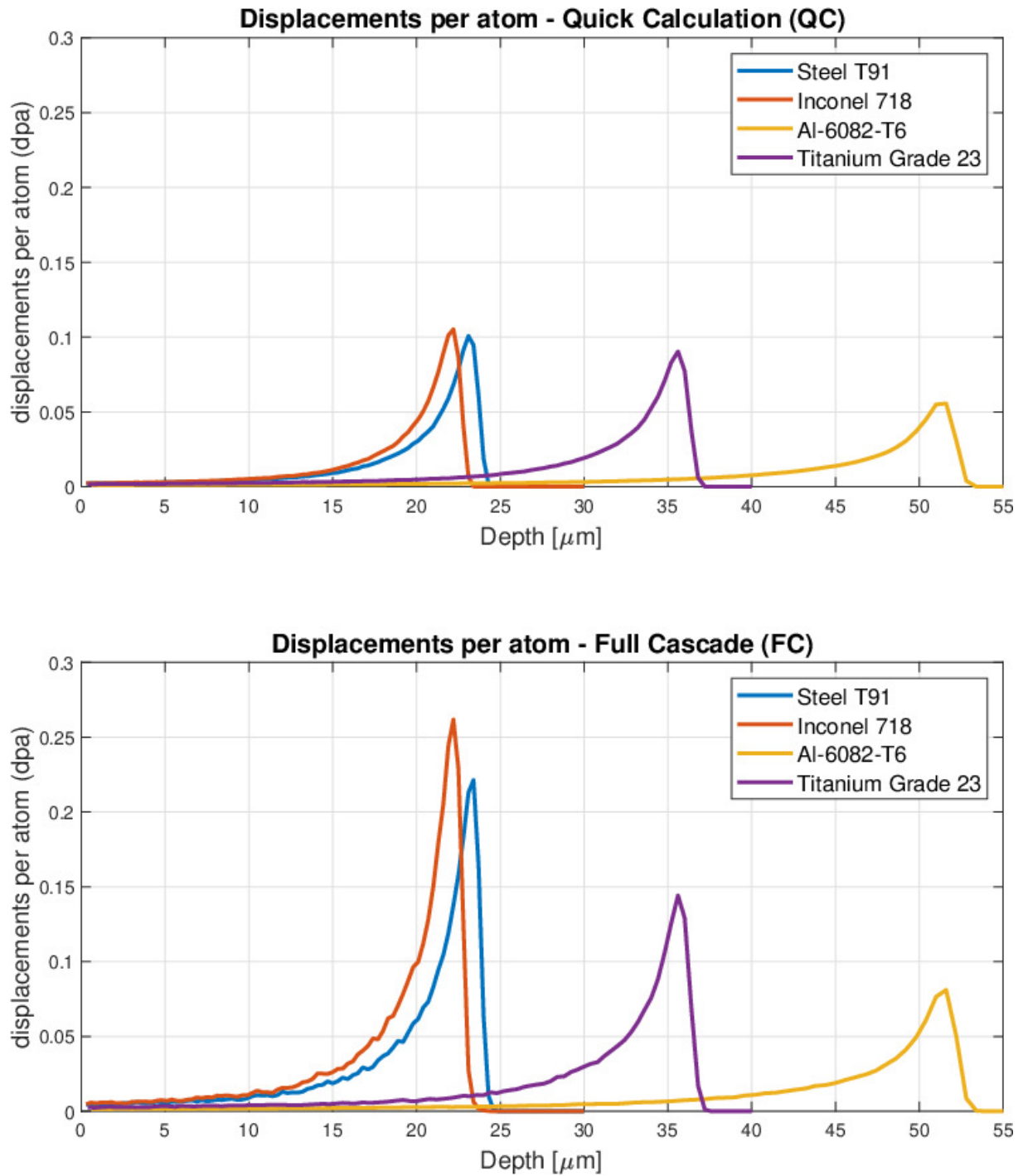


**Figure 4.10:** Displacements per ion, as a function of penetration depth for 1.14 GeV U-ions for the four materials, as calculated by the "Quick Calculation" (top) and "Full Cascade" (bottom) options in the TRIM-2013 code. The graphs have been produced to allow an easier comparison of the penetration depth and the vacancy peak for all the materials.

PKA energy that is transferred to other target atoms through elastic collisions is known as **damage energy**  $T_{dam}$ . By adopting a simplified but accurate version of the NRT (Norgett-Robinson-Torrens) model, the number of stable Frenkel pairs produced by a

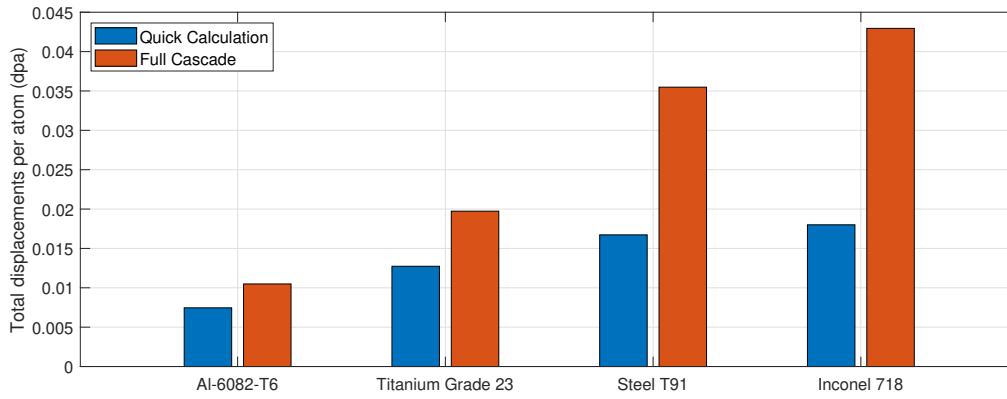


**Figure 4.11:** Bar graph of the total displacements per atom calculated using "Quick Calculation" and "Full cascade" options of the TRIM-2013 code.

PKA with damage energy  $T_{dam}$  is equal to:

$$\nu_{\text{NRT}} = \begin{cases} 0 & \text{if } T_{dam} < E_d \\ 1 & \text{if } E_d < T_{dam} < 2.5E_d \\ \frac{0.8T_{dam}}{2E_d} & \text{if } T_{dam} > 2.5E_d \end{cases} \quad (4.7)$$

with  $E_d$  representing the energy required to create a stable Frenkel pair (namely, the threshold displacement energy). The depth-dependant damage energy  $T_{dam}$  can be obtained by the SRIM output text files by subtracting the energy absorbed by the "recoils column" from "E2RECOIL.txt" to the ionisation energy loss of the "recoil ion column" from "IONIZ.txt":

$$T_{dam} = E_{recoil} - E_{ionizr} \quad (4.8)$$

The threshold displacement energy ( $E_d$ ) of each target can be obtained in two ways: by using the predetermined values of the SRIM software in the "TDATA.txt" file or by using values from the literature.

The total dpa computed by SRIM-2013 ( $\nu_{max}$ ) have as a unit of measurement the displacement per ion. To remove the dpa dependence from the type of ion source, the total displacements per atom of the target material can be obtained by the following formula:

$$dpa = \frac{\nu_{max} \cdot \Phi}{d_p \cdot N} \quad (4.9)$$

where  $N = \rho N_A / A$  is the target atomic density [atoms/cm<sup>3</sup>],  $\Phi$  is the total fluence [ions/cm<sup>2</sup>],  $\nu_{max}$  the displacements per ion and  $d_p$  the penetration depth, in cm.

The figure 4.9 shows the difference in dpa calculation using the two methods proposed for Q-C option. As can be seen, all four graphs are practically the same for the two

methods: which means that the calculation performed by SRIM is correct and accurate. The figure 4.8-4.10 show the dpa results for "Full cascade" option. As expected, dpa calculation for F-C is higher than what obtained from Q-C: in the case of Inconel 718, the difference is very wide, with a ratio between F-C and Q-C of about 2.5. The table 4.1 and the bar plot 4.11 summarise the results obtained in terms the dpa and show how the difference of dpa calculation between F-C and Q-C options increases as the Z number increases.

## 4.2 Thermomechanical simulations

The benchmark of the results obtained by the LDV and the Thermal Camera measurements was carried out by using the numerical simulation software ANSYS [88].

### 4.2.1 Model description

The first step in developing the simulation model was to reproduce the same geometry as the specimens irradiated on the simulation software and to produce the most appropriate mesh for accurate and efficient solutions of the thermomechanical simulations.

#### Geometry Modelling

ImageJ, a Java-based software for processing and analysing scientific images, was utilised to determine the precise geometry of the samples and, in particular, the area of the beam spot [89]. A change in colouration (easily visible even with the naked eye) of the area irradiated by the U-ions during the experiment was experienced by both the Titanium and Inconel samples. A high-resolution picture of the Inconel 718 sample was used to establish the position and the dimension of the beam spot, considered the same for all the irradiated specimens: if the unclamped diameter of the disc is known (18 mm), the beam spot was found to have an almost circular shape with a diameter of around 6 mm, as can be seen from the figure 4.12 (a).

The geometry of each sample was designed by using the solid modelling CAD software SpaceClaim, integrated in the ANSYS Simulation packages [90]. The result of the SpaceClaim model for the Inconel 718 sample is shown in figure 4.12 (b). Each design of the samples has been composed of four separated bodies, but all of them are firmly attached to one another through the Shared topology function. Shared topology is the only way to achieve a conformal mesh where bodies meet, and it is the only way to be certain that the intersection of bodies will be properly meshed. The four bodies in question are the "Rim", corresponding to the outer volume in which the sample is clamped to the sample

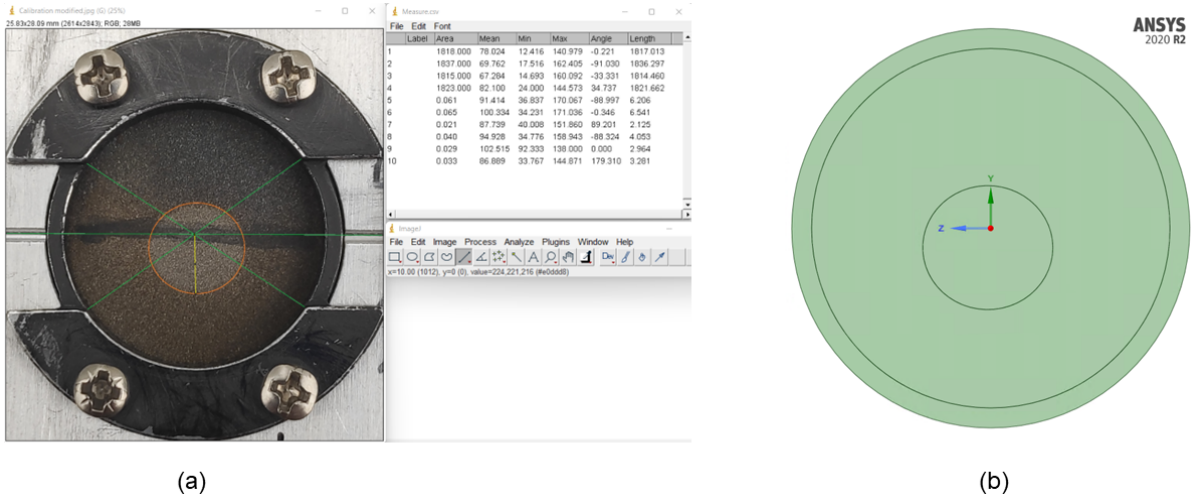


**Figure 4.12:** (a) Inconel 718 sample analysed by ImageJ software to identify the size of the beam spot. (b) ANSYS SpaceClaim model of Inconel sample.

holder, the "Deposition volume", a cylindrical volume with an area equal to the beam spot and thickness equal to the specific penetration depth of the material, as calculated by the SRIM-2013 code (table 4.1), the "Back Volume", i.e. the volume behind the "Deposition volume", and the "Disk", that consists in the annular volume between the beam spot and the rim.

### Mesh generation

Since the mesh influences the accuracy, convergence and speed of the thermomechanical simulations, it is very important to forecast the size of the elements — to be created by meshing the geometry — that allows for performing reliable numerical simulations. In order to fully appreciate the dynamic effects induced by the impact of the Uranium ions on the beam spot, where the ions release heat, a more dense mesh is required in the centre. The slower phenomena of thermal diffusion externally to the beam spot may be captured with elements slightly larger than the central ones. Taking this into consideration, the ANSYS functions of "Edge sizing" and "Face sizing" were used to create a mesh that becomes more sparse as the radius of the sample increases.

To understand if a certain mesh density is sensitive to catch the typical quantities of a quasi-instantaneous event or if it is needed to be adjusted to improve the accuracy of the simulation, the convergence condition by Courant–Friedrichs–Lewy was used. The CFL condition can be written in the following way:

$$C = \frac{u\Delta t}{\Delta x} \leq C_{max} \quad (4.10)$$

where the dimensionless number  $C$  is called the Courant number,  $u$  is the magnitude of the velocity of a given phenomenon (whose dimension is length/time),  $\Delta t$  is the time step

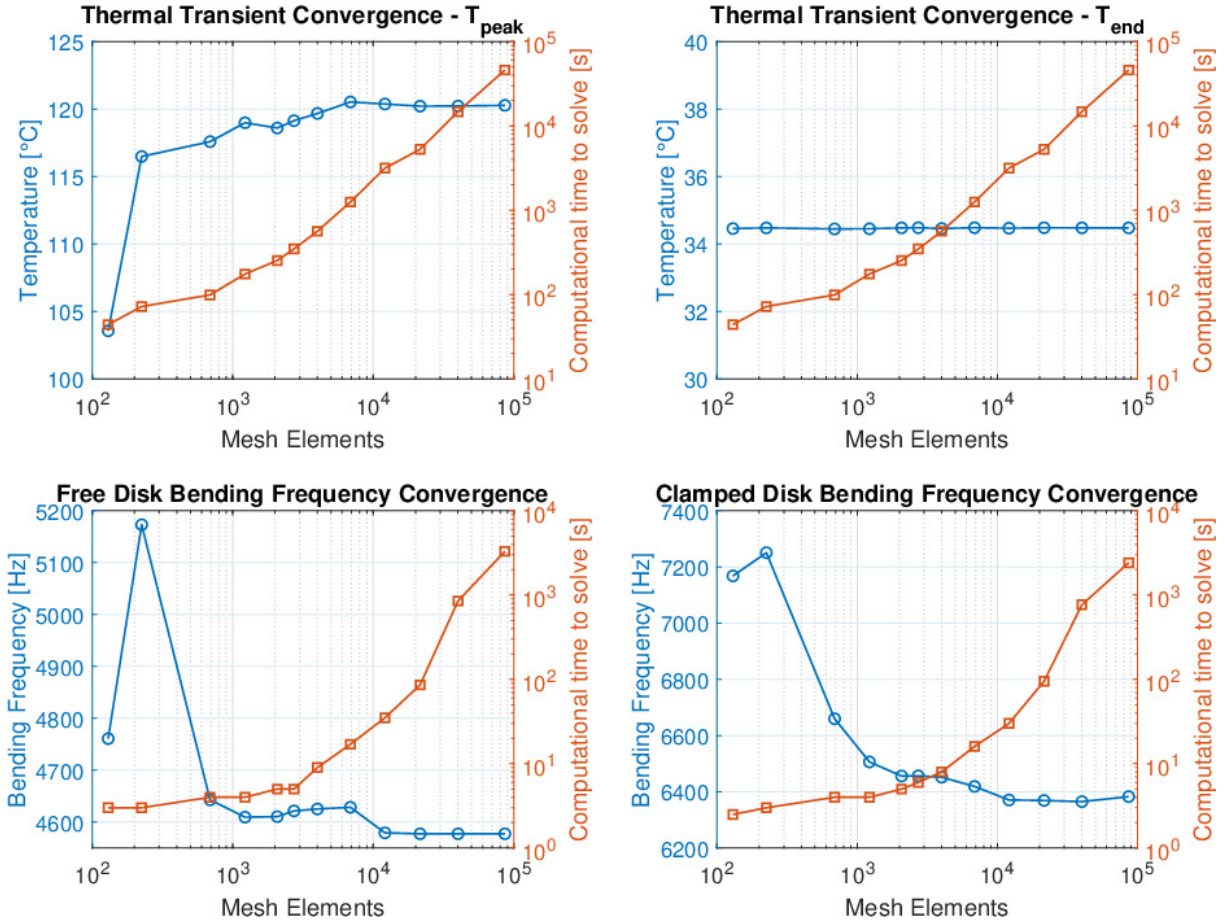


**Figure 4.13:** Convergence criterion: the four graphs were plotted with the aim of correlating the results in the calculation of a certain quantity (temperature, vibration frequency, etc.) to the computational time to solve the simulation and to the number of elements in the mesh.

(whose dimension is time) and  $\Delta x$  is the length interval (whose dimension is length). For simplicity, a single mesh for each material sample was created for both thermal and structural simulations. The solution of the CFL condition took into account the main phenomena involved in the process of beam impact, from the point of view of both dynamic and thermal effects: the key input parameters were the time of beam heat deposition ( $t_{pulse}$ ), the velocity of heat propagation along the radius and through the thickness ( $v_{th,diff}^r \approx \alpha/R$  and  $v_{th,diff}^{th} \approx \alpha/h$ ), the velocity of the pressure waves through the thickness ( $v_P$ ) and the velocity of the shear-vertical waves along the radius ( $v_S$ ). Guessed values of radial and axial  $\Delta x$  have been alternatively used to find  $\Delta t$ , and vice versa.

A more intuitive method to verify the accuracy of the chosen mesh is to perform the same type of numerical analysis with an increasing number of nodes and elements in the mesh: in this way, depending on the results obtained, it is straightforward to understand if the convergence for a certain numerical calculation was achieved. For the geometry designed, two parameters were progressively increased, namely the number of radial slices and the number of subdivisions of the thickness. The results of this procedure are shown



in the four graphs in figure 4.13, in which the left vertical axes represent the specific quantities simulated, the right vertical axes present the computational time needed to perform the simulation, and the abscissae indicate the number of elements. The two graphs at the top of the figure 4.13 represent the results in terms of peak temperature and end-of-transient (1 second after the beam pulse) temperature at the centre of the geometry of Inconel 718, as it was found by performing *ANSYS Thermal Transient* simulations. The two charts below show the results of the natural vibration frequency in the clamped and free edge conditions for the geometry of Inconel 718, as a result of the *ANSYS Modal* simulations. As can be seen by the charts, the convergence is reached for all the quantities simulated with a mesh that includes about 10000 elements.

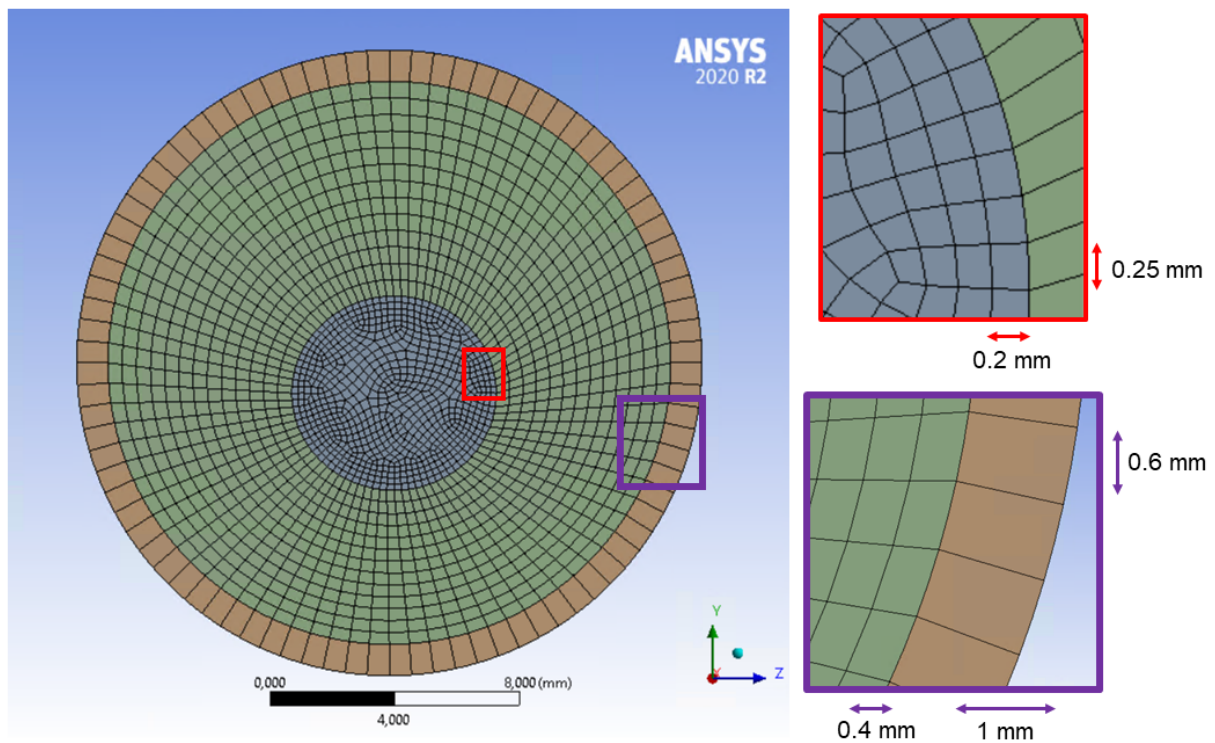


**Figure 4.14:** Mesh on the front side of the Inconel 718 sample. The highlighted parts on the right show the difference in mesh density as the radius increases, with the element width that changes from 2 mm up to 10 mm.

Accordingly, a mesh density of around 20000 elements was chosen for the 200  $\mu\text{m}$ -thick samples (T91, Inconel and Ti23), while about 40000 elements were considered appropriate for the 405  $\mu\text{m}$ -thick Aluminium alloy sample. Such a choice comply the considerations concerning the Courant–Friedrichs–Lewy conditions seen before.

The figures 4.14 and 4.15 illustrate the meshed geometry of the Inconel 718 sample from the front and lateral sides. The zoom-ins at the right of the figures show much more clearly the element sizes in various points of the modelled geometry. The element width at the centre is around 0.2 mm, which is about one-hundredth of the diameter of

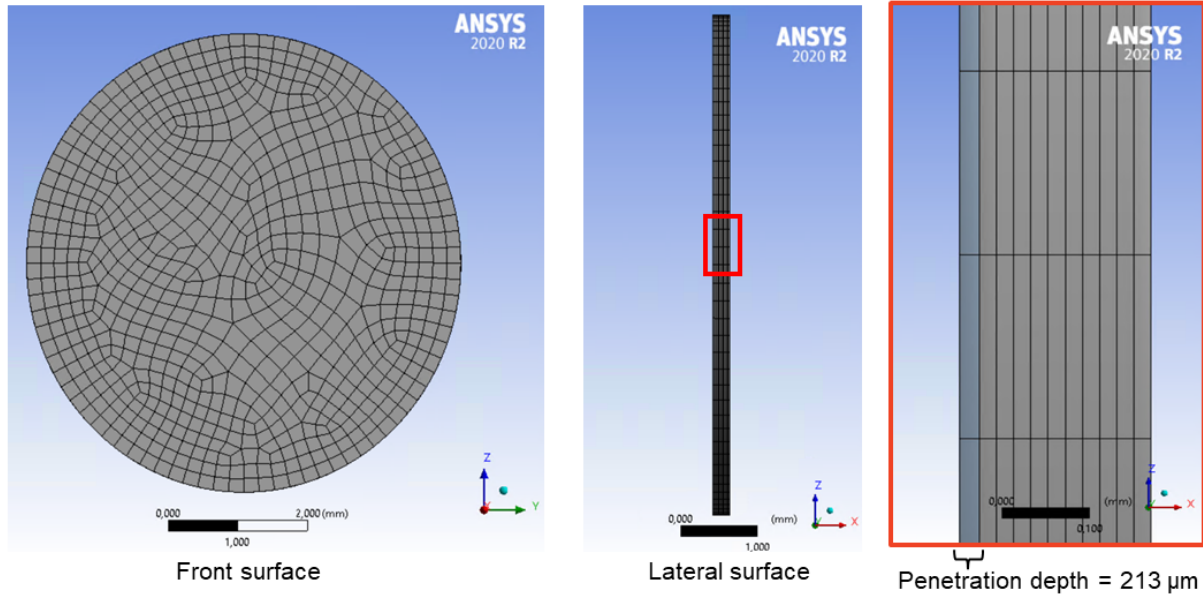


**Figure 4.15:** Mesh on the lateral side of the Inconel 718 sample. The highlighted part on the right shows the number of elements along the thickness.

the sample. The number of subdivisions along the thickness was selected in such a way that the thickness of one element was smaller than the penetration depth (that can be distinguished from the other bodies by the blue colour, as can be seen in the figure 4.15 (right)).

#### 4.2.2 Transient thermal simulations

The transient thermal simulations, performed by *ANSYS Transient Thermal*, are essential to map the temperature distribution after the beam impact and to compare the numerical results with the experimental findings of the Thermal Camera and with results obtained analytically. Moreover, considering that the TC resolution time is around 0.678 ms, a higher value than the pulse deposition time ( $t_{\text{pulse}} = 0.1\text{ms}$ ), numerical simulations allow achieving a more reliable value of the maximum temperature reached in the material samples compared to what observed by the Thermal Camera.

The *ANSYS Transient Thermal* simulations were performed in the interval of time between two successive pulses, equal to 1 second, in order to estimate the temperature distribution on the entire sample resulting from the beam heat deposition before the impact of the successive pulse. This thermal analysis is founded on the following considerations and assumptions:

1. All the energy content of the incident beam particles is ultimately converted into heat because of the mechanism of ionisation energy loss.
2. The entire amount of energy is deposited uniformly into a volume with a surface

equal to the beam spot (6 mm x 6 mm, approximately) and thickness equal to the penetration depth ( $d_p$ ) of the U-ions into the target samples.

3. The conductive heat transfer between the outer diameter of the samples and the circular clamping rims can be neglected since it is unlikely that the heat can reach the outer edges before the impact of the successive pulse<sup>1</sup>
4. The amount of heat removed by convection is practically zero, given that high-vacuum conditions were established inside the M3-Branch Spectroscopy Chamber, where the sample holders had been mounted, for the irradiation experiment.
5. The heat removal by thermal radiation with the walls of the Spectroscopy Chamber could be relevant only for the surface of the beam spot and must be considered in the simulations<sup>2</sup>.

The total amount of energy (i.e. heat) deposited by a U-ion pulse on the beam spot of the material samples can be implemented in *ANSYS Transient Thermal* as a specific heat power (or "Internal Heat Generation, as it is called in ANSYS) inside the geometry body called "Deposition Volume". To calculate it, the ion flux was first converted to thermal flux by using the following equation:

$$q''[MW/cm^2] = \frac{E_u[MeV/u] \cdot N_{U238}[u/ion] \cdot \varphi[ions/cm^2] \cdot C_f[MeV \text{ to MJ}]}{t_{pulse}[s]} \quad (4.11)$$

where  $\varphi$  is the ion flux per pulse,  $E_u$  is the kinetic energy per nucleon,  $N_{U238}$  is the number of nucleons per U-ion,  $C_f$  is the conversion factor from MeV to MJ and  $t_{pulse}$  the pulse-length, equal to 100  $\mu s$ . From this calculation, a thermal flux of about 91.52 MW/m<sup>2</sup> has been found. If this value is divided by the specific penetration depth of each target sample:

$$q''' = \frac{q''}{d_p} \quad (4.12)$$

the specific heat power  $q'''$ , the main input data for thermal simulations, is obtained.

### Thermal analytical calculations

Thermal analytical calculations, based on the concept of the specific heat power inside the beam spot, were performed to support and check the results of the thermal simulations. These calculations are essentially founded on the law of energy conservation, written in a

<sup>1</sup>The thermal diffusion time, a useful quantity for assessing the heat spreading in the radial direction, is higher than 1 second for all the irradiated samples (cf. Table 3.2).

<sup>2</sup>A unit value of emissivity (as for a black body) was chosen for all the geometries because black paintings were applied on the central surface of each sample by a conductive graphite spray.

Thermal data			Materials			
			T91 Steel	Inconel 718	Al 6082 T6	Ti Grade 23
U-ion beam	Thermal flux per single pulse	q'' [MW m-2]	91,52	91,52	91,52	91,52
	Penetration depth (SRIM)	dp [ $\mu$ m]	23,26	22,21	51,39	35,73
	Internal Heat Generation	q''' [W mm-3] (ANSYS input)	3935,35	4121,25	1780,72	2561,19
Thermal Camera	T ambient [°C]	First pulse	26,17	28,12	28,05	26,94
		2E+13 ions cm-2	32,83	39,69	28,69	51,34
Analytical calculations	Peak	First pulse	136,27	143,18	101,33	136,79
	Temperature [°C]	2E+13 ions cm-2	142,94	154,75	101,97	161,19
	Steady-state	First pulse	27,39	29,31	29,00	28,75
	Temperature [°C]	2E+13 ions cm-2	34,05	40,87	29,63	53,15

**Table 4.2:** Thermal data for ANSYS transient thermal simulations and analytical findings.

way that allows assessing the maximum temperature and the temperature at the end of the thermal transient.

The **theoretical maximum temperature**, namely the peak in temperature reached at the end of the phase of heat deposition, can be easily computed in the hypothesis that no thermal diffusion occurs in the short period of pulse impact. The equation of conservation of energy can be written as:

$$q''' V_{\text{irr}} t_{\text{pulse}} = \rho c_p V_{\text{irr}} (T_{\text{max}} - T_{\text{amb}}) \quad (4.13)$$

from which the theoretical maximum temperature  $T_{\text{max}}$  is derived:

$$T_{\text{max}} = T_{\text{amb}} + \frac{q''' t_{\text{pulse}}}{\rho c_p} \quad (4.14)$$

where  $T_{\text{amb}}$  is the ambient temperature, i.e. the temperature of the samples before the pulse,  $V_{\text{irr}}$  the "Deposition Volume" and  $V_{\text{tot}}$  the entire volume of the sample.

Similarly, the temperature at the end of the transient can be found. If all the heat deposited in the "Deposition volume" is perfectly spread for the whole sample, all the sample reaches the same asymptotic temperature  $T_{\infty}$ , given by the equation:

$$T_{\infty} = T_{\text{amb}} + \frac{q''' t_{\text{pulse}} V_{\text{irr}}}{\rho c_p V_{\text{tot}}} \quad (4.15)$$

The  $T_{\text{amb}}$  was obtained from the thermal camera findings for all the pristine and fully-irradiated samples (first and last pulse). All the results of the calculations described so far can be found in the table 4.2.

## Results of the thermal simulations

The following figures 4.16, 4.17, 4.18, 4.19, 4.20, 4.21, 4.22 and 4.23 show the results obtained by the *ANSYS Transient Thermal* simulations carried out for the pristine (first

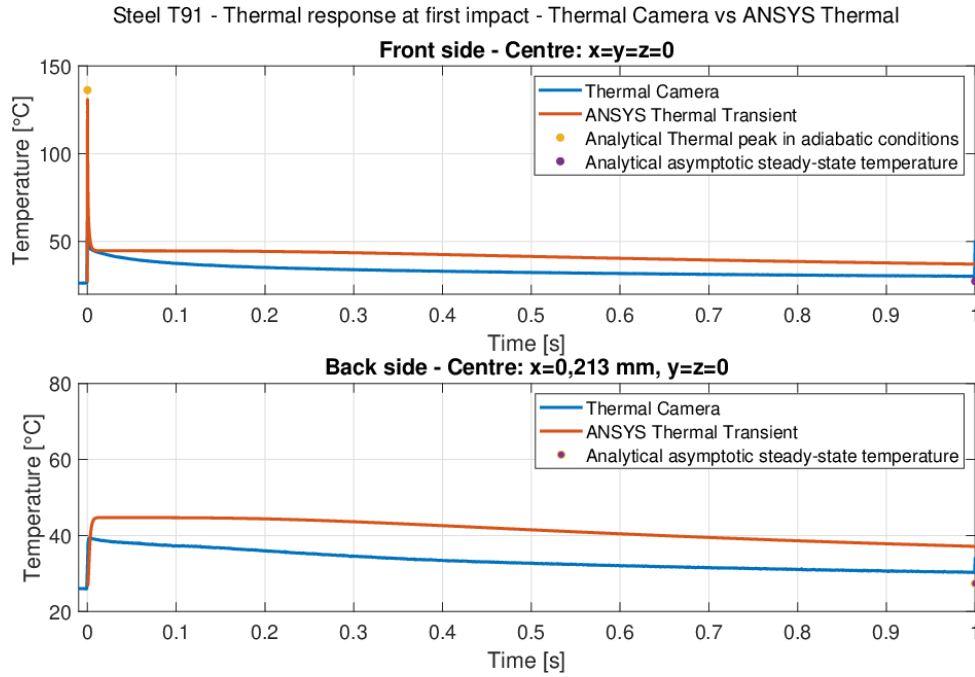


**Figure 4.16:** Temperature distribution at the centre of the Steel T91 sample on the front side (top) and on the back side (bottom) at the first pulse and comparison with both the Thermal Camera data and the analytical findings.

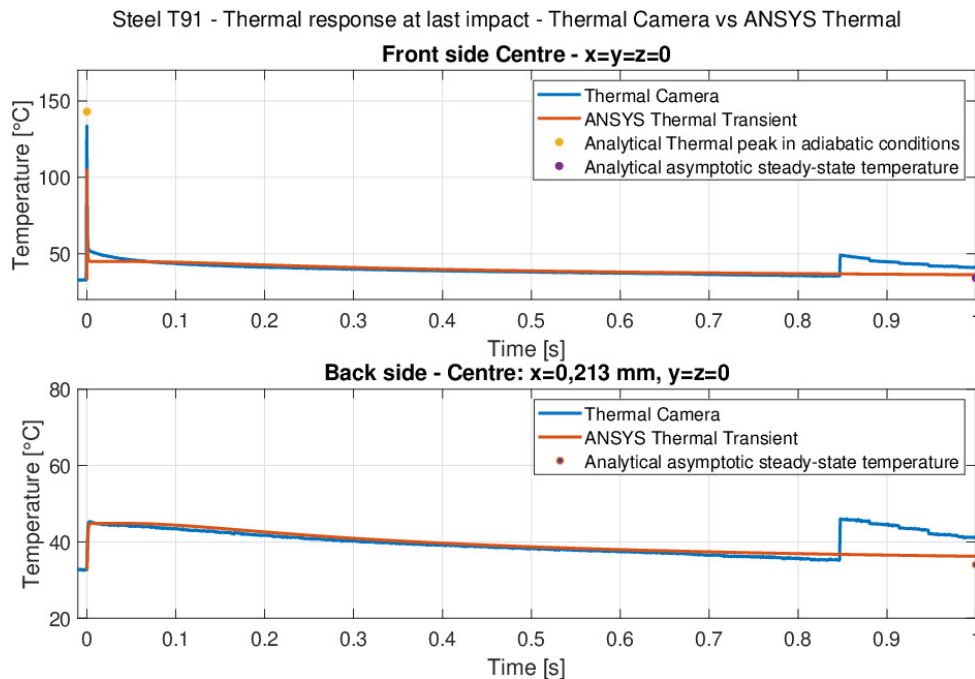


**Figure 4.17:** Temperature distribution at the centre of the Steel T91 sample on the front side (top) and on the back side (bottom) at the last pulse and comparison with both the Thermal Camera data and the analytical findings.

pulse) and fully-irradiated (last pulse) conditions of the four samples. These data have been extracted by a "Temperature Probe" located on a central node of the front and back

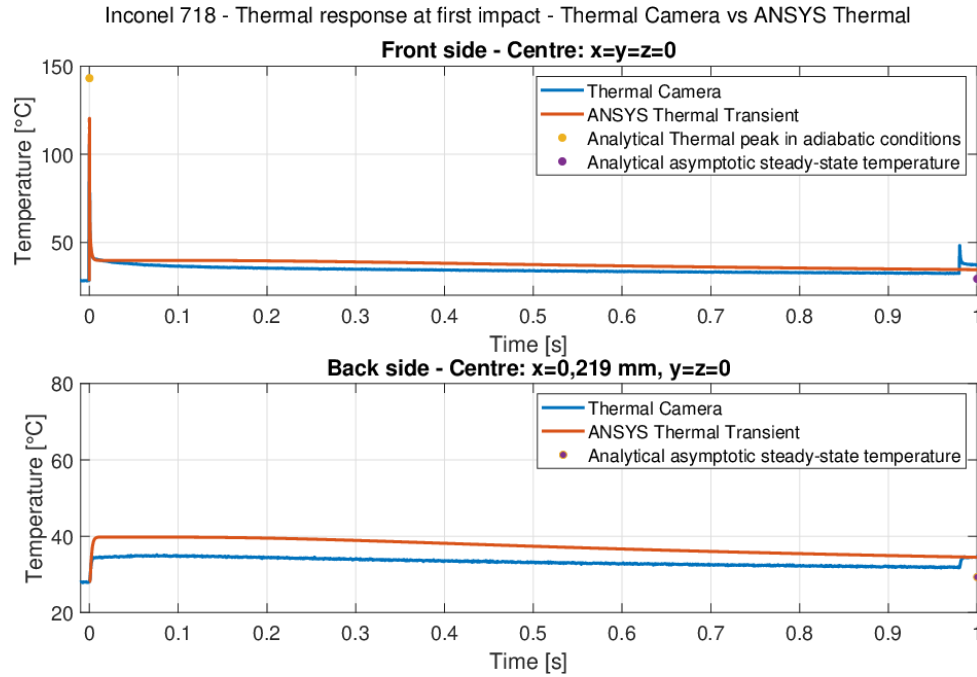


**Figure 4.18:** Temperature distribution at the centre of the Inconel 718 sample on the front side (top) and on the back side (bottom) at the first pulse and comparison with both the Thermal Camera data and the analytical findings.

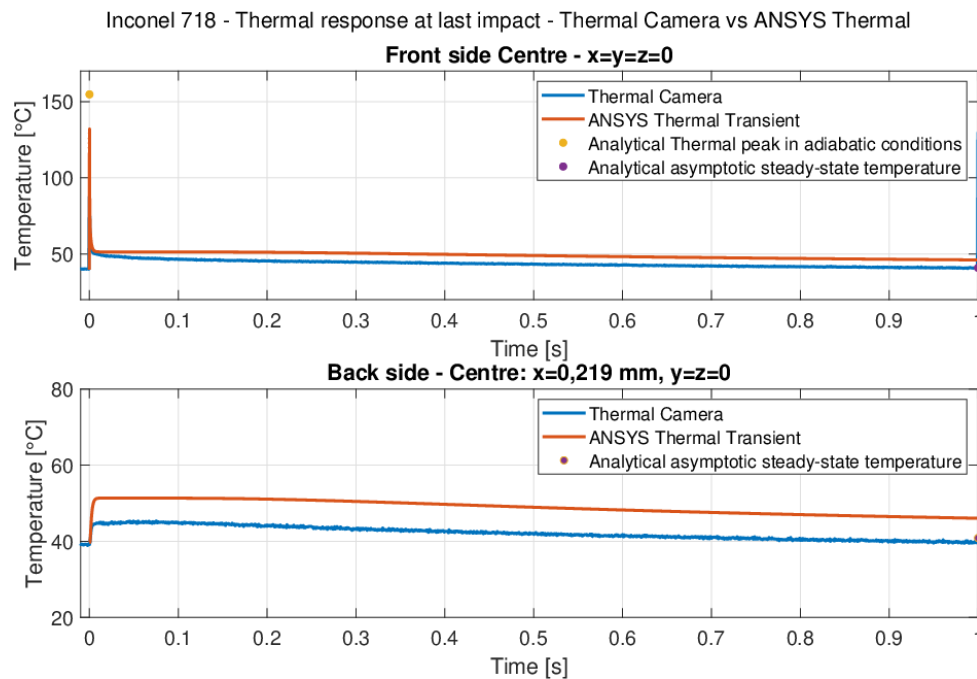


**Figure 4.19:** Temperature distribution at the centre of the Inconel 718 sample on the front side (top) and on the back side (bottom) at the last pulse and comparison with both the Thermal Camera data and the analytical findings.

surface of the designed sample, in such a way to compare them with the data from the Thermal Camera related to the front and back surface of the samples.



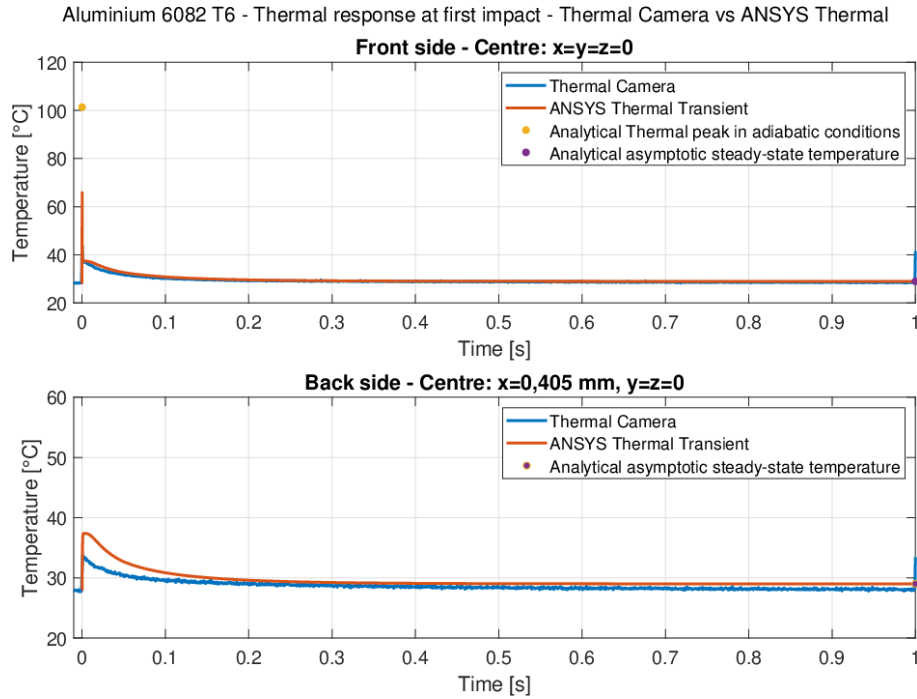


**Figure 4.20:** Temperature distribution at the centre of the Al-6082-T6 sample on the front side (top) and on the back side (bottom) at the first pulse and comparison with both the Thermal Camera data and the analytical findings.

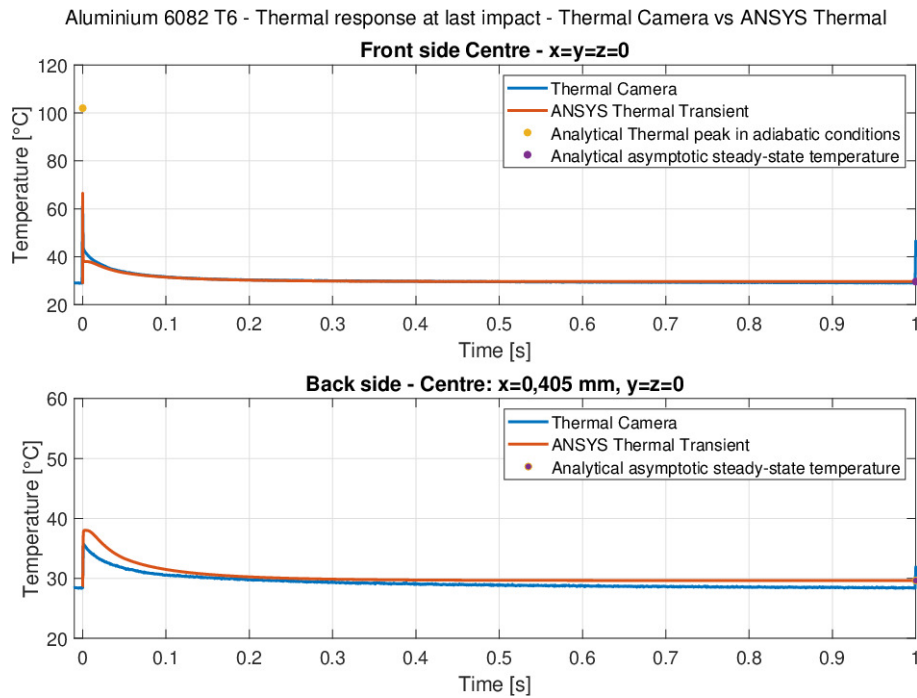


**Figure 4.21:** Temperature distribution at the centre of the Al-6082-T6 sample on the front side (top) and on the back side (bottom) at the last pulse and comparison with both the Thermal Camera data and the analytical findings.

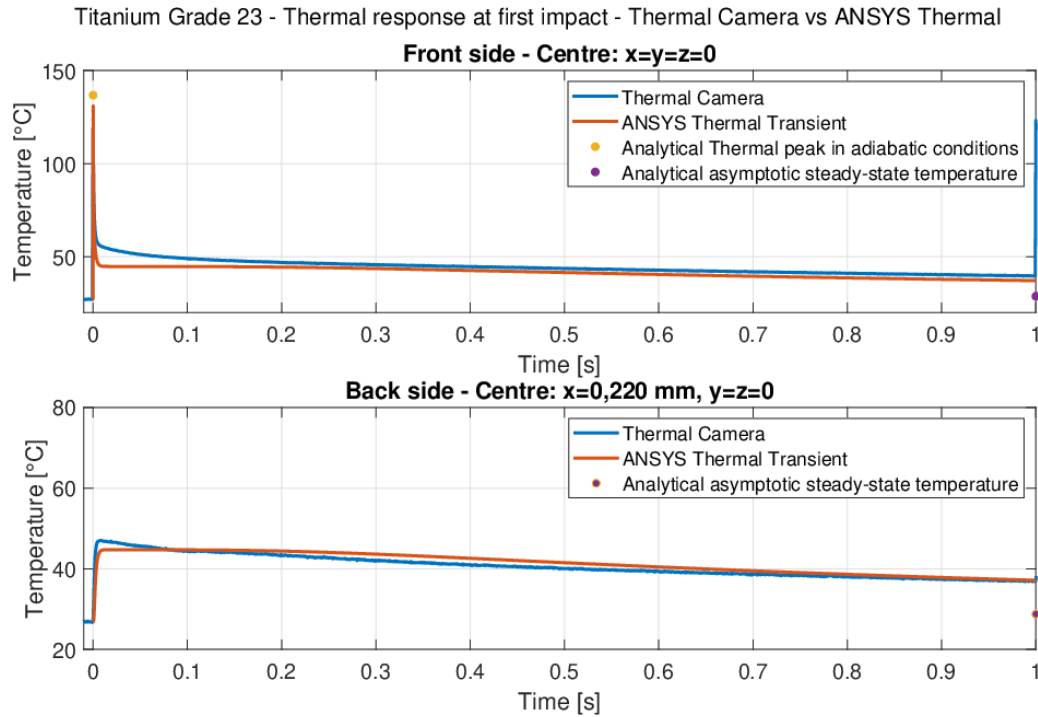


**Figure 4.22:** Temperature distribution at the centre of the Titanium Grade 23 sample on the front side (top) and on the back side (bottom) at the first pulse and comparison with both the Thermal Camera data and the analytical findings.

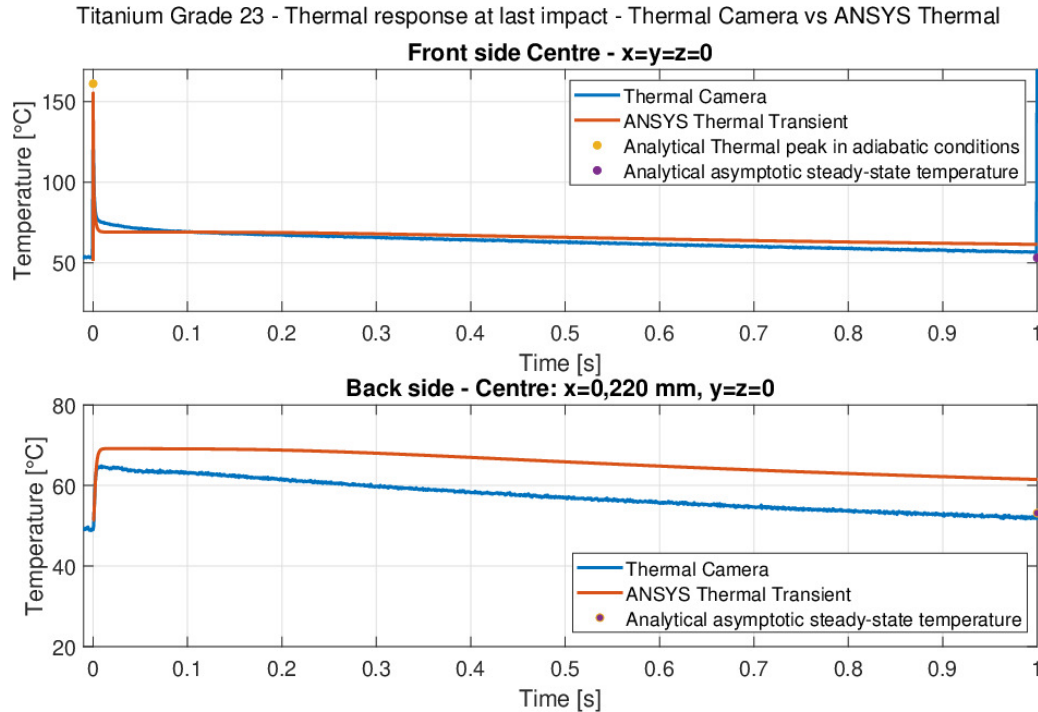


**Figure 4.23:** Temperature distribution at the centre of the Titanium Grade 23 sample on the front side (top) and on the back side (bottom) at the last pulse and comparison with both the Thermal Camera data and the analytical findings.

The time steps of the simulation have been properly tuned to catch the thermal phenomena: during the rapid heat deposition, a time step of  $10^{-6}$  seconds was used to search the value of the peak, then the time step was reduced to  $5 \cdot 10^{-5}$  seconds for the first 50 ms of steep temperature decreasing and, finally, it was further reduced to 0.01 seconds for the phase of thermalisation up to the end of the transient (at 1 second, when the next pulse is expected).

Another interesting thing to note in these figures is the discrepancy between the analytically calculated points and the location of the numerical curve. That results in two essential considerations:

- The difference between the maximum temperatures ( $\Delta T_{\text{peak}} = T_{\text{peak}}^{\text{analytical}} - T_{\text{peak}}^{\text{numerical}}$ ) is inversely proportional to the thermal conductivity of the material:  $\Delta T_{\text{peak}}$  is almost zero for the Titanium alloy, a material with low thermal conductivity, while the difference is distinct (around 40°C) in the case of the more conductive Aluminium alloy.
- On the contrary, the difference between the steady-state temperatures ( $\Delta T_{\infty} = T_{\infty}^{\text{numerical}} - T_{\infty}^{\text{analytical}}$ ) is proportional to thermal conductivity since a material with higher conductivity (and, therefore, thermal diffusivity) thermalises in a shorter period of time (compare the figure 4.20 with the figure 4.22).

The figures 4.24 and 4.25, referred to the thermal transient of the Titanium Grade 23 at the first pulse, allow us to describe more precisely the thermal diffusion phenomena and the thermal waves which are generated during this quasi-instantaneous process of heat deposition. Four main stages can be identified in the thermal transient:

- **Stage 1: Deposition of heat inside the volume.** In this very short stage (100  $\mu\text{s}$ ), the temperature increases only in the deposition volume, and thermal diffusion effects are negligible. At the end of this stage, the maximum temperature (peak temperature) is obtained, and concentric waves, with a temperature lower than the ambient one, are generated outside the beam spot surface.
- **Stage 2: Rapid spread of heat.** Temperature decreases very quickly in the 10 ms after the pulse, with a negative exponential trend. The heat diffusion occurs only axially (in the thickness direction), while the heat is not dissipated outside the beam spot in the "Disk" volume. This stage stops when the heat manages to reach the back surface.
- **Stage 3: Plateau.** After the completion of axial diffusion, the heat starts to diffuse radially. In the following 300 ms, only the peripheral parts of the beam spot diffuse with the "Disk" volume, while the centre remains at a constant temperature.

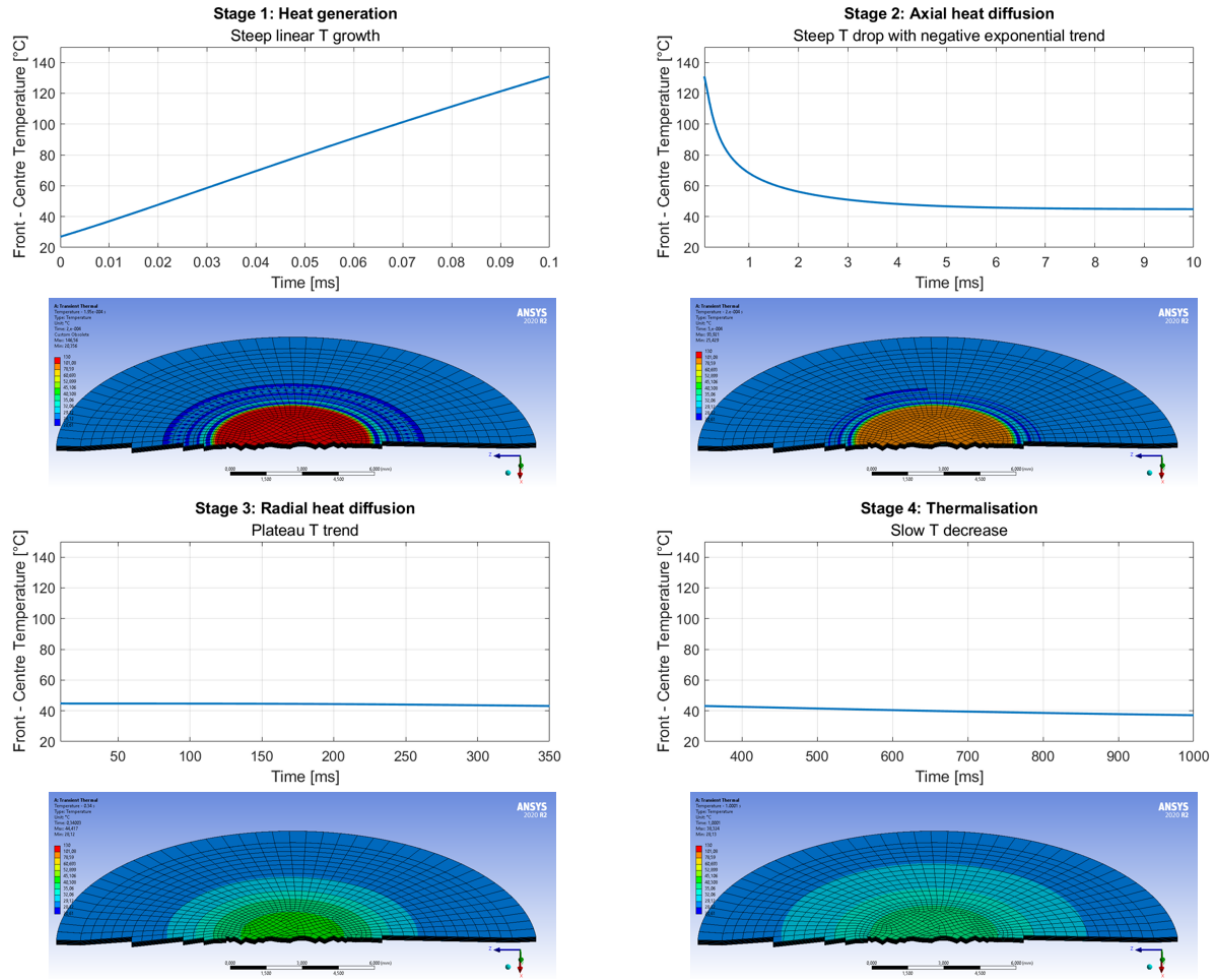


**Figure 4.24:** Temperature distribution at the centre of the Titanium Grade 23 sample on the front side as a function of time. The temperature distribution is divided into four plots, representing significant stages in the heat diffusion process. An ANSYS screenshot corresponding to the end time of each plot is reported.

- Stage 4: **Thermalisation.** The thermal diffusion process is completely established throughout the disc, and even the temperature at the Front-Centre starts to decrease linearly with a very low slope (very slow process). From the analytical calculations presented in table 3.2, the process of thermalisation for the sample of Titanium Gr. 23 is expected to run out after around 35 seconds from the beam pulse.

### 4.2.3 Modal and Transient structural simulations

Transient structural simulations, connected to the solution of thermal transient simulations, have been carried out to investigate the dynamic effects due to the beam impact on the samples. Moreover, these simulations play the role of the benchmark with respect to the vibration phenomena observed in-situ by the LDV, the analytical calculations on the characteristic frequencies and the radiation damages in terms of increase in Young's

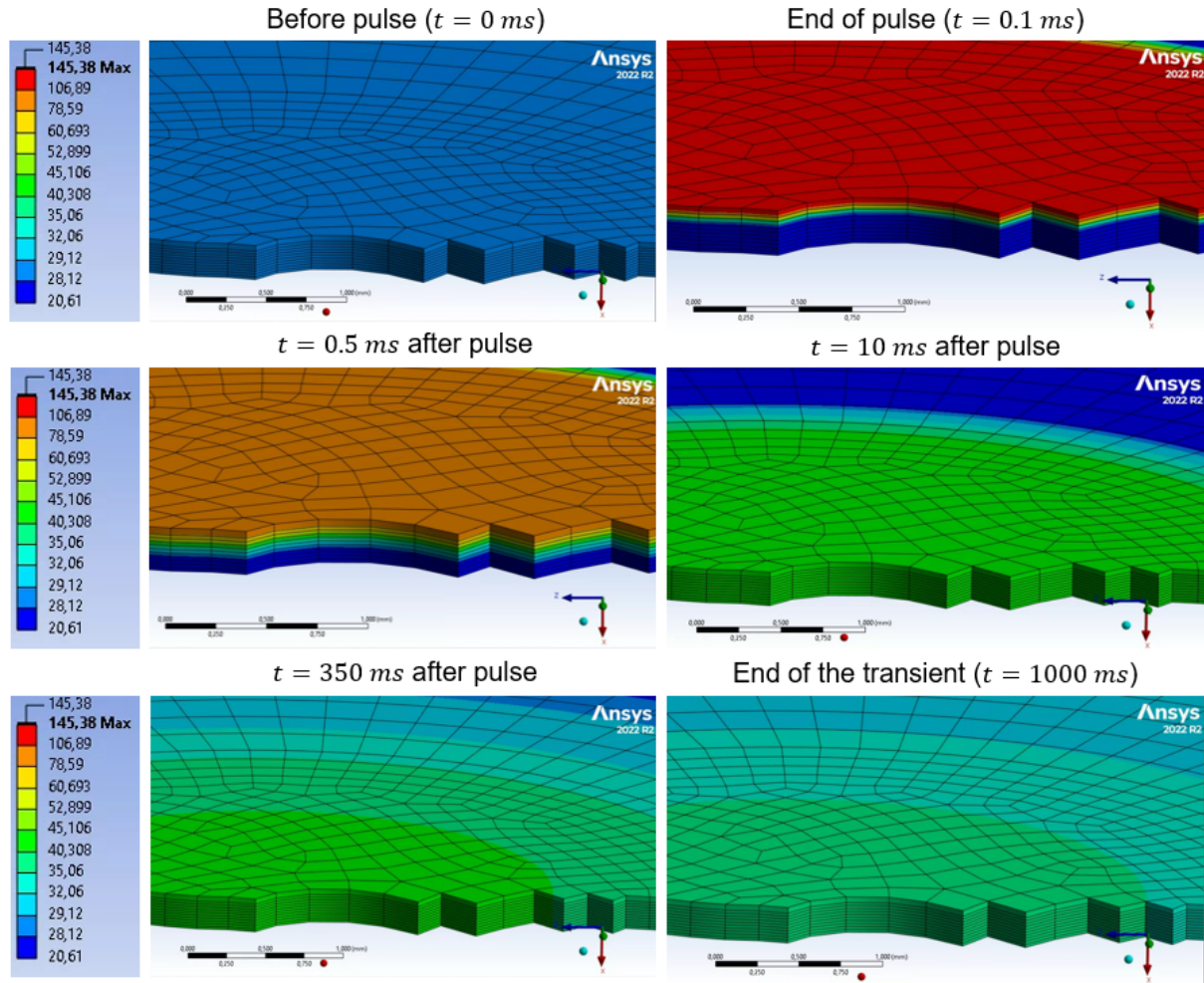


**Figure 4.25:** Focus on the temperature distribution at the centre of the Titanium Grade 23 sample on the front side at the first pulse as a function of relevant moments of the heat diffusion process.

modulus, as found by the microindentation tests.

Since the propagation of waves was not captured by the LDV, the structural simulations have been focused on identifying the first bending frequency of vibration and matching this frequency to the one recorded by the Laser Doppler Vibrometer for the pristine and fully-irradiated samples.

As explained above, the beam-induced rapid heat deposition increases the temperature of the superficial zone only, thus inducing the thermal expansion of the surface and leading to the generation of bending modes. The quasi-instantaneous nature of the resulting dynamic phenomena and their effects on the global behaviour of the irradiated samples can make it complex to carry out successful numerical simulations.

The most challenging part of these analyses consists in implementing mechanical and thermal boundary conditions that reflect the actual conditions experienced by the material samples during the entire GSI experiment of irradiation. As indicated in chapter 3, each

sample was clamped to a 1 mm-thick rim in such a way that it adhered as much as possible to the sample holder. However, no measure of the amount of tightening force applied by screws to the edges of the samples was performed.

By the comparison between the LDV frequency peaks and the analytical formulas for the first-order bending frequencies in different conditions (free edge, simply-supported edge and clamped edge) it has been seen that the vibration frequency of all the samples can be described by an intermediate boundary condition between simply-supported and free edge.

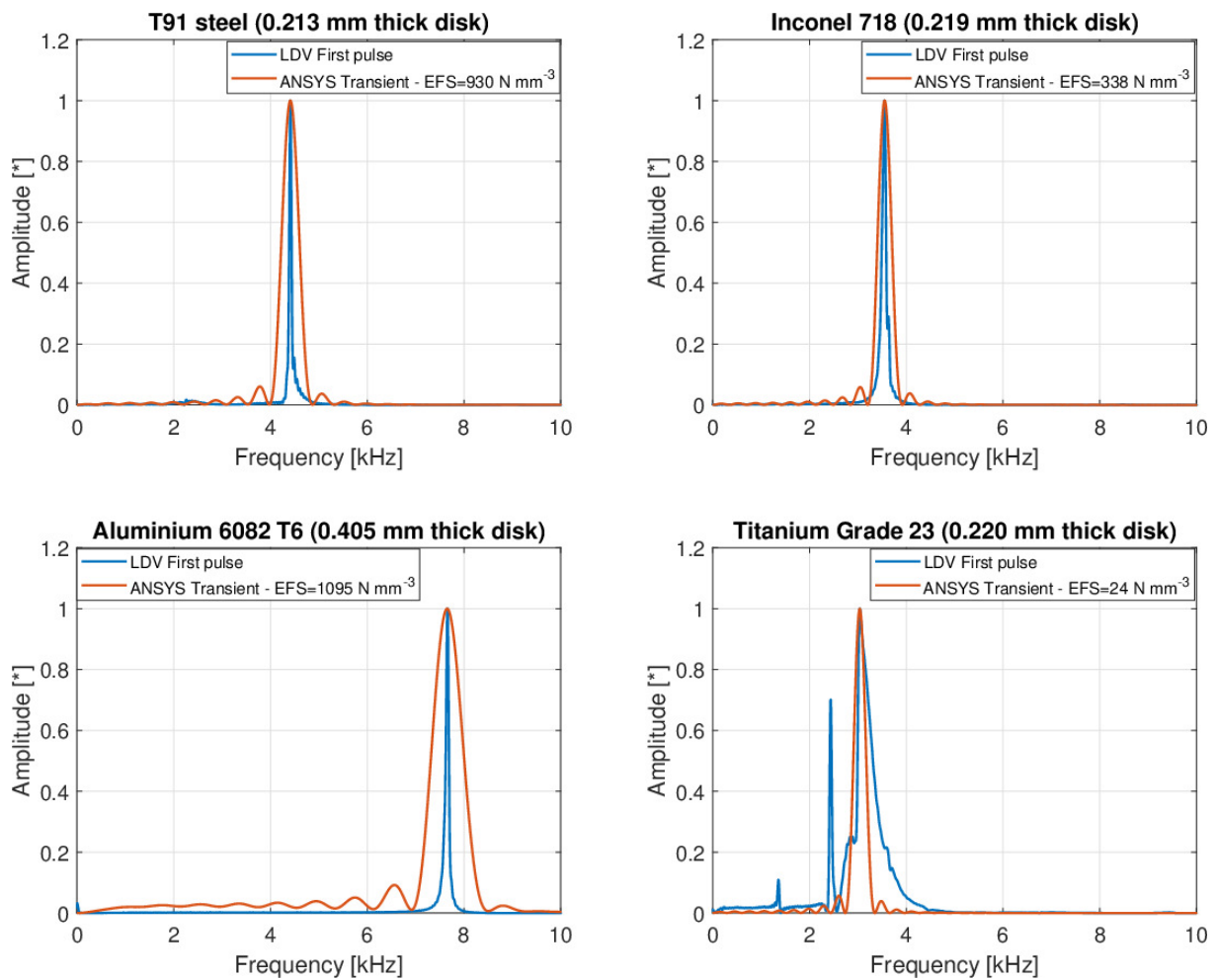


**Figure 4.26:** Comparison of the FFT results in terms of frequency of the ANSYS velocity signal and LDV velocity signal for pristine materials.

An intermediate mechanical boundary condition that may be implemented easily on ANSYS is the **Elastic Support**. In common practice, an Elastic Support defines an elastic foundation between the selected faces of a part or assembly and the ground. The magnitude of the Elastic Support is based on the Elastic Foundation Stiffness, which is defined as the pressure required to produce a unit normal deflection of the foundation [91]. The Elastic Support was hence applied to the front surface of the "Rim" body of all the



samples. The vibration frequency varies greatly with the values of Elastic Foundation Stiffness (EFS): an almost zero value of Stiffness is equal to the condition of Free Edge, while a very high value reflects a simply-supported condition.

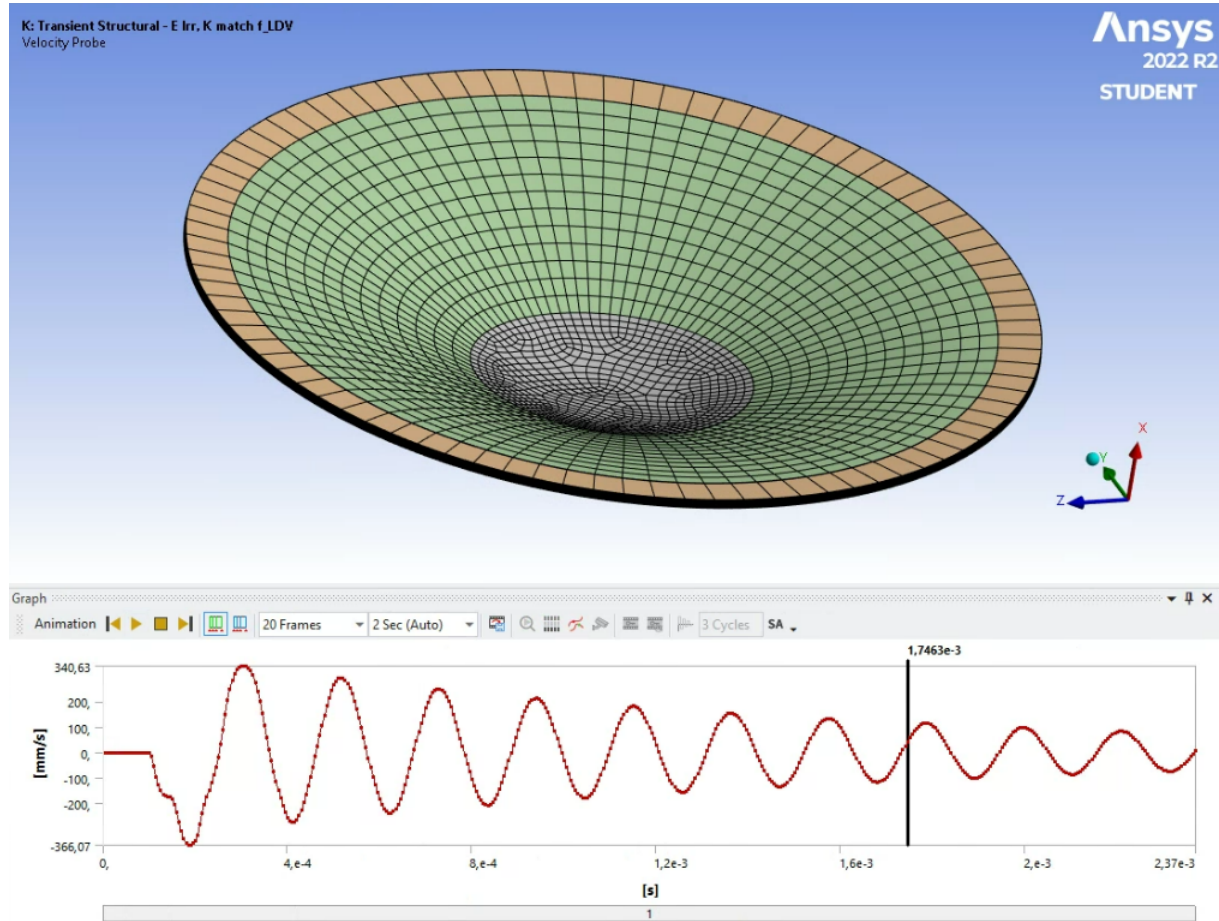


**Figure 4.27:** Screenshot from ANSYS Transient Structural of a disc sample, with results of the Velocity Probe.

The best way to match the LDV Velocity Signal with *ANSYS Transient Structural* numerical analysis is to simulate the beam impact by applying a "Velocity Probe" to the Front-Centre of each material disc (example in ANSYS in figure 4.27). Since the LDV frequency is fairly high, the time step configured in the analysis settings panel of ANSYS Transient must take into account this extreme velocity in order to be able to catch the dynamic response of materials to quasi-instantaneous heating. So it has been decided to apply a time step of  $5 \cdot 10^{-6}$  seconds in only one simulation step, the duration of which is equal to the time required to the velocity signal to represent ten crests of the wave.

Considering that the computational time necessary for a Transient simulation of this length is very long, an easier way to foresee the magnitude of the frequency response is by using the *ANSYS Modal* simulations. A series of Modal analyses were performed in order to find the value of Elastic Foundation Stiffness for which the frequency (calculated

by utilising FFT) of the Velocity Probe better approximated the frequency from LDV for all the pristine materials. The results in terms of frequency are illustrated in the figure 4.26.

After having determined this value of EFS for pristine samples, the value of Young's modulus in the "Deposition volume" was changed with the Young's modulus found through the microindentation measurements for the irradiated beam spot (Chapter 3) and the transient simulations were performed again.

The only change of Young's modulus is unable to explain the larger change in frequency recorded by the LDV, except for the case of Aluminium alloy. This fact led us to think that the change of the Young's modulus is not the sole responsible for the change in frequency and that the other effect that strongly affects the bending frequency is the change of boundary conditions due to the increased temperature and heat accumulation.

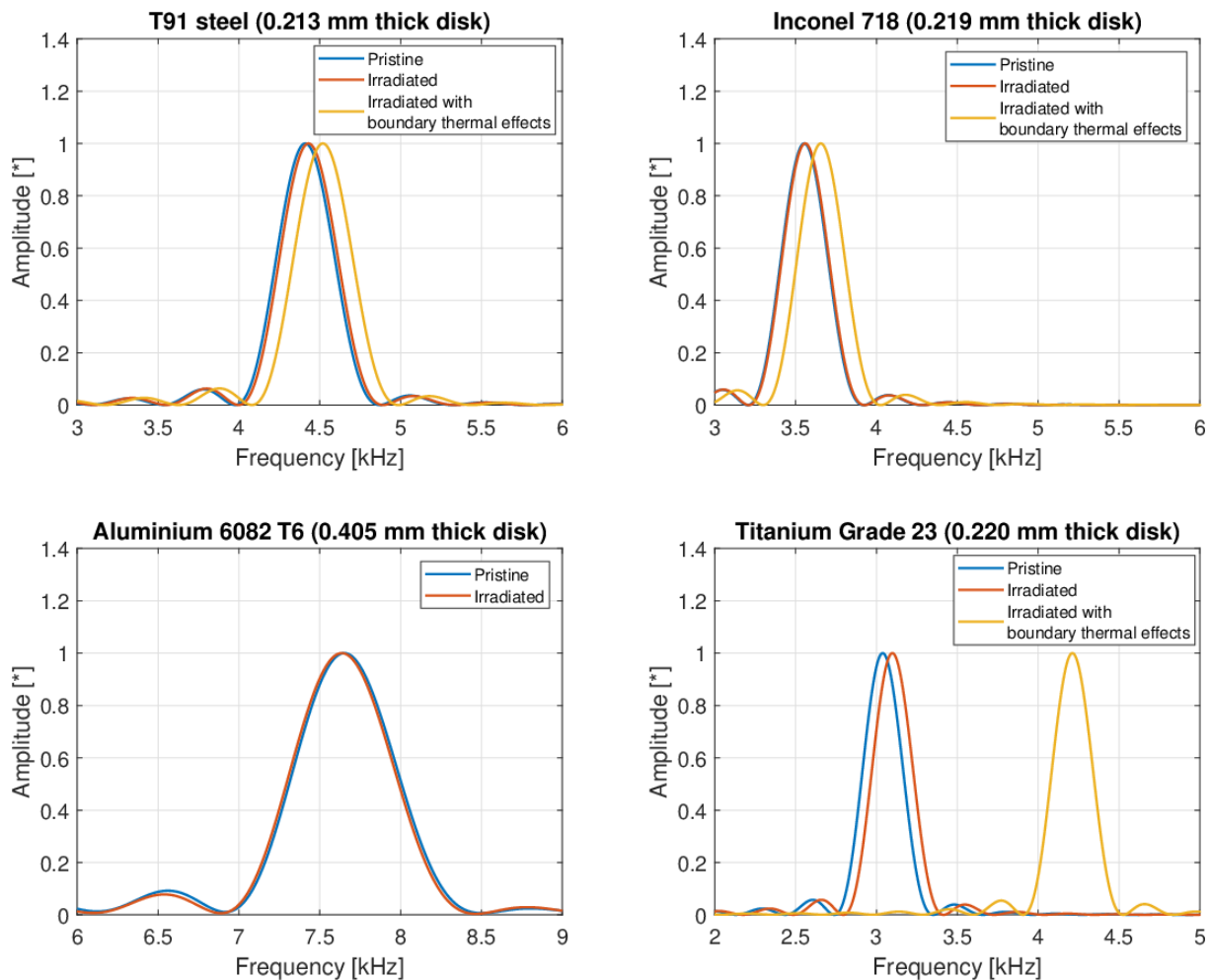


**Figure 4.28:** Comparison of the FFT results in terms of frequency of the ANSYS velocity signal for pristine and irradiated materials.

The increase in temperature translates to a thermal expansion of both rim and disk at the borders, with the effect of a tightening force applied to the boundary constraint. This

tightening force has the effect of stiffening of the springs of the Elastic Support, which results in increasing the EFS and, therefore, in increasing the frequency.

In light of these considerations, the value of EFS was increased for the last-pulse simulations to the point of the exact match with the frequency value from LDV measurements.

The figure 4.28 shows the change of frequency from pristine to irradiated material, with the same EFS, and to irradiated material, with different EFS to match the frequency to the LDV bending frequency.

Finally, the velocity signal damping experienced during the irradiation was implemented even in the numerical simulations. To do that, the damping ratio  $\zeta$  relative to the last-pulse LDV signals was calculated by the formula 3.2. Then, the **Stiffness damping**  $\beta$ , computed by the following formula [92], was directly inserted as an input in the simulation software:

$$\beta = \frac{\zeta}{\pi f_{b0}} \quad (4.16)$$

where  $f_{b0}$  is the last-pulse LDV bending frequency.

### Results of the numerical benchmarks

The figures 4.29-4.32 show the comparison between the time-dependent velocity signal from ANSYS Transient Velocity Probe (in the irradiated case, with the value of EFS changed) and the last-pulse LDV recorded measurements in terms of time-dependant velocity signal for all the materials. The Stiffness damping calculated by the equation 4.16 was properly inserted after having assessed the damping ratio from the LDV measurements.

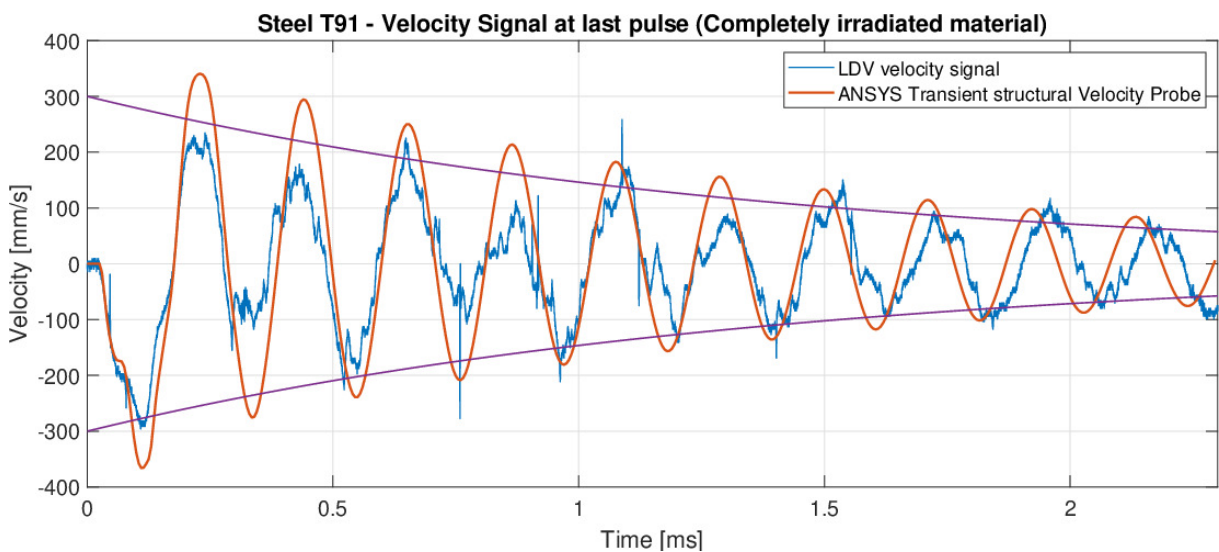


**Figure 4.29:** Time-dependent velocity signal measured by LDV and velocity results obtained by ANSYS Structural Transient simulations for Steel T91 at last pulse.

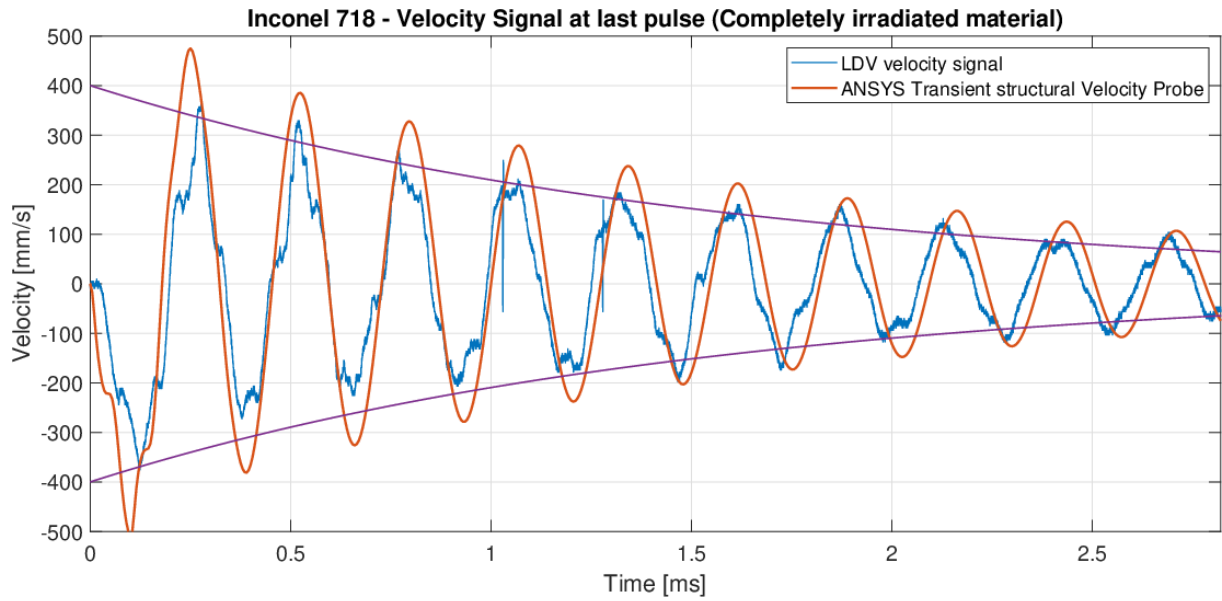


**Figure 4.30:** Time-dependent velocity signal measured by LDV and velocity results obtained by ANSYS Structural Transient simulations for Inconel 718 at last pulse.

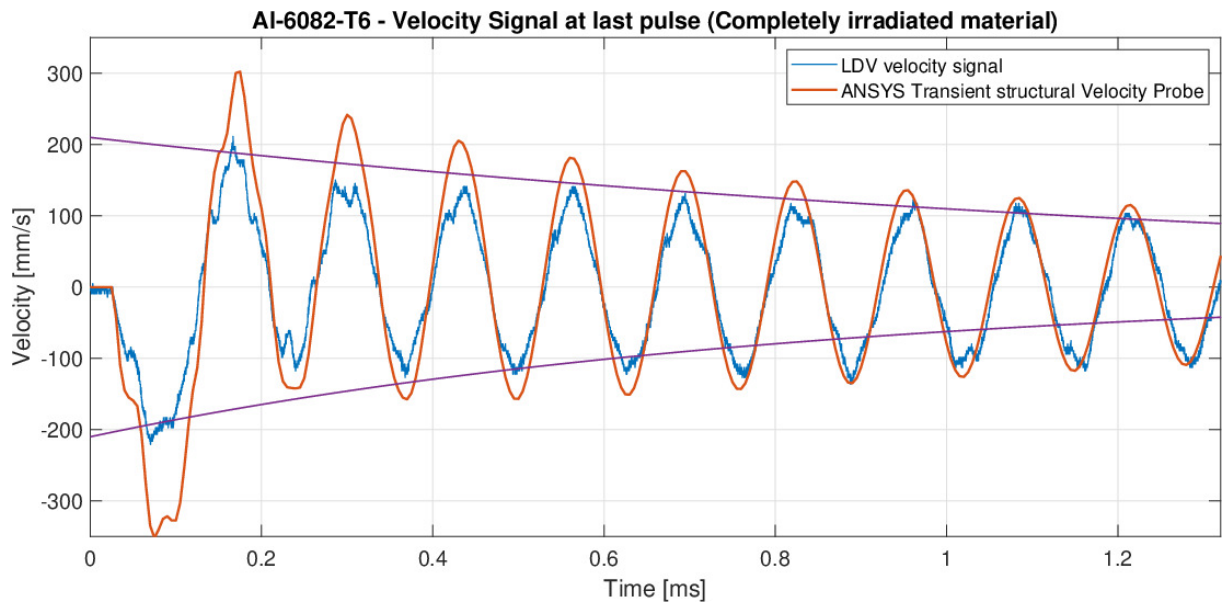


**Figure 4.31:** Time-dependent velocity signal measured by LDV and velocity results obtained by ANSYS Structural Transient simulations for Al-6082-T6 at last pulse.

The amplitude of the numerical signals results to be a little larger, but still in line with the LDV signal. In the case of the signals of Ti Gr. 23 samples, this difference is more pronounced, and it is probably due to the fact that the ion flux slightly decreased in the final stages of GSI irradiation (from  $5.0 \cdot 10^9$  ions/cm<sup>2</sup> to approximately  $4.0 \cdot 10^9$  ions/cm<sup>2</sup>), while the specific heat power deposited inside the "Deposition volume" was maintained constant and equal to the value computed for the first-pulse irradiation (cf. figure 3.14).

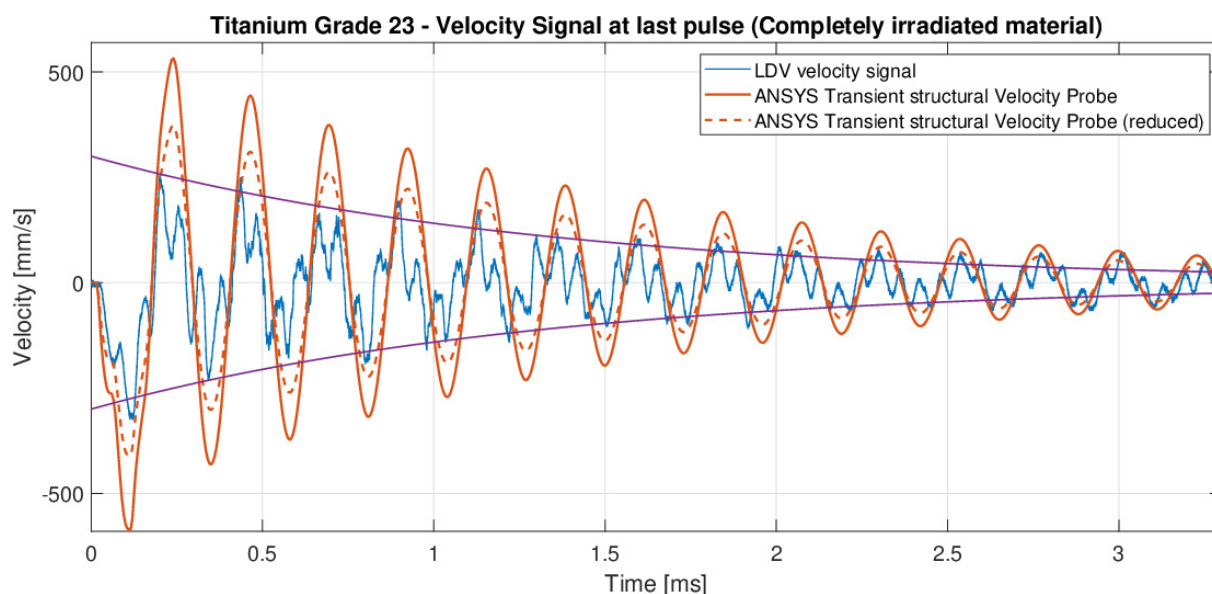


**Figure 4.32:** Time-dependent velocity signal measured by LDV and velocity results obtained by ANSYS Structural Transient simulations for Titanium Grade 23 at last pulse.

The bar plot in figure 4.33 was used to give a qualitative indication of which effect (Young's modulus change or change of the boundary conditions due to the variation of temperature) mostly influences the change of frequency between the first and last pulse.

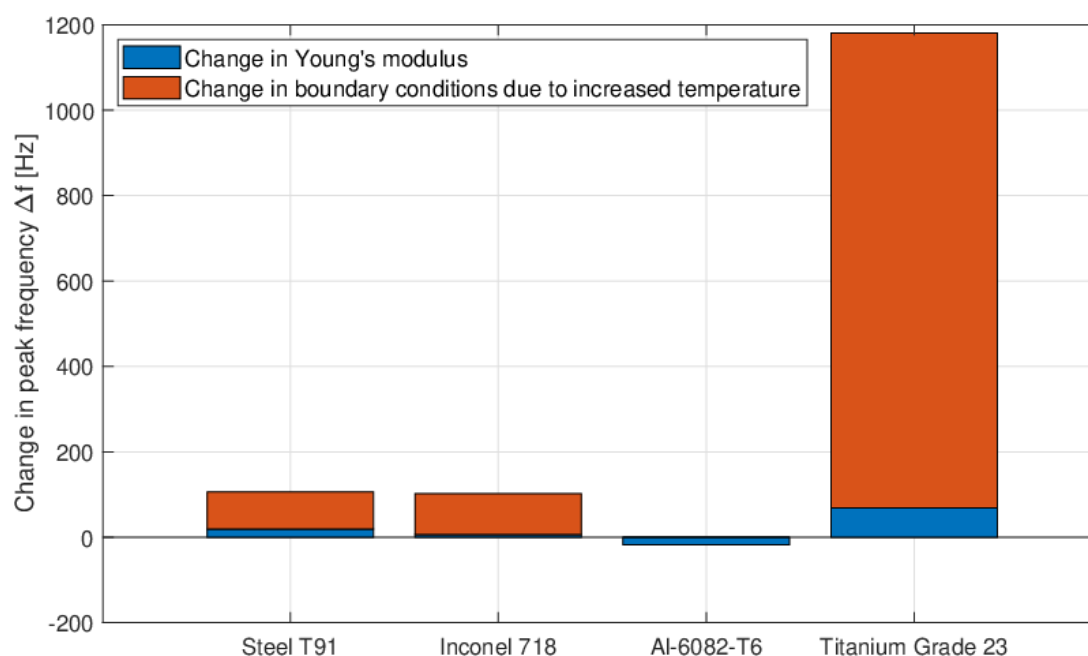


**Figure 4.33:** Effect of Young's modulus change and change of the boundary conditions due to the variation of temperature on the irradiated samples.

Finally, the table 4.3 summarises the frequency values obtained from experimental, analytical and numerical analyses. The analytical calculations for irradiated samples were carried out (for both free and simply-supported edge conditions) by using the well-known

equation 2.34:

$$f_{b0} = \frac{\lambda_{b0}^2}{2\pi a^2} \sqrt{\frac{\bar{E}h^2}{12\rho(1-\nu^2)}} \quad (4.17)$$

where  $\bar{E}$  is the volume-weighted average Young's modulus:

$$\bar{E} = \frac{E_{pris}(V_{tot} - V_{irr}) + E_{irr}V_{irr}}{V_{tot}} \quad (4.18)$$

where  $E_{pris}$  and  $E_{irr}$  are the pristine and irradiated Young's modulus, respectively, as derived from the microindentation results (cf. table 3.6). The preponderance of the thermal boundary effects on the radiation damage (change of Young's modulus) of the irradiated samples is, once again, proved by a simple consideration that spontaneously emerges from observing the difference between the frequency values calculated analytically: the irradiated volume is too small (no more than the 2.5% of the total volume) to affect so strongly the natural bending frequency of the samples.

Materials	Frequency in pristine samples					
	Experimental (LDV)	Analytical		Numerical (ANSYS)		
		Simply-Supported	Free Edge	EFS	Modal	Transient
<b>Steel T91</b>	4411	3173,57	4688,96	930,00	4500,90	4411,39
<b>Inconel 718</b>	3550	3102,00	4587,52	338,00	3630,00	3553,80
<b>Al-6082-T6</b>	7656	6494,55	9582,01	1095,00	7817,30	7652,48
<b>Ti Grade 23</b>	3039	3373,62	4976,10	24,00	3108,60	3038,85
Materials	Frequency in irradiated samples					
	Experimental (LDV)	Analytical		Numerical (ANSYS)		
		Simply-Supported	Free Edge	EFS	Modal	Transient
<b>Steel T91</b>	4517	3175,59	4691,96	1070,00	4604,90	4518,99
<b>Inconel 718</b>	3656	3103,07	4589,10	393,00	3731,80	3655,82
<b>Al-6082-T6</b>	7639	6490,89	9576,60	1095,00	7786,30	7634,75
<b>Ti Grade 23</b>	4217	3392,41	5003,82	325,00	4285,30	4210,90

**Table 4.3:** Summary table of the first-order bending frequencies obtained by experimental measurements, analytical calculations and numerical simulations.



# Chapter 5

## Conclusions

The objective of this thesis has been the research and the study of materials to be adopted in future beam windows. A beam window is any type of thin interface of separation traversed by particle beams which is located between the accelerator vacuum beamline and an external environment at higher pressure. The increasingly high energies of the new generations of accelerator facilities as well as the development of innovative high-power proton beam applications, such as Spallation Neutron Sources and Accelerator-driven systems, require a detailed investigation of the materials of these components in terms of dynamic response to severe and quasi-instantaneous thermal loads.

In this thesis, an extensive bibliographical research has been first carried out focusing on materials adopted for beam-windows applications in accelerator facilities and nuclear research centres worldwide. This has led to a broad selection of materials considered attractive which have undergone a series of preliminary analytical studies.

As a result, a shortlist of four materials deemed interesting for further testing has been derived. In particular, such materials have been chosen to be exposed to short-pulsed U-ions beams irradiation at the M3-branch beamline of the GSI *Helmholtzzentrum für Schwerionenforschung* in Darmstadt.

Disc-shaped samples of four materials (Steel T91, Inconel 718, Al-6082-T6 and Titanium Grade 23) were irradiated with U-ion pulses with GeV kinetic energy. Beam-induced heating of the samples was controlled with a thermal camera, while the dynamic response of the targets was monitored by recording the surface velocity signal of the samples using Laser Doppler Vibrometry. The mechanical properties of the specimens have been explored through post-irradiation examinations, including measurements of microindentation and SEM spectroscopy.

Experimental findings have been investigated and compared with the results of analytical and numerical analyses. The SRIM-2013 Monte Carlo simulation-based software has been used to assess relevant parameters for the transport of ions in targets, including

the range, the stopping power and the displacements-per-atom (dpa), the most common quantity to predict the operating lifetime of materials in radiation environments. ANSYS Workbench was used to numerically benchmark the experimental data acquired from the LDV, the Thermal Camera and the microindentation measurements by implementing appropriate thermo-mechanical models.

Numerical simulations have shown that no clear indication of the state of damage of the irradiated samples (modelled as a change of Young's modulus in the beam spot region) can be derived from a consequent change in the frequency content associated to the samples' dynamic response to beam impacts, measured via a shift in the bending frequency of the samples.

The microindentation findings have recognised a slight hardening of the materials irradiated (in particular for Titanium Grade 5 ELI), as confirmed by the images from the SEM microscopy. However, this change in Young's modulus does not greatly modify the frequency response. In the first place, this limited relevance can be attributed to the small portion of irradiated volume (1-2% of the total volume), especially for metallic samples, in which a large part of the beam irradiation is arrested on the front surface, with short penetration depth. In the second place, the condition that most affects the shift of the bending frequency is to be found in the variation of the boundary conditions due to:

- a mechanical effect associated with beam impact which, in presence of non-perfectly rigid clamped conditions implemented in the tests, caused a shift of the boundary conditions experienced by the samples from the simply-supported case to the free edge one. This behaviour was particularly evident for Steel T91 and Titanium 23 samples: in the dynamic response of these materials, in fact, a first phase characterised by large amplitudes of the oscillations and a quasi simply-supported boundary condition was followed by a decrement of the vibration response and a consequent transition to a free edge boundary condition. This occurrence was confirmed by a mostly bi-modal distribution of the power spectral density of both experimental and numerical response, where the power of the signal was found to gather around the frequencies characteristic of a simply-supported and a free edge condition.
- a thermal effect due to the gradual increase of temperature during irradiation. The irradiation-induced thermal expansion of both rim and disk at the borders produced in fact the effect of a tightening force applied to the boundaries, causing a consequent shift in the frequency content of the beam-induced vibrations. It is no coincidence that the frequency of the Aluminium alloy, the material with the highest thermal diffusivity, is almost not altered as the fluence increases, whilst the frequency of the Titanium Grade 23, the metal with the lowest diffusivity, is dramatically influenced by the increasing temperature during the whole irradiation experiment.

The accurate considerations of such effects in the implementation of the boundary conditions of the numerical models granted a very good agreement with the experimental data for all tested materials, allowing an enhanced dynamic characterisation via the extraction of additional constitutive parameters (e.g. damping ratio).

The next phase of the experimental campaign, which will see the definition of a more refined procedure for the identification of irradiation-induced damages in the samples via the analysis of their dynamic response, will encompass the effects associated with boundary conditions variations taking place during the test resorting to a more accurate testing routine.

Finally, a viable alternative to enhance the quality of the online measurements of the dynamic phenomena may be to move from monitoring techniques centred on the global motion of a system (identification of the natural frequency of vibration) towards techniques based on wave propagation, such as the Lamb waves: the latter high-frequency monitoring systems result to be more suitable for assessing local damages on the irradiated samples and, besides, propagation phenomena are less dependent on the boundary conditions, which — as has been seen during the development of the thesis — are very difficult to control in the experimental tests.

# Bibliography

1. Wang, H. *et al.* *Primary Study of High-Power Graphene Beam Window in 9th International Particle Accelerator Conference* (June 2018).
2. Monteil, M., Blanco, J. & Veness, R. A transparent vacuum window for high-intensity pulsed beams. *Vacuum. Selected Papers from the 11th European Vacuum Conference, EVC-11 8th Iberian Vacuum Meeting, IVM-8 6th European Topical Conference on Hard Coatings, ETCHC-6, 20-24 September 2010, Salamanca, Spain* **85**, 1165–1169. ISSN: 0042-207X. <https://www.sciencedirect.com/science/article/pii/S0042207X11001199> (2021) (June 5, 2011).
3. Correa, A. A. Calculating electronic stopping power in materials from first principles. *Computational Materials Science* **150**, 291–303. ISSN: 0927-0256. <https://www.sciencedirect.com/science/article/pii/S0927025618302234> (2022) (July 1, 2018).
4. Gupta, M. *Calculation of radiation length in materials - CERN PH-EP-Tech-Note-2010-013* [https://www.google.com/search?q=radiation+length+for+protons&rlz=1C1CHBF\\_itIT980IT980&oq=radiation+length+for+protons&aqs=chrome..69i57j33i160l2.12350j0j7&sourceid=chrome&ie=UTF-8](https://www.google.com/search?q=radiation+length+for+protons&rlz=1C1CHBF_itIT980IT980&oq=radiation+length+for+protons&aqs=chrome..69i57j33i160l2.12350j0j7&sourceid=chrome&ie=UTF-8). (Accessed on 09/21/2022). July 2010.
5. Hotchi, H. High-power proton accelerators for pulsed spallation neutron sources. *AAPPS Bulletin* **31**, 23. ISSN: 2309-4710. <https://doi.org/10.1007/s43673-021-00025-0> (2022) (Oct. 4, 2021).
6. Klein, H. *Spallation Neutron Sources* in. *Proceedings of the 1994 International Linac Conference, Tsukuba, Japan (1994)*, 6. <https://accelconf.web.cern.ch/l94/papers/tu1-02.pdf>.
7. Bauer, G. S. Physics and technology of spallation neutron sources. *Nuclear Instruments and Methods in Physics Research Section A: Accelerators, Spectrometers, Detectors and Associated Equipment* **463**, 505–543. ISSN: 0168-9002. <https://www.sciencedirect.com/science/article/pii/S016890020100167X> (2001).

8. Ferrari, A. & Ziemann, V. *Conceptual design of a vacuum window at the exit of the CLIC post-collision line* [https://www.eurotev.org/reports\\_\\_presentations/eurotev\\_reports/2008/e1090/EUR0TeV-Report-2008-009.pdf](https://www.eurotev.org/reports__presentations/eurotev_reports/2008/e1090/EUR0TeV-Report-2008-009.pdf). (Accessed on 09/21/2022). Feb. 2008.
9. Murdoch, C. *et al.* *Beam dump window design for the spallation neutron source in Proceedings of the 2003 Bipolar/BiCMOS Circuits and Technology Meeting (IEEE Cat. No.03CH37440)* 2003 Bipolar/BiCMOS Circuits and Technology Meeting (IEEE Cat. No.03CH37440). **3** (IEEE, Portland, OR, USA, 2003), 1467–1469. ISBN: 978-0-7803-7738-7. <http://ieeexplore.ieee.org/document/1288563/> (2022).
10. Wang, H., Jing, H., Qu, H. & Tang, J. Design of High-power Graphene Beam Window. *Proceedings of the 5th Int. Particle Accelerator Conf. IPAC2014*. In collab. with Christine (Ed.), P.-J.-G., Gianluigi (Ed.), A., Peter (Ed.), M. & RW (Ed.) Volker, S. Artwork Size: 3 pages, 0.374 MB ISBN: 9783954501328 Medium: PDF Publisher: JACoW Publishing, Geneva, Switzerland, 3 pages, 0.374 MB. <http://jacow.org/ipac2014/doi/JACoW-IPAC2014-MO0CA03.html> (2022) (2014).
11. Ader, C., Mcgee, M., Nobrega, L. & Voirin, E. *Overview of Fabrication Techniques and Lessons Learned With Accelerator Vacuum Windows* (Aug. 23, 2018).
12. Western, J. L. Mechanical safety subcommittee guideline for design of thin windows for vacuum vessels, FERMILAB-TM-1380 (Mar. 1993).
13. Roark, R. & Young, W. *Roark's Formulas for Stress and Strain* ISBN: 978-0-07-100373-5. <https://books.google.it/books?id=JM5yAQAACAAJ> (McGraw-Hill, 1989).
14. *Carbon Fiber-Reinforced Carbon* SGL Carbon Group ().
15. Monteil, M. *Review of Beam Vacuum Windows at CERN* <https://indico.cern.ch/event/114535/attachments/47147/67804/Monteil-26-Nov-2010.pdf>. (Accessed on 09/20/2022). Nov. 2010.
16. Accettura, C. *Investigation of radiation damage effects in HL-LHC collimator materials* PhD thesis (Nov. 1, 2021). <https://zenodo.org/record/5636524> (2021).
17. Presland, A., Ramos, D., Goddard, B., Jimenez, J.-M. & Veness, R. *A Large Diameter Entrance Window for the LHC Beam Dump Line in Proceedings of the 2005 Particle Accelerator Conference* 2005 Particle Accelerator Conference (IEEE, Knoxville, TN, USA, 2005), 1698–1700. ISBN: 978-0-7803-8859-8. <http://ieeexplore.ieee.org/document/1590882/> (2021).
18. *CNGS Reference Parameter List* (Oct. 3, 2005).

19. McClintock, D. A., Janney, J. G. & Parish, C. M. Characterization of an explosively bonded aluminum proton beam window for the Spallation Neutron Source. *Journal of Nuclear Materials* **450**, 163–175. ISSN: 0022-3115. <https://www.sciencedirect.com/science/article/pii/S0022311514000786> (2014).
20. Ader, C. R. *et al.* Accelerator Vacuum Windows: A Review of Past Research and a Strategy for the Development of a New Design for Improved Safety and Longevity for Particle Accelerators, 4.
21. Žohar, A., Lengar, I. & Snoj, L. Analysis of water activation in fusion and fission nuclear facilities. *Fusion Engineering and Design* **160**, 111828. ISSN: 0920-3796. <https://www.sciencedirect.com/science/article/pii/S0920379620303768> (2020).
22. Wang, H. *et al.* The proton beam window for China Spallation Neutron Source. *Nuclear Instruments and Methods in Physics Research Section A: Accelerators, Spectrometers, Detectors and Associated Equipment* **1042**, 167448. ISSN: 0168-9002. <https://www.sciencedirect.com/science/article/pii/S0168900222007409> (2022).
23. Ader, C. *Overview of Fabrication Techniques and Lessons Learned With Accelerator Vacuum Windows* in. IPAC 2018 (Apr. 30, 2018). [https://accelconf.web.cern.ch/ipac2018/talks/mozgbe4\\_talk.pdf](https://accelconf.web.cern.ch/ipac2018/talks/mozgbe4_talk.pdf).
24. Dai, Y. *et al.* Summary on the preliminary assessment of the T91 window performance in the MEGAPIE conditions. *Nuclear Instruments and Methods in Physics Research Section A: Accelerators, Spectrometers, Detectors and Associated Equipment* **562**, 698–701. ISSN: 0168-9002. <https://www.sciencedirect.com/science/article/pii/S0168900206002609> (2006).
25. *Beryllium PF-60, Foil Grade, Matweb* <https://www.matweb.com/search/datasheet.aspx?matguid=491a2a0e251e44c491a7645e261a4e58&ckck=1>. (Accessed on 09/26/2022).
26. Kuksenko, V. *et al.* Irradiation effects in beryllium exposed to high energy protons of the NuMI neutrino source. *Journal of Nuclear Materials* **490**, 260–271. ISSN: 0022-3115. <https://www.sciencedirect.com/science/article/pii/S0022311516312867> (2017).
27. Monteil, M. *Inventory of windows for CERN accelerators / Document 1074871 (v.1)* (). <https://edms.cern.ch/ui/#!master/navigator/document?D:1178121776:1178121776:subDocs> (2022).
28. Densham, C. J., Fitton, M., Harvey-Fishenden, E. & Atherthon, A. Presentation at Neutrino Beams and Instrumentation (NBI2019), Fermilab, USA, Oct. 2019, 25.



29. Ishida, T. *et al.* Tensile behavior of dual-phase titanium alloys under high-intensity proton beam exposure: Radiation-induced omega phase transformation in Ti-6Al-4V. *Journal of Nuclear Materials* **541**, 152413. ISSN: 00223115. <https://linkinghub.elsevier.com/retrieve/pii/S0022311520310217> (2022) (Dec. 2020).
30. Ishida, T. *et al.* *Radiation Damage Studies on Titanium Alloys as High Intensity Proton Accelerator Beam Window Materials in Proceedings of the 14th International Workshop on Spallation Materials Technology* Proceedings of the 14th International Workshop on Spallation Materials Technology (Journal of the Physical Society of Japan, Fukushima, Japan, Feb. 6, 2020). ISBN: 978-4-89027-138-2. <https://journals.jps.jp/doi/10.7566/JPSCP.28.041001> (2022).
31. Pinson, J. *A window of opportunity: Physicists test titanium target windows for particle beam* News. <https://news.fnal.gov/2020/05/a-window-of-opportunity-physicists-test-titanium-target-windows-for-particle-beam/> (2022).
32. Byun, T. & Farrell, K. Tensile properties of Inconel 718 after low temperature neutron irradiation. *Journal of Nuclear Materials* **318**, 292–299. ISSN: 00223115. <https://linkinghub.elsevier.com/retrieve/pii/S0022311503000060> (2022) (May 2003).
33. Fincher, C. D. *et al.* Damage relief of ion-irradiated Inconel alloy 718 via annealing. *Nuclear Instruments and Methods in Physics Research Section B: Beam Interactions with Materials and Atoms* **479**, 157–162. ISSN: 0168-583X. <https://www.sciencedirect.com/science/article/pii/S0168583X20303189> (2020).
34. O'Brien, E. M. *et al.* Novel design and diagnostics improvements for increased production capacity and improved reliability at the Los Alamos Isotope Production Facility. *Nuclear Instruments and Methods in Physics Research Section A: Accelerators, Spectrometers, Detectors and Associated Equipment* **956**, 163316. ISSN: 0168-9002. <https://www.sciencedirect.com/science/article/pii/S0168900219315578> (2020).
35. McClintock, D. A. *et al.* Observations of radiation-enhanced ductility in irradiated Inconel 718: Tensile properties, deformation behavior, and microstructure. *Acta Materialia* **231**, 117889. ISSN: 1359-6454. <https://www.sciencedirect.com/science/article/pii/S1359645422002749> (2022).
36. Bach, H. T. *et al.* Proton irradiation damage of an annealed Alloy 718 beam window. *Journal of Nuclear Materials* **459**, 103–113. ISSN: 0022-3115. <https://www.sciencedirect.com/science/article/pii/S0022311514010484> (2015).

37. Maloy, S. A., Romero, T. J., Hosemann, P., Toloczko, M. B. & Dai, Y. Shear punch testing of candidate reactor materials after irradiation in fast reactors and spallation environments. *Journal of Nuclear Materials* **417**, 1005–1008. ISSN: 0022-3115. <https://www.sciencedirect.com/science/article/pii/S0022311511001887> (2011).
38. Brager, H. R. & Garner, F. A. Influence of neutron spectra on the radiation-induced evolution of AISI 316. *Journal of Nuclear Materials* **108-109**, 347–358. ISSN: 0022-3115. <https://www.sciencedirect.com/science/article/pii/0022311582905049> (1982).
39. G.Bregliozzi. *New LHC beam dump entrance window* [https://indico.cern.ch/event/1077835/contributions/4615043/attachments/2345211/4010735/TE\\_VSC\\_EVIAN\\_2021\\_LHC\\_BEAM\\_DUMP\\_Windows.pdf](https://indico.cern.ch/event/1077835/contributions/4615043/attachments/2345211/4010735/TE_VSC_EVIAN_2021_LHC_BEAM_DUMP_Windows.pdf). (Accessed on 10/03/2022). Nov. 23.
40. *LHC - Beam Dump* <https://www.lhc-facts.ch/index.php?page=beamdump>. (Accessed on 10/03/2022).
41. Dai, Y. *et al.* Microstructure in Martensitic Steel DIN 1.4926 after 800 MeV proton irradiation. *Journal of Nuclear Materials* **265**, 203–207. ISSN: 0022-3115. <https://www.sciencedirect.com/science/article/pii/S0022311598005054> (1999).
42. SUGAWARA, T., NISHIHARA, K., OBAYASHI, H., KURATA, Y. & OIGAWA, H. Conceptual Design Study of Beam Window for Accelerator-Driven System. *Journal of Nuclear Science and Technology* **47**, 953–962. eprint: <https://www.tandfonline.com/doi/pdf/10.1080/18811248.2010.9720974>. <https://www.tandfonline.com/doi/abs/10.1080/18811248.2010.9720974> (2010).
43. Zanini, L. *et al.* Experience from the post-test analysis of MEGAPIE. *Journal of Nuclear Materials* **415**, 367–377. ISSN: 0022-3115. <https://www.sciencedirect.com/science/article/pii/S0022311511003965> (2011).
44. Sugawara, T., Eguchi, Y., Obayashi, H., Iwamoto, H. & Tsujimoto, K. Conceptual design study of beam window for accelerator-driven system with subcriticality adjustment rod. *Nuclear Engineering and Design* **331**, 11–23. ISSN: 0029-5493. <https://www.sciencedirect.com/science/article/pii/S0029549318300864> (2018).
45. Sgobba, S. *Vacuum for accelerators: introduction to materials and properties* June 2020.

46. Dai, Y. & Hamaguchi, D. Mechanical properties and microstructure of AlMg3 irradiated in SINQ Target-3. *Journal of Nuclear Materials* **343**, 184–190. ISSN: 0022-3115. <https://www.sciencedirect.com/science/article/pii/S0022311505001637> (2005).
47. Lopez Daniel, B. *An engineering review of the ISIS facility extracted proton beam windows* [https://indico.fnal.gov/event/15204/contributions/30159/attachments/18935/23730/21-An\\_engineering\\_review\\_of\\_ISIS\\_PBW.pdf](https://indico.fnal.gov/event/15204/contributions/30159/attachments/18935/23730/21-An_engineering_review_of_ISIS_PBW.pdf). (Accessed on 10/08/2022).
48. Takada, H. *et al.* Materials and Life Science Experimental Facility at the Japan Proton Accelerator Research Complex I: Pulsed Spallation Neutron Source. *Quantum Beam Science* **1**. ISSN: 2412-382X. <https://www.mdpi.com/2412-382X/1/2/8> (2017).
49. Japan Atomic Energy Agency Ibaraki (Japan), T. *Technical design report of spallation neutron source facility in J-PARC* JAEA-Technology–2011-035 INIS Reference Number: 43119260 (Japan, 2012), 550.
50. Wang, H.-J. *et al.* Thermal analysis and optimization of proton beam window for the CSNS. *Chinese Physics C* **37**, 077001. <https://doi.org/10.1088/1674-1137/37/7/077001> (July 2013).
51. Farrell, K. Microstructure and tensile properties of heavily irradiated 5052-0 aluminum alloy. *Journal of Nuclear Materials* **97**, 33–43. ISSN: 0022-3115. <https://www.sciencedirect.com/science/article/pii/0022311581904153> (1981).
52. Farrell, K. *Assessment of aluminum structural materials for service within the ANS reflector vessel* ORNL/TM–13049 INIS Reference Number: 27048252 (United States, 1995), 45.
53. Singh, B. N., Horsewell, A., Sommer, W. F. & Lohmann, W. Gas accumulation at grain boundaries during 800 MeV proton irradiation of aluminium and aluminium-alloys. *Journal of Nuclear Materials* **141-143**, 718–722. ISSN: 0022-3115. <https://www.sciencedirect.com/science/article/pii/0022311586900796> (1986).
54. Vivanco, R. *et al.* ESS Proton Beam Window Design Update. *Journal of Physics: Conference Series* **1021**, 012065. <https://doi.org/10.1088/1742-6596/1021/1/012065> (May 2018).
55. Butzek, M., Wolters, J. & Laatsch, B. Proton beam window for High Power Target Application, 15.

56. Quaranta, E. *Investigation of collimator materials for the High Luminosity Large Hadron Collider* Presented 18 Jul 2017 (June 2017). <http://cds.cern.ch/record/2276659>.
57. Bertarelli, A. Beam-Induced Damage Mechanisms and their Calculation. en. *CERN Yellow Reports*, Vol 2 (2016): Proceedings of the 2014 Joint International Accelerator School: Beam Loss and Accelerator Protection. <https://e-publishing.cern.ch/index.php/CYR/article/view/234> (2016).
58. *Atomic and Nuclear Properties of Materials for more than 350 materials* <https://pdg.lbl.gov/2022/AtomicNuclearProperties/index.html>. (Accessed on 10/13/2022).
59. Bolz, P. *et al. Dynamic Radiation Effects Induced by Short-Pulsed GeV U-Ion Beams in Graphite and h-BN Targets* Sept. 2021. <https://doi.org/10.1155/2021/8825142>.
60. Bolz, P. *Analyzation of radiation resistance of carbon-based materials for accelerator components* PhD thesis (Technische Universität Darmstadt, Mar. 22, 2022). 136 pp.
61. Carra, F. *Thermomechanical Response of Advanced Materials under Quasi Instantaneous Heating* PhD thesis (Politecnico di Torino, May 2018). <https://doi.org/10.5281/zenodo.1240450>.
62. Blevins, R. D. & Plunkett, R. Formulas for natural frequency and mode shape. *Journal of Applied Mechanics* **47**, 461 (1980).
63. Leissa, A. W. Vibration of Plates. *NASA SP-160*, 362 (1969).
64. Narita, Y. *FREE VIBRATION OF ELASTIC PLATES WITH VARIOUS SHAPES AND BOUNDARY CONDITIONS* PhD thesis (Hokkaido University Collection of Scholarly and Academic Papers (HUSCAP), Mar. 1980). <http://hdl.handle.net/2115/32630>.
65. Wah, T. Vibration of Circular Plates. *The Journal of the Acoustical Society of America* **34**, 275–281. ISSN: 0001-4966. <http://asa.scitation.org/doi/10.1121/1.1928110> (2022) (Mar. 1962).
66. Lin, S.-Y. Coupled vibration and natural frequency analysis of isotropic cylinders or disks of finite dimensions. *Journal of Sound and Vibration* **185**, 193–199. ISSN: 0022-460X. <https://www.sciencedirect.com/science/article/pii/S0022460X85703744> (1995).

67. Sgobba, S. *et al.* Metallurgical assessment of large size tensioning components for the precompression structure of the ITER central solenoid. *Fusion Engineering and Design* **170**, 112543. ISSN: 0920-3796. <https://www.sciencedirect.com/science/article/pii/S0920379621003197> (2021).
68. *EN 10204/3.1 Inspection Certificate - Grade of steel 1.4903* 1. T91 Steel. SIJ Metal Ravne (Mar. 2018).
69. *44.05.10.A - ROUND BARS - TITANIUM* 1. Titanium Grade 23. CERN Stores Catalogue (Apr. 2022).
70. *44.02.07 - ROUND BARS - EN AW-6082 - ANTICORODAL* 1. EN AW-6082 T6. CERN Stores Catalogue (Apr. 2022).
71. *News GSI*. <https://www.gsi.de/en/start/news> (2022).
72. *UNILAC GSI*. <https://www.gsi.de/work/beschleunigerbetrieb/beschleuniger/unilac/unilac> (2022).
73. *GSI - ENSAR2 - JYVÄSKYLÄN YLIOPISTO Wiki* <https://wiki.jyu.fi/display/ensar2/GSI> (2022).
74. *The MEVVA ion source for high current metal ion implantation - ScienceDirect* <https://www.sciencedirect.com/science/article/abs/pii/S0168583X87908263>. (Accessed on 07/21/2022).
75. *M-branch GSI*. [https://www.gsi.de/work/forschung/appamml/materialforschung/irradiation\\_facilities/m\\_branch](https://www.gsi.de/work/forschung/appamml/materialforschung/irradiation_facilities/m_branch) (2022).
76. Lindsten, F. *A remark on zero-padding for increased frequency resolution* <https://www.control.isy.liu.se/en/student/tsrt78/zeropadding.pdf>. (Accessed on 09/06/2022). Nov. 2010.
77. *Rise Time, Frequency Response, and 3 dB Bandwidth* [https://www.thorlabs.com/images/TabImages/Rise\\_Time\\_3dB\\_Bandwidth\\_Relationship\\_Lab\\_Fact.pdf](https://www.thorlabs.com/images/TabImages/Rise_Time_3dB_Bandwidth_Relationship_Lab_Fact.pdf). (Accessed on 09/07/2022). 2019.
78. Beake, B. *et al.* NanoTest On-line Help File Version 1.0 and NanoTest Manual Version 3.0, 121 (2004).
79. Oliver, W. C. & Pharr, G. M. An improved technique for determining hardness and elastic modulus using load and displacement sensing indentation experiments. *Journal of Materials Research; (United States)*. ISSN: 0884-2914. <https://www.osti.gov/biblio/7238008> (June 1992).

80. Oliver, W. C. & Pharr, G. M. Measurement of hardness and elastic modulus by instrumented indentation: Advances in understanding and refinements to methodology. *Journal of Materials Research* **19**, 3–20 (2004).
81. Brooks, C. R. & McGill, B. L. The application of scanning electron microscopy to fractography. *Materials Characterization* **33**, 195–243. ISSN: 1044-5803. <https://www.sciencedirect.com/science/article/pii/1044580394900450> (1994).
82. Valenzuela, J. G. Optimization of Graphite-Matrix Composites for Collimators in the LHC Upgrade, 292.
83. Ghossain, M. O. E. Calculations of Stopping Power, and Range of Ions Radiation (Alpha Particles) Interaction with Different Materials and Human Body Parts. *International Journal of Physics* **5**. Number: 3 Publisher: Science and Education Publishing, 92–98. <http://www.sciepub.com/IJP/abstract/7521> (2022) (May 20, 2017).
84. Nordlund, K. *et al.* Primary radiation damage: A review of current understanding and models. *Journal of Nuclear Materials* **512**, 450–479. ISSN: 0022-3115. <https://www.sciencedirect.com/science/article/pii/S002231151831016X> (2022) (Dec. 15, 2018).
85. Norgett, M. J., Robinson, M. T. & Torrens, I. M. A proposed method of calculating displacement dose rates. *Nuclear Engineering and Design* **33**, 50–54. ISSN: 0029-5493. <https://www.sciencedirect.com/science/article/pii/0029549375900357> (1975).
86. Ziegler, J. F. *SRIM - The Stopping and Range of Ions in Matter* <http://www.srim.org/>. (Accessed on 10/05/2022).
87. Agarwal, S., Lin, Y., Li, C., Stoller, R. E. & Zinkle, S. J. On the use of SRIM for calculating vacancy production: Quick calculation and full-cascade options. *Nuclear Instruments and Methods in Physics Research Section B: Beam Interactions with Materials and Atoms* **503**, 11–29. ISSN: 0168-583X. <https://www.sciencedirect.com/science/article/pii/S0168583X21002299> (2021).
88. ANSYS — Engineering Simulation Software <https://www.ansys.com/en-gb>. (Accessed on 12/05/2022).
89. ImageJ <https://imagej.net/software/imagej/>. (Accessed on 12/05/2022).
90. Ansys SpaceClaim — 3D CAD Modeling Software <https://www.ansys.com/en-gb/products/3d-design/ansys-spaceclaim>. (Accessed on 12/05/2022).



91. Imaoka, S. *Elastic Foundation Stiffness - ANSYS Technical Support Group* <https://www.yumpu.com/en/document/read/16905292/elastic-foundation-stiffness-ansys-users>. (Accessed on 12/06/2022).
92. *Fundamentals of Damping - Damping Effects, lesson 2* <https://courses.ansys.com/wp-content/uploads/2020/12/2.6.2-Fundamentals-of-Damping-New-Template.pdf>. (Accessed on 12/06/2022).